

# The fate of charge carriers in solar materials investigated by time resolved X-ray and optical spectroscopy

THÈSE N° 7438 (2017)

PRÉSENTÉE LE 31 JANVIER 2017

À LA FACULTÉ DES SCIENCES DE BASE  
LABORATOIRE DE SPECTROSCOPIE ULTRARAPIDE  
PROGRAMME DOCTORAL EN PHOTONIQUE

ÉCOLE POLYTECHNIQUE FÉDÉRALE DE LAUSANNE

POUR L'OBTENTION DU GRADE DE DOCTEUR ÈS SCIENCES

PAR

Fabio Giacomo SANTOMAURO

acceptée sur proposition du jury:

Prof. J.-E. Moser, président du jury  
Prof. M. Chergui, directeur de thèse  
Prof. V. Sundström, rapporteur  
Prof. E. Vauthey, rapporteur  
Prof. A. Hagfeldt, rapporteur



ÉCOLE POLYTECHNIQUE  
FÉDÉRALE DE LAUSANNE

Suisse  
2017



To my best discovery of all,

Elena





# Abstract

This thesis investigates the photoinduced charge carrier dynamics of  $\text{TiO}_2$  nanoparticles and  $\text{CsPbX}_3$  ( $\text{X} = \text{Cl}, \text{Br}$ ) nanocrystals, by means of ultrafast x-ray absorption spectroscopy (XAS) and transient absorption spectroscopy (TAS).

$\text{TiO}_2$  is among the most promising transition metal oxides for applications such as photocatalysis and photovoltaics. In the latter,  $\text{TiO}_2$  has been used over the years in dye-sensitized solar cells (DSSCs) as electron transport material.  $\text{CsPbX}_3$  belongs to the class of lead halide perovskites and is currently one of the most investigated materials for solar energy applications, due to the high conversion efficiencies and ease of preparation. These materials are commonly used in solar cells with an all-solid-state DSSC architecture as light absorbers.

Solar energy conversion is governed by the generation of charge carriers, their subsequent evolution as excitons or free charge carriers, and eventually their localization. Ultrafast spectroscopy can gain insights into the evolution of charge carriers by following their dynamics in real time. For this reason, ultrafast XAS was the main technique used in this work, as it combines elemental and structural sensitivity to study the fate of charge carriers and their evolution under operating conditions.

The early stages of electron localization in  $\text{TiO}_2$  anatase nanoparticles upon photoexcitation at 3.5 eV, are investigated by fs-XAS at the Ti K-edge using the synchrotron slicing technique. The results show that localization of electrons at Ti atoms occurs in  $< 300$  fs, forming  $\text{Ti}^{3+}$  centres, in or near the unit cell where the electron is excited. Moreover, electron localization is due to its trapping at pentacoordinated sites, mostly present in the surface shell region.

Similar conclusions are drawn for another polymorph of  $\text{TiO}_2$ , rutile, from ps-XAS at the Ti K-edge. Here electrons are trapped next to oxygen vacancies at 100 ps after photoexcitation. Electrons in rutile though, show a weaker tendency to localization than in anatase and this could explain the differences in photocatalytic performances between these two polymorphs.

In the second part of this thesis, the ultrafast charge carrier dynamics of  $\text{CsPb}(\text{ClBr})_3$  nanocrystals is investigated using fs-TAS in the visible region ( $\sim 1.8$ -3.1 eV) upon photoexcitation at 3.1 eV. This material represents an ideal system to study the ultrafast physics of lead halide perovskite in general, because ultrafast TA studies suggest that the charge carrier dynamics are similar to the organic-inorganic materials but do not suffer from the same stability issues. Here, the ultrafast transition from free charge carriers to excitons is observed in a fluence dependent study, which sheds light on the interpretation of a long lived spectral feature rising from a transient electroabsorption effect.

Finally, the charge carrier dynamics of CsPbX<sub>3</sub> (X = Cl, Br) is investigated using ps-XAS at the Br K-edge, the Pb L<sub>3</sub>-edge and Cs L<sub>2</sub>-edge upon photoexcitation at 3.5 eV. The Br K-edge transients at 100 ps delay show evidence for a full electron charge being withdrawn from the Br atoms, *i.e.* the hole is localized due to formation of a small polaron. The transients at the Pb L<sub>3</sub>-edge point to the opposite, *i.e.* the electrons are fully delocalized as conduction band electrons and there is no hint of trapping. Lastly, the Cs L<sub>2</sub>-edge shows no transient signal, in agreement with predictions based on the partial density of states in the material.

**KEYWORDS:** *Ultrafast spectroscopy, time-resolved x-ray absorption spectroscopy, transient absorption spectroscopy, Titanium dioxide, Lead halide perovskites, photovoltaics, photocatalysis*

# Sommario

Questa tesi investiga le dinamiche fotoindotte dei portatori di carica in nanoparticelle di  $\text{TiO}_2$  e nanocristalli di  $\text{CsPbX}_3$  ( $X = \text{Cl}, \text{Br}$ ), usando spettroscopia di assorbimento a raggi x ultraveloce e spettroscopia di assorbimento transiente.

$\text{TiO}_2$  è tra i più promettenti ossidi dei metalli di transizione per applicazioni come la fotocatalisi e il fotovoltaico. Per ciò che riguarda il fotovoltaico,  $\text{TiO}_2$  è stato usato negli anni nelle *dye sensitized solar cells* (DSSCs) come materiale atto al trasporto degli elettroni.  $\text{CsPbX}_3$  appartiene alla classe delle perovskiti a base di Piombo ed alogenuri ed è oggi tra i materiali più studiati per le applicazioni nel campo dell'energia solare, a causa delle alte efficienze di conversione e della facilità di preparazione. Questi materiali sono comunemente usati nelle celle solari con una architettura DSSC totalmente allo stato solido come assorbitori di luce.

La conversione dell'energia solare è governata dalla generazione dei portatori di carica, la loro evoluzione come eccitoni o cariche libere, ed infine la loro localizzazione. La spettroscopia ultraveloce può acquisire conoscenze nell'evoluzione dei portatori di carica osservandoli in tempo reale. Per questa ragione, la spettroscopia ultraveloce di assorbimento a raggi x è la principale tecnica usata in questo lavoro, poiché combina sensibilità strutturale ed elementare per studiare il destino dei portatori di carica e la loro evoluzione in condizioni operative.

I primi momenti della localizzazione dell'elettrone nelle nanoparticelle di anatasio  $\text{TiO}_2$  in seguito a fotoeccitazione a 3.5 eV, sono stati investigati usando spettroscopia a raggi x al femtosecondo alla soglia K del Ti mediante la tecnica di sincrotrone dello *slicing*. I risultati mostrano che la localizzazione degli elettroni agli atomi di Ti avviene in  $< 300\text{fs}$ , formando centri di  $\text{Ti}^{3+}$ , nelle vicinanze della cella unitaria dove l'elettrone è stato eccitato. Inoltre, la localizzazione dell'elettrone è dovuta all'intrappolamento su siti pentacoordinati, presenti per la maggior parte nello strato superficiale del materiale.

Conclusioni simili sono trovate per un altro polimorfo del  $\text{TiO}_2$ , il rutilo, dalla spettroscopia di assorbimento a raggi x al picosecondo sulla soglia K del Ti. Qui gli elettroni sono intrappolati in prossimità delle vacanze di ossigeno dopo 100 ps dall'eccitazione. Gli elettroni nel rutilo però, mostrano una tendenza minore alla localizzazione rispetto all'anatasio e questo potrebbe spiegare le differenze nelle prestazioni fotocatalitiche tra questi due polimorfi.

Nella seconda parte di questa tesi, la dinamica ultraveloce dei portatori di carica per i nanocristalli di  $\text{CsPb}(\text{ClBr})_3$  è investigata usando spettroscopia di assorbimento transiente al femtosecondo nel visibile ( $\sim 1.8\text{-}3.1\text{ eV}$ ) in seguito a fotoeccitazione a 3.1 eV. Questo materiale rappresenta un sistema ideale per studiare la fisica ultraveloce delle perovskiti a base di Piombo ed alogenuri in generale, poiché studi ultraveloci di assorbimento transiente

suggeriscono che la dinamica dei portatori di carica sia simile ai materiali organici-inorganici ma non soffre degli stessi problemi di stabilità. Qui, la transizione tra cariche libere ed eccitoni è osservata in uno studio dipendente dalla flukenza, che chiarisce l'interpretazione di un segnale a lunga durata originato da un effetto di *electroabsorption* transiente.

Infine, la dinamica dei portatori di carica in  $\text{CsPbX}_3$  ( $X = \text{Cl}, \text{Br}$ ) è investigata usando spettroscopia di assorbimento a raggi x al picosecondo alle soglie K del Br,  $L_3$  del Pb e  $L_2$  del Cs dopo fotoeccitazione a 3.5 eV. I transienti alla soglia K del Br a 100 ps di ritardo suggeriscono che un'intera carica di elettrone sia strappata dagli atomi di Br, *i.e.* la buca è localizzata a causa della formazione di un piccolo polarone. I transienti alla soglia  $L_3$  del Pb indicano l'opposto, *i.e.* gli elettroni sono completamente delocalizzati come elettroni in banda di conduzione e non c'è un segnale indicativo dell'intrappolamento. In ultimo, la soglia del  $L_2$  del Cs non mostra un segnale transiente, in accordo con le previsioni basate sulla densità parziale degli stati nel materiale.

**PAROLE CHIAVE:** *Spettroscopia ultraveloce, spettroscopia a raggi x risolta nel tempo, spettroscopia di assorbimento transiente, biossido di Titanio, perovskiti a base di Piombo ed alogenuri, fotovoltaico, fotocatalisi*

# Acknowledgements

In these two pages I would like to thank all the people which support and help me to achieve the results of this PhD. I believe this might be the most complicated pages of all the thesis, because I fear that I may forget someone and therefore I ask her/him to forgive me already if that is going to be the case.

When I joined the laboratory of ultrafast spectroscopy (LSU) in 2012, my only goal and motivation for starting a PhD was to do scientific research. Looking back now to what this PhD has been, I realized that doing good research was only a minor part of it. It has been a turning point in my life, a priceless professional experience in which I learned to deal with people of completely different cultures to solve problems of all kinds.

The first person I would like to thank is Majed, my supervisor during these four years which made possible the writing of this work. In 2012, after I obtained a master in Industrial Chemistry and Management, he gave me the possibility to drastically change my path in the more fundamental aspects of Physics. Moreover, during these years, he always trusted me and gave me opportunity to deal with responsibilities often privileges only of experienced postdocs, starting from the writing of a grant proposal to drafting of a final manuscript. This allowed me to acquire a set of skills, besides the one which can be built in a lab, that in other groups I could not have had. Finally, I thank him for accepting my request of moving from Paul Scherrer Institute to EPFL, after about 2 years of PhD. This broadened my knowledge of ultrafast techniques but more importantly, it kept me in a learning phase until the last day of this experience.

A “sub-group” of people I have to thank separately, are the LSU members part of the X-ray team. Beamtimes are definitely the most intense experiences a scientist can have. Working in shifts of about 13 hours for 7 days consecutively, trying to achieve what it is often at the edge of what it is possible, is a very stressful situation. The absolute need of operating in a team, requires people with a unique capability of working under pressure and trust each other. I want to thank Jochen, Hannelore, Chris (the ginger one), Andrea, Jacinto, Mahsa, Lars, Jakob, Thomas, James and Dominik for being the best colleagues during this hard time. With most of you I had several beamtimes together and in particular I would like to thank you for what we have achieved in my project. It would have never been possible to measure fs-XAS of  $\text{TiO}_2$  or ps-XAS of perovskites at synchrotron without your commitment, experience but more than anything else, trust in me. We have failed two beamtimes consecutively on perovskites, it was hard to find a sample which could work for this, but the third beamtime you were all there, trusting that it was going to be the right one, like if it was the first time. Without you, it had no chances to happen. A special thanks goes to Jochen, Chris, Andrea, Jacinto and Jakob for being not only great members of the team, but also mentors during the time in Paul Scherrer Institute and overall good friends outside the labs. Jakob, an amazing

scientist and person, helped me a lot to correct mistakes and improve this thesis. Without him I would have had a very hard time to reach the same results.

Moving to EPFL was another intense and exciting step. After 2 years of PhD, I had to start learning, as in the first day, a new set of techniques. Luckily the LSU crew based in Lausanne made this new challenge possible. Enrico, Chris (this time the British one), Frank, Ingalena, Luca, Roberto, Josè, André, Malte, Tania, Edoardo, Gloria, Marine, Monique and Anissa. We have spent excellent time together. Another special thanks to Lars and André in particular, colleagues with remarkable technical skills which spent weekends in the labs to teach me how to work with a laser and even more nice time outside in pubs.

This project could not be done without the help of external collaborators. Among the many I had the pleasure to work with, the collaboration with the group of Professor Kovalenko from ETH gave the most fruitful results. This was definitely not by chance, indeed in this group I had the opportunity to work with two great scientists. Georgian, which provided always high quality samples, often with short deadlines and in outstanding amounts. Sergii, which helped me a lot during the fluorescence measurements in ETH, from the technical point of view but also during the data analysis.

Moreover, I should thank two of my best friends, which have been in Milano during most of these four years and were always there for me anytime I was back. Guido, which grown up with me as a scientist during the years of the university, sharing passions such as wine and gourmet cuisine that became contagious. Marco, which grown up with me as a man during the years of the military school and has been present in all the most important steps of my life.

Per concludere, devo ringraziare la mia famiglia: mamma Silvia, papà Pino e mia sorella Giulia. Mi hanno sempre supportato, da quando ho iniziato i miei studi, ed in tutte le ambizioni che mi hanno caratterizzato negli anni. Sono i pilastri del mio essere, le fondamenta del mio carattere. Con loro ringrazio Elena, nuovo membro nella nostra famiglia; la sua presenza ha dato un senso a tutto.

# TABLE OF CONTENTS

<b>Abstract .....</b>	<b>i</b>
<b>Sommario .....</b>	<b>iii</b>
<b>Acknowledgements .....</b>	<b>v</b>
<b>TABLE OF FIGURES .....</b>	<b>xi</b>
<b>1 Introduction .....</b>	<b>1</b>
<b>2 Basic concepts .....</b>	<b>3</b>
2.1 <i>General aspects of semiconductor physics</i> .....	3
2.1.1 Free charge carriers and excitons.....	4
2.1.2 Defects and disorder .....	7
2.1.3 Self-trapping: polaron and self-trapped exciton .....	8
2.2 <i>Many-body and electric field effects on semiconductor physics</i> .....	10
2.2.1 Exciton screening and Mott-transition.....	11
2.2.2 Bandgap renormalization .....	12
2.2.3 Electroabsorption effects .....	12
2.3 <i>Relaxation processes in semiconductors</i> .....	14
2.3.1 Radiative recombination .....	14
2.3.2 Relaxation through defects: Shockley-Read-Hall recombination.....	14
2.3.3 Auger recombination.....	15
2.3.4 Phonon bottleneck .....	16
<b>3 Experimental methods .....</b>	<b>17</b>
3.1 <i>Femtosecond transient absorption spectroscopy</i> .....	17
3.1.1 Technical details .....	18
3.2 <i>X-ray absorption spectroscopy</i> .....	19
3.2.1 X-ray matter interaction .....	20
3.2.2 Picosecond x-ray absorption spectroscopy .....	22
3.2.3 Femtosecond X-ray absorption spectroscopy: slicing method .....	24
3.3 <i>Time correlated single photon counting</i> .....	26
3.3.1 Technical details .....	26
3.4 <i>Samples preparation and characterization</i> .....	27
3.4.1 TiO <sub>2</sub> nanoparticles .....	27
3.4.2 CsPbX <sub>3</sub> nanocrystals.....	28

<b>4</b>	<b>Titanium Dioxide.....</b>	<b>31</b>
4.1	<i>Applications of TiO<sub>2</sub>.....</i>	31
4.2	<i>Geometric structure .....</i>	32
4.3	<i>Electronic structure .....</i>	33
4.4	<i>Previous studies of charge carrier dynamics.....</i>	35
4.5	<i>Polaronic localization in TiO<sub>2</sub>.....</i>	40
<b>5</b>	<b>Femtosecond x-ray absorption of anatase TiO<sub>2</sub> nanoparticles .....</b>	<b>43</b>
5.1	<i>Introduction.....</i>	43
5.2	<i>Results and discussion .....</i>	46
5.3	<i>Conclusions.....</i>	51
<b>6</b>	<b>Picosecond x-ray absorption of rutile TiO<sub>2</sub> nanoparticles .....</b>	<b>53</b>
6.1	<i>Introduction.....</i>	53
6.2	<i>Results and discussion .....</i>	54
6.3	<i>Conclusions.....</i>	60
<b>7</b>	<b>Lead Halide Perovskites .....</b>	<b>63</b>
7.1	<i>The rise of hybrid organic/inorganic perovskites.....</i>	63
7.2	<i>Geometric and electronic structure.....</i>	64
7.3	<i>Polaronic localization in perovskites .....</i>	68
7.4	<i>Stability issues .....</i>	69
7.5	<i>CsPbX<sub>3</sub> perovskites .....</i>	69
<b>8</b>	<b>Femtosecond transient absorption of CsPb(ClBr)<sub>3</sub>.....</b>	<b>73</b>
8.1	<i>Introduction.....</i>	73
8.2	<i>Results and discussion .....</i>	78
8.2.1	<i>Investigation of the transient spectral features .....</i>	78
8.2.2	<i>Investigation of the temporal dynamics.....</i>	87
8.3	<i>Conclusions.....</i>	91
<b>9</b>	<b>Picosecond x-ray absorption and photoluminescence of CsPbBr<sub>3-x</sub>Cl<sub>x</sub> nanocrystals .....</b>	<b>93</b>
9.1	<i>Introduction.....</i>	93



9.2	<i>Results and discussion</i> .....	95
9.2.1	X-ray absorption spectroscopy at Br K-edge, Pb L <sub>3</sub> -edge and Cs L <sub>2</sub> -edge .....	96
9.2.2	Photoluminescence .....	106
9.2.3	The emerging picture of the photophysics of CsPbBr <sub>3-x</sub> Cl <sub>x</sub> perovskites .....	110
9.3	<i>Conclusions</i> .....	112
<b>10</b>	<b>Conclusion and outlook</b> .....	<b>115</b>
<b>11</b>	<b>Appendix</b> .....	<b>119</b>
11.1	<i>Femtosecond transient absorption of CsPb(ClBr)<sub>3</sub></i> .....	119
11.2	<i>Picosecond x-ray absorption and photoluminescence of CsPbBr<sub>3-x</sub>Cl<sub>x</sub> nanocrystals</i> .....	121
	<b>References</b> .....	<b>125</b>
	<b>Curriculum vitae</b> .....	<b>151</b>



# TABLE OF FIGURES

FIGURE 2.1 - SCHEMATIC REPRESENTATION OF DIRECT AND INDIRECT BANDGAP TRANSITION IN A SEMICONDUCTOR. ON THE LEFT, THE CB EDGE AND VB EDGE OCCURS AT THE SAME VALUE OF $k$ AND THEREFORE A DIRECT OPTICAL TRANSITION IS ALLOWED. ON THE RIGHT, AN INDIRECT TRANSITION WHICH INVOLVES A PHOTON AND A PHONON (WHERE $\Omega$ IS ITS FREQUENCY) IS REQUIRED TO COMPENSATE THE DIFFERENCE IN MOMENTUM BETWEEN THE TWO BAND EDGES. TAKEN FROM REF. <sup>20</sup> .	4
FIGURE 2.2 - SCHEMATIC REPRESENTATION OF THE ELECTRONIC LEVELS RELATED TO AN EXCITON IN A DIRECT BANDGAP SEMICONDUCTOR. TAKEN FROM REF. <sup>20</sup>	5
FIGURE 2.3 - SCHEMATIC OF POINT DEFECTS (ABOVE) AND DISLOCATIONS (BELOW) IN A SOLID. THE EDGE DISLOCATION IS HIGHLIGHTED BY A CLOSED LOOP, TYPICAL OF BURGERS VECTOR REPRESENTATION. TAKEN FROM REF. <sup>42</sup> .	8
FIGURE 2.4 - A SELF-TRAPPED ELECTRON ON A CATION (HATCHED AREA) IN A LATTICE, WHERE ANIONS ARE LARGE CIRCLES AND CATIONS SMALL CIRCLES. THE SURROUNDING IONS ARE SHIFTED FROM THEIR EQUILIBRIUM POSITIONS (OPEN LARGE AND SMALL CIRCLES) IN A NEW CONFIGURATION (FILLED LARGE AND SMALL CIRCLES) WHICH PRODUCES A POTENTIAL WELL FOR THAT CARRIER. TAKEN FROM REF. <sup>45</sup> .	9
FIGURE 2.5 - SCHEMATIC OF A WANNIER EXCITON WITH BOHR RADIUS $A_{BOHR}$ (A). AN EXCITON GAS BELOW THE MOTT DENSITY, WITH THE AVERAGE DISTANCE BETWEEN EXCITATIONS MUCH LARGER THAN THE BOHR RADIUS (B). AN EXCITON SYSTEM ABOVE THE MOTT DENSITY (C). TAKEN FROM REF. <sup>58</sup> .	11
FIGURE 2.6 - SCHEMATIC OF AUGER RECOMBINATION IN A SEMICONDUCTOR. IN THIS NONRADIATIVE TRANSITION AN ELECTRON-HOLE PAIR TRANSFERS ENERGY TO A SPECTATOR CHARGE, WHICH CAN BE EITHER AN ELECTRON (LEFT TWO PICTURES) OR A HOLE (RIGHT TWO PICTURE). READAPTED FROM REF. <sup>26</sup> .	15
FIGURE 3.1 - SCHEMATIC REPRESENTATION OF THE THREE PROCESSES (I.E. GROUND STATE BLEACH, STIMULATED EMISSION AND EXCITED STATE ABSORPTION) WHICH MODULATE THE TRANSIENT ABSORPTION SPECTRA OF A PUMP PROBE MEASUREMENT. READAPTED FROM REF. <sup>78</sup> .	17
FIGURE 3.2 - SCHEMATIC REPRESENTATION OF THE FEMTOSECOND TRANSIENT ABSORPTION SETUP FROM THE OUTPUT OF THE AMPLIFIER TO THE DETECTION SYSTEM. WL REPRESENTS THE $CaF_2$ WINDOW FOR THE PROBE WHITELIGHT GENERATION AND SHG, THE SECOND HARMONIC GENERATION B-BBO CRYSTAL FOR THE 3.1 EV PUMP.	18
FIGURE 3.3 - CALCULATED EMITTED X-RAY RADIATION FROM A BENDING MAGNET AND A SUPERBENDING MAGNET (A) AT THE SWISS LIGHT SOURCE IN PAUL SCHERRER INSTITUTE. THE SUPERBENDING MAGNET IS USED IN THE SUPERXAS BEAMLINE. BELOW, THE X-RAY SPECTRUM CALCULATED FOR THE MINIGAP UNDULATOR AT THE MICROXAS BEAMLINE (B) OF THE SWISS LIGHT SOURCE. THE GREY BAR SHOWS A GAP IN WHICH X-RAY ARE NOT GENERATED. TAKEN FROM REF. <sup>80</sup> .	20
FIGURE 3.4 - EXAMPLE OF AN X-RAY ABSORPTION SPECTRUM. HIGHLIGHTED ARE THE PRE-EDGE, XANES AND EXAFS REGIONS. TAKEN FROM REF. <sup>80</sup> .	21
FIGURE 3.5 - FILLING PATTERN OF THE SWISS LIGHT SOURCE AT PAUL SCHERRER INSTITUTE. IN TOTAL ARE PRESENT 480 ELECTRONS BUCKETS (2 NS OF TIME SEPARATION BETWEEN EACH OTHER) OF WHICH 390 ARE FILLED WITH THE ELECTRONS AND THE REMAINING 90 ONES FOR THE GAP IN WHICH THERE IS THE CAMSHAFT PULSE. THE CAMSHAFT HAS 4 TIMES MORE INTENSITY THAN THE OTHER ELECTRON BUNCHES IN THE MULTIBUNCH AND THE STORAGE RING REPETITION RATE IS OF 1.04 MHZ. TAKEN FROM REF. <sup>87</sup> .	22
FIGURE 3.6 - SIMPLIFIED REPRESENTATION OF THE HIGH REPETITION RATE SETUP FOR PICOSECOND X-RAY ABSORPTION SPECTROSCOPY. READAPTED FROM REF. <sup>87</sup> .	23

FIGURE 3.7 - LIQUID SHEET JET OF 200 MM THICKNESS FLOWING WATER. THE GREEN AREA IS THE MOST STABLE BECAUSE THERE IS LAMINAR FLOW AND THEREFORE IT IS HERE THAT LASER AND X-RAY ARE OVERLAPPED. TAKEN FROM REF. <sup>89</sup> .....	24
FIGURE 3.8 - SCHEMATIC REPRESENTATION OF THE SLICING SETUP FOR FEMTOSECOND X-RAY ABSORPTION SPECTROSCOPY. FROM THE LEFT, THERE IS THE MODULATOR IN WHICH THE FEMTOSECOND LASER PULSE AND PICOSECOND ELECTRON BUNCH INTERACTS. UPON INTERACTION THERE IS A SPATIAL SEPARATION OF THE FEMTOSECOND MODULATED MICROBUNCH BY A MAGNETIC FIELD AND FINALLY ON THE RIGHT THE UNDULATOR FOR GENERATING X-RAY RADIATION. THANKS TO THE SPATIAL SEPARATION OF THE FEMTOSECOND X-RAY ELECTRON BUNCH, IT IS POSSIBLE TO UNIQUELY COLLECT ITS EMITTED RADIATION. BY COURTESY OF ANDRIN CAVIEZEL. ....	25
FIGURE 3.9 - PULSE DURATION OF THE 3.5 EV LASER LIGHT RECORDED USING TIME CORRELATED SINGLE PHOTON COUNTING SETUP WITH DIFFERENT TIME WINDOWS (50 NS FOR THE RED CURVE AND 150 NS FOR THE BLUE CURVE) AND A GAUSSIAN FIT WITH 300 PS OF FULL WIDTH AT HALF MAXIMUM (BLACK DOTTED CURVE).....	27
FIGURE 3.10 - XRD PATTERN OF THE DRIED SAMPLE (BLACK TRACE). THE RED STICKS REPRESENT THE DIFFRACTION REFERENCE DATA OF ANATASE TiO <sub>2</sub> AT 25 °C. TAKEN FROM REF. <sup>15</sup> . ....	28
FIGURE 3.11 - TRANSMISSION ELECTRON MICROGRAPH OF MONODISPERSE CSPBBR <sub>3</sub> (A) AND CSPB(CLBR) <sub>3</sub> (B) NANOCRYSTALS WITH AN AVERAGE SIZE OF 12 NM. ....	29
FIGURE 3.12 - POWDER X-RAY DIFFRACTION PATTERN OF CUBIC CSPBBR <sub>3</sub> NCS MATCHING THE CUBIC PHASE OF THE REFERENCE FOR CSPBBR <sub>3</sub> (SPACE GROUP PM-3M) <sup>97</sup> .....	30
FIGURE 3.13 - POWDER X-RAY DIFFRACTION PATTERN OF CSPB(CLBR) <sub>3</sub> NCS DISPLAYING THE DIFFRACTION PEAKS BETWEEN THE REFERENCES FOR CSPBBR <sub>3</sub> (GREEN LINES) <sup>97</sup> AND CSPBCL <sub>3</sub> (BLUE LINES) <sup>97</sup> .....	30
FIGURE 4.1 - SCHEMATIC VIEW OF PHOTOCATALYTIC PROCESSES IN A NANOPARTICLE OF TiO <sub>2</sub> FOR SOLAR FUEL GENERATION. TAKEN FROM REF. <sup>14</sup> .....	31
FIGURE 4.2 - SCHEMATIC DIAGRAM OF A DYE SENSITIZED SOLAR CELL. ON THE BOTTOM PART THERE IS THE PHOTOACTIVE AREA AND IN THE UPPER PART A Pt COUNTER ELECTRODE. TAKEN FROM REF. <sup>106</sup> . ....	32
FIGURE 4.3 - RUTILE AND ANATASE TiO <sub>2</sub> CRYSTAL STRUCTURES. IN BOTH CASES, SLIGHTLY DISTORTED OCTAHEDRA ARE THE BASIC BUILDING UNITS. TAKEN FROM REF. <sup>115</sup> . ....	33
FIGURE 4.4 - MOLECULAR-ORBITAL BOND STRUCTURE FOR ANATASE CONTAINING ATOMIC LEVELS (A), CRYSTAL FIELD SPLIT LEVELS (B), AND FINAL INTERACTION STATES (C). THE SOLID LINES REPRESENT LARGE CONTRIBUTIONS AND THE DASHED LINES SMALLER ONES. TAKEN FROM REF. <sup>117</sup> .....	34
FIGURE 4.5 - ON THE TOP, SCHEMATIC ELECTRONIC STRUCTURE SHOWING THE EXCITATION OF ELECTRONS WITHIN TRAP POLARONIC STATES BY ABSORPTION OF IR (~ 1000 cm <sup>-1</sup> ). ON THE BOTTOM, THE ELECTRON SPIN DENSITY OF A SELF-TRAPPED POLARONS ON A Ti <sup>3+</sup> CENTER OF RUTILE AS CALCULATED FROM DFT. TAKEN FROM REF. <sup>148</sup> .....	40
FIGURE 5.1 - EPR SPECTRA OF OXIDIZED ANATASE NANOPARTICLES, BEFORE (A) AND AFTER (B) 20 MINUTES OF UV LIGHT IRRADIATION AT 90 K. THE OXIDATION IS DONE AT 870 K FOR 2 HOURS IN HIGH VACUUM CONDITIONS TO REMOVE ALL THE ORGANICS REMAINING FROM THE SYNTHESIS. TRAPPED ELECTRONS ON Ti <sup>3+</sup> CENTERS SHOW TWO DIFFERENT SIGNALS IN THE SPECTRUM DUE TO A DIFFERENT g TENSOR COMPONENT, SUGGESTING THE PRESENCE OF TWO DIFFERENT TRAPPING SITES. THE EPR SPECTRUM AT ROOM TEMPERATURE (C) SHOWS NO SIGNAL, SUPPORTING THE NEED OF WORKING AT LOW TEMPERATURE TO OBSERVE TRAPPING OF CHARGE CARRIERS. TAKEN FROM REF. <sup>162</sup> . ....	44
FIGURE 5.2 - A) NORMALIZED STATIC Ti K-EDGE XANES SPECTRUM OF COLLOIDAL NANOPARTICLES OF ANATASE TiO <sub>2</sub> WITH THE PRE-EDGE FEATURES LABELLED A <sub>1</sub> , A <sub>2</sub> , A <sub>3</sub> AND B. B) TRANSIENT (DIFFERENCE) Ti K-EDGE XANES SPECTRA (DIFFERENCE OF THE EXCITED MINUS THE UNEXCITED SAMPLE ABSORPTION) FOR 3.5 EV EXCITATION OF COLLOIDAL NANOPARTICLES OF ANATASE TiO <sub>2</sub> , RECORDED AT TIME DELAYS OF 100 PS (GREEN SQUARES, RIGHT VERTICAL AXIS) <sup>164</sup> AND 1 PS (BLUE DOTS, LEFT VERTICAL AXIS). ..	47

FIGURE 5.3 - TEMPORAL EVOLUTION OF THE PHOTO-INDUCED X-RAY ABSORPTION CHANGE AT 4.982 KEV OF $\text{TiO}_2$ NANOPARTICLES EXCITED AT 3.5 EV (BLUE DOTS). AFTER THE RISE, THE SIGNAL REMAINS CONSTANT UP TO THE LIMIT OF OUR TIME SCAN (~50 PS, SEE FIGURE 5.4). THE BROWN TRACE REPRESENTS THE BEST FIT OF THE DATA, YIELDING A RISE TIME OF 170 FS. THE GREY TRACE SHOWS A SATISFACTORY FIT OF THE DATA WITH THE LONGEST RISE TIME OF 300 FS THAT REPRESENTS AN UPPER LIMIT. ....	48
FIGURE 5.4 - TEMPORAL EVOLUTION OF THE PHOTOINDUCED X-RAY ABSORBANCE CHANGE AT 4.982 KEV, MONITORING THE LOCALIZATION OF ELECTRONS AT TI SITES THUS THEIR REDUCTION TO $\text{Ti}^{3+}$ . THE SIGNAL STAYS CONSTANT FOR ABOUT 50 PS. ....	49
FIGURE 5.5 - SCHEMATIC REPRESENTATION OF THE ELECTRON LOCALIZATION AT TI CENTRES IN ANATASE $\text{TiO}_2$ . THE BLUE SPHERES ARE THE TI ATOMS, WHILE THE RED ONE ARE THE O ATOMS. THE ELECTRON BECOMES TRAPPED AT THE PENTACOORDINATED TI ATOM, TO FORM A $\text{Ti}^{3+}$ CENTRE, LEADING TO AN ADDITIONAL STRUCTURAL RELAXATION DUE TO THE CHANGE OF THE FIELD OF FORCES BETWEEN THE TI ATOM AND THE O ATOMS. THIS SCHEME REPRESENTS ONLY ONE OF THE TWO POSSIBLE SCENARIOS, PARTICULARLY THE ONE IN WHICH THE VACANCY DERIVES FROM AN OXYGEN REMOVED ON THE EQUATORIAL PLANE. ....	50
FIGURE 6.1 - GROUND STATE X-RAY ABSORPTION NEAR EDGE STRUCTURE (XANES) FOR THE RUTILE, ANATASE AND AMORPHOUS NPS. THE DOTTED VERTICAL LINES HIGHLIGHT THE MAIN FEATURES IN THE PRE-EDGE REGION ( $A_1$ , $A_2$ , $A_3$ , B AND C) AND THE ABOVE THE EDGE ( $D_1$ , $D_2$ AND E). THE ABSENCE OF THE $A_2$ FEATURE IN CASE OF RUTILE NPS CAN BE SEEN MORE CLEARLY IN FIGURE 6.2. ....	54
FIGURE 6.2 - GROUND STATE X-RAY ABSORPTION SPECTRA IN THE PRE-EDGE REGION FOR THE RUTILE (BLUE LINE), ANATASE (RED LINE) AND AMORPHOUS $\text{TiO}_2$ NPS (BLACK LINE). THE DOTTED VERTICAL LINES HIGHLIGHT THE MAIN FEATURES ( $A_1$ , $A_2$ , $A_3$ , B AND C). ....	55
FIGURE 6.3 - (A) COMPARISON BETWEEN THE GROUND STATE SPECTRA AT THE TI K-EDGE OF THE ANATASE (RED CURVE), THE RUTILE (BLUE CURVE) AND AMORPHOUS (BLACK CURVE) $\text{TiO}_2$ NANOPARTICLES. (B) TRANSIENT SPECTRUM OF ANATASE (RED CURVE) AT 100 PS TIME DELAY AND SIMULATED DIFFERENCE WITH 1 EV SHIFT (DOTTED GREY CURVE, TAKEN FROM REF. <sup>17</sup> ). (C) TRANSIENT SPECTRUM OF RUTILE (BLUE CURVE, THIS WORK) AT 100 PS TIME DELAY AND SIMULATED DIFFERENCE WITH 1 EV SHIFT (DOTTED GREY CURVE). ....	56
FIGURE 6.4 - SIMULATED SPECTRA (AMORPHOUS SHIFTED IN ENERGY MINUS RUTILE SPECTRUM) USING DIFFERENT ENERGY SHIFTS. THE DIFFERENCE SIMULATED SPECTRA HAVE BEEN RESCALED WITH DIFFERENT FACTOR IN ORDER TO MATCH THE POSITIVE FEATURE AT 4983 EV. THE RESCALING FACTORS ARE 0.33, 0.30, 0.24, 0.21% FOR SHIFTS OF 0.5, 1.0, 1.5 AND 2.0 EV RESPECTIVELY. ....	57
FIGURE 6.5 - COMPARISON BETWEEN THE TIME TRACES AT 4982 EV OF ANATASE (RED DOTS, TAKEN FROM REF. <sup>17</sup> ) AND RUTILE (BLUE DOTS, THIS WORK) $\text{TiO}_2$ NPS UPON EXCITATION AT 3.5 EV AND 260 KHZ WITH 48 MJ/ $\text{cm}^2$ . THE SOLID BLUE AND RED LINES ARE OBTAINED BY THE FITTING THE DATA USING BIEXPONENTIAL FUNCTIONS CONVOLUTED WITH THE INSTRUMENT RESPONSE FUNCTION OF THE SYSTEM (70 PS), THE BLACK LINE IS OBTAINED BY FITTING THE RUTILE DECAY KINETIC BY A MONOEXPONENTIAL. ....	59
FIGURE 6.6 - UV-VIS DIFFUSE REFLECTANCE SPECTRA OF ANATASE (RED CURVE) AND RUTILE (BLUE CURVE) POWDERS COLLECTED USING AN INTEGRATING SPHERE. THE EXCITATION ENERGY USED DURING THE PS-XAS EXPERIMENT (3.5 EV) IS HIGHLIGHTED IN THE FIGURE. IN THE INSET THERE IS A ZOOM AROUND THIS ENERGY REGION. ....	60
FIGURE 7.1 - (A) REAL SOLID-STATE DEVICE. (B) CROSS-SECTIONAL STRUCTURE OF THE DEVICE. (C) CROSS-SECTIONAL SEM IMAGE OF THE DEVICE, SHOWING (FROM TOP TO BOTTOM): THE GOLD ELECTRODE, THE HOLE TRANSPORT MATERIAL (HTM, SPIRO-MEOTAD), THE MESOPOROUS $\text{TiO}_2$ WITH $\text{CH}_3\text{NH}_3\text{PbI}_3$ AS AN ABSORBER AND THE FLUORINE DOPED TIN OXIDE (FTO) LAYER. (D) ACTIVE LAYER/FTO UNDERLAYER-INTERFACIAL JUNCTION STRUCTURE. TAKEN FROM REF. <sup>105</sup> ....	63
FIGURE 7.2 - A CASE STUDY OF THE PHASE TRANSITION SCHEME AS OBSERVED WITH SYNCHROTRON POWDER DIFFRACTION ( $\lambda = 0.413906 \text{ \AA}$ ) FOR THE $\text{CSPbI}_3$ COMPOUND. INITIALLY, THE ROOM TEMPERATURE	

REGIONS, NUMBERED FROM 1 TO 4 IN ORDER OF INCREASING ENERGY, TO AID THE DISCUSSION OF THE DIFFERENT TRANSIENT FEATURES. THE INSET SHOWS A ZOOM INTO SIGNAL PA <sub>1</sub> IN REGION 1.....	79
FIGURE 8.7 - FLUENCE DEPENDENCE OF THE TRANSIENT SPECTRA AT 300 FS (A) AND 1 NS (B) AFTER PHOTOEXCITATION AT 3.1 EV . THE INSET SHOWS A ZOOM INTO SIGNAL PA <sub>1</sub> IN REGION 1.....	80
FIGURE 8.8 - INTENSITY OF THE TRANSIENT SIGNAL AT 1.800 (PA <sub>1</sub> ), 2.561 EV (PA <sub>2</sub> ) AND 2.620 EV (PB <sub>3</sub> ) UPON PHOTOEXCITATION AT 3.1 EV AND 300 FS OF TIME DELAY. IN ORDER TO HAVE ALL THE SIGNALS GRAPHICALLY COMPARABLE, PA <sub>1</sub> IS MULTIPLY BY 15, PA <sub>2</sub> IS MULTIPLY BY 2 AND PB <sub>3</sub> IS MULTIPLY BY -1. ....	83
FIGURE 8.9 - RESULTS OF THE FIT (RED DOTTED CURVES) AT DIFFERENT TIME DELAYS FOR THE FLUENCE OF 100 $\mu\text{J}/\text{CM}^2$ , USING A MAXWELL-BOLTZMANN DISTRIBUTION TO EXTRACT THE TEMPERATURE OF THE CHARGE CARRIERS IN THE HIGH ENERGY REGION OF PB <sub>3</sub> ( <i>I.E.</i> FROM 2.770 EV TO 3.040 EV). THE QUALITY OF THE FIT REDUCES AT HIGHER TIME SCALES BECAUSE PA <sub>4</sub> CONTRIBUTES INCREASINGLY TO THE SIGNAL. ....	83
FIGURE 8.10 - TEMPERATURE DECAYS OF CHARGE CARRIERS UPON PHOTOEXCITATION AT 3.1 EV WITH DIFFERENT FLUENCES. THE TEMPERATURE IS EXTRACTED BY REPRODUCING THE HIGH ENERGY SIDE OF PB <sub>3</sub> (FROM 2.770 TO 3.040 EV) WITH A MAXWELL-BOLTZMANN DISTRIBUTION BUT THE FITTINGS ARE HINDERED ABOVE CERTAIN TIME DELAY, WHICH DEPENDS ON THE FLUENCE, DUE TO THE APPEARANCE OF PA <sub>4</sub> . ....	84
FIGURE 8.11 - KINETIC TRACES UPON PHOTOEXCITATION AT 3.1 EV WITH 18 (A) AND 100 $\mu\text{J}/\text{CM}^2$ (B) MEASURED AT 1.800 EV (PA <sub>1</sub> , RED CURVE), 2.620 EV (PB <sub>3</sub> , BLACK CURVE) AND 2.746 EV (PA <sub>4</sub> , BLUE CURVE). ....	85
FIGURE 8.12 - SCHEMATIC OF THE INTERFACIAL INTERACTION BETWEEN CSPBBR <sub>3</sub> NCS AND THE ORGANIC MOLECULES IN SOLUTION. THE OLEYAMMONIUM CATION BINDS TO SURFACE BROMIDE, PROBABLY THROUGH A HYDROGEN BRIDGE, AND IT DONATES ONE ELECTRON TO THE NANOCRYSTAL-LIGAND BOND. THE BROMIDE OR OLEATE ANION BINDS TO THE SURFACE CAESIUM AND LEAD IONS. ....	87
FIGURE 8.13 - TRANSIENT SPECTRUM AT 18MJ/CM <sup>2</sup> AND 1 NS REPORTING THE 23 ENERGIES (RED DOTS) CHOSEN FOR THE GLOBAL FIT OF THE DYNAMICS. ....	88
FIGURE 8.14 - DECAY ASSOCIATED SPECTRA FOR THE DATA AT 18 (A) AND 100 MJ/CM <sup>2</sup> (B). ....	89
FIGURE 8.15 - NORMALIZED KINETIC TRACES FOR DIFFERENT FLUENCES AT THE ENERGY OF 2.620 EV (AROUND THE MAXIMUM OF PB <sub>3</sub> ) IN $(\Delta T/T)^{-1}$ . THE LINEAR BEHAVIOR OVER TIME IS SHOWN ONLY AT 2.5 AND 5 $\mu\text{J}/\text{CM}^2$ AND FOR THE OTHER FLUENCES THE GROWTH IS PROPORTIONAL TO T INDICATING THAT AUGER RECOMBINATION IS THE PRIMARY PROCESS. ....	90
FIGURE 9.1 - PHOTOLUMINESCENCE AND ABSORPTION SPECTRA AFTER 30 MINUTES OF LASER IRRADIATION AT 355 NM AND 260 KHZ USING DIFFERENT FLUENCES FOR CSPB(CLBR) <sub>3</sub> NCS. THE CHANGES OBSERVED IN THE OPTICAL PROPERTIES OF THE SAMPLES ARE IRREVERSIBLE. ....	95
FIGURE 9.2 - ABSORPTION SPECTRA (DOTTED) AND PHOTOLUMINESCENCE SPECTRA (FULL LINES) OF CSPB(CLBR) <sub>3</sub> (GREY AND RED TRACES) AND CSPBBR <sub>3</sub> (BLACK AND BLUE TRACES) NCS. THE SAME SPECTRA ARE SHOWN AFTER >12 HOURS OF LASER IRRADIATION AT 355 NM, 260 KHZ REP. RATE AND A FLUENCE OF 15 MJ/CM <sup>2</sup> . ....	96
FIGURE 9.3 - PFY X-RAY ABSORPTION SPECTRA AT THE BR K-ALPHA EMISSION NEAR THE EDGE REGION OF CSPBBR <sub>3</sub> (RED TRACE) AND CSPB(CLBR) <sub>3</sub> (BLUE TRACE) NCS. IN GREY DOTS THE TFY X-RAY ABSORPTION SPECTRUM OF CH <sub>3</sub> NH <sub>3</sub> PBBR <sub>3</sub> NPS AT THE BR K-EDGE TAKEN FROM REF. <sup>316</sup> ....	97
FIGURE 9.4 - PFY X-RAY ABSORPTION SPECTRUM OF CSPB(CLBR) <sub>3</sub> AT THE BR K-EDGE (BLACK TRACE) WITH TRANSIENTS AT 100 PS OF CSPB(CLBR) <sub>3</sub> (BLUE TRACE) AND CSPBBR <sub>3</sub> (RED TRACE) EXCITED AT 355 NM WITH 15 MJ/CM <sup>2</sup> . THE TRANSIENTS WERE RECORDED IN TOTAL FLUORESCENCE YIELD (TFY) DETECTION MODE. THE GREEN TRACE REPRESENTS THE DIFFERENCE OF THE STEADY STATE SPECTRUM (BLACK TRACE) SHIFTED BY +5 EV MINUS THE UNSHIFTED STEADY-STATE SPECTRUM. ....	97

STABLE $\Delta$ -PHASE (YELLOW) CONVERTS TO THE BLACK PEROVSKITE A-PHASE UPON HEATING ABOVE 360 °C. ON COOLING, THE PEROVSKITE STRUCTURE REMAINS KINETICALLY STABILIZED CONVERTING TO THE BLACK PEROVSKITE B- AND $\Gamma$ -PHASES AT 260 AND 175 °C, RESPECTIVELY. FULL CONVERSION OF THE $\Gamma$ - TO THE INITIAL YELLOW $\Delta$ -PHASE OCCURS AFTER ~48H. TAKEN FROM REF. <sup>212</sup> .	65
FIGURE 7.3 - TOTAL DENSITY OF STATES (DOS) OF $\text{CH}_3\text{NH}_3\text{PbI}_3$ IN THE CUBIC STRUCTURE (A) AND PARTIAL DOS FOR $\text{CH}_3\text{NH}_3^+$ (B), Pb (C) AND I (E) OBTAINED BY FIRST-PRINCIPLES CALCULATIONS USING GENERALIZED GRADIENT APPROXIMATION (GGA) FOR THE EXCHANGE CORRELATION. THE ZERO IN DOS IS REFERRED TO THE VALENCE BAND MAXIMUM. THE Pb PARTIAL DOS IS ENLARGED BY FIVE TIMES FOR A CLEAR INDICATION OF THE S ORBITAL CONTRIBUTION. TAKEN FROM REF. <sup>25</sup> .	66
FIGURE 7.4 - BAND STRUCTURE OF THE FULLY RELAXED $\text{CH}_3\text{NH}_3\text{PbI}_3$ CRYSTAL OBTAINED USING FIRST-PRINCIPLES CALCULATIONS WITH GENERALIZED GRADIENT APPROXIMATION (GGA). THE BANDS ARE SHOWN FOR MOLECULE ORIENTATIONS ALONG (A) (111) AND (B) (011) DIRECTION. THE INSETS SHOW A MAGNIFICATION OF THE BANDS (WHICH HAVE BEEN SHIFTED IN ENERGY FOR CONVENIENCE) AROUND THE BANDGAP AND HIGHLIGHT THE CHANGES IN THE VB MAXIMUM AND CB MINIMUM CAUSED BY ROTATION OF $\text{CH}_3\text{NH}_3^+$ . NOTE THAT FOR THE (011) ORIENTATION THE BANDGAP BECOMES INDIRECT. TAKEN FROM REF. <sup>216</sup> .	66
FIGURE 7.5 - ABSORPTION COEFFICIENT FOR A THIN FILM OF $\text{CH}_3\text{NH}_3\text{PbI}_3$ COMPARED WITH OTHER SEMICONDUCTORS USED IN PHOTOVOLTAICS APPLICATIONS. THE SHARPNESS OF THE ABSORPTION EDGE (HIGHLIGHTED BY A BLACK LINE) IS INVERSELY PROPORTIONAL TO THE URBACH TAIL ENERGY OF WHICH A LOW VALUE, INDICATES HIGH CRYSTALLINE QUALITY OF THE MATERIAL AND THEREFORE LOW PRESENCE OF DEFECTS. SURPRISINGLY, THE LOW TEMPERATURE PROCESSED $\text{CH}_3\text{NH}_3\text{PbI}_3$ FILM SHOWS AN URBACH TAIL SIMILAR TO THE ONE OF GaAs, A MONOCRYSTALLINE DIRECT SEMICONDUCTOR OF VERY HIGH ELECTRICAL QUALITY. TAKEN FROM REF. <sup>220</sup> .	67
FIGURE 7.6 - SPIN DENSITY (TOTAL ELECTRON DENSITY OF ELECTRONS OF ONE SPIN MINUS THE TOTAL ELECTRON DENSITY OF THE ELECTRONS OF THE OTHER SPIN) CALCULATED FOR $\text{CH}_3\text{NH}_3\text{PbI}_3$ CLUSTERS USING AN <i>AB INITIO</i> SIMULATION. TAKEN FROM REF. <sup>50</sup> .	68
FIGURE 7.7 - COLLOIDAL PEROVSKITE $\text{CsPbX}_3$ NANOCRYSTALS (X = Cl, Br, I) EXHIBIT SIZE- AND COMPOSITION-TUNABLE BANDGAP ENERGIES COVERING THE ENTIRE VISIBLE SPECTRAL REGION WITH NARROW AND BRIGHT EMISSION: (A) COLLOIDAL SOLUTIONS IN TOLUENE UNDER UV LAMP AND (B) REPRESENTATIVE PL SPECTRA. TAKEN FROM REF. <sup>22</sup> .	70
FIGURE 8.1 - FEMTOSECOND TA SPECTRA OF A $\text{CH}_3\text{NH}_3\text{PbI}_3$ FILM EXCITED AT 3.20 eV (387 nm). THE ARROWS INDICATE THE RECOVERY OF THE BLEACH SIGNALS DISCUSSED IN THE TEXT. TAKEN FROM REF. <sup>261</sup> .	73
FIGURE 8.2 - NORMALIZED FS-TA SPECTRA OF A $\text{CH}_3\text{NH}_3\text{PbI}_3$ FILM EXCITED AT 2.25 eV. IN THE INSET, A ZOOM OF THE SPECTRAL BROADENING AT EARLY TIMES WHICH INDICATES A HOT-CARRIER DISTRIBUTION. READAPTED FROM REF. <sup>62</sup> .	75
FIGURE 8.3 - FEMTOSECOND-TA SPECTRUM AROUND T = 0 EXCITED AT 3.1 eV (400 nm). IN THE TRANSIENT SPECTRUM ARE HIGHLIGHTED THE PHOTOINDUCED ABSORPTIONS ( $\text{PA}_1$ AND $\text{PA}_2$ ) AND THE MAIN PHOTOBLEACH (PB). READAPTED FROM REF. <sup>269</sup> .	76
FIGURE 8.4 - FEMTOSECOND-TA SPECTRA OF $\text{CsPbBr}_3$ QUANTUM DOTS EXCITED AT 3.1 eV (400 nm). IN THE INSET, A ZOOM OF THE BROAD PHOTOINDUCED ABSORPTION (PA) BELOW BANDGAP ENERGY. TAKEN FROM REF. <sup>12</sup> .	77
FIGURE 8.5 - PHOTOLUMINESCENCE (DOTTED CURVES) AND ABSORPTION (SOLID CURVES) SPECTRA BEFORE (BLACK CURVES) AND AFTER (RED CURVES) ABOUT 30 HOURS OF LASER IRRADIATION AT 3.1 eV, 1 kHz AND DIFFERENT FLUENCES BETWEEN 2.5 AND 100 $\mu\text{J}/\text{cm}^2$ . THE ABSORPTION SPECTRUM IS NORMALIZED AROUND 2.6 eV TO COMPENSATE FOR THE CHANGE IN CONCENTRATION DUE TO THE EVAPORATION OF THE SOLVENT.	78
FIGURE 8.6 - FEMTOSECOND TRANSIENT SPECTRA AT DIFFERENT TIME DELAYS UPON PHOTOEXCITATION AT 3.1 eV WITH A FLUENCE OF 18 (A) AND 100 $\mu\text{J}/\text{cm}^2$ (B). THE SPECTRA ARE DIVIDED IN FOUR ENERGIES	



FIGURE 9.5 - PFY X-RAY ABSORPTION SPECTRUM OF CSPB(CLBR) <sub>3</sub> NCS AT THE BR K-EDGE (BLACK TRACE) WITH THE TRANSIENT SPECTRA AT 100 PS (RED TRACE), 1 NS (BLUE TRACE) AND 1 NS NORMALIZED TO THE 100 PS INTENSITY (VIOLET DOTTED TRACE). .....	98
FIGURE 9.6 - PFY X-RAY ABSORPTION SPECTRUM OF CSPB(CLBR) <sub>3</sub> NCS AT THE BR K-EDGE (BLACK TRACE) WITH THE TRANSIENT AT 100 PS UPON PHOTOEXCITATION AT 355 NM (RED TRACE) AND CALCULATED DIFFERENCE SPECTRA OF THE GROUND STATE SPECTRUM MINUS THE UNSHIFTED ONE FOR DIFFERENT VALUES OF THE SHIFT (1 TO 8 EV, DIFFERENT OFFSETS ON THE GRAPH). THE DIFFERENCE SPECTRA HAVE BEEN RESCALED WITH FACTORS BETWEEN 0.05 AND 0.006 IN ORDER TO BEST MATCH THE INTENSITY OF THE EXPERIMENTAL NEGATIVE TRANSIENT FEATURE AT 13.480 KEV. ....	99
FIGURE 9.7 - FLUENCE DEPENDENCE OF THE INTENSITY OF THE BR K-EDGE TRANSIENT SIGNAL AT 13.480 KEV FOR CSPB(CLBR) <sub>3</sub> NCS PHOTOEXCITED AT 355 NM. THE BLACK DASHED LINE SHOWS A LINEAR FITTING OF THE EXPERIMENTAL DATA (BLUE DOTS). ....	101
FIGURE 9.8 - KINETIC TRACES OF THE X-RAY SIGNAL AT 13.048 KEV UPON PHOTOEXCITATION AT 355 NM OF CSPB(CLBR) <sub>3</sub> (BLUE DOTS) AND CSPBBR <sub>3</sub> (RED DOTS) NCS USING A FLUENCE OF 15 MJ/CM <sup>2</sup> . THE DASHED LINES REPRESENT A BIEXPONENTIAL FIT YIELDING THE FIT PARAMETERS LISTED IN TABLE 9.1. THE INSET IS A ZOOM OF THE FIRST 4 NS AFTER EXCITATION. ....	102
FIGURE 9.9 - NORMALIZED KINETIC TRACES AT 13.480 (BLACK DOTS) AND 13.4863 KEV (RED SQUARES) AND FIT USING A BIEXPONENTIAL (BLUE DOTTED CURVE) OF CSPB(CLBR) <sub>3</sub> (A) AND CSPBBR <sub>3</sub> (B) NCS UPON PHOTOEXCITATION AT 355 NM. ....	103
FIGURE 9.10 - PFY X-RAY ABSORPTION SPECTRA NEAR THE EDGE REGION OF CSPBBR <sub>3</sub> (RED TRACE) AND CSPB(CLBR) <sub>3</sub> (BLUE TRACE) NCS AT THE PB L <sub>3</sub> -EDGE. THE DIFFERENCE IN INTENSITY AT ABOUT 13.05 KEV BETWEEN THE TWO COMPOUNDS IS RELATED TO A HIGHER DENSITY OF UNOCCUPIED STATES DUE TO THE PRESENCE OF CL. ....	104
FIGURE 9.11 - PFY STEADY-STATE X-RAY ABSORPTION SPECTRUM OF CSPB(CLBR) <sub>3</sub> NCS AT THE PB L <sub>3</sub> -EDGE (BLACK TRACE) AND TRANSIENT SPECTRA AT 100 PS TIME DELAY AFTER PHOTOEXCITATION AT 355 NM WITH 15 MJ/CM <sup>2</sup> OF CSPB(CLBR) <sub>3</sub> (BLUE TRACE) AND CSPBBR <sub>3</sub> (RED TRACE). ....	104
FIGURE 9.12 - X-RAY ABSORPTION SPECTRUM OF CSPBBR <sub>3</sub> NCS AT THE CS L <sub>2</sub> -EDGE (BLACK TRACE) WITH THE TRANSIENT SPECTRA AT 100 PS (RED TRACE) SHOWING NO SIGNAL WITHIN THE S/N OF THE MEASUREMENT. ....	105
FIGURE 9.13 - NORMALIZED PHOTOLUMINESCENCE KINETIC TRACES FOR CSPB(CLBR) <sub>3</sub> NCS UPON PHOTOEXCITATION AT 355 NM WITH DIFFERENT FLUENCES AND GLOBAL FITTING CURVES (RED DOTTED CURVES) USING A QUADRI-EXPONENTIAL FUNCTION. THE INSET SHOWS THE TOTAL PHOTOLUMINESCENCE INTENSITY AT DIFFERENT FLUENCES, WHICH IS OBTAINED BY INTEGRATING THE KINETIC TRACES UNTIL 120 NS DELAY. ....	107
FIGURE 9.14 - NORMALIZED PHOTOLUMINESCENCE KINETIC TRACES FOR CSPB(CLBR) <sub>3</sub> NCS UPON PHOTOEXCITATION AT 355 NM WITH 80 NJ/CM <sup>2</sup> (LIGHT GREY DOTS), 40 MJ/CM <sup>2</sup> (DARK GREY DOTS) AND 8 MJ/CM <sup>2</sup> (BLACK DOTS) AND INDEPENDENT FITTING FUNCTIONS WITH BI-EXPONENTIAL (RED DOTTED CURVES), TRI-EXPONENTIAL (BLUE DOTTED CURVES) AND QUADRI-EXPONENTIAL (GREEN DOTTED CURVES) DECAYS. ....	107
FIGURE 9.15 - NORMALIZED PHOTOLUMINESCENCE SPECTRA OF CSPB(CLBR) <sub>3</sub> NCS UPON PHOTOEXCITATION WITH 355 NM AT 6.5 MJ/CM <sup>2</sup> (BLACK CURVE), 40 μJ/CM <sup>2</sup> (BLUE CURVE) AND 3 μJ/CM <sup>2</sup> (RED CURVE). THE SPECTRAL SHIFT SHOWN IN THIS FIGURE IS REVERSIBLE AND THEREFORE DOES NOT IMPLY LASER DAMAGING. ....	109
FIGURE 9.16 - NORMALIZED PHOTOLUMINESCENCE SPECTRA OF CSPB(CLBR) <sub>3</sub> NCS UPON PHOTOEXCITATION WITH 355 NM AT 6.5 MJ/CM <sup>2</sup> (BLACK CURVE) AND 3 MJ/CM <sup>2</sup> (RED CURVE) WHICH IS FITTED BY A VOIGT FUNCTION (BLUE DOTTED CURVE). THE DIFFERENCE BETWEEN THE 6.5 MJ/CM <sup>2</sup> AND 3 MJ/CM <sup>2</sup> SPECTRA (BLUE CURVE) IS COMPARED WITH THE SIMULATED DIFFERENCE FROM THE RIGIDLY RED-SHIFTED 3 MJ/CM <sup>2</sup> SPECTRUM (GREY CURVE). ....	109



FIGURE 9.17 - NORMALIZED KINETIC TRACES OF PHOTOLUMINESCENCE (BLUE DOTS) AND X-RAY ABSORPTION SPECTROSCOPY AT 13.480 KEV (BLACK DOTS) FOR CSPB(CLBR) <sub>3</sub> NCS. IN THE INSET A ZOOM OF DECAY IN FIRST 5 NS AFTER PHOTOEXCITATION. ....	110
FIGURE 11.1 - TRANSIENT MAPS UPON EXCITATION WITH 3.1 EV FOR THE FLUENCE OF 2.5 (A), 5 (B), 10 (C), 18 (D), 37 (E), 65 (F) AND 100 $\mu\text{J}/\text{CM}^2$ (G).....	119
FIGURE 11.2 - FEMTOSECOND TRANSIENT SPECTRA AT DIFFERENT TIME DELAYS UPON PHOTOEXCITATION AT 3.1 EV WITH FLUENCE OF 2.5 (A), 5 (B), 10 (C), 37 (D) AND 65 $\mu\text{J}/\text{CM}^2$ (E). IN THE INSET, THERE IS A ZOOM OF THE LOW ENERGY REGION (FROM ABOUT 1.8 TO 2.4 EV) IN WHICH IS VISIBLE THE PA <sub>1</sub> SIGNAL. ..	121
FIGURE 11.3 - NORMALIZED X-RAY ABSORPTION SPECTRA OF CSPBBr <sub>3</sub> NEAR THE BR K-EDGE REGION ACQUIRED IN TFY. THE AGREEMENT BETWEEN THE SPECTRUM AVERAGED OVER THE FIRST 2 HOURS OF DATA ACQUISITION OF THE PUMP-PROBE EXPERIMENT (RED CURVE) AND THAT OVER THE CONSECUTIVE 2 HOURS (BACK CURVE), SUPPORTS THE ABSENCE OF DAMAGE DURING THE MEASUREMENTS UPON IRRADIATION AT 15 MJ/CM <sup>2</sup> AND 3.5 EV. ....	122
FIGURE 11.4 - PB L <sub>3</sub> -EDGE SPECTRA OF CSPB(CLBR) <sub>3</sub> SAMPLE (BLUE). THE XANES (RED) AND THE HREFD (BLACK) FOR PBO ARE REPRODUCED FROM REF. <sup>325</sup> .....	122
FIGURE 11.5 - X-RAY ABSORPTION SPECTRUM OF CSPB(CLBR) <sub>3</sub> NCS AT THE PB L <sub>3</sub> -EDGE (BLACK TRACE) WITH THE TRANSIENT AT 100 PS UPON PHOTOEXCITATION AT 3.5 EV (BLUE TRACE) AND SIMULATED TRANSIENT SPECTRA VIA THE RIGID SHIFT OF DIFFERENT MAGNITUDE AND SIGNS OF THE GROUND STATE SPECTRUM. ....	123



# 1 Introduction

The environmental concerns and increasing demand for energy, together with the constant progress in renewable energy technologies, open new opportunities for the use of renewable energy resources.<sup>1</sup> Solar energy is one of the few renewables with the scalability and the technological maturity to meet the global demand for electricity.

Among the solar power technologies, photovoltaics (PV) are the most deployed and provided 0.87 % of the world's electricity in 2013.<sup>2</sup> PV have a unique scalability, being capable of supplying from milliwatts to megawatts using a replicated modular technology.<sup>3</sup> Crystalline Si is the dominant commercial technology, with about 90% of the global production capacity (35% single-crystalline and 55% multicrystalline). It is the most mature PV technology because its evolution profited significantly from the production processes developed by micro-chip companies. The record cell efficiencies are 25.6% and 20.8%, for single-crystalline and multicrystalline respectively.<sup>2</sup>

Among the emerging PV technologies, dye-sensitized solar cells (DSSCs) represented a new paradigm of a device working at a molecular scale. DSSCs have lower production costs (payback time <1 year) and interesting design opportunities (*e.g.* transparency).<sup>4</sup> They became popular in 1991, after a publication by O'Regan and Grätzel,<sup>5</sup> which revolutionized the field of dye-sensitized photoelectrochemical cells using a mesoporous TiO<sub>2</sub> electrode with a high surface to volume ratio. In the early DSSC research, Ruthenium-complex dyes were developed (*e.g.* N719, N3, N749) and they remain among the most promising metal-complex sensitizers (record efficiency of ~11% using a Ru-based dye).<sup>4</sup> In the case of the hole conductor, an important achievement was the development of a solid state material<sup>6</sup> instead of the standard liquid electrolyte based on the I<sup>-</sup>/I<sub>3</sub><sup>-</sup> redox couple.

It is from these all-solid state dye-sensitized cells that lead halide perovskite solar cells evolved becoming nowadays one of the most important emerging PV technology. Starting from a 3.8% efficiency in 2009<sup>7</sup> they have achieved over 20% of certified efficiency recently.<sup>8</sup> Although the most efficient cells have a DSSC architecture with TiO<sub>2</sub> as electron acceptor, the material showed efficient ambipolar charge carriers transport.<sup>9</sup> Their low processing temperature (150 °C) and high conversion efficiencies make them ideal candidates for low-cost solar cells. In order to rationalize the outstanding efficiencies and unraveling the physics behind this class of semiconductors, several time-resolved studies have been performed in the last years.<sup>10,11</sup> Despite the interest in the charge carrier dynamics of lead halide perovskite, still several questions remain open about their fate. Solar energy conversion is governed by the generation of charge carriers (electrons and holes), their subsequent evolution as excitons or free charge carriers, and eventually their localization either as self-trapped excitons, polarons or simply at defects. These steps, that are crucial for the device performance, take place on a femto- to picosecond time scale. For this reason,

ultrafast XAS is the main technique used in this work, because it combines uniquely elemental and structural sensitivity to study the fate of charge carriers and their evolution under operating conditions (*i.e.* room temperatures and ambient pressure).

In the following pages, fully inorganic Cesium-based perovskites ( $\text{CsPbX}_3$ ) are investigated. They represent an ideal system to study the general ultrafast physics of lead halide perovskite because they show similar spectral features as the aforementioned organic-inorganic materials (*e.g.*  $\text{CH}_3\text{NH}_3\text{PbBr}_3$ ) in time-resolved studies<sup>11,12</sup> but do not suffer from the same stability problems.<sup>13</sup> Moreover,  $\text{TiO}_2$  is investigated, which is not only the most common electron acceptor in dye-sensitized and perovskite solar cells but also among the most promising metal-oxide photocatalysts.<sup>14</sup> The fate of the charge carriers is a significant problem for both applications.

Chapter 2 contains the basic concepts of semiconductor physics. Chapter 3 consists of a brief description of the experimental methods, meaning a general introduction of the time-resolved technique used and synthesis and characterization of the samples. In Chapter 4 and 7 a brief review of the literature introduces  $\text{TiO}_2$  and lead halide perovskites, respectively. Each of the following chapters contain a brief introduction as well, dealing solely with specific issues regarding the results of the experimental work and therefore focused on the charge carrier dynamics.

Chapter 5 discusses the early stages of electron localization in  $\text{TiO}_2$  anatase nanoparticles upon photoexcitation at 3.5 eV, using fs-XAS at the Ti K-edge.<sup>15</sup> The synchrotron study uses the slicing technique and is the first demonstration of femtosecond X-ray absorption spectroscopy applied to nanoparticles. This demonstration of the fs hard X-ray absorption capabilities opens the way to a detailed description of the charge carrier dynamics in transition metal oxides with higher time resolution and flux, which is now achievable at free electron lasers. Chapter 6 describes studies on the electron localization in rutile, another polymorph of  $\text{TiO}_2$ . Rutile has a different structure and optical properties than anatase and overall presents a lower activity in photocatalytic applications.<sup>16</sup> Using picosecond X-ray absorption spectroscopy at the Ti K-edge, the aim is to probe the electron delivered to the conduction band and to identify trapping sites in rutile  $\text{TiO}_2$  nanoparticles, similarly to a previous study on anatase  $\text{TiO}_2$ .<sup>17</sup>

Chapter 8 examines the ultrafast nature of the elementary excitation in  $\text{CsPb}(\text{ClBr})_3$  nanocrystals using broadband fs-TAS in the visible region ( $\sim 1.8\text{-}3.1$  eV) upon photoexcitation at 3.1 eV. In chapter 9 the charge carrier dynamics of  $\text{CsPbX}_3$  ( $X = \text{Cl}, \text{Br}$ ) is investigated for the first time using ps-XAS at the Br K-edge, the Pb  $L_3$ -edge and Cs  $L_2$ -edge upon photoexcitation at 3.5 eV. The results of this investigation bears important consequences for the understanding of the charge transport in perovskites. Finally, chapter 10 contains the general conclusions for this work and an outlook.

## 2 Basic concepts

### 2.1 General aspects of semiconductor physics

A semiconductor is a solid characterized by an electronic band structure with a forbidden gap that separates two bands of states, respectively called valence band (VB) and conduction band (CB). The basics of the theory for describing the electronic structure of a semiconductor were derived by Felix Bloch, who in 1928<sup>18</sup> defined the spatial dependence of the potential experienced by an outer electron in a crystal. In general, in a perfectly periodic lattice, a band electron should have an infinite mean free path. In real solids though, because the free path of an electron terminates when it encounters an interruption of the perfect periodicity, defects and phonons result in a finite mean free path.<sup>19</sup>

The bandgap is defined as the difference in energy between the highest point of the valence band (valence band edge) and the lowest point of the conduction band (conduction band edge).<sup>20</sup> This energy barrier can be overcome via an external excitation and this results in promoting an electron from the VB to the CB and therefore a hole is left behind in the VB. In the case of wide bandgap semiconductors, such as the ones presented in this work, electromagnetic radiation and electric fields are the most common source of excitation.

Semiconductors can be divided in two categories, based on their electronic band structure across the band gap position. When the location of the VB edge coincides with the CB edge in the reciprocal space (*i.e.*  $k$ -space) they are called *direct bandgap* semiconductors (Figure 2.1). If the two band edges are separated by a substantial wavevector  $k_c$ , they are called *indirect bandgap* semiconductors (Figure 2.1). This difference has significant effects on the optical absorption. Indeed, photons have a negligible momentum and therefore their absorption process is represented by a vertical transition in Figure 2.1. Thus, in order to have an indirect transition there is the need of both a photon and a phonon which provides the momentum to cross the separation in  $k$ -space. This makes the transition less probable and *indirect bandgap* semiconductors are hence characterized by smaller extinction coefficients. In this work, TiO<sub>2</sub> anatase and rutile have an indirect bandgap<sup>21</sup> while CsPbX<sub>3</sub> (X=Br, Cl) are, instead, direct bandgap semiconductors<sup>22,23</sup> (as the hybrid organic/inorganic perovskites are).<sup>24,25</sup>

Generally, when working with semiconducting nanoparticles as in this thesis, it should be considered that, under certain conditions, the electronic properties can be tuned by the particle dimensions. A fundamental parameter which has to be considered in order to understand the physics at the nanoscale is the exciton Bohr radius  $a_B$ , which indicates the spatial extension of the exciton wavefunction. Indeed, if the nanocrystal size becomes smaller than or comparable to  $a_B$ , the spatial confinement of the electron-hole pair can modify the electronic energy states. This *quantum-confinement* effect results in size dependent

properties: the bandgap energy increases with the decrease of the particle size and the continuum of transition, typical of a band structure, start to become discrete as in an atomic system.<sup>26</sup> In this work, the semiconducting nanoparticles studied should be treated more as bulk semiconductors because  $a_B$  is smaller than the crystallite size (*i.e.*  $a_B$  of 7 and 5 nm for CsPbBr<sub>3</sub> and CsPbCl<sub>3</sub><sup>22</sup>, with a particle size of 12 nm, and of 1.5 nm for TiO<sub>2</sub><sup>27</sup> with a particle size of tens of nm).

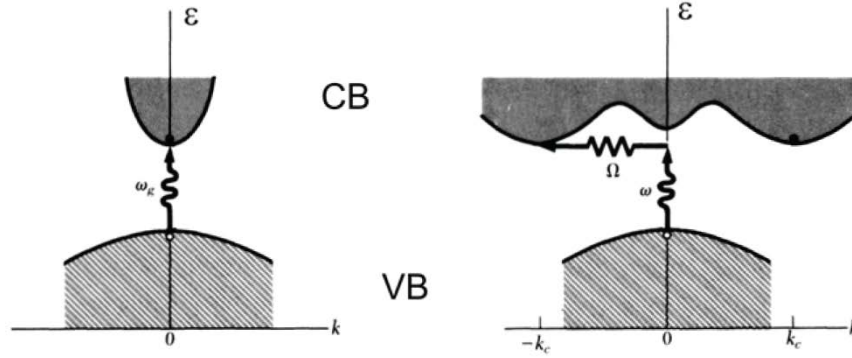


Figure 2.1 - Schematic representation of direct and indirect bandgap transition in a semiconductor. On the left, the CB edge and VB edge occurs at the same value of  $k$  and therefore a direct optical transition is allowed. On the right, an indirect transition which involves a photon and a phonon (where  $\Omega$  is its frequency) is required to compensate the difference in momentum between the two band edges. Taken from ref.<sup>20</sup>.

In the following sections the different possible states in which charge carriers can exist in a semiconductor will be described. In general, they can be either delocalized in the bands (free carriers), or localized in electronic states lying within the gap. Localization can arise from different sources (*e.g.* defects, amorphicity, electron-phonon coupling, Coulomb interaction) which will be discussed in details.

### 2.1.1 Free charge carriers and excitons

Electron and holes in a semiconductor can exist as free charge carriers, which are delocalized in the bands similarly to a metal, or as interacting pairs which forms a quasi-particle called exciton.

In the case of free charge carriers in a mild charge carrier density regime, the electron and hole are scattered only infrequently by other electrons and holes as a consequence of the Pauli exclusion principle. The system can therefore be defined as a *Fermi gas* and the Drude model can be used to describe it.<sup>19</sup> Indeed, the Drude theory, developed at the beginning of the last century, can be used to simply describe the electrical and optical properties of free carriers in metals and semiconductors.

In general, free carrier absorption is characterized by a monotonic and often structureless spectrum which can be reproduced by the simple expression:

$$\alpha \propto \lambda^p$$

where  $\alpha$  is the absorption coefficient,  $\lambda$  is the photon wavelength and  $p$  is a coefficient which can range from 1.5 to 3.5.<sup>28,29</sup> From the classical Drude theory, the oscillation of an electron in a metal which is driven by a periodic electric field leads to an attenuation which is proportional to  $\lambda^2$ .<sup>28</sup> Considering on the other hand what is described in literature as “the quantum description” of the free carrier absorption in semiconductors,<sup>30</sup> the exponent  $p$  can acquire values of:

- 1.5 when collisions with the lattice result in scattering by acoustic phonons.
- 2.5 when there is scattering by optical phonons.
- 3 or 3.5 when the scattering is caused by ionized impurities.

Generally, because the optical response of free charge carriers decreases as a power function with the probing energy,<sup>30</sup> the most successful spectroscopic regions to study delocalized carriers are the infrared and the terahertz.<sup>31,32</sup>

An electrostatically bound electron-hole pair is called exciton. An exciton can be seen as a quantum of electronic excitation energy that travels in the periodic lattice of a crystal transporting energy but not charge, because it is electrically neutral.<sup>33</sup> Figure 2.2 shows a schematic representation of the exciton states in a simplified band diagram for a direct semiconductor.

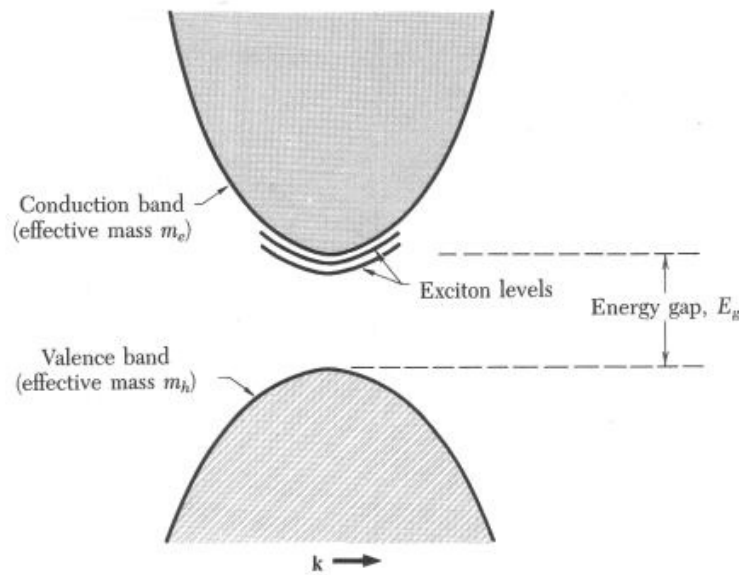


Figure 2.2 - Schematic representation of the electronic levels related to an exciton in a direct bandgap semiconductor. Taken from ref.<sup>20</sup>.

The existence of bound states is due to the attraction of electron and hole by the Coulomb potential energy  $-e^2/\epsilon r$  where  $r$  is the distance between them and  $\epsilon$  the dielectric constant. This dielectric constant plays a very important role in the exciton properties, as it determines the screening of the potential energy and therefore, the strength of the electron-hole interaction. This strength is characterized by the exciton binding energy, which can vary from a few meV to  $\sim 1$  eV. Excitons can be divided in two groups, depending on their spatial localization: *Frenkel* and *Wannier-Mott* excitons.<sup>20</sup>

Frenkel excitons, described for the first time in 1931,<sup>34</sup> are characterized by electron and hole tightly bound and localized. Indeed, the exciton binding energy is in the order of 0.1 to 1 eV and the exciton radius is often comparable or smaller than the lattice constant. They are typically found in materials with small dielectric constants such as alkali halide crystals or organic molecular crystals.<sup>20</sup> Wannier-Mott excitons instead, first described in 1936,<sup>35</sup> have a large radius in comparison to the lattice constant, covering tens to hundreds of atomic sites and have exciton binding energies of a few tens of meV. There is yet another type of exciton, called charge-transfer (CT) exciton which has a spatial extension in between a Frenkel and a Wannier-Mott exciton. Differently from those two though, it is characterized by a permanent dipole moment. Indeed, typical excitons have a symmetric charge distribution for electrons and holes, which occupy the same spatial region. In presence of an interface, the Coulombically bound electron and hole can be located in different spatial regions.<sup>36</sup> This is often the case for organic semiconductor surfaces, where the low dielectric constants ensure the formation of a bound electron-hole pair across the interface, a CT exciton.<sup>36</sup> Therefore understanding of CT excitons is fundamental for the development of excitonic solar cells. In general, the energy of an exciton is modified by the vibrational motion of atoms in solid, and by increasing the temperature, broadening can be observed in the optical absorption spectra due to exciton-phonon scattering.<sup>33</sup> For this reason, Mott-Wannier excitons are often too broad to be clearly observed at room temperature. Therefore, particularly when aiming at optical studies of the higher hydrogenic energy levels of an exciton, the experiments are usually performed at cryogenic temperatures.

At low charge carrier densities, excitons can be considered as non-interacting bosons which are in equilibrium with free electrons and holes. An increase of charge carrier density though, can trigger interactions between the excitons which can form exciton-exciton pairs called *biexcitons*.<sup>26</sup> If an exciton could be seen in analogy with a hydrogen atom, the bound state of two excitons can be seen as a hydrogen molecule and can be excited by two photon absorption. In 1958, Lampert considered for the first time the possibility of observing a state due to an interaction between two excitons.<sup>37</sup> A few years later, a new emission line in the luminescence of Si was interpreted as biexciton fingerprint in the material.<sup>37</sup> Indeed, photoluminescence is among the most effective techniques to observe this state. The binding energy of a biexciton is expressed as:

$$E_b = 2E_x - E_{xx}$$



where  $E_b$  is the biexciton binding energy,  $E_x$  and  $E_{xx}$  correspond to the energy of a single and biexciton, respectively. Therefore, when a biexciton is annihilated forming an exciton and a photon, the photoluminescence of the emitted photon is on the low energy side of the exciton peak. Recently, the emission due to biexciton recombination in  $\text{CsPbBr}_3$  has been observed using time resolved photoluminescence.<sup>38</sup>

### 2.1.2 Defects and disorder

Real crystalline solids, besides the surface which clearly terminates the periodicity of the lattice, are characterized by the presence of bulk defects. Indeed, within a crystalline particle there is a finite concentration of *point defects* and *dislocations*. While point defects extend only for a few atomic spacings, dislocations can extend for millions of atomic spacings. In general, defects can act as trap states, forming electronic levels within the gap of the semiconductor and promoting charge carrier localization. This is clearly detrimental for applications where high charge carrier mobility is critical, such as photovoltaics.

Point defects can originate from *extrinsic impurities* or can simply be *native point defects*. Extrinsic impurities are often unwanted byproducts of the crystal growth and chemical synthesis, and can modify the electrical, magnetic and optical properties of a semiconductor. Interestingly, the difference between a dopant and an extrinsic point defect is based on the resulting properties that the impurity will assign to the material. In fact, often extrinsic impurities are added during the synthetic procedure to affect and control the equilibrium concentration of native defects.<sup>19</sup>

*Vacancies* are the simplest native point defect which consist of the absence of an atom from a regular atomic site (Figure 2.3). When they are formed in an ionic compound, electroneutrality has to be satisfied and therefore excess electrons can be left in the volume space of the vacant site. This can affect the optical properties of the solid with the formation of so-called color centers. In the case of a simultaneous presence of vacancies for the various atomic species in the right proportion, the electroneutrality can be preserved automatically. This is called *Schottky disorder* and it has been hypothesized for hybrid organic-inorganic lead halide perovskite through quantum mechanical calculation.<sup>39</sup>

*Interstitial* atoms are another type of native point defect, where an atom is fitted into the crystal wherever it can find space through a distortion of the lattice (Figure 2.3). When an interstitial atom and a vacancy of the same kind are within the lattice, the electroneutrality is ensured and this is called a *Frenkel defect*.<sup>19</sup>

As mentioned above, the surface of a crystal is a natural place to find defects due to the truncation of the lattice and the presence of dangling bonds. In this work, it is of a particular importance because crystalline nanomaterials, characterized by a high surface to volume ratio, are studied. Moreover, near the surface of nanomaterials an amorphous region can be present, where crystalline order is lost.<sup>40</sup> Disorder itself can be a source of charge carrier localization through *Anderson localization*. Indeed, as recognized by Anderson in 1958,<sup>41</sup> in

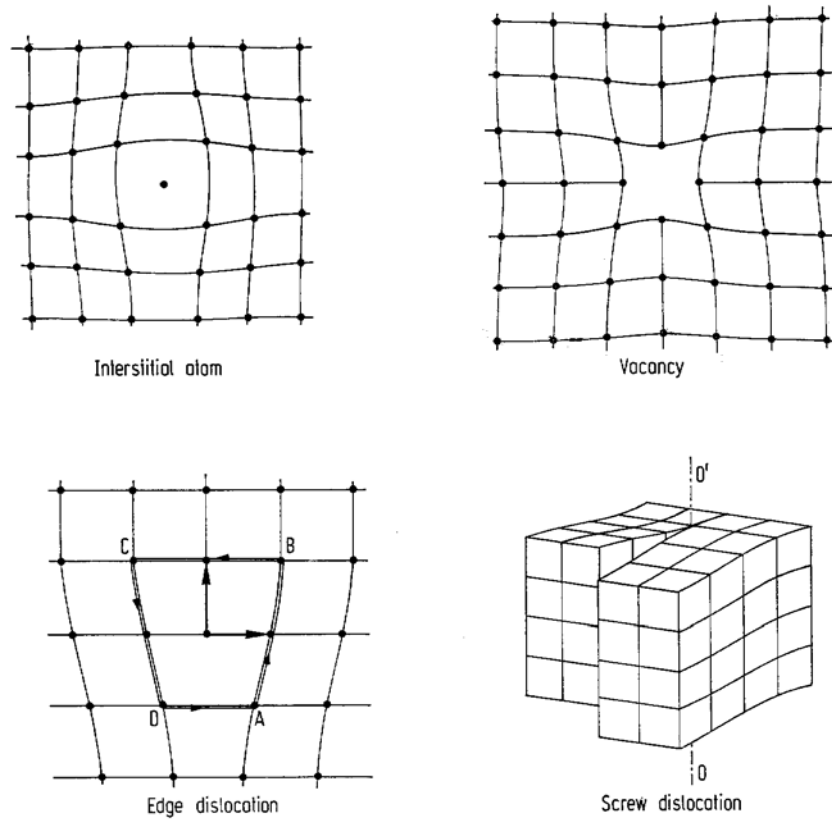


Figure 2.3 - Schematic of point defects (above) and dislocations (below) in a solid. The edge dislocation is highlighted by a closed loop, typical of Burgers vector representation. Taken from ref.<sup>42</sup>.

the case of amorphous materials where the charge carrier scattering becomes very strong, a localized wavefunction appears within the gap of the semiconductor, even if there is a strong overlap between wavefunctions of neighbouring states.<sup>43,44</sup> Therefore, the surface is intrinsically the most common center for carrier localization, due to concomitant presence of a high density of defects and disorder.

### 2.1.3 Self-trapping: polaron and self-trapped exciton

Localization is a phenomenon which can simply arise by the presence of defects which introduce pre-existing states within the gap that are populated by electrons and holes, as seen in the previous section. After the population of these states, an additional structural rearrangement caused by the shift of electronic density can further stabilize the localized state. From 1933 onwards, Landau advanced the idea that charge carriers added to an insulator could be *self-trapped*,<sup>45</sup> due to a displacing of the equilibrium positions of the surrounding atoms (Figure 2.4).<sup>45</sup> Basically, in this case of localization, charge carriers in a polar lattice are stabilized by a structural rearrangement due to their presence via an intrinsic process. Indeed, when the Coulomb coupling between charge carriers and lattice ions is

strong, the charge carriers are always surrounded by a cloud of optical phonons, which consists physically of an electron pulling nearby positive ions towards it and pushing nearby negative ions away.<sup>46</sup> The corresponding process is also possible for holes. Therefore, the effective mass of this quasi-particle is always larger than the mass of the originating electron or hole, since it has to drag the lattice distortion when it moves, suffering a larger inertia.<sup>46</sup> Depending on the intensity of the electron-phonon coupling, the atomic displacement can result either in a quasi-particle called *large polaron* (weak coupling) or *small polaron* (strong coupling). Large polarons (also called *Fröhlich polarons*) are self-trapped carriers which extend over several sites. Their mobility is limited by scattering with phonons and therefore decreases with rising temperature (*i.e.* as the density of phonons increases). Small polarons instead, are carriers confined at a single site and they move by thermal hopping, a phonon-assisted quantum-mechanical tunneling, from one localized state to another.<sup>44,45</sup> Their mobility increases as the temperature raises. In some cases, large and small polarons can co-exist separately in the same material, as in general self-trapped and free charge carriers.<sup>47</sup> Moreover, the potential well of a lattice defect can have an additive effect on the electron-phonon coupling in the localization processes.<sup>48</sup> It can lead, for example, to a collapse of a large polaron into a small one in the vicinity of the defect site. The theory, developed by Shinozuka and Toyozawa in 1979,<sup>48</sup> for which the electron-phonon coupling and the effects arising from weak external potentials due to defects are considered to be additive, results in the localization of an electronic excitation even when one of these mechanisms is in itself not sufficient to induce it.

In this work, for both  $\text{TiO}_2$  and lead halide perovskites there is a tendency to form polarons<sup>49,50</sup> due to a significant electron-phonon coupling (details in chapters 4.5 and 7.3, respectively).

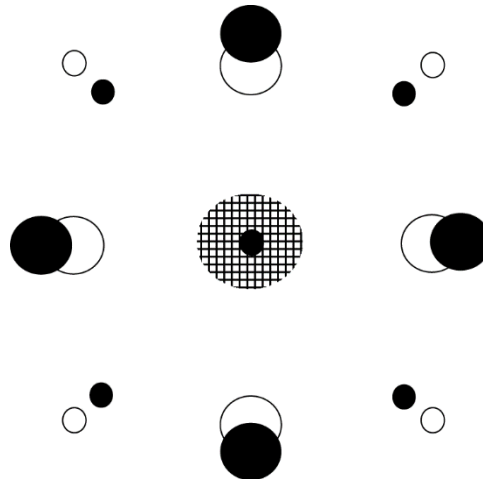


Figure 2.4 - A self-trapped electron on a cation (hatched area) in a lattice, where anions are large circles and cations small circles. The surrounding ions are shifted from their equilibrium positions (open large and small circles) in a new configuration (filled large and small circles) which produces a potential well for that carrier. Taken from ref.<sup>45</sup>.

Similarly to what was presented in the case of biexcitons, polarons can also coalesce into pairs forming *bipolarons* provided high enough charge carrier density. Indeed, the electron-phonon interaction promotes this state because the energy depth of the self-trapping potential well doubles when it is occupied by two carriers.<sup>45</sup> On the other side, Coulomb repulsion opposes this merging of identical charges and therefore, the final outcome, depends on the strength of these two competing effects.

Also excitons can be affected by the presence of the electron-phonon coupling in a solid which leads to the formation of self-trapped excitons. In a first analysis, the self-trapped exciton can be seen as an analog to a polaron for an electron or a hole, but the forces that influence the formation of a self-trapped exciton, starting from a free exciton, are often different. For example, in case of alkali halides, the hole can self-trap in the crystal due to short range (molecular bonding) and long-range (dielectric polarization) interaction, which are cooperatively contributing to the self-trapping mechanism. By contrast, since the exciton is a neutral particle, the long-range polarization has no effects on the self-trapping process, leading to a different result.<sup>51</sup> Moreover, the Coulomb interaction between an electron and a hole is always attractive. For what concerns the phonon mediated interaction, it will be attractive if the electron and hole equally expand (or contract) the lattice; but it will be repulsive in the opposite case owing to the competition between Coulomb and charge carrier phonon interaction.<sup>52</sup> In anatase  $\text{TiO}_2$  the formation of self-trapped excitons has been found and investigated using time resolved luminescence spectroscopy.<sup>53</sup>

## 2.2 Many-body and electric field effects on semiconductor physics

The physics of semiconductors including their absorption spectra can be strongly affected by many-body effects, which arise from the interaction of carriers, or more simply by external perturbations. As seen before, the Coulomb potential is attractive for charge carriers in different bands (interband interaction) but is repulsive for carriers in the same band (intraband interaction). The resulting effects from these opposite interactions are called many-body effects, since the Coulomb interaction always involves more than one carrier.<sup>54</sup> Previously, the effects of a significant charge carrier density, which can lead to the formation of biexcitons and bipolarons, were discussed. Together with the formation of these quasi-particles, charge carrier interaction leads to the renormalization of the exciton binding energy and of the bandgap, as it will be discussed in the next two sections. Finally, the impact of an external electric field will be discussed, particularly for what concerns the absorption spectrum of a semiconductor. These phenomena are of exceptional importance for understanding the physics of semiconductors upon optical excitation with ultrashort pulses, because in this case high transient charge carrier densities or electric fields can be easily generated.

### 2.2.1 Exciton screening and Mott-transition

In presence of a significant carrier density, the exciton-exciton and exciton-carrier scattering screens the Coulomb interaction between electron and hole pairs. Interestingly, it has been shown that free charge carriers are about 50 times more efficient in the screening process than excitons.<sup>55</sup> In both cases, this many-body effect results in the reduction of the exciton binding energy. This can be easily observed in the optical absorption spectrum of the semiconductor, because it results in a blue-shift of the exciton absorption resonance. This modulation of the optical absorption spectrum was reported in two-dimensional organic/inorganic lead iodide perovskite quantum wells<sup>56</sup> and more recently in polycrystalline films of  $\text{CH}_3\text{NH}_3\text{PbI}_3$  and  $\text{CH}_3\text{NH}_3\text{PbBr}_3$ .<sup>57</sup>

It exists a specific carrier density (that varies depending on the material properties), which leads to a complete screening of the electron-hole interaction and this results in the formation of a *Fermi liquid*. A Fermi liquid is described by Landau's theory and in contrast to a Fermi gas, which represents a system of noninteracting fermions, it allows for interactions.<sup>20</sup> The transition from excitons to this electron-hole plasma in a solid is known as *Mott transition*.<sup>16</sup> The critical carrier density in an excitonic material at which the Mott transition takes place is characterized by an average distance between excitons similar to the exciton Bohr radius, as showed in Figure 2.5. In this condition, the exciton wavefunctions overlap and lead to a complete screening of electron and hole interactions. This effect has been experimentally studied in metal oxides wide bandgap semiconductors such as  $\text{ZnO}$ ,<sup>58</sup> but not yet observed in lead halide perovskite materials.<sup>10</sup>

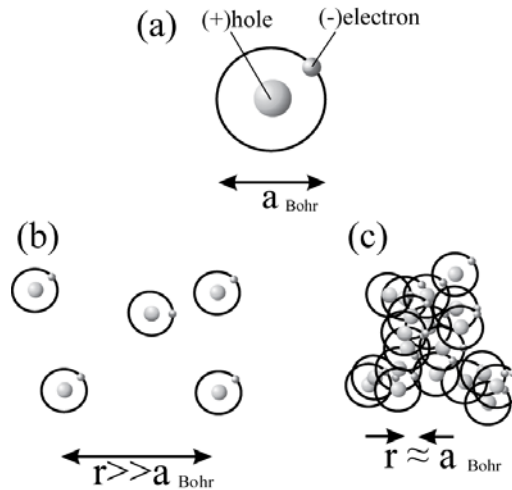


Figure 2.5 - Schematic of a Wannier exciton with Bohr radius  $a_{\text{Bohr}}$  (a). An exciton gas below the Mott density, with the average distance between excitations much larger than the Bohr radius (b). An exciton system above the Mott density (c). Taken from ref.<sup>58</sup>.

### 2.2.2 Bandgap renormalization

As seen above, the band structure and optical properties of a semiconductor with a significant carrier density strongly differ from those resulting from non-interacting electron-hole pairs, due to many-body effects. One of the most important many-body effects derives from the interaction of free charge carriers among each other and it is a density-dependent renormalization of the fundamental bandgap of the semiconductor. The renormalization is mainly due to exchange interaction — a quantum mechanical effect that occurs between identical particles and leads for fermions to the *Pauli repulsion* — and to simple Coulomb repulsion. In fact, Pauli principle prevents two electrons or holes with identical spin from occupying the same spatial position (exchange energy), whereas the Coulombic repulsion maximizes the distance between like charges in space. In presence of high charge carrier densities, the system minimizes its total energy through a reduction of the bandgap energy.<sup>10</sup> Since this renormalization is a result of a change in the potential felt by electrons and holes, it influences all the electronic states simultaneously and independently of their energy.<sup>59</sup> This correction of the bandgap energy in the system is known as *bandgap renormalization* (BGR) and results in an increasing absorption in the spectral region below the lowest exciton resonance.<sup>60</sup>

In this regard, it is interesting to notice that when carrier interactions are “switched on”, there are two competing effects in the optical absorption spectrum of a semiconductor: a redshift of the optical absorption due to the electronic gap shrinkage that derives from BGR, and a blueshift due to exciton binding energy reduction which derives from screening.<sup>59</sup> Whether or not these two effects compensate each other depends on the material, dimensionality and the charge carrier density. The experimental study of Reynolds *et al.*<sup>61</sup> on ZnO and GaN crystals clearly demonstrates this. In case of ZnO there is a clear predominance of BGR at all the carrier densities explored, hence a redshift of the optical absorption. In GaN, on the other side, there is an almost perfect compensation of the two effects, with a little predominance of a blueshift due to screening in the lower carrier density regime and a redshift due to BGR at the higher carrier density regime. In case of  $\text{CH}_3\text{NH}_3\text{PbI}_3$  films, a short-lived redshift ( $\sim 1$  ps) of the absorption spectra upon bandgap photoexcitation has been attributed to BGR.<sup>62</sup> The signal is short-lived due to the fact that the charge carriers have to interact to produce this effect, therefore their concentration has to be significantly high and the BGR vanishes in a few ps after photoexcitation because of charge carrier recombination.

### 2.2.3 Electroabsorption effects

Semiconductors absorption edges are broadened and shifted in energy when a static electric field is applied. The broadening clearly indicates a decrease of the exciton lifetime due to the field ionization while the shift is a Stark effect on the exciton ground state. Interestingly,



when the static electric field exerts a local force stronger than those which bind electrons and holes, the exciton is ionized and the carriers free to move in their bands.<sup>63</sup>

The discovery of Johannes Stark on the splitting of the atomic spectral lines in the presence of an applied static electric field, rewarded with the Nobel prize in 1919, set the beginning of a new type of spectroscopy. Indeed, not only atoms, but also molecules, solids and biological systems present modulation in their absorption spectra when a static external electric field is applied.<sup>64</sup> The spectroscopic technique which investigates the effects of a static electric field on an absorption spectrum is called *electroabsorption spectroscopy* and provides information regarding changes in the system's dipole moment, polarizability and transition moment. The technique is used in molecules to study charge transfer processes and in semiconductors to provide insight into the excitonic transition of the sample, allowing to retrieve the exciton binding energy.

In 1958 Franz and Keldysh developed a quantitative theory to describe the effect of a uniform electric field applied on a direct band-to-band optical transition in a semiconductor.<sup>65</sup> Their primary prediction was that upon a static electric field perturbation the optical absorption edge of a semiconductor would broaden and shift to lower energies. This hypothesis was confirmed experimentally a few years later. Franz-Keldysh theory though, does not include correlation effects and therefore can only be used in the electroabsorption interpretation of semiconductors where upon absorption of a photon are generated uncorrelated free charge carriers. In 1966 it was recognized that excitonic interactions have a prominent role on the electroabsorption spectra and eventually the Stark effect theory for semiconductors was developed.<sup>65</sup> The field-invariant line shape and quadratic amplitude scaling of the electroabsorption signal characterize a third-order nonlinear response which is typical of both theories, the excitonic quadratic Stark effect and the one-electron Franz-Keldysh theory.<sup>66</sup> A way to distinguish these two mechanism and therefore the presence of exciton or free charge carriers in the material, is to consider if the electroabsorption signal resembles the second or the third order derivative of the unperturbed complex dielectric function which can be measured through ellipsometry. In the former case the electroabsorption can be attributed to a Stark effect, in the latter case to a Franz-Keldysh effect.

Moreover, upon bandgap photoexcitation, semiconductors can display a transient electroabsorption due to the electric field of the generated free charge carriers or excitons, as the one observed in the femtosecond transient absorption measurements on  $\text{CH}_3\text{NH}_3\text{PbI}_3$  thin films<sup>56</sup> and discussed in chapter 8. Here, the results interpretation by Trinh *et al.*<sup>56</sup> of a transient electroabsorption is supported by the fact that the same spectral shape was recently observed in the electroabsorption spectroscopy measurements of  $\text{CH}_3\text{NH}_3\text{PbI}_3$ .<sup>66</sup> For the authors, this photoinduced effect derives from the electric field of hot charge carriers which is proportional to their excess energy and therefore, while hot carriers cool down, the intensity of this signal decreases as well.

## 2.3 Relaxation processes in semiconductors

In this thesis, the physics of semiconducting materials which are placed out of the thermodynamic equilibrium by illumination is investigated. Electron-hole pairs are radiatively generated using ultrashort laser pulses (see chapter 3 for details) and a recombination mechanism will bring the system back to equilibrium. Between these two states, semiconductors undergo several stages of relaxation. In the first moment after photoexcitation ( $< 100$  fs), the distribution of the excitation is non-thermal, *i.e.* it cannot be characterized by Boltzmann statistics.<sup>67</sup> The investigation of this time scales provides information on the carrier-carrier scattering which will bring the system to a hot, thermalized distribution. Thereby electrons and holes will reach the lattice temperature in picoseconds through the carrier-phonon interaction.<sup>68</sup> Finally, the charge carriers will recombine. In the following sections three recombination mechanisms are presented: radiative, Shockley-Read-Hall and Auger recombination. The last section is devoted to an important phenomenon in the intraband relaxation processes called phonon bottleneck.

### 2.3.1 Radiative recombination

Radiative recombination can be seen as the opposite process of optical absorption. For this reason, as for the absorption transition, it is more efficient in direct bandgap semiconductor than in indirect ones. The probability of radiative emission for electron hole pairs is given by the square of the overlap integral:

$$P \propto |\langle \Psi_{eh} | e \cdot p | 0 \rangle|^2$$

where  $\langle \Psi_{eh} |$  represents the exciton wavefunction,  $e \cdot p$  the dipole operator and  $|0\rangle$  the ground state.<sup>26</sup>

Under suitable conditions, the spontaneous radiative recombination is replaced by the presence of stimulated radiative recombination, which can be used for lasing application.<sup>19</sup> This is the case of lead halide perovskites, which showed to be promising semiconductors for this type of application.<sup>69,70</sup>

### 2.3.2 Relaxation through defects: Shockley-Read-Hall recombination

Recombination in indirect semiconductors is dominated by a two steps process, which is mediated by trapping. The presence of a trap level within the gap facilitates the recombination process splitting it into two parts.<sup>71</sup> Recombination through defect states in direct bandgap semiconductors can instead hardly be a dominant process, because it cannot compete with the more efficient radiative recombination. The statistics which describes the trap assisted recombination has been developed by W. Shockley, W. T. Read and R. N. Hall,<sup>72,73</sup> and therefore these processes takes their names.



The presence of an intermediate state in the recombination process can lead to radiative or nonradiative recombination in the last step, but the nonradiative one is the most common owing to the energy transfer to phonons. Indeed, to have radiative recombination from the intermediate state, this should have similar properties to those of VB and CB, meaning it should be delocalized;<sup>74</sup> to achieve delocalization, the defects cannot be placed randomly in the lattice but should possess an ordered periodic structure.<sup>74</sup> This is usually not the case so nonradiative recombination dominates.

### 2.3.3 Auger recombination

Auger recombination is a three particle interaction process in which an electron and hole recombine, donating the energy to a spectator charge (another electron or hole, see Figure 2.6), therefore it is nonradiative. As for radiative recombination, this process is more common for direct bandgap semiconductors because the event must occur in a way which simultaneously conserves energy and momentum;<sup>19</sup> the mutual conservation of energy and momentum is clearly less likely for indirect bandgap semiconductors because of their electronic structure. This process becomes significant only in presence of high charge carrier densities due to the higher probability of a three body interaction. The rate of the Auger process  $k_A$  is characterized by the following relations, depending on which particle is the spectator in the process:

$$k_A \propto np^2 \quad \text{or} \quad k_A \propto n^2p$$

where  $p$  and  $n$  are respectively the concentration of holes and electrons.<sup>75</sup>

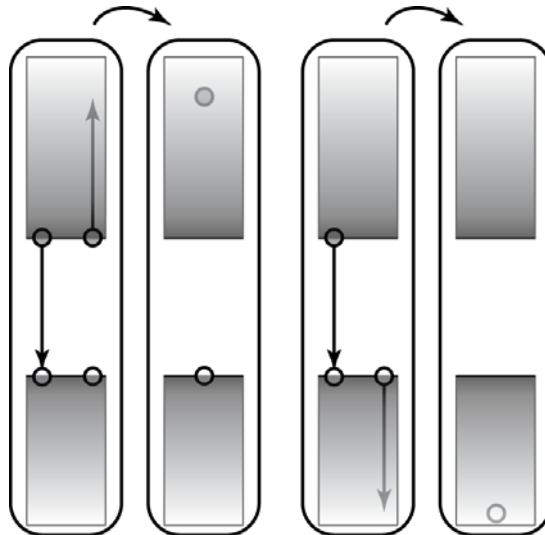


Figure 2.6 - Schematic of Auger recombination in a semiconductor. In this nonradiative transition an electron-hole pair transfers energy to a spectator charge, which can be either an electron (left two pictures) or a hole (right two picture). Readapted from ref.<sup>26</sup>.

### 2.3.4 Phonon bottleneck

A hot charge carrier distribution, which is undergoing intraband relaxation for cooling to the band edges, dissipates the excess energy through coupling with optical phonons which eventually transfer energy into the acoustic phonons. Usually in quantum confined semiconducting nanostructures, the discretization of the electronic levels requires an interaction with multiple phonons at a time for an intraband transition which respects energy conservation. This process, that slows down the relaxation because it is very unlikely, is known as *phonon bottleneck*.<sup>67</sup>

On the other hand, in bulk semiconductors can also be observed a phonon bottleneck. In this case the slow down charge carrier cooling is due to an inefficient coupling between optical and acoustic phonons. This inefficient coupling can arise from a phononic bandgap which occurs when there is a large mass ratio between anions and cations in the investigated sample.<sup>76</sup> Moreover, ferroelectricity in a material can also produce a large splitting of phonon energies.<sup>77</sup> This creates a hot optical phonon population that takes a significant time to reach equilibrium, indeed the excess hot phonon population increases the phonon reabsorption and reduces the net thermalization rate.<sup>77</sup> Moreover, should be considered that at high charge carrier density the decrease of the cooling process can also be due to Coulomb screening, which screens the carrier-optical phonon interaction and decelerates the rate of phonon emission. Recently, phonon bottleneck arising in bulk hybrid organic inorganic lead halide perovskites has been observed upon photoexcitation in fs-transient absorption measurements.<sup>77</sup>

## 3 Experimental methods

### 3.1 Femtosecond transient absorption spectroscopy

Optical spectroscopy is a powerful tool for investigating the electronic properties of semiconductors and insulators. Thanks to the advent of picosecond and femtosecond laser systems in the 1960s, it can provide insights into aspects such as charge carrier dynamics upon photoexcitation.<sup>68</sup> In particular, femtosecond transient absorption spectroscopy (fs-TAS) allows to study non-equilibrium phenomena in semiconductors. It uses a pump-probe scheme where a single laser pulse is split into two, a pump and a probe, and during a measurement the time delay between these two is changed in order to record transient spectra at different time delays after photoexcitation. Using this approach is possible to measure changes in transmission over time upon sample photoexcitation. Figure 3.1 shows the processes which can be observed in a transient absorption spectrum, though it cannot grasp the complexity behind the origin of the different transient feature, *i.e.* ground state bleach (GSB), excited state absorption (ESA) and stimulated emission (SE), in condensed matter.

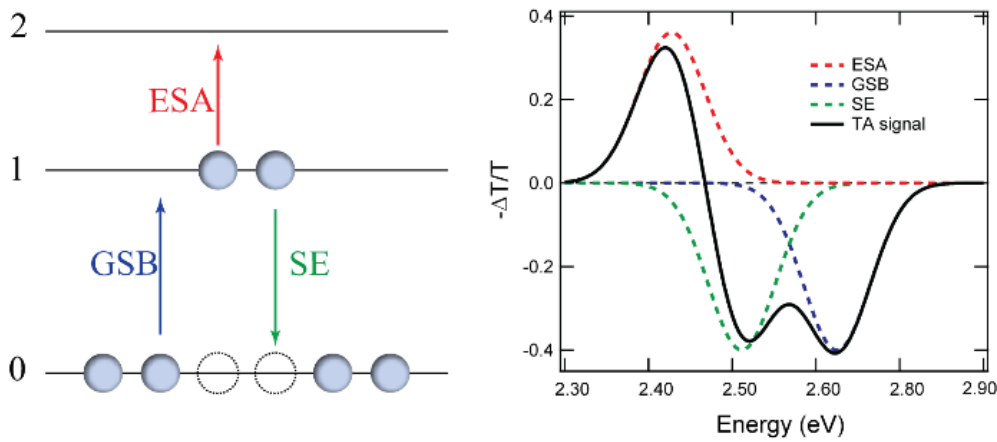


Figure 3.1 - Schematic representation of the three processes (*i.e.* ground state bleach, stimulated emission and excited state absorption) which modulate the transient absorption spectra of a pump probe measurement. Readapted from ref.<sup>78</sup>.

In a solid indeed, many-body effects which result, for example, in a change of the energy band structure (*e.g.* band-gap renormalization or a change in the exciton binding energy) or a broadening of the energy levels, can easily take place. All these effects, as showed chapter 8, strongly depend on the photoexcited charge carrier density and the nature of the system being investigated (*e.g.* excitons vs free charge carriers).<sup>68</sup>

### 3.1.1 Technical details

The measurements of fs-TAS in chapter 8 have been performed using a femtosecond pump/continuum-probe setup with 1 kHz repetition rate. In this system, a continuous wave Nd:YVO<sub>4</sub> laser (*Millenia V*s, Spectra Physics) is used to pump a Ti:Al<sub>2</sub>O<sub>3</sub> oscillator (*Tsunami*, Spectra Physics) which is mode-locked and produces pulses at 1.55 eV that are used to seed a regenerative amplifier (*Spitfire*, Spectra Physics). The system provides pulses at 1 kHz with a duration of about 100 fs and pulse energy of 0.65 mJ.<sup>79</sup>

Figure 3.2 shows a scheme of the optical pump-probe setup from the amplifier output to the detector. The samples are excited with a pump of 3.1 eV, which is obtained through frequency doubling inside a 0.5 mm thick  $\beta$ -BBO crystal. A neutral density filter to control the pump fluence is placed before the frequency doubling, in order to reduce the chirping of the pump pulses and retain the highest possible time resolution. The pump beam is phase chopped by a phase-locked mechanical chopper which operates at half of the system repetition rate. The probe is a broad white light continuum, which covers all the visible region (from about 3.1 to 1.8 eV) and it is produced by focusing the 1.55 eV beam into a CaF<sub>2</sub> window. In order to avoid damaging of the crystal, just a small portion of the main beam is used (about 1 mW) and the crystal is constantly moved. Finally, the difference spectrum is recorded in a single-shot detection scheme<sup>26</sup> which consists of a photodiode array that is read out by a fast analog-to-digital converter (ADC) for each probe pulse.

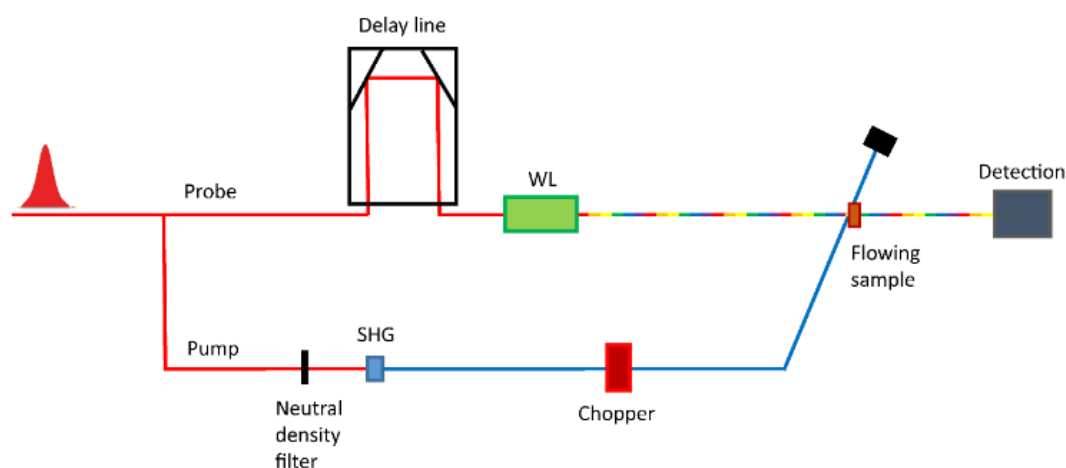


Figure 3.2 - Schematic representation of the femtosecond transient absorption setup from the output of the amplifier to the detection system. WL represents the CaF<sub>2</sub> window for the probe whitelight generation and SHG, the second harmonic generation  $\beta$ -BBO crystal for the 3.1 eV pump.

The instrument response function (IRF) of the setup is about 100 fs. The suspended sample is recirculated using a peristaltic pump in a quartz flow cell (500  $\mu\text{m}$  thick) at room temperature to refresh the sample between the consecutive pump pulses in order to reduce any laser induced damaging.

## 3.2 X-ray absorption spectroscopy

Synchrotrons provide an intense source of tunable x-rays, making them ideal for performing x-ray spectroscopy measurements.<sup>80</sup> Over the years, these large x-ray sources continuously improved in performances with a promising outlook in time resolved techniques, which brought recently to the design of free electron lasers (FELs).<sup>81</sup> In general, synchrotron storage rings produce high energy photons by deviating the path of relativistic electrons using strong magnetic fields. This forced motion results in energy dissipation from the charged particles which manifests itself as emission of electromagnetic radiation. In order to apply this magnetic field there are mainly three different devices which are the main discriminating factor for the different generations of synchrotrons: bending magnets, wigglers and undulators. The bending magnet is the first synchrotron light source in historical terms, indeed this device applies the necessary centripetal force to keep the electrons in a circular orbit. However, this double function of keeping electrons in the trajectory and emitting light limits their flexibility. Indeed, they generate a broad spectrum of x-rays and the maximum x-ray flux depends on the magnetic field strength and electron energy in the storage ring.<sup>80</sup> In Figure 3.3a there is an example of bending magnet radiation at the Swiss Light Source (SLS). Bending magnets can not only generate x-ray photons but also infrared and vacuum ultraviolet radiation.<sup>82,83</sup> A wiggler is composed of a periodic series of magnets which are inserted in the straight sections of the storage ring. Here each “wiggler” is equivalent to a bending magnet, emits independently from the other wigglers but provides more flexibility in tuning the emission parameters. When the emission becomes spectrally narrow, meaning almost monochromatic, for reason related to the wiggling parameters, the wiggler becomes an undulator.<sup>84</sup> In Figure 3.3b the spectrum of an undulator at the SLS. In general, undulators produce the highest spectral brilliance in x-ray beamlines. For XAS measurements, a fundamental step following the production of high intensity x-ray is to monochromatize the radiation. In hard x-ray beamlines monochromators are based on crystals which can provide a bandwidth of  $\Delta E/E$  0.01-0.03 % that is on the order of an eV, in this energy region.<sup>80</sup> Finally, the x-ray beam needs to be focused onto the sample, particularly for time resolved experiments where the x-ray beam is the probe and needs to be smaller than the laser pump beam. This is done using reflective achromatic x-ray optics called Kirkpatrick-Baez mirrors.<sup>85</sup>

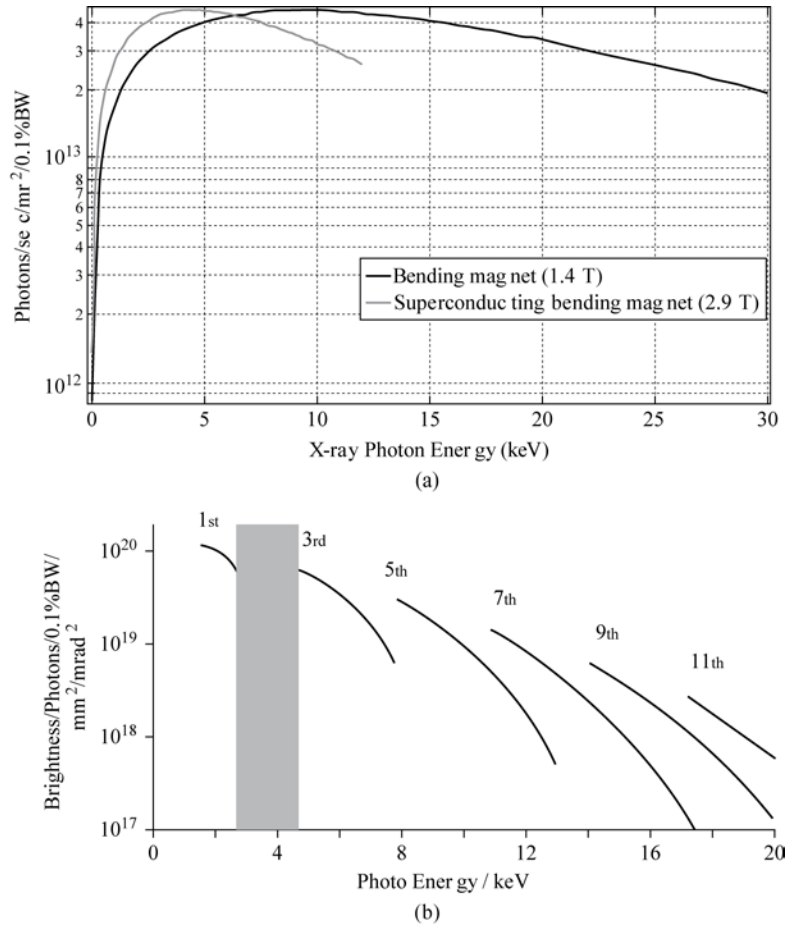


Figure 3.3 - Calculated emitted x-ray radiation from a bending magnet and a superbending magnet (a) at the Swiss Light Source in Paul Scherrer Institute. The superbending magnet is used in the SuperXAS beamline. Below, the x-ray spectrum calculated for the minigap undulator at the microXAS beamline (b) of the Swiss Light Source. The grey bar shows a gap in which x-ray are not generated. Taken from ref.<sup>80</sup>.

### 3.2.1 X-ray matter interaction

X-ray absorption spectroscopy allows to study the variations of the absorption coefficient, mostly in a range of energy between 1 to 40 keV. The absorption coefficient within this energy range is mainly affected by photoelectric absorption, meaning an absorption which excites or ionizes specific atoms. In general, when the energy of the x-rays increases the absorption coefficient decreases, but there are discontinuities in this trend called absorption edges. The absorption edges are given by the transition or extraction of core electrons from an atom. Because the binding energy of electrons increases monotonically with the atomic number, absorption edges are specific for a particular atomic species.<sup>84</sup> The transitions from the different atomic core energy levels are designated with the following letters for historical reasons.

Edge:	M <sub>V</sub>	M <sub>IV</sub>	M <sub>III</sub>	M <sub>II</sub>	M <sub>I</sub>	L <sub>III</sub>	L <sub>II</sub>	L <sub>I</sub>	K
Core level:	3d <sub>5/2</sub>	3d <sub>3/2</sub>	3p <sub>3/2</sub>	3p <sub>1/2</sub>	3s	2p <sub>3/2</sub>	2p <sub>1/2</sub>	2s	1s

Upon absorption of x-rays the atom can be excited, if the transition is between a core and an unoccupied valence state, or ionized if the transition is between the core and the continuum. In the latter case, the kinetic energy of the emitted photoelectron depends on the excess energy of the absorbed photon with respect to the ionization threshold. In general, the absorption edge is divided in three main energy regions:

- Pre-edge region: This region is just few eV below the edge position and represents transitions to bound localized states. These transitions are mainly dipole allowed and, because in this region the hybridization of the electronic levels is strongly affected by local geometries, elements in the same valence state can presents large differences.<sup>84</sup>
- X-ray absorption near edge structure (XANES) region: This region extends for about 50 eV above the absorption edge and together with the pre-edge region provides information on the local electronic and geometric structure.
- Extended x-ray absorption fine structure (EXAFS) region: This region is the widest and extends from 100 to 1000 eV above the absorption edge. From the analysis of this region is possible to retrieve the local structure in the proximity of the absorbing atom (typically limited to about 10Å).

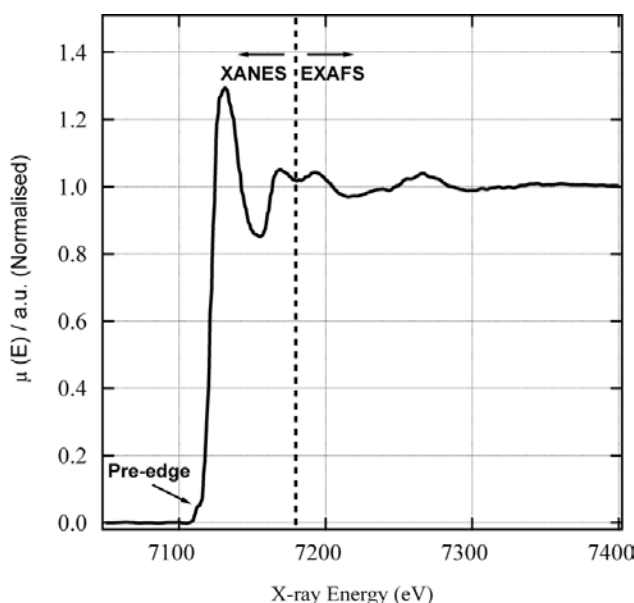


Figure 3.4 - Example of an x-ray absorption spectrum. Highlighted are the pre-edge, XANES and EXAFS regions. Taken from ref.<sup>80</sup>.

The EXFAS region is nowadays easier interpreted than the XANES region, using well established simulation codes which apply a single scattering approach.<sup>86</sup> The emitted photoelectron can be thought as a spherical wave (the wavelength of which depends on its kinetic energy) that propagates and scatters with the neighboring atoms. Eventually, this

interaction produces a backscattered wave which interferes with the forward-propagating wave and the result is an interference that modulates the probability of absorption. In the XANES region, since getting closer to the absorption edge increases the mean free path of photoelectron, it is necessary to consider a multiple scattering level which makes the interpretation more complex. Qualitatively and in first approximation the edge position can be correlated to the oxidation state of the absorbing atom. Indeed, the edge position depends on the ionization energy and a change in the formal charge of the atom modifies the required energy for ionizing the core electrons. It should be kept in mind though, that the absorption edge position is also affected by the bond lengths of the coordinative atoms and therefore often this is a too simplistic approximation.

### 3.2.2 Picosecond x-ray absorption spectroscopy

The filling pattern of electrons in a storage ring determines the time structure of the x-rays. Synchrotrons operate in pulsed mode, since usually their filling patterns consist of bunches of electrons separated by a few nanoseconds. Typically, the x-ray pulses are delivered at MHz repetition rate and ps-XA experiments in third generation synchrotron sources, such as SLS, make use of a hybrid filling pattern called “camshaft”. The camshaft mode (Figure 3.5) consists of an isolated electron bunch which lies in a gap of 180 ns in the filling pattern of SLS and is filled with 4 times more current than the average multibunch current (4 mA instead of 1 mA).<sup>87</sup>

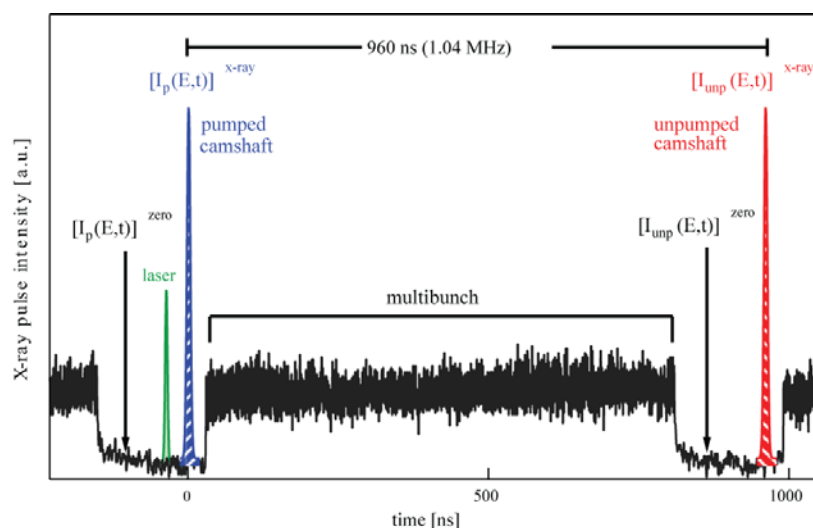


Figure 3.5 - Filling pattern of the Swiss Light Source at Paul Scherrer Institute. In total are present 480 electrons buckets (2 ns of time separation between each other) of which 390 are filled with the electrons and the remaining 90 ones for the gap in which there is the camshaft pulse. The camshaft has 4 times more intensity than the other electron bunches in the multibunch and the storage ring repetition rate is of 1.04 MHz. Taken from ref.<sup>87</sup>.



Thanks to this filling pattern, detectors with a time resolution of 10-20 ns can be gated in order to only measure the x-ray pulses generated from the camshaft electron bunch and this provides a time resolution of about 80 ps (FWHM duration of the electron bunch). To ensure synchronization between pump and probe sources, our electronics use the radio frequency (RF) master clock of SLS, which is synchronized to the 500 MHz signal of the RF cavities that are responsible for creating the potential wells inside the storage ring and therefore generating the time structure of the emitted radiation. The time jitter between laser pump and x-ray probe is less than a picosecond during measurements. Finally, the delay between x-ray and laser is adjusted via a computer controlled timing system which shifts the laser arrival time at the sample position (Figure 3.6).

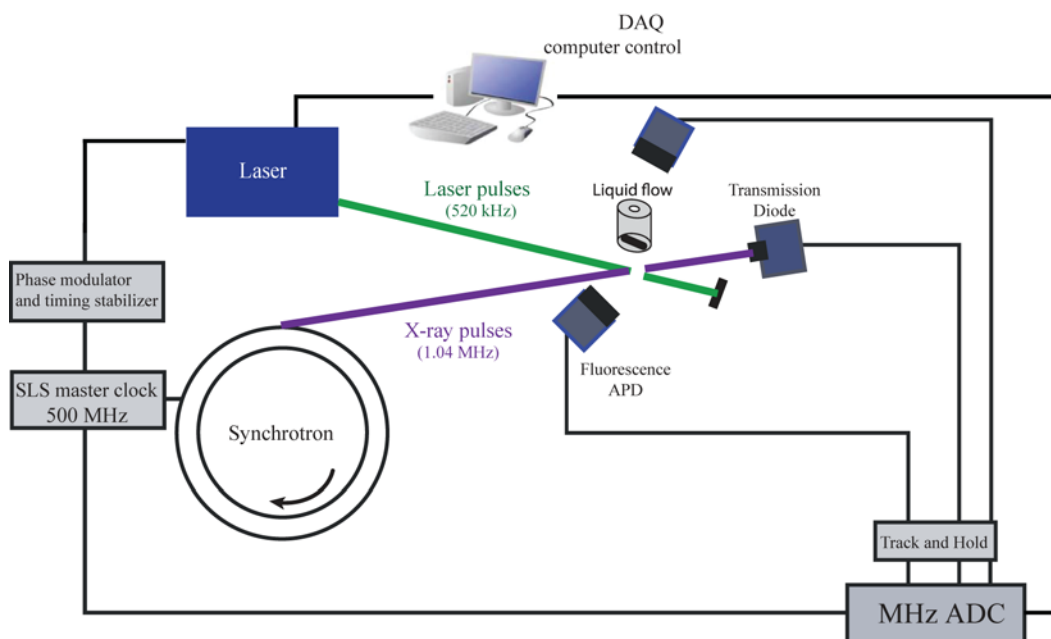


Figure 3.6 - Simplified representation of the high repetition rate setup for picosecond x-ray absorption spectroscopy. Readapted from ref.<sup>87</sup>.

In order to have the best signal to noise ratio (S/N) achievable, it is used a MHz repetition rate laser system which allows to pump at half of the repetition rate of the synchrotron, namely 520 kHz. This picosecond laser is a high-average power Nd:YVO<sub>4</sub> (Duetto, Time Bandwidth Products, Zürich) which can operate with a variable repetition rate (from 50 kHz to 8 MHz) and produces 10 ps pulses. When operated at 520 kHz, it provides 28  $\mu$ J per pulse at the fundamental energy, 1.17 eV. Frequency doubling and tripling provide 15  $\mu$ J per pulse at 2.33 eV and 6  $\mu$ J per pulse at 3.5 eV.<sup>87</sup>

In the works presented in chapter 6 and 9, the samples are recirculated in a free flowing jet of 200  $\mu$ m thickness, tilted 45° with respect to the incident x-ray beam (Figure 3.7). This is done to avoid laser damaging by refreshing the sample between one laser pulse and the next.

The measurements are performed at two different beamlines, MicroXAS and SuperXAS of the SLS at the Paul Scherrer Institute (Villigen). These two beamlines work with different insertion devices; MicroXAS is equipped with a minigap in-vacuum undulator capable of generating x-ray from 4 to 23 keV and SuperXAS uses a superbending magnet<sup>88</sup> (2.9 T) which provides radiation between 4.5 and 35 keV. Both beamlines use a Si (111) monochromator which has a nominal resolution of about 1.5 eV at 13 keV (Pb L<sub>3</sub> and Br K-edge) and about 0.7 eV at 5 keV (Ti K and Cs L<sub>2</sub>-edge). There is a minor difference in energy resolution between the two beamlines (lower energy resolution for SuperXAS) because of the different collimation of the x-ray beam. The ps-XAS measurements are performed using a transmission Si diode detector and two Si avalanche photodiodes in total fluorescence yield (TFY) mode. Transient XAS spectra (x-ray absorbance difference of the excited minus the unexcited sample) are recorded on pulse-to-pulse basis and the transient signals intensity is normalized to the edge-jump magnitude.

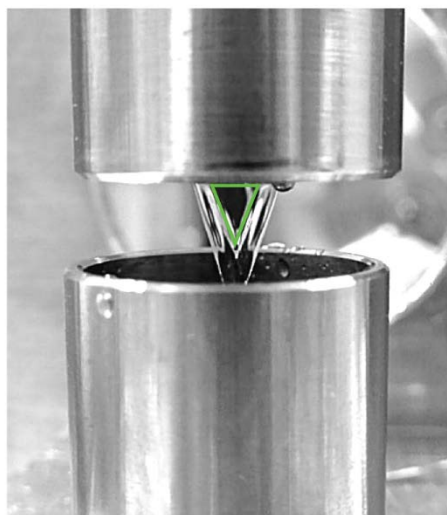


Figure 3.7 - Liquid sheet jet of 200  $\mu\text{m}$  thickness flowing water. The green area is the most stable because there is laminar flow and therefore it is here that laser and x-ray are overlapped. Taken from ref.<sup>89</sup>.

### 3.2.3 Femtosecond X-ray absorption spectroscopy: slicing method

In 1996, Zholents *et al.* proposed a technique to improve the temporal resolution of synchrotron experiments, called femto-slicing.<sup>90</sup> This technique consists of the interaction between an intense laser pulse and an electron bunch inside a modulator, which brings to the formation of a bunch of electrons having the time scale of the femtosecond laser pulse (*i.e.* about 100 fs). Even with the advent of free electron laser (FELs), this technique suffering from poor x-ray flux offers still some advantages. First of all, because the optical pump and x-ray probe pulses are derived from the same Ti:sapphire laser, they are inherently

synchronized<sup>91</sup> and this avoid any time jitter between pump and probe which is typical of time-resolved FEL experiments.<sup>92</sup> Second, most of the *modus operandi* used in time resolved synchrotron experiments can be still retained because there are no problems arising from a very intense x-ray source.<sup>93</sup> Finally the cost of implementing such a technique in a synchrotron is much lower than the cost of building a FEL and therefore it is of easier access to users. Slicing experiments at the SLS are possible only at the MicroXAS beamline. Most of the slicing experiments are of femtosecond x-ray diffraction because this technique deals with more intense transient signals than time resolved XAS.

Here, the femtosecond laser pulses are created in a Ti:sapphire oscillator which is phased-locked to the fifth submultiple of the synchrotron RF master clock. These pulses split into two parallel optical branches, the pump which is used to excite the sample and the probe which is used for modulating the energy of the electrons. The pump enters a regenerative amplifier (115 fs FWHM, 1 kHz, 2.1 mJ, 1.55 eV) and is transported to the experiment via a 22 m long vacuum pipe. The probe is instead amplified in two steps, first by a regenerative amplifier and then by a 2-pass amplifier (50 fs FWHM, 1 kHz, 5.2 mJ, 1.54 eV).<sup>91</sup> Eventually, the probe femtosecond pulses are focused in vacuum for about 45 m to interact with electrons in the modulator. Finally the electron bunch passes through a magnetic chicane where the part of the bunch with higher or lower energy is spatially separated from the main bunch (Figure 3.8).

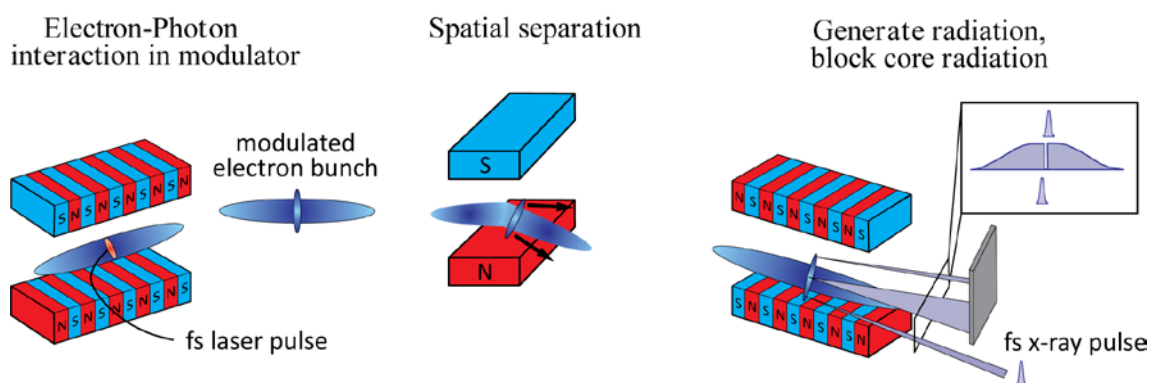


Figure 3.8 - Schematic representation of the slicing setup for femtosecond x-ray absorption spectroscopy. From the left, there is the modulator in which the femtosecond laser pulse and picosecond electron bunch interacts. Upon interaction there is a spatial separation of the femtosecond modulated microbunch by a magnetic field and finally on the right the undulator for generating x-ray radiation. Thanks to the spatial separation of the femtosecond x-ray electron bunch, it is possible to uniquely collect its emitted radiation. By courtesy of Andrin Caviezel.

The slicing source operates at 2 kHz. The difference in repetition rate between optical pump and x-ray probe pulses combined with a single shot data acquisition allows to measure the photo-induced differences on a pulse-to-pulse basis. The experimental details for the work using the slicing technique on TiO<sub>2</sub> and presented in chapter 5,<sup>15</sup> will be summarized in the following lines. It has been used a Ge(111) double crystal monochromator which provides higher flux than the usual Si(111) at the cost of energy resolution. The energy range in the

experiment is from 4.97 keV to 4.99 keV, at an energy resolution of  $<2$  eV. At the sample position, a single X-ray slice in this energy range contains  $\sim 12$  photons per pulse, resulting in a flux five orders of magnitude lower than in ps-XAS experiments at similar energies.<sup>17</sup> Pulses are split at variable pulse energies employing a half wave plate and a thin film polarizer. One part is used to pump an optical parametric amplifier (TOPAS) to provide pulses at 3.5 eV (after two frequency doubling stages). These pulses are focused onto the sample by a spherical UV-enhanced aluminum mirror and the remaining part of the 1.55 eV light is transferred via a delay line and focused by the same spherical mirror onto the same spot as the 3.5 eV pulses. Difference frequency generation in a nonlinear  $\beta$ -Barium Borate (BBO) crystal is used to find the temporal overlap between the UV and the 1.55 eV pulses. The 1.55 eV pulses are required instead, to find the temporal overlap with the X-ray probe pulse. This is achieved in consecutive steps: 1) A fast photodiode measures the rough timing between the X-ray core beam and the 1.55 eV laser pulse with a precision of few ps; 2) The temporal overlap between the x-ray and 1.55 eV pulses is found by recording the coherent optical phonons in a superlattice of  $(\text{Ba}_{0.7}\text{Sr}_{0.3})\text{TiO}_3$  and  $(\text{La}_{0.7}\text{Sr}_{0.3})\text{MnO}_3$ ,<sup>94</sup> 3) The difference frequency generation in a BBO crystal ensures temporal overlap between the 1.55 eV and 3.5 eV pulses. The x-ray pulse duration is about 140 fs, *i.e.* the temporal resolution of the experiment is on the order of 200 fs. X-ray absorption is measured in transmission mode with an avalanche photodiode. The x-rays are focused onto a 100  $\mu\text{m}$  thick, flat liquid jet of sample solution in order to decrease sample damaging by laser irradiation by refreshing the sample from one laser shot and the other.

### 3.3 Time correlated single photon counting

Time-resolved luminescence spectroscopy of semiconductors is used to investigate carrier relaxation processes. One of the most common techniques is time-correlated single photon counting (TCSPC), which probes dynamics from the picosecond to the microsecond time scale. In this regard, TCSPC operates in the same time window of ps-XAS and is therefore a complementary tool to gain information on the sample dynamics.

The principle of TCSPC<sup>91</sup> is the detection of single photons and the measurement of their arrival times with respect to a reference signal. The excitation is performed using ultrashort laser pulses and therefore the limiting factor for the time resolution is usually the electronic gating. The distribution of the time intervals between the excitation and the first detected fluorescence photon is recorded with a combination of a time-to-amplitude converter (TAC, which is the fast clock), an analog-to-digital converter and a multichannel analyzer.<sup>95</sup>

#### 3.3.1 Technical details

The time-correlated single photon counting setup used to determine the fluorescence decay in chapter 9 employs the same high repetition rate laser of synchrotron experiments (Time-Bandwidth Duetto, here running at 82 kHz) and the liquid jet of 200  $\mu\text{m}$ . The fluorescence

emitted from the samples is collected at 90 degrees through a long-pass filter (FEL450) from Thorlabs and neutral density filters with different OD to ensure a single photon counting regime. The setup is equipped with a SPC-130-EM counting module (Becker & Hickl GmbH) and an IDQ-ID-100-20-ULN avalanche photodiode (Quantique) for recording the decay traces. The sample is excited by 3.5 eV pulses (frequency-tripled to 3.5 eV from the fundamental wavelength of Duetto) synchronized to the TCSPC counting module through an electronic delay generator (DG535 from Stanford Research Systems). The instrument response function of the TCSPC setup is limited by the electronics to 300 ps (Figure 3.9). The fluorescence spectra at different fluences, presented in chapter 9, have been instead measured using a LR1 fiber CCD spectrometer (ASEQ Instruments) with an integration time of 1 second.

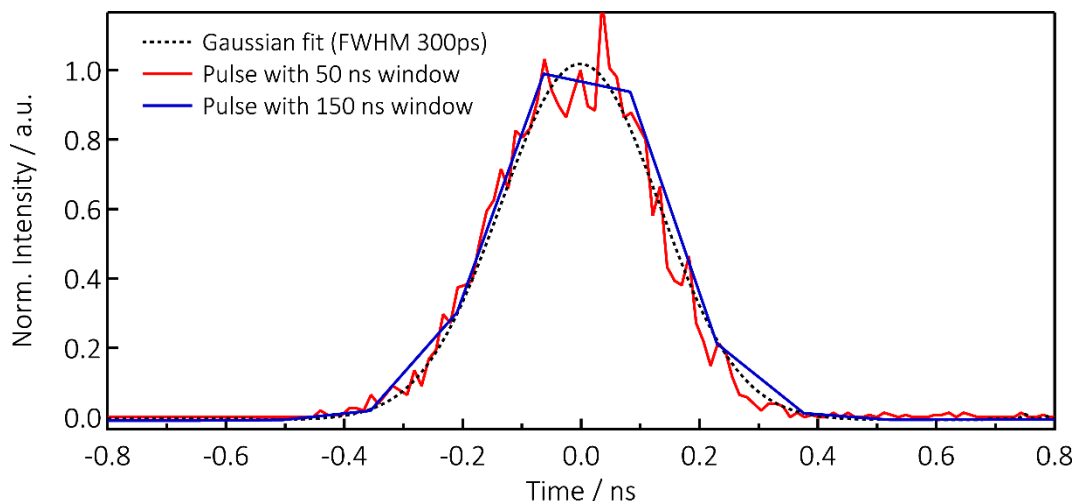


Figure 3.9 - Pulse duration of the 3.5 eV laser light recorded using time correlated single photon counting setup with different time windows (50 ns for the red curve and 150 ns for the blue curve) and a Gaussian fit with 300 ps of full width at half maximum (black dotted curve).

## 3.4 Samples preparation and characterization

### 3.4.1 TiO<sub>2</sub> nanoparticles

The anatase TiO<sub>2</sub> sample is a colloidal suspension of 20 nm large TiO<sub>2</sub> nanoparticles in acetic water. The suspension is prepared via a sol-gel synthesis, which is carried out in an inert atmosphere using a glove box. The precursor used for the NPs preparation is Titanium isopropoxide (Sigma Aldrich, 99.999% purity). The solution obtained by mixing the precursor in 250 ml H<sub>2</sub>O (18 MΩ) and 80 ml of acetic acid was peptized at 80 °C for about 2 h until it turned into a transparent gel. The sample was then heated at 230 °C in an autoclave for 12 hours. The final solution is characterized via UV-Vis spectroscopy to adjust the concentration and XRD (Bruker D8 Advance diffractometer) in order to establish the crystal structure (Figure 3.10). From the reproducibility of the synthesis an average diameter for

anatase  $\text{TiO}_2$  of about 20 nm is expected, as in a previous work.<sup>17</sup> More details about the sample preparation and characterization using UV-Vis spectroscopy, dynamics light scattering and TEM can be found in ref.<sup>17</sup>. The sample preparation for the nanoparticles of amorphous  $\text{TiO}_2$  consists of the same synthetic steps of the anatase sample but without the heating in the autoclave<sup>17</sup>.

Finally, the rutile  $\text{TiO}_2$  is a commercial sample provided by Sigma-Aldrich (product number 637262) which has an average particle size <100 nm and it has been used as delivered. X-ray diffraction data and transmission electron microscope images can be found in ref.<sup>96</sup>. This sample is suspended in acetic water (250 ml  $\text{H}_2\text{O}$  18 M $\Omega$  and 80 ml of acetic acid) after about 30 minutes of sonication.

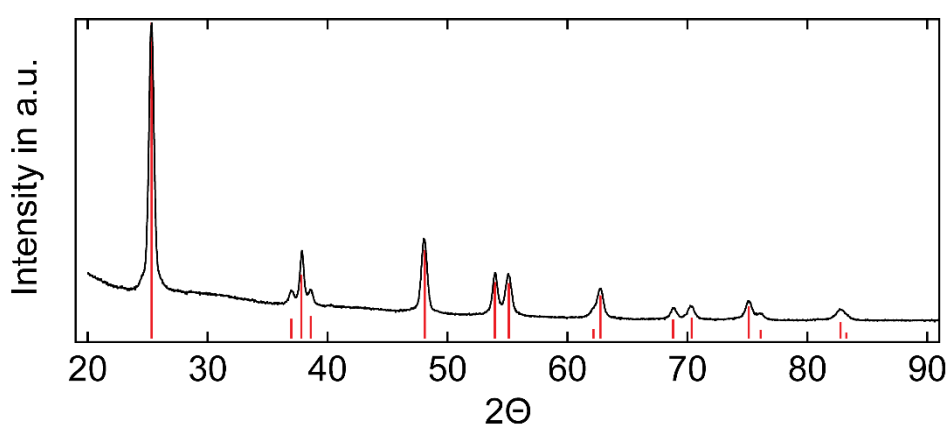


Figure 3.10 - XRD pattern of the dried sample (black trace). The red sticks represent the diffraction reference data of anatase  $\text{TiO}_2$  at 25 °C. Taken from ref.<sup>15</sup>.

### 3.4.2 $\text{CsPbX}_3$ nanocrystals

The synthetic procedure for the preparation of suspended perovskite nanocrystals is based on the recipe presented in the work of Protesescu *et al.*<sup>22</sup> with minor changes as discussed below.

**Synthesis of  $\text{CsPbBr}_3$  NCs:** 11.28 mmol  $\text{PbBr}_2$  (ABCR, 98%), 200 mL octadecene (Aldrich, 90%) were loaded into a 500 mL 3-neck flask and degassed for 45 minutes under vacuum at 120 °C. 30 mL of dried oleic acid (Sigma-Aldrich, 90%) and 30 mL of dried oleylamine (Acros Organics, 80-90%) were injected at 120 °C under  $\text{N}_2$  flow. The temperature was raised to 200 °C and 32 mL of stock solution of Cs-oleate (prepared as described in ref.<sup>22</sup>) was swiftly injected and 40 seconds later the reaction mixture was cooled down by the water bath.

**Synthesis of  $\text{CsPb}(\text{ClBr})_3$  NCs:** 0.392 mmol  $\text{PbCl}_2$  (ABCR, 99.999%), 0.730 mmol  $\text{PbBr}_2$  (ABCR, 98%), 20 mL octadecene (Aldrich, 90%) and 4 mL n-Trioctylphosphine (Strem, 97%) were loaded into a 100 mL 3-neck flask and degassed for 45 minutes under vacuum at 120 °C. 3 mL of dried oleic acid (Sigma-Aldrich, 90%) and 3 mL of dried oleylamine (Acros



Organics, 80-90%) were injected at 120 °C under N<sub>2</sub> flow. The temperature was raised to 200 °C and 3.2 mL of stock solution of Cs-oleate was swiftly injected and 40 seconds later the reaction mixture was cooled down by the water bath.

**Isolation and purification:** The product is isolated by centrifugation and the supernatant was discarded. Hexane (1.2 mL, Sigma-Aldrich,  $\geq 95\%$ ) is added to disperse the NCs and centrifuged again. After centrifugation, the supernatant is discarded and 0.5 mL of hexane are added to precipitate and centrifuge again. The resulting precipitate is redispersed in 7 mL toluene (Fischer Scientific, HPLC grade). Finally, the samples are diluted using a solution of toluene with 0.2 % of 1:1 mixture of oleylamine and oleic acid until an optical density (OD) of 1.2 at 3.5 eV for X-ray and fluorescence measurements and 0.3 at 3.1 eV for femtosecond visible transient absorption is reached.

**Transmission electron microscopy (TEM)** images are recorded using a Philips CM 12 microscope operated at 120kV. Figure 3.11 shows the images for the two samples, which are both monodispersed with an average size of 12 nm.

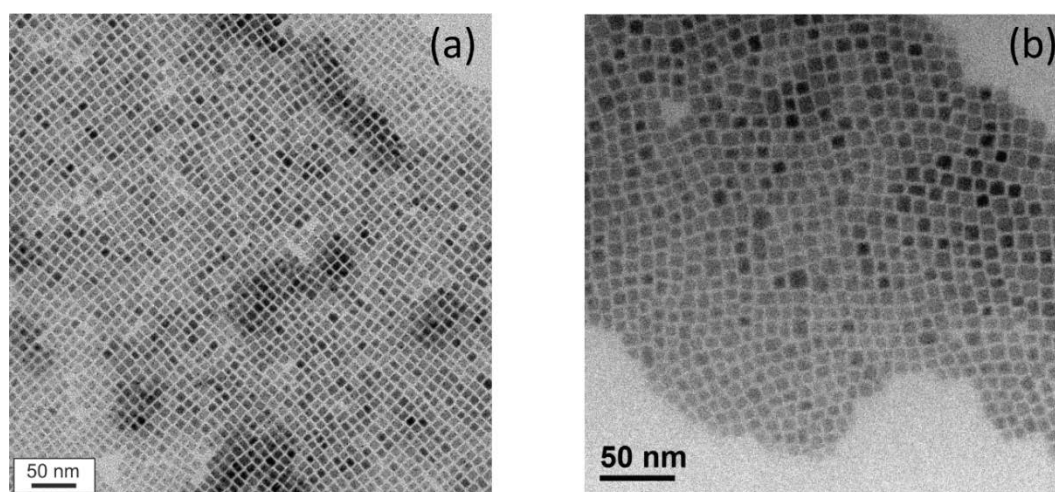


Figure 3.11 - Transmission electron micrograph of monodisperse CsPbBr<sub>3</sub> (a) and CsPb(ClBr)<sub>3</sub> (b) nanocrystals with an average size of 12 nm.

**Powder X-ray diffraction patterns (XRD)** are collected with a STOE STADI P powder diffractometer, operating in transmission mode. A Germanium monochromator, Cu K $\alpha$ 1 irradiation and a silicon strip detector (Dectris Mythen) were used. Figure 3.12 and Figure 3.13 show the diffraction patterns for the two samples, compared with reference patterns of CsPbBr<sub>3</sub> and CsPbCl<sub>3</sub><sup>97</sup>. The diffraction peaks of CsPb(ClBr)<sub>3</sub> are between the one of these two references which indicates the hybrid nature of this sample. Indeed, as indicated by the amount of precursors in the synthesis, it should result in a final stoichiometry of 2 Br<sup>-</sup> per each Cl<sup>-</sup>.

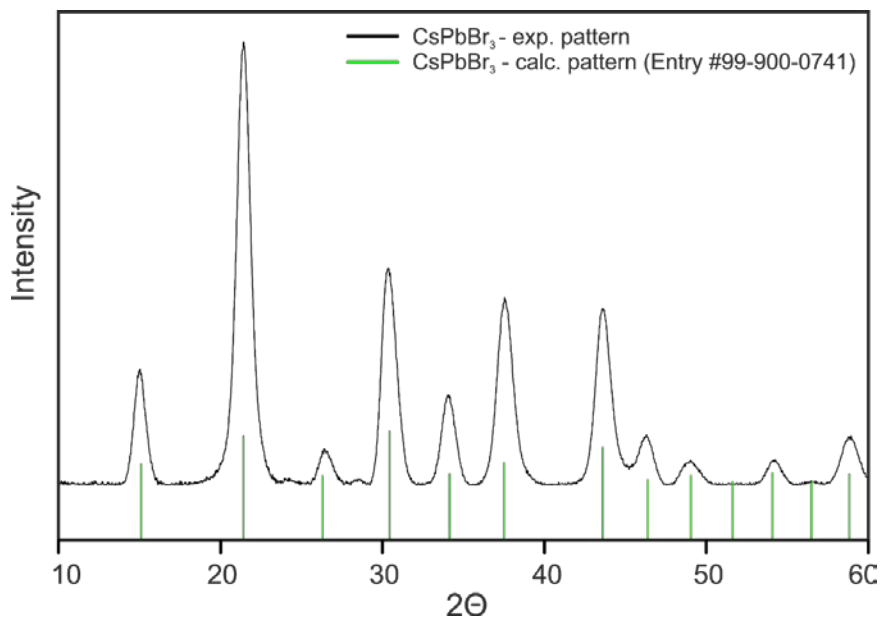


Figure 3.12 - Powder X-ray diffraction pattern of cubic CsPbBr<sub>3</sub> NCs matching the cubic phase of the reference for CsPbBr<sub>3</sub> (space group Pm-3m)<sup>97</sup>.

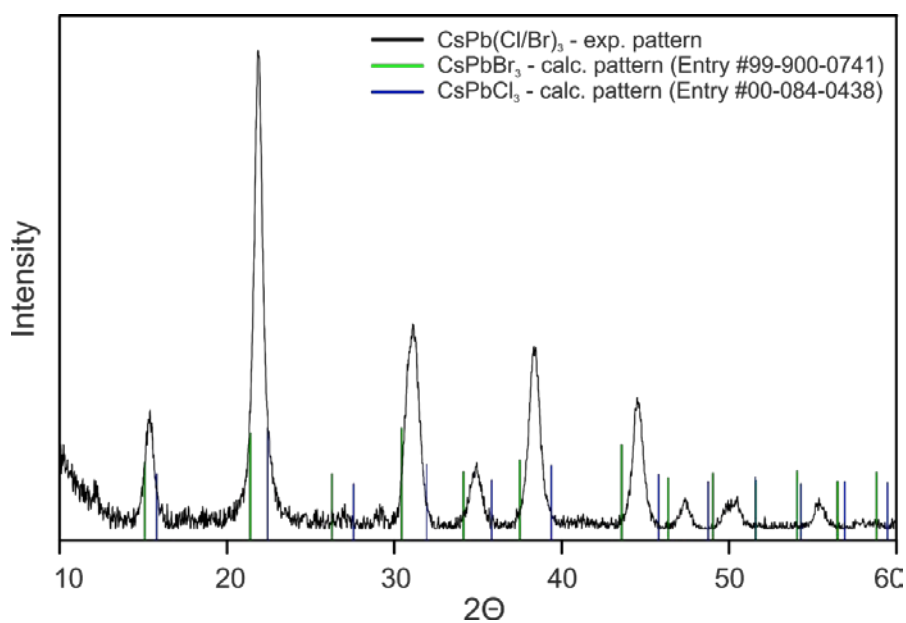


Figure 3.13 - Powder X-ray diffraction pattern of CsPb(Cl/Br)<sub>3</sub> NCs displaying the diffraction peaks between the references for CsPbBr<sub>3</sub> (green lines)<sup>97</sup> and CsPbCl<sub>3</sub> (blue lines)<sup>97</sup>.



## 4 Titanium Dioxide

### 4.1 Applications of $\text{TiO}_2$

Transition metal oxides (TMOs) have emerged as key players in energy research due to their applications in solar energy conversion<sup>5,98</sup> and in photocatalysis<sup>99,100</sup>. Among these, Titanium dioxide ( $\text{TiO}_2$ ) retains a special place being cheap, non-toxic and a stable material.

When a photon with enough energy to overcome the bandgap of  $\text{TiO}_2$  is absorbed, an electron is transferred to the conduction band and a hole is left in the valence band. These charges migrate to the surface where they can react with species adsorbed onto it (Figure 4.1). For this reason, in photocatalytic applications, nanomaterials with their high surface to volume ratio have been very popular. In general,  $\text{TiO}_2$  is known to be an extremely effective photocatalyst in the degradation of organic pollutants.<sup>101</sup> Moreover, in 1972, Fujishima and Honda reported<sup>102</sup> that  $\text{TiO}_2$  electrodes could photocatalytically split water into  $\text{H}_2$  and  $\text{O}_2$  under application of a bias potential and UV light irradiation. This work, in which photocatalysis was first used for a thermodynamically uphill reaction, set a milestone in the field. Indeed, from this point in history, a prominent part of the scientific community worked on modification of  $\text{TiO}_2$  nanostructures (*i.e.* bandgap engineering via doping, use of co-catalyst etc.) for improving the efficiencies in the photocatalytic generation of fuel.<sup>14</sup> This mainly consists in the water splitting reaction for production of hydrogen and the more challenging reduction of  $\text{CO}_2$  for production of solar fuels such as methanol, methane, etc..

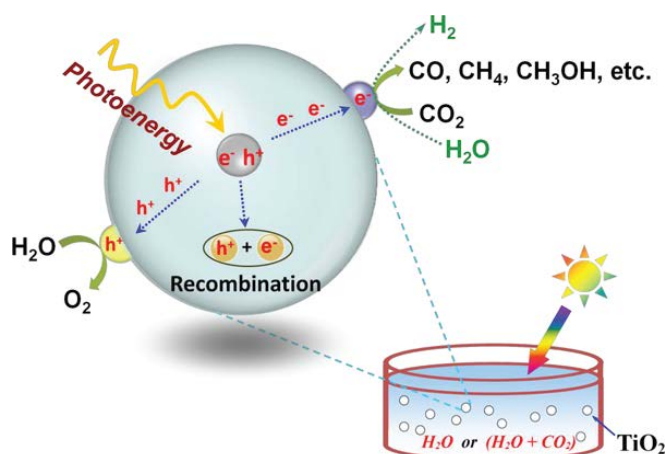


Figure 4.1 - Schematic view of photocatalytic processes in a nanoparticle of  $\text{TiO}_2$  for solar fuel generation. Taken from ref.<sup>14</sup>.

The other main application of  $\text{TiO}_2$  is photovoltaics, particularly after the discovery of dye sensitized solar cells (DSSCs).<sup>1</sup> These are photoelectrochemical cells in which the metal oxide is sensitized to absorb low energy photons of the solar spectrum (Figure 4.2). In 1991, a power conversion efficiency of  $\sim 7\%$  was reached using a large surface area mesoporous  $\text{TiO}_2$  substrate which remained among the most promising configuration in the following years.<sup>103</sup> Recent DSSCs use  $\text{TiO}_2$  films with grain sizes in the order of 10's of nm,<sup>104</sup> which is the same size of the samples investigated in chapter 5 and 6. More recent photovoltaic cells which use innovative materials such as lead halide perovskites, adopt a DSSC architecture using mesoporous films of  $\text{TiO}_2$  as well.<sup>105</sup>

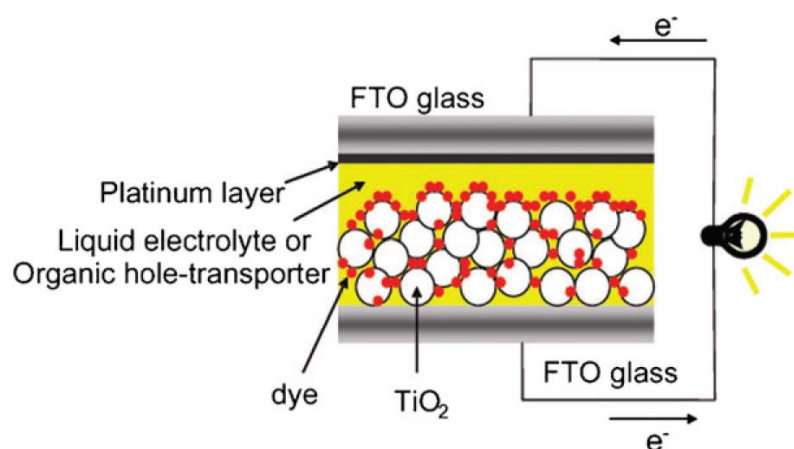


Figure 4.2 - Schematic diagram of a dye sensitized solar cell. On the bottom part there is the photoactive area and in the upper part a Pt counter electrode. Taken from ref.<sup>106</sup>.

Finally,  $\text{TiO}_2$  surfaces under UV irradiation show self-cleaning and anti-fogging characteristics. These applications are due to the photogenerated super-amphiphilic properties (both super-hydrophilic and super-oleophilic, where the contact angle of water and oil on a surface is almost  $0^\circ$ ).<sup>107</sup>  $\text{TiO}_2$  surfaces indeed, can change their wettability under UV irradiation<sup>100,108</sup> but this mechanism remains elusive, and the conclusions reached by different authors contradict each other.<sup>109,110</sup>

All the applications seen above rely on the charge carrier dynamics and for this reason the works presented in chapter 5 and 6 aim at investigating these aspects.

## 4.2 Geometric structure

Titanium dioxide can exist in different crystalline phases (anatase, rutile and brookite) or amorphous. The two main polymorphs used in applications are anatase and rutile which are characterized by a tetragonal structure. Rutile is a thermodynamically stable phase at room temperature, instead anatase is a metastable phase.<sup>103</sup> Both crystal structures consist of distorted  $\text{TiO}_6$  octahedra, sharing four edges in anatase and two in rutile. Moreover, the

distortion of the  $\text{TiO}_6$  octahedron is slightly larger for the anatase phase (Figure 4.3). This structural difference leads to a smaller bandgap energy for the rutile phase, namely  $\sim 3.0$  eV instead of  $\sim 3.2$  eV for anatase.<sup>111</sup>

The  $\text{TiO}_2$  amorphous structure is composed of distorted  $\text{TiO}_6$  octahedra together with a significant number of penta- and tetra-coordinated sites.<sup>112,113</sup> Although, amorphous  $\text{TiO}_2$  is rarely used for the mentioned above applications, due to the limited mobility of charge carriers, it has been recently exploited for solar cell devices.<sup>114</sup>

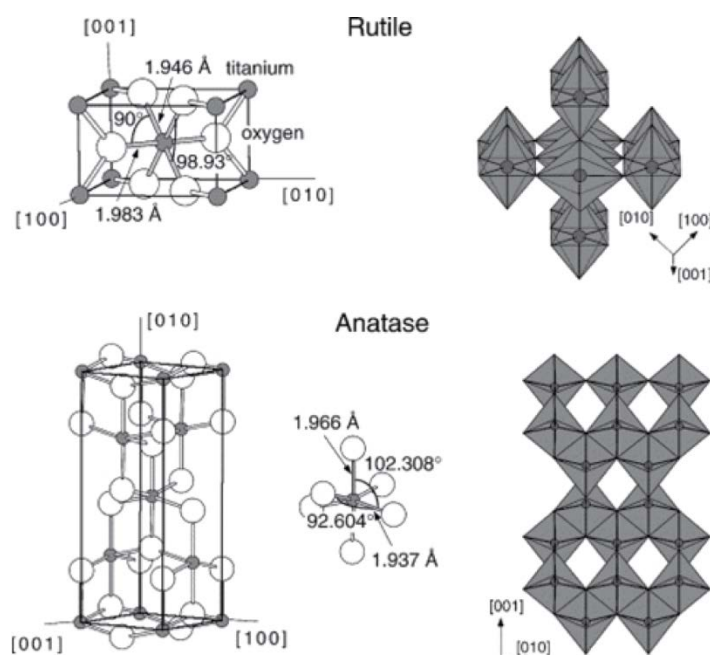


Figure 4.3 - Rutile and anatase  $\text{TiO}_2$  crystal structures. In both cases, slightly distorted octahedra are the basic building units. Taken from ref.<sup>115</sup>.

For investigating the specific morphology and properties of anatase and rutile NPs, Luca<sup>40</sup> performed a systematic study of the size effects on the x-ray absorption near edge spectra (XANES) of the Ti K-edge. The pre-edge region of the Ti K-edge is able to deliver information on the coordination of the Ti sites.<sup>116</sup> The results indicate that anatase NPs consists of a core-shell structure in which the core is bulk like and the shell interphase is less ordered with a high degree of Ti under-saturated sites.<sup>40</sup> For the rutile NPs instead, this amorphous shell region is so thin that it cannot be detected by x-ray absorption spectroscopy, indeed the spectra are independent on the size of the NPs.

### 4.3 Electronic structure

In  $\text{TiO}_2$  anatase and rutile, the metal ion  $\text{Ti}^{4+}$  is characterized by the electronic configuration  $(\text{Ar})4s^03d^0$ . The electronic and therefore optical properties of  $\text{TiO}_2$  anatase have been

theoretically investigated,<sup>117</sup> yielding the molecular orbital diagram of Figure 4.4. From this diagram, it is clear that the empty orbitals of the conduction band (CB) are mainly given by the contribution of the Ti 3d and 4s orbitals, instead the valence band (VB) is mainly of Oxygen 2p character, particularly in the energy region near the gap. Similar conclusions are drawn, using hybrid density functional calculations, for the density of states in TiO<sub>2</sub> rutile.<sup>118</sup>

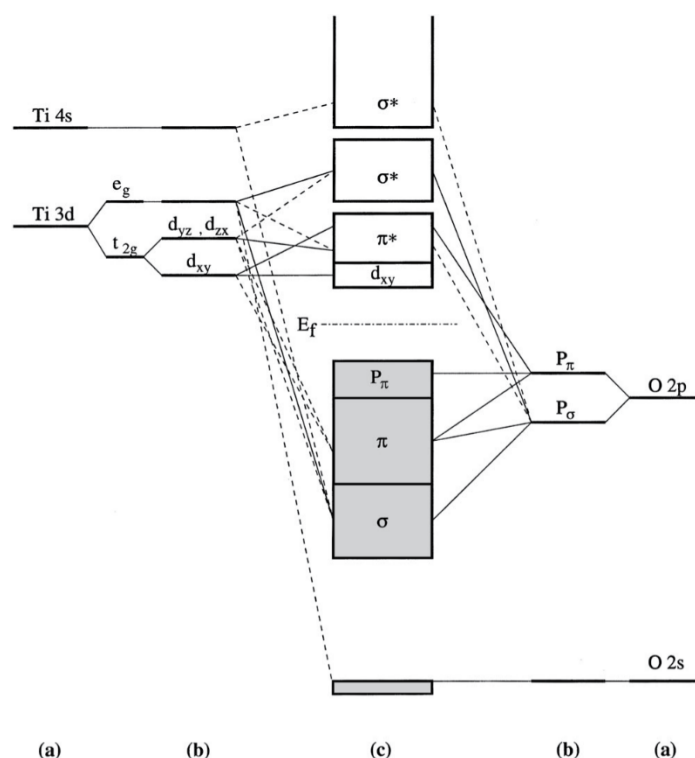


Figure 4.4 - Molecular-orbital bond structure for anatase containing atomic levels (a), crystal field split levels (b), and final interaction states (c). The solid lines represent large contributions and the dashed lines smaller ones. Taken from ref.<sup>117</sup>.

Therefore, to study the fate of the photoexcited charge carriers in the CB and VB of TiO<sub>2</sub>, the use of an element selective technique allows to map separately electrons and holes, simply by probing at Ti or O orbitals. As introduced in chapter 3.2, x-ray absorption spectroscopy (XAS) is element selective but also structural sensitive, thus time resolved XAS at the Ti K-edge is an ideal tool to study dynamics in the CB, particularly looking at the pre-edge region where the transition is from core to the valence states (see chapter 3.2 for details). This region is also useful for evaluating the Ti coordination in oxides thanks to the systematic study performed by Farges *et al.*<sup>116</sup> on a large set of well-characterized model oxide compounds, representative of the coordination chemistry of Ti<sup>4+</sup>. In particular, studying the position and relative intensity of the pre-edge features should help distinguish between sites coordinated by 4, 5 and or 6 oxygens. Although this approach is commonly used, it is based on a simplify view of the problem because also other effects such as oxidation state and structural changes have a strong impact on the pre-edge modulation of TiO<sub>2</sub>.<sup>119</sup> In general though, coordination

is the most influencing factor and therefore defects in the material have a strong impact on it.

Point defects in the lattice of TiO<sub>2</sub> anatase and rutile can heavily modulate the electronic and optical properties and are therefore a relevant issue. They can be of two types, extrinsic or native, as explained in chapter 2.1.2. Extrinsic defects refer to any interstitial or substitutional atoms which is an impurity in the stoichiometric formula of the pristine material. This type of defect is very common, often introduced on purpose in the structure for doping the material and tuning its electronic and optical properties. The dopants can be metals, which give rise to a cationic doping<sup>120,121</sup> or anionic species, of which particularly successful is the case of nitrogen<sup>122</sup> used to shift the absorption spectrum into the visible.

The native defects are of two types: interstitials or vacancies. It should be considered that also in pure TiO<sub>2</sub> crystals, self-interstitial defects and vacancies can be present for thermodynamic reasons because their presence is associated with an increase of entropy in the system. In this case they are called intrinsic defects. Interstitial Ti defects (Ti<sub>i</sub><sup>3+</sup>) are common in TiO<sub>2</sub> and they have been recognized as important actors of surface reactivity. This is due to the electrons provided by these defects which can be transferred to the surface and facilitate O<sub>2</sub> adsorption and dissociation.<sup>123</sup> On the other side, oxygen interstitials have only been theoretically suggested but there is yet a lack of experimental evidence for their existence.<sup>123</sup> Vacancies of Ti have recently been induced through refined material engineering in a TiO<sub>2</sub> sample for obtaining *p*-type conductivity, which increased the performances in photocatalytic generation of H<sub>2</sub> and organics degradation.<sup>124</sup>

In general though, TiO<sub>2</sub> inherently exhibits *n*-type conductivity due to the intrinsic presence of oxygen vacancies, which are therefore the most common defects of all. Each oxygen vacancy leaves two excess electrons and produces three pentacoordinated Ti sites, the oxidation state of which is still a matter of debate.<sup>125</sup> Indeed, from density functional theory (DFT) calculations the possibility that two electrons could be localized on two of the three pentacoordinated sites, one could be localized and the other instead delocalized over several Ti atoms or simply both could be delocalized, have similar energies.<sup>125</sup> Finally, for samples at the nanoscale, as already discussed in chapter 2.1, the surface is the main source of unavoidable defects, because of lattice truncation, which leads to undercoordinated Ti sites and a high concentration of oxygen vacancies.<sup>113</sup> On these defects water dissociates and produces surface bound OH species which play a fundamental role in the field of photocatalysis and self-cleaning applications. In fact, the generation of hydroxyl radicals (·OH) upon bandgap photoexcitation is considered to have a major role in photocatalytic oxidation of organic compounds.<sup>126</sup>

## 4.4 Previous studies of charge carrier dynamics

As discussed in chapter 2.1, upon bandgap photoexcitation defects play a role of trapping centres for the electrons and holes. Over the last 20 years, several studies have been

performed in order to investigate charge carrier dynamics in TiO<sub>2</sub> nanoparticles,<sup>127-131</sup> films<sup>132,133</sup> and single crystals.<sup>31,134,135</sup> In particular, studies in the optical domain (IR, UV-visible, etc.), such as time-resolved transient absorption spectroscopy (TR-TAS)<sup>31,127-130,132,133</sup> and photoluminescence (PL)<sup>131,135</sup> have been the most commonly used for revealing the different aspects of electron and hole diffusion and trapping in TiO<sub>2</sub>. The main limitation of optical spectroscopy is that the interpretation of results such as charge carriers trapping lacks of direct finger print in the transient signal and is therefore indirect. Indeed, the interpretation usually relies on steady state spectra of TiO<sub>2</sub> in the presence of electron and hole scavengers. For example, Yoshihara *et al.*<sup>133</sup> concluded that electron and hole are trapped at the surface of nanocrystalline TiO<sub>2</sub> films, based on a steady state spectrum of the sample in methanol, under UV irradiation for 30 minutes. This approach, under the assumption that all the holes reacted with the methanol and just electrons remain in the material, allowed to extract the absorption spectrum of electrons. Then subtracting the absorption spectrum obtained from the transient spectra should leave just the contribute of the holes. This procedure for interpreting the transient absorption is based on assumptions due to the absence of a direct observable of the traps. Similarly, the presence of a self-trapped exciton (STE) in the PL experiments has been deduced indirectly from the fact that the emission energy of the different forms (*i.e.* single crystals, films and nanosized structures) of anatase TiO<sub>2</sub> is well below the absorption edge ( $\sim 1$  eV redshifted)<sup>136</sup> and anatase has a strong electron-phonon coupling.<sup>137</sup>

In the following pages is reported a table which summarized the main results of charge carriers trapping and STE formation timescales found using optical methods.

Sample	Process	Technique	T (K)	E <sub>pump</sub> (eV)	Fluences	Timescales	Reference
TiO <sub>2</sub> (12 nm) NPs	e <sup>-</sup> and h <sup>+</sup> trapping	ps-TAS	RT	3.5	-	e <sup>-</sup> < 30 ps h <sup>+</sup> ~ 250 nm	Rothenberger <i>et al.</i> <sup>138</sup>
TiO <sub>2</sub> (2 nm) NPs	e <sup>-</sup> trapping	fs-TAS	RT	4.0	-	< 500 ps	Colombo <i>et al.</i> <sup>128</sup>
TiO <sub>2</sub> anatase (2, 13, 27 nm) NPs	e <sup>-</sup> and h <sup>+</sup> trapping	ps-TAS	RT	3.5	from 1 to 1800 photons per particle	e <sup>-</sup> / h <sup>+</sup> < 10 ps	Serpone <i>et al.</i> <sup>130</sup>
TiO <sub>2</sub> (2 nm) NPs	e <sup>-</sup> trapping	fs-TAS	RT	4.0	-	~ 180 fs	Skinner <i>et al.</i> <sup>127</sup>
TiO <sub>2</sub> anatase (4.5 nm) NPs doped with Al <sup>3+</sup>	e <sup>-</sup> and h <sup>+</sup> trapping	ns-TAS (2 pulses excitation)	RT	I 3.5 II 2.33/1.16	-	< 3 ns	Skhrob <i>et al.</i> <sup>139</sup>
TiO <sub>2</sub> anatase (10-30 nm) and rutile (hundreds of nm) NPs	e <sup>-</sup> and h <sup>+</sup> trapping	TR-PL	from 77 to 293	from 3.18 to 4.13	-	lifetimes from 1.25 to 2800 μs	Wang <i>et al.</i> <sup>140</sup>

Sample	Process	Technique	T (K)	E <sub>pump</sub> (eV)	Fluences	Timescales	Reference
TiO <sub>2</sub> NPs anatase and rutile	STE formation and recombination	TR-PL	RT	from 3.5 to 4.66	-	formation < 30 ps lifetimes from 30 ps to 1.6 ns	Fujiyihara <i>et al.</i> <sup>141</sup>
TiO <sub>2</sub> anatase (20-130 nm) NPs	STE recombination	ps-PL	12	3.68 and 4.13	from 0.3 to 100 W/cm <sup>2</sup>	lifetimes ~100 ps and 3 ns	Cavigli <i>et al.</i> <sup>142</sup>
TiO <sub>2</sub> anatase (20-130 nm) NPs	STE recombination	ps-PL	12	4.13	from 0.3 to 100 W/cm <sup>2</sup>	lifetimes 500 ps and 100 ns	Cavigli <i>et al.</i> <sup>136</sup>
TiO <sub>2</sub> anatase (21, 400 nm) and rutile (40, 640 nm) NPs	e <sup>-</sup> trapping	fs-diffuse reflectance spectroscopy	RT	3.18	~ 1 mJ/cm <sup>2</sup>	< 400 fs	Furube <i>et al.</i> <sup>143</sup>
TiO <sub>2</sub> anatase (2-5 µm) film	e <sup>-</sup> and h <sup>+</sup> trapping	TAS	295	3.5	from 16 to 520 µJ/cm <sup>2</sup>	< 50ns lifetimes 1 µs	Yoshihara <i>et al.</i> <sup>133</sup>
TiO <sub>2</sub> anatase (1.5 µm) film	e <sup>-</sup> and h <sup>+</sup> trapping	fs-TAS	295	3.5/4.66	from 32 to 130 µJ/cm <sup>2</sup>	< 100 fs (3.5 eV) ~ 150 fs (4.66 eV)	Furube <i>et al.</i> <sup>132</sup>



Sample	Process	Technique	T (K)	E <sub>pump</sub> (eV)	Fluences	Timescales	Reference
TiO <sub>2</sub> anatase (1.5 μm) film	e <sup>-</sup> and h <sup>+</sup> trapping	fs-TAS	295	3.5	from 32 to 130 μJ/cm <sup>2</sup>	~ 100 fs lifetime 500 ps	Tamaki <i>et al.</i> <sup>129</sup>
TiO <sub>2</sub> anatase (240 nm) film	STE formation and recombination	TR-TAS	77	4.66	-	< 20 ps lifetimes 19.8 ps and 671 ps	Miyashita <i>et al.</i> <sup>144</sup>
TiO <sub>2</sub> rutile and anatase single crystals (100)	e <sup>-</sup> and h <sup>+</sup> recombination	TR-PL fs-TAS	77	3.5	from 0.02 to 1 mJ/cm <sup>2</sup>	rutile lifetime few tens of ns anatase > 1 μs e <sup>-</sup> and few ns h <sup>+</sup>	Yamada <i>et al.</i> <sup>135</sup>
TiO <sub>2</sub> anatase (001) thin film	e <sup>-</sup> and h <sup>+</sup> recombination	fs-TAS	294	4.0/5.0	from 0.004 to 0.048 photons per Ti	~ 100 ps	Matsuzaki <i>et al.</i> <sup>31</sup>

## 4.5 Polaronic localization in TiO<sub>2</sub>

The electron-phonon coupling of TiO<sub>2</sub> supports the polaron model for describing the excited conduction electrons in this material.<sup>49</sup> In the case of TiO<sub>2</sub>, electrons localize at Ti<sup>4+</sup> sites forming polarons and this has been extensively studied by theoretical works.<sup>125,145,146</sup> In particular, Denskins *et al.*<sup>145</sup> analyzed, using periodic density functional theory (DFT)+*U*, the intrinsic charge transport in a perfect crystalline lattice structure of anatase and rutile finding that both polymorphs present polaronic transport, but in the case of rutile, this is faster than in anatase. This result, which seems to contradict experimental measurements, has been assigned to effects which were not considered, such as those introduced by structural defects in the material.

Experimentally, studies on the polaronic fate of the conduction band electrons in TiO<sub>2</sub> have mainly been performed using *n*-type doped materials, which can be easily obtained by introducing oxygen vacancies through UV-irradiation<sup>147</sup> or exposure to H-atoms.<sup>148</sup> Sezen *et al.*<sup>148</sup> investigated the nature of the excess electrons in rutile single crystal (110) and rutile powder at room temperature by infrared spectroscopy. Thanks to this probe, they detected the large polaron formed about 380 meV below the conduction band, observing the signal of electrons excited from the ground state to the first excited state within the polaron trap potential well (Figure 4.5).

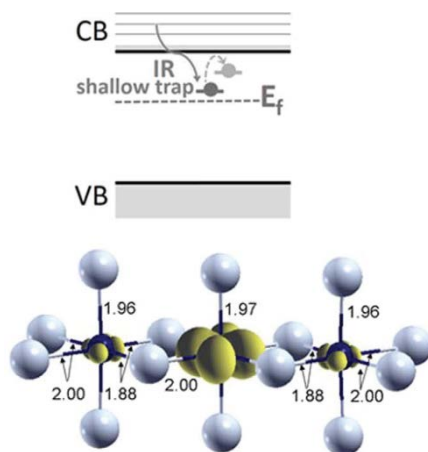


Figure 4.5 - On the top, schematic electronic structure showing the excitation of electrons within trap polaronic states by absorption of IR ( $\sim 1000\text{ cm}^{-1}$ ). On the bottom, the electron spin density of a self-trapped polarons on a Ti<sup>3+</sup> center of rutile as calculated from DFT. Taken from ref.<sup>148</sup>.

An angle resolved photoemission study<sup>147</sup> performed on TiO<sub>2</sub> anatase single crystals (001) presented a similar result of large polaron formation in the lattice. As discussed in chapter 2.1.3 though, large polarons can co-exist with small polarons in certain cases.<sup>45</sup> This explains the theoretical findings of Di Valentin *et al.*<sup>146</sup> who indicate a higher localization energy in

TiO<sub>2</sub> anatase, that brings to the formation of a small polarons at the pentacoordinated Ti sites of the surface region. The higher lattice relaxation energy of these undercoordinated Ti sites, which relax with fewer constraints than the hexacoordinated ones, suggests that it is energetically favorable for electrons to travel from the bulk to the surface of the material. Recently, using scanning tunneling microscopy and spectroscopy, this theoretical result has been experimentally supported.<sup>149</sup> Indeed, the formation of small polarons from the excess electrons was seen in rutile (110) and anatase (101) single crystals near the surface region. Moreover, rutile shows a polaronic state less localized within the gap than anatase (0.7 eV against 1 eV respectively) and anatase presented just electrons strictly localized at the oxygen vacancies. Finally, Selloni *et al.*<sup>150</sup> indicated that the electron localization at the surface is facet dependent for anatase and indeed, can easily take place on the (101) surface but not on the (001). This finding supports the approach of optimizing the ratio between these two facets in order to improve the photocatalytic activity of TiO<sub>2</sub> and highlights the complexity of charge localization in this material.



## 5 Femtosecond x-ray absorption of anatase TiO<sub>2</sub> nanoparticles

This chapter is based on the work published in Scientific Reports in 2015.<sup>15</sup>

### 5.1 Introduction

In anatase TiO<sub>2</sub>, upon absorption of a UV photon (bandgap 3.2 eV), an electron is promoted to the conduction band (CB, mainly Ti 3d character) while a hole is left in the valence band (VB, mainly O 2p character), as discussed in chapter 4. Electrons in the CB compete between delocalized (band-like) and localized states in the form of small or large polarons. This competition is key to understanding the transport properties of the material, yet it is still a matter of discussion.<sup>151</sup> Trapped charges (electron and holes) have been probed by steady-state methods, such as electron paramagnetic resonance (EPR),<sup>152-154</sup> photoluminescence,<sup>155</sup> and O<sub>2</sub> photodesorption.<sup>156</sup> The EPR studies on powdered anatase TiO<sub>2</sub> under high vacuum conditions, low temperatures (90 K) and continuous irradiation in the 3.2-6.2 eV range, showed two distinct traces attributed to electrons trapped at paramagnetic Ti<sup>3+</sup> sites, whose geometry remained unspecified, as well as O<sup>-</sup> signals due to holes (Figure 5.1).<sup>154</sup> However, the signal of the holes was significantly larger than that of the electrons at Ti<sup>3+</sup> sites, implying that only a limited fraction of the electrons (~10% in these samples) in the CB was trapped at Ti<sup>3+</sup> sites, while the rest are EPR-silent. At 90 K, the rate of the electron-hole recombination processes is reduced and the trapped electrons exhibit lifetimes of hours. However, above 90 K, the EPR signals due to Ti<sup>3+</sup> traps start to decrease to eventually disappear completely by 140 K, while those due to holes are still present, though weaker.<sup>154</sup> Heating to 298 K after irradiation at 90 K, led to the complete annihilation of the photogenerated charges (Figure 5.1).

In previous photoemission and electron energy loss spectroscopy (EELS) studies of the surface of low temperature single crystals of the rutile and anatase forms with a controllable concentration of Oxygen vacancies,<sup>157-160</sup> Ti<sup>3+</sup> centres were observed which were attributed to polarons. For the anatase (101) surface, photoemission data always show a significant gap state ~1 eV below the Fermi level (E<sub>F</sub>), characteristic of a small polaron.<sup>157,158,160</sup> However, for the (001) plane of anatase, no such signal was observed,<sup>159,161</sup> and a delocalized, large polaron (~40 meV below E<sub>F</sub>) was reported. The small polaron formation was attributed to pentacoordinated Ti<sup>3+</sup> centres, due to the presence of an Oxygen vacancy.<sup>157,158,160</sup> This was also supported by scanning tunnelling microscopy/spectroscopy (STM/STS) studies of anatase TiO<sub>2</sub> at 6 K, which showed that small polarons form in the proximity of an oxygen vacancy (*i.e.* at pentacoordinated sites) and never move.<sup>160</sup>

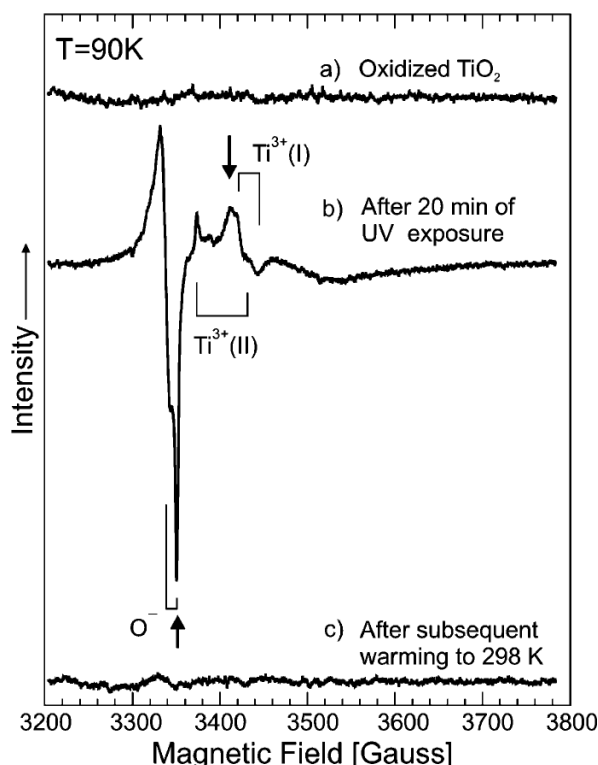


Figure 5.1 - EPR spectra of oxidized anatase nanoparticles, before (a) and after (b) 20 minutes of UV light irradiation at 90 K. The oxidation is done at 870 K for 2 hours in high vacuum conditions to remove all the organics remaining from the synthesis. Trapped electrons on  $\text{Ti}^{3+}$  centers show two different signals in the spectrum due to a different  $g$  tensor component, suggesting the presence of two different trapping sites. The EPR spectrum at room temperature (c) shows no signal, supporting the need of working at low temperature to observe trapping of charge carriers. Taken from ref.<sup>162</sup>.

Indeed, the removal of one neutral lattice oxygen atom leaves two extra electrons which fill the empty states of  $\text{Ti}^{4+}$  ions. A point defect and three undercoordinated (five-fold) Ti ions are formed.<sup>151</sup> The two electrons associated to the defect may be both delocalized on several Ti ions or localized on single (different) Ti ions; of course, intermediate situations are also possible in which one electron is localized and the second is not. The intragap polaronic states give rise to absorption bands observed by optical spectroscopy of anatase  $\text{TiO}_2$ , with various degrees of O vacancies.<sup>163</sup>

From the above, it appears that two types of  $\text{Ti}^{3+}$  centres exist in anatase  $\text{TiO}_2$ : those resulting from the presence of O vacancies,<sup>157,158,160,161,163</sup> and those that are created by UV irradiation,<sup>154,164</sup> which are not mutually exclusive. While the former seem to be well established as pentacoordinated centres, it is still not clear how the latter are created and what the nature of the traps is. Recent theoretical studies addressed the issue of photoinduced small polarons in anatase  $\text{TiO}_2$ <sup>165</sup>, as introduced in chapter 4.4. For the bulk (*i.e.* hexacoordinated), they predicted an  $\sim 80\%$  charge localization at the  $\text{Ti}^{3+}$  centre, associated with a trapping energy of 0.23 eV, and that the equatorial Ti-O bonds elongate by  $\sim 0.06$  Å and the axial ones by  $\sim 0.03$  Å. The hole was found to be 85% localized on the axial O atom associated to the  $\text{Ti}^{3+}$  centre, *i.e.* the two charges are close to each other. For the case of the (101) surface of

anatase, polaron trapping at pentacoordinated Ti centres was found to be favourable in the sub-surface region with 81% of the charge being localized and an energy gain of 0.67 eV. Elucidating the issues whether small polarons are formed and how requires element- and geometry-sensitive time resolved tools.

In the past decades, various ultrafast spectroscopic techniques have been used to probe the charge carrier dynamics in room temperature anatase  $\text{TiO}_2$  upon UV excitation above the band-gap. These experiments used probe pulses in the visible,<sup>166-169</sup> the IR,<sup>129,169,170</sup> and the THz range,<sup>171</sup> which all are sensitive to the overall charge dynamics in the conduction and valence bands of the material. Conclusions were drawn about the mobility and trapping of the electrons and holes, and in particular that both localize at the surface within 200 fs for 10-15 nm nanoparticles.<sup>129</sup> The conclusion of surface trapping though, it is itself drawn from quasi steady-state studies, in particular photoluminescence and  $\text{O}_2$  photodesorption,<sup>155,156</sup> whose outcome is determined by the long time scales of these experiments (on the order of microseconds or longer<sup>169</sup>), allowing for surface reactions to occur.

In 2016 Yoo *et al.*<sup>172</sup> investigated the spatiotemporal behaviour of Titanium and Oxygen in a titanosilicate material (*i.e.*  $\text{Na}_4\text{Ti}_2\text{Si}_8\text{O}_{22} \cdot \text{H}_2\text{O}$ ) using 4D femtosecond electron microscopy. In their sample, pentacoordinated  $\text{Ti}^{4+}$  ions are accommodated within the crystalline phase of silica in a square pyramidal arrangement. Titanosilicates can be used as single-site heterogeneous photocatalysts and structurally differ from bulk  $\text{TiO}_2$  in which  $\text{Ti}^{4+}$  ions are hexacoordinated. On the other side, they could be seen as model systems for  $\text{TiO}_2$  nanostructures, where there is a significant density of undercoordinated  $\text{Ti}^{4+}$  sites.<sup>123</sup> Upon excitation at 3.58 eV is triggered a ligand-to-metal charge transfer from the O 2p to the empty Ti 3d orbitals, which could be seen in analogy with the excitation from the VB to CB in  $\text{TiO}_2$ . Consequent to this transition, the electron diffraction data suggest an asymmetric dilation of the Ti-O bond lengths due to the reduction of  $\text{Ti}^{4+}$  to  $\text{Ti}^{3+}$ , which takes place in 350 ( $\pm$  250) fs. Although this could suggest a similar time scale for the localization of electrons at pentacoordinated Ti sites in  $\text{TiO}_2$ , it should be considered that these two materials have a different physics. In particular,  $\text{TiO}_2$  is a wide bandgap semiconductor where a band structure arises from the periodical overlap between the different Ti and O orbitals, instead these titanosilicates have single-sites pentacoordinated Ti centres which are characterized by molecular orbitals rather than a band structure.

In order to determine the fate of the electron excited in the CB of the  $\text{TiO}_2$ , it was implemented X-ray absorption spectroscopy (XAS) with 80 ps time resolution at the Ti K-edge of room temperature colloidal solutions of  $\text{TiO}_2$  nanoparticles (NPs).<sup>164</sup> In the following paragraphs, the main results of the work will be discussed. XAS is ideal because it is element-specific, sensitive to the local geometry and it provides information about the electronic structure of the Ti centres via the dipole-forbidden but weakly allowed 1s-3d pre-edge transitions that probe the density of unoccupied states above the Fermi level, as discussed in chapter 4.3. The results on ~10-20 nm (typical size of nanostructures in dye-sensitized solar cells) bare anatase and amorphous  $\text{TiO}_2$  NPs excited above the band gap showed that the

electrons reduce Ti sites, forming Ti<sup>3+</sup> centres, with nearly a full electron charge localizing on them.<sup>164</sup> Indeed, in those experiments it was observed an edge shift of  $\leq 1$  eV to lower energies, in line with the fact that an edge shift of  $\sim \pm 1$  eV corresponds to an oxidation state change of  $\mp 1e^-$ .<sup>173</sup> This situation is reminiscent of the small polaron, as described above. Because anatase TiO<sub>2</sub> NPs have been shown to have an ordered core with a defect-rich surface shell containing a high degree of Ti under-coordination,<sup>174</sup> and the fact that the spectral changes pointed to the reduced centres being in an amorphous-like environment, it was also concluded that these traps are mostly localized in that shell, and they were tentatively assigned to distorted hexa-coordinated and to penta-coordinated sites, based on the fact that the dipole forbidden pre-edge transition were significantly enhanced due to symmetry breaking. In addition, it was observed that the Ti<sup>3+</sup> centres decay in a bi-exponential mode on time scales of hundreds of ps and a few nanoseconds. The experiment performed on amorphous TiO<sub>2</sub> NPs, also showed formation of photoinduced Ti<sup>3+</sup> centres, which quite remarkably, underwent a biexponential decay kinetics on time scales close to those of anatase NPs.

The 80 ps time resolution of the experiment did not allow to follow the evolution of the electron prior to trapping and in particular, the time scale for trapping. This is important in order to elucidate how these photoinduced Ti<sup>3+</sup> centres are created. In addition, in the event of small polaron formation, the electron-phonon interaction leads to lattice relaxation which is confined on a single structural unit. Whether this proceeds via the formation of a large polaron, which collapses to a small one is unclear, nor is it clear if the polaron has an extrinsic (formation assisted by defects) or intrinsic (simply due to electron-phonon coupling) nature<sup>47</sup> (see chapter 2.1.3).

For these reasons, it has been implemented a femtosecond X-ray absorption near-edge spectroscopy (XANES) measurement for electron localization in photoexcited anatase TiO<sub>2</sub> colloidal nanoparticles at room temperature. The following study has been conducted at the Ti K-edge with a temporal resolution of  $\sim 200$  fs using the fs-slicing scheme at the Swiss Light Source,<sup>175</sup> described in details in chapter 3.2.3. Excitation of the electron to the CB is carried out via an indirect band gap excitation<sup>176</sup> using 3.5 eV (355 nm), 150 fs pump pulses.

## 5.2 Results and discussion

Figure 5.2a shows the steady state Ti K-edge spectrum of TiO<sub>2</sub>, already discussed in ref.<sup>164</sup>, with the edge at  $\sim 4.985$  keV and the pre-edge features, labelled A<sub>1</sub>-A<sub>3</sub> and B, around 4.97 keV. Figure 5.2b reproduces the transient spectrum (X-ray absorbance difference between excited and unexcited sample) recorded 100 ps after excitation at 355 nm (from ref.<sup>164</sup>). It shows an enhancement of the pre-edge features, while the  $\leq 1$  eV red shift of the edge is manifested by the strong absorption increase at 4.982 keV (just below the edge). The transient recorded at 1 ps time delay is also shown in Figure 5.2b.



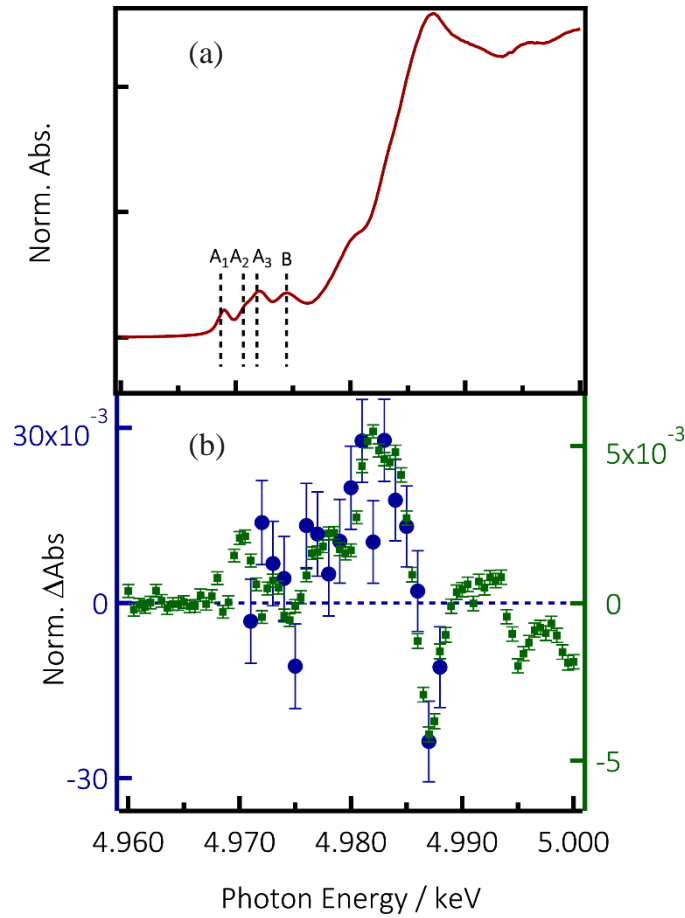


Figure 5.2 - a) Normalized static Ti K-edge XANES spectrum of colloidal nanoparticles of anatase  $\text{TiO}_2$  with the pre-edge features labelled  $A_1$ ,  $A_2$ ,  $A_3$  and B. b) Transient (difference) Ti K-edge XANES spectra (difference of the excited minus the unexcited sample absorption) for 3.5 eV excitation of colloidal nanoparticles of anatase  $\text{TiO}_2$ , recorded at time delays of 100 ps (green squares, right vertical axis)<sup>164</sup> and 1 ps (blue dots, left vertical axis).

The amplitude of the signal is similar to the 100 ps transient, taking into account the different excitation yields, but the data are much noisier due to the four orders of magnitude lower x-ray flux in the slicing scheme compared to the picosecond experiments. Still, the main features found at 100 ps are reproduced in the 1 ps transient. The excitation yield  $f$  has been estimated using the same approach as in ref. <sup>164</sup>. The sample concentration is  $c = 833 \text{ mM}$  and the thickness of the liquid jet  $d = 0.010 \text{ cm}$ . Using the following equation:

$$f = \frac{N_{ph.}}{N_A \cdot c \cdot \text{vol.}} (1 - 10^{(-\epsilon \cdot c \cdot d)})$$

Where  $N_{ph}$  gives the number of laser photons, vol. is the volume irradiated by the laser and  $\epsilon$  is the extinction coefficient at the excitation wavelength (3.5 eV). For the experimental conditions used, where  $N_{ph} = 3 \cdot 10^{13}$ ,  $\epsilon_{355\text{nm}} = 180 \text{ M}^{-1}\text{cm}^{-1}$  and  $\text{vol.} = 4.8 \cdot 10^{-7} \text{ cm}^3$ , it is found an excitation yield  $f \sim 12\%$  which is about 6 times higher than in the previous work.<sup>164</sup>

The scan was not carried out far enough to cover the entire pre-edge region, but the trend at 4.97 keV seems similar to that in the 100 ps transient. Figure 5.3 shows the temporal

evolution of the signal at the maximum transient intensity (4.982 keV), which maps the evolution of the population of reduced Ti sites.

The signal shows a prompt rise within 200 fs, reaching a level that remains near constant up to the limit of the scan (50 ps, Figure 5.4). The data are fitted to a model, which takes into account a single rate ( $k$ ) describing the increase of Ti<sup>3+</sup> population, convoluted with a Gaussian of 200 fs width ( $W$ ) to account for the time resolution of the experiment. The time-dependent signal can thus be described by:

$$f(t) = \frac{1}{2} A \cdot \left\{ \text{Erfc} \left[ -\sqrt{2} \cdot \frac{t - t_0}{W} \right] - e^{\frac{1}{8} k^2 W^2} \cdot e^{-k(t-t_0)} \cdot \text{Erfc} \left[ \frac{kW}{2\sqrt{2}} - \sqrt{2} \cdot \frac{t - t_0}{W} \right] \right\}$$

where  $A$  is the maximum transient signal and  $t_0$  is the time at which pump and probe pulses overlap. The best fit of the signal delivers a rise time of 170 fs, after deconvolution. However, given the scatter of data points and large error bars, a satisfactory fit was also obtained with a 300 fs rise time (grey trace in Figure 5.3) that can be considered the upper limit. The similarity of the transient spectra (Figure 5.2) and the fact that the signal shows no evolution beyond 0.5 ps (Figure 5.4), suggest that the traps observed in both experiments are identical.<sup>164</sup>

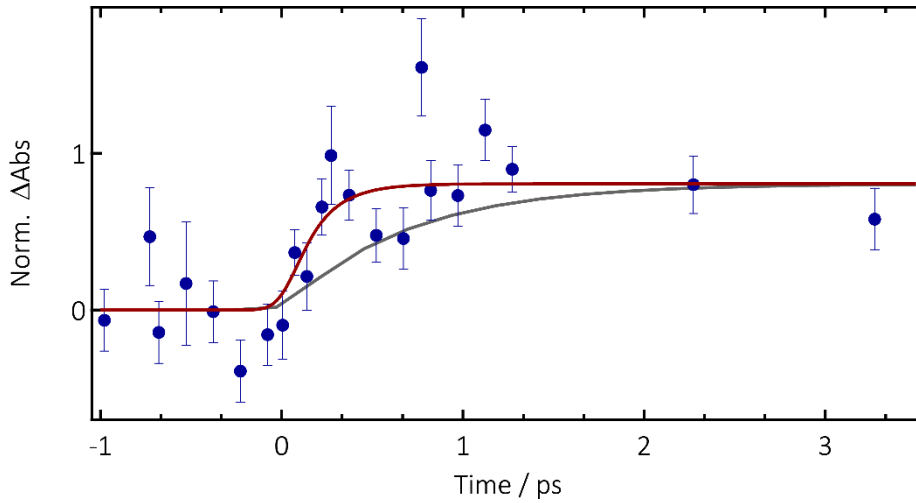


Figure 5.3 - Temporal evolution of the photo-induced X-ray absorption change at 4.982 keV of TiO<sub>2</sub> nanoparticles excited at 3.5 eV (blue dots). After the rise, the signal remains constant up to the limit of our time scan (~50 ps, see Figure 5.4). The brown trace represents the best fit of the data, yielding a rise time of 170 fs. The grey trace shows a satisfactory fit of the data with the longest rise time of 300 fs that represents an upper limit.

An estimate of the diffusion length  $l = \sqrt{D\tau}$ , of the electrons in the NPs can be obtained from the diffusion coefficient  $D$  of anatase TiO<sub>2</sub>, about  $10^{-6} \text{ m}^2/\text{s}$ ,<sup>177</sup> which is typical for the type of samples investigated here. For a rise time of  $\tau = 170$  to 300 fs, it is found that  $l \sim 4.0\text{-}5.5 \text{ \AA}$ . On the other hand, travelling from the centre of the NP to the surface of the 20 nm diameter particles would require  $\sim 100$  ps. Bearing in mind the uncertainty on the value of  $D$ , even an

increase by one order of magnitude would only increase the distance by a factor of three, and would not change the conclusions, *i.e.* that the electron does not migrate a long distance, least of all, of the order of the NP size. Thus, these results imply that the electron is localized within the unit cell in which it was generated or in its immediate vicinity. Given the near full electron charge localization, it can be associated to the formation of a small polaron, as schematically depicted in Figure 5.5.

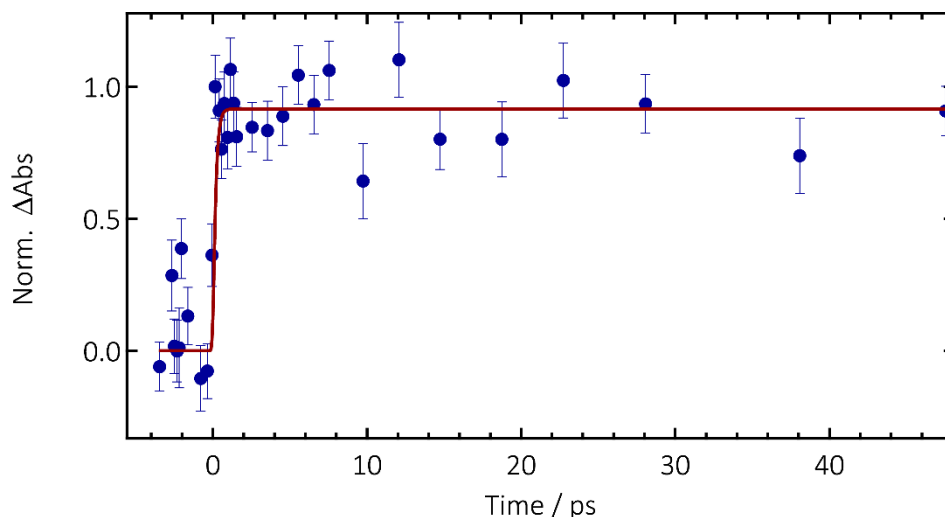


Figure 5.4 - Temporal evolution of the photoinduced X-ray absorbance change at 4.982 keV, monitoring the localization of electrons at Ti sites thus their reduction to  $\text{Ti}^{3+}$ . The signal stays constant for about 50 ps.

As already discussed above, the occurrence of small polarons resulting from oxygen vacancies is a well-established fact by virtue of the excess electrons present in the lattice. Less obvious is however how the photoinduced  $\text{Ti}^{3+}$  centres are created, like those reported here and in refs<sup>154,164</sup>. The pre-edge 1s-3d transitions (Figure 5.2a) are partially allowed because the 3d orbitals are partially mixed with the 4p orbitals. They are thus sensitive to symmetry changes of the Ti sites. In particular, the  $A_{2,3}$  features are associated to a mixed dipole/quadrupole character.<sup>178</sup> In view of the above: a) the distortion calculated by Di Valentin et al<sup>151,165</sup> for bulk polarons would not lead to the enhanced pre-edge  $A_{2,3}$  bands seen in Figure 5.2a, because the final symmetry does not lead to an enhanced mixing of *s* and *p* orbitals; b) upon formation of  $\text{Ti}^{3+}$ , all Ti-O bond lengths increase,<sup>151,165</sup> but also an asymmetric distortion around the  $\text{Ti}^{3+}$  centres would not lead to an increased intensity of the pre-edge features, as demonstrated in ref.<sup>179</sup>.

At this point, some observations from the previous ps XAS study<sup>164</sup> are reiterated: i) the transients reflect a spectral shift from anatase to reduced amorphous Ti centres; ii) the biexponential decay kinetics of the signal in photoexcited anatase and amorphous NPs are quite similar both in terms of decay constants and pre-exponential factors. Several experimental and simulations studies of amorphous  $\text{TiO}_2$  NPs<sup>180-182</sup> imply that the average

coordination number of Ti atoms is between 5 and 6, while anatase NPs are supposed to have a shell region with a greater proportion of five-fold coordinate sites.<sup>174</sup> Thus, the most likely trapping sites are pentacoordinated ones, which are mostly present in the shell. This does not rule out trapping in the bulk, but considering the high crystal quality of these anatase NPs (XRD in chapter 3.4.1), this is believed to be less likely.

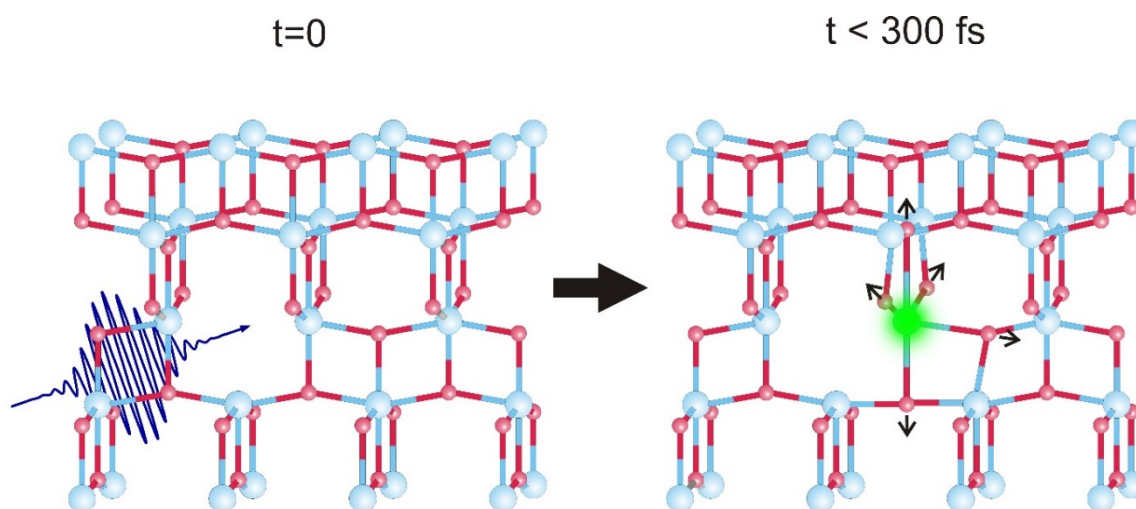


Figure 5.5 - Schematic representation of the electron localization at Ti centres in anatase TiO<sub>2</sub>. The blue spheres are the Ti atoms, while the red one are the O atoms. The electron becomes trapped at the pentacoordinated Ti atom, to form a Ti<sup>3+</sup> centre, leading to an additional structural relaxation due to the change of the field of forces between the Ti atom and the O atoms. This scheme represents only one of the two possible scenarios, particularly the one in which the vacancy derives from an oxygen removed on the equatorial plane.

This ties in nicely with the following observations:<sup>164</sup> a) pentacoordination leads to an enhancement of the pre-edge features even if the Ti-O bond lengths increase for polaron formation; b) The presence of two inequivalent classes of O neighbours (4+2) around the Ti atoms in the D<sub>2d</sub> symmetry of anatase TiO<sub>2</sub>, implies two possible pentacoordinated sites. The presence of two trapping sites, which were reported by EPR studies<sup>154</sup> and confirmed by the biexponential decay kinetics of the transient XAS signals,<sup>164</sup> may well be related to these two pentacoordinated conformations (*i.e.* equatorials and axials); c) the ratio of pre-exponential factors of the biexponential fit is ~2.4, quite close to the expected ratio of 2, if a statistical distribution of populated pentacoordinated sites is assumed. However, this interpretation for the pre-exponential factors leaves open questions on the nature of the biexponential behaviour observed in the amorphous TiO<sub>2</sub>.<sup>17</sup> Indeed, the absence of an ordered structure, clearly present in such a sample, should not lead to a simple biexponential decay, because of the several configurations with different bond lengths possible, but more likely to a stretched exponential.

The physics of charge localization in materials is a complex problem,<sup>47</sup> and in the case of TiO<sub>2</sub>, it is crucial to its numerous applications. This complexity arises from the interplay between different localizing effects, such as the electron-phonon interaction and the presence of weak potentials generated by static lattice imperfections.<sup>183</sup> Charge localization occurs at Ti<sup>4+</sup> sites by electron-phonon coupling, turning them to Ti<sup>3+</sup>, is expected to take place within one vibrational period of the infrared-active E<sub>u</sub> antiphase breathing mode of the oxygen atoms (about 41 fs),<sup>184</sup> which is directly involved in the lattice distortion.<sup>185</sup> In the presence of intrinsic or extrinsic defects, polaron self-trapping and trapping by the weak potential of these static lattice imperfections combine to freeze the motion of the carriers.<sup>183</sup> In the theory of Shinozuka and Toyozawa<sup>48</sup> the electron-phonon coupling and the effects arising from weak external potentials due to defects are considered to be additive: as a consequence, localization of an electronic excitation occurs even when one of these mechanisms is in itself not sufficient to induce it. The present scenario where the electron is trapped in the same unit cell where it was created or in its vicinity, implies that the pre-existing defects (mostly in the shell region) are dominating the trapping dynamics, even though anatase TiO<sub>2</sub> has an intermediate-to-strong electron-phonon coupling.<sup>186</sup> The local structural distortion (Figure 5.5) provides an additional energetic stabilization for the localized electron in the lattice.

### 5.3 Conclusions

Using femtosecond x-ray absorption spectroscopy, it has been shown that near full electron charge localization occurs at Ti centres in < 300 fs, implying that it localizes in the same unit cell in which it is excited or in its immediate vicinity. The localization process should correspond to formation of a small polaron, which induces a structural distortion of the surroundings. Based on the changes in the pre-edge features, it is concluded that this occurs at pre-existing pentacoordinated Ti defect sites, mostly located in the shell region. Although, single crystals of TiO<sub>2</sub> are known to contain O vacancies, whose concentration is controllable,<sup>163</sup> it remains to be established if photoinduced electron trapping occurs at such pentacoordinated Ti sites as previously discussed.<sup>151</sup> Moreover, due to the low photon flux intrinsically related to the slicing technique, high laser fluences (here ~ 340 mJ/cm<sup>2</sup>) are required in order to obtain an acceptable signal to noise ratio in the measurements. High fluences can affect the physics of charge localization in the material, indeed at high charge carrier concentrations a Fermi liquid in the CB could be formed due to a screening of the electron-phonon coupling, as discussed in chapter 2.2.1. In this case, the importance of the defects in the localization process would be drastically changed, with defect trapping becoming the main driving force, while instead at low fluences a purely intrinsic self-trapping mechanism could be the leading process. For this reason, free electron laser measurements would be the natural continuation of this study, thanks to the femtosecond time resolution together with the high x-ray flux of these machines. In this case, the effect of the laser fluence on the localization of electrons could be investigated. This would provide not only the time dynamics of the process at different charge carrier densities but also high resolution XA spectra in the femtosecond time region. Moreover, the higher x-ray flux would allow a

dispersive x-ray emission spectrometer (*e.g.* von Hamos geometry) to be used which would yield detailed information on the occupied electronic states.<sup>187</sup> Indeed, x-ray emission spectroscopy probes the density of occupied states (*i.e.* those below the Fermi energy, such as the VB states) and it is therefore the ideal tool to probe the dynamics of holes in the VB, avoiding the need to measure XA spectra at the O K-edge ( $\sim 543$  eV) and thus working in very restricted experimental conditions (*e.g.* high vacuum). This would result in a complete picture of the charge carriers fate in TiO<sub>2</sub>.

## 6 Picosecond x-ray absorption of rutile TiO<sub>2</sub> nanoparticles

### 6.1 Introduction

In the previous chapter, the ps-XAS study of anatase TiO<sub>2</sub> NPs<sup>17</sup> was extended to the femtosecond time scale, providing new insights in the localization process. Here, are explored the effects of a different crystalline structure on the electron's fate, under the same experimental conditions. In particular, TiO<sub>2</sub> exists in different polymorphs (*i.e.* anatase, rutile and brookite) with largely different properties. In the following, rutile is investigated, the most common natural phase of TiO<sub>2</sub>. The sample is a suspension of commercial rutile NPs with an average size of <100 nm, as described in chapter 3.4. Interestingly, the most promising commercial photocatalyst is a mixture of rutile and anatase (P25, Evonik Degussa GmbH) and it has been a benchmark for several years in the field.<sup>188,189</sup> Therefore, comparison and understanding of these two polymorphs is a hot topic.<sup>190</sup>

Although both anatase and rutile phases have a tetragonal structure, they have different space groups, as mentioned in chapter 4, I4/amd and P4<sub>2</sub>/mmn respectively. Both crystal structures consist of distorted TiO<sub>6</sub> octahedra, sharing four edges in anatase and two in rutile. This structural difference leads to a significant smaller bandgap energy for the rutile phase, namely ~3.0 eV instead of ~3.2 eV for anatase.<sup>111</sup>

For rutile, localization of excess electrons has been found using low temperature scanning tunnelling microscopy studies and shows similarities to the anatase case, with the main difference being that in anatase electrons localized almost exclusively at the surface, instead in case of rutile, also the sub-surface region seems to be effective.<sup>160</sup> However, the fate of photoexcited electrons in the material has not been determined yet using a direct technique such as ps-XAS.

Moreover, contrasting to anatase TiO<sub>2</sub>, the rutile form does not exhibit any hints of a defect rich shell in its X-ray absorption spectra.<sup>174,191</sup> Indeed, as mentioned in chapter 4, while anatase shows a clear dependence of the pre-edge transitions with particle size, this is not the case for rutile. The pre-edge region is characterised by 4 peaks (labelled A<sub>1-3</sub> and B in Figure 6.2) in the anatase while in the rutile case the A<sub>2</sub> peak, on the low-energy side of the central A<sub>3</sub> peak, is missing. The A<sub>2</sub> band in anatase is sensitive to NP size and it was concluded that it is a surface-specific pentacoordinated site. All the common crystal faces of both anatase and rutile are likely to contain both penta-coordinated Ti, therefore the question arises as to why the pre-edge region of rutile nanoparticles shows no variation with NP size. Luca<sup>174</sup> concluded that the shell region in rutile NPs must be either very thin or contain few undercoordinated Ti sites compared to anatase. He suggested that the fewer undercoordinated

sites may result from the ability of water to complete the coordination in rutile, while the thicker shell region in anatase would avoid all the undercoordinated sites to be reached by water molecules. In the previous ps-XAS study on anatase<sup>17</sup>, it was shown that in the case of the injection from a dye, the electron is indeed on the outer surface, confirming that coordination to water is not effective enough.

## 6.2 Results and discussion

Figure 6.1 shows the steady state XANES spectra of amorphous, anatase (20 nm) and rutile NPs, where the former two are taken from ref.<sup>164</sup>. Figure 6.2 is a zoom of these spectra in the pre-edge region. The pre-edge XAS region of anatase and amorphous exhibits the four peaks A<sub>1</sub>-A<sub>3</sub> and B, mentioned above.

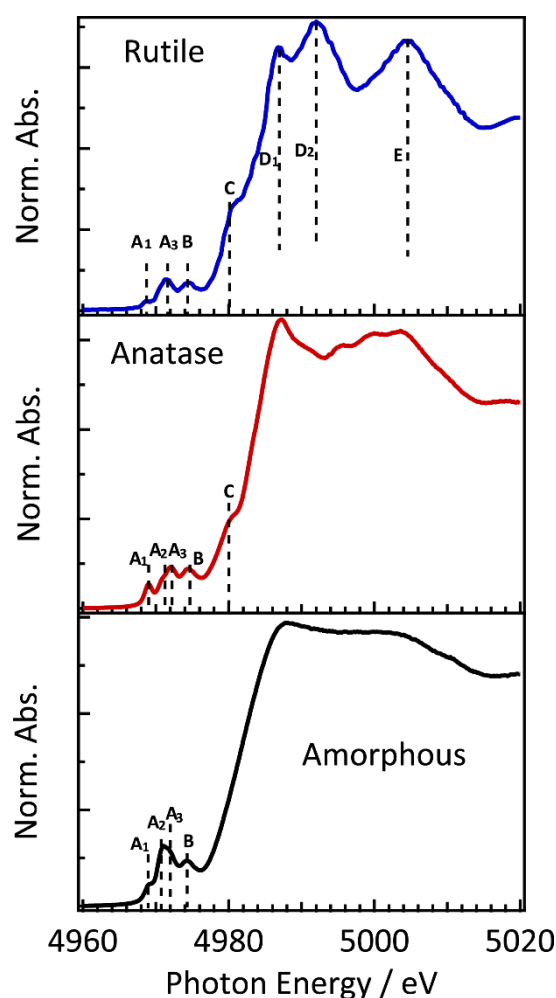


Figure 6.1 - Ground state x-ray absorption near edge structure (XANES) for the rutile, anatase and amorphous NPs. The dotted vertical lines highlight the main features in the pre-edge region (A<sub>1</sub>, A<sub>2</sub>, A<sub>3</sub>, B and C) and the above the edge (D<sub>1</sub>, D<sub>2</sub> and E). The absence of the A<sub>2</sub> feature in case of rutile NPs can be seen more clearly in Figure 6.2.



The  $A_2$  and  $A_3$  peaks are separated by  $\sim 1$  eV and in the amorphous NPs, they appear stronger (Figure 6.2), as also reported in refs<sup>174,182</sup>. These pre-edge peaks are typical of K-shell spectra<sup>192</sup>, *i.e.* transitions from the 1s core orbital to unoccupied Ti 3d valence orbitals. In the regular octahedral  $Ti^{4+}$  ( $3d^0$ ) hexacoordinated sites of bulk anatase, these transitions have a quadrupole character, but anatase  $TiO_2$  presents a weak  $D_{2d}$  distortion that makes them partially allowed by virtue of 3d/4p mixing, which introduces a dipole component.<sup>178,193</sup>

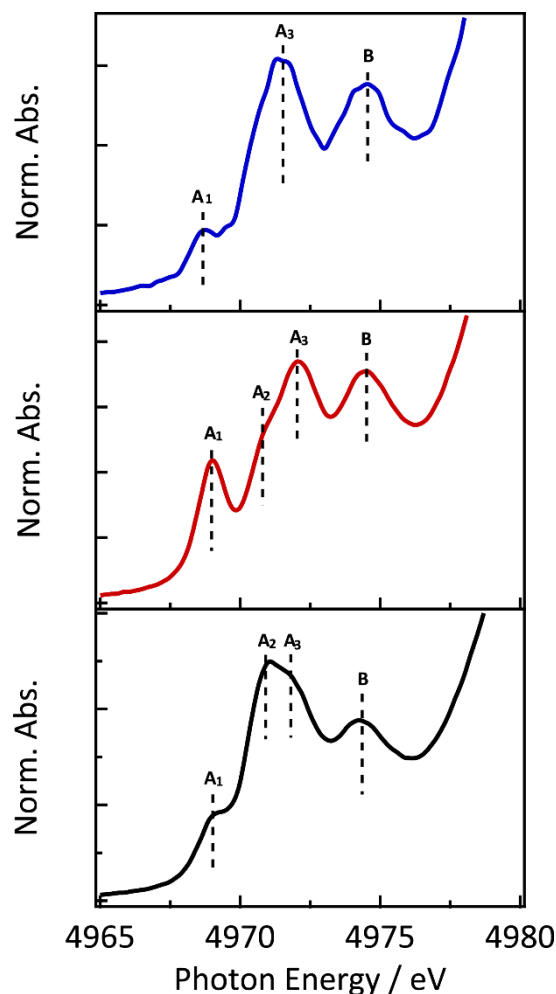


Figure 6.2 - Ground state X-ray absorption spectra in the pre-edge region for the rutile (blue line), anatase (red line) and amorphous  $TiO_2$  NPs (black line). The dotted vertical lines highlight the main features ( $A_1$ ,  $A_2$ ,  $A_3$ , B and C).

Stronger deviations from octahedral symmetry would further enhance such mixings. The exact assignment of these peaks is still a matter of debate, but there is consensus that  $A_1$  has a predominantly quadrupole character,  $A_2$  and  $A_3$  have a quadrupole + dipole character, while B is predominantly a dipole transition.<sup>174,182,192-194</sup> The pre-edge region of the rutile NPs exhibits only three peaks  $A_1$ ,  $A_3$  and B (Figure 6.2), as previously reported.<sup>174</sup>  $A_1$  and  $A_3$  are forbidden transitions to  $d(t_{2g})$  and  $d(e_g)$ , respectively, of the absorbing octahedral and they are made allowed by thermal vibrations.<sup>174</sup> Feature B instead, is predominantly dipolar as in

the anatase case. Other strong features can be seen above the edge (C, D<sub>1</sub>, D<sub>2</sub> and E in Figure 6.1), which are principally of dipole character.<sup>195</sup> The spectral differences between anatase, rutile and amorphous NPs suggest different coordination geometries around the Ti atoms<sup>196</sup>. Above the edge, the absorption spectra of anatase and rutile are, as expected, clearly more structured than that of amorphous NPs. This, along with the very different powder diffraction patterns of the three types,<sup>164</sup> points to both short and long range disorder in the amorphous case.

The transient XAS (difference of the excited minus the unexcited sample x-ray absorption spectra) recorded 100 ps after 3.5 eV excitation are shown in Figure 6.3b and c. Significant changes are observed in the pre-edge, the edge and above-edge regions, reflecting substantial photoinduced modifications of both the electronic and the geometric structure of Ti centres.

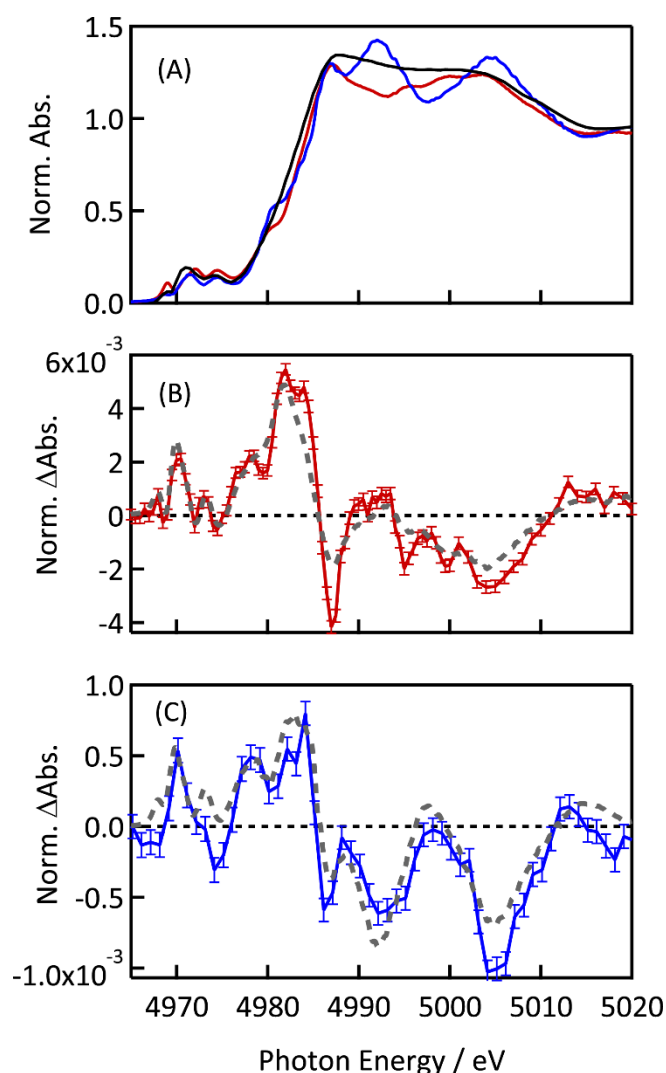


Figure 6.3 - (A) Comparison between the ground state spectra at the Ti K-edge of the anatase (red curve), the rutile (blue curve) and amorphous (black curve) TiO<sub>2</sub> nanoparticles. (B) Transient spectrum of anatase (red curve) at 100 ps time delay and simulated difference with 1 eV shift (dotted grey curve, taken from ref.<sup>17</sup>). (C) Transient spectrum of rutile (blue curve, this work) at 100 ps time delay and simulated difference with 1 eV shift (dotted grey curve).

These changes are quite different between the rutile and the anatase cases, especially above the edge. In ref.<sup>164</sup>, the transient spectrum of anatase was reproduced by taking the scaled difference of the amorphous static spectrum shifted by 1 eV minus the anatase static spectrum. The scaling was done by normalizing the static difference and the transient spectra at the maximum (*i.e.* at the edge) with a scaling factor of 0.016. The fact that the spectra could be simulated with this approach, clearly showed that together with a change in the oxidation state of  $\text{Ti}^{4+}$  sites given by the electron localization there is a shift of spectral weight from anatase-like to amorphous-like. It was argued that the electrons created in the CB act as contrast agents by preferentially localizing in the defect-rich shell region.<sup>164</sup> In general, rigidly shifted spectra showed deviations in the pre-edge region because the occupancy of  $\text{Ti}(3d)$  orbitals upon reduction is neglected in the static difference. It is interesting to note that some changes in the pre-edge region (Figure 6.3b and c) are similar for the anatase and the rutile cases, particularly for the rise of the  $A_2$  feature. This suggests that possibly the same scenario also takes place in rutile NPs. Therefore the same approach was adopted as for the anatase NPs and was considered the difference of the -1eV shifted amorphous spectrum minus the rutile spectrum (dotted grey curve in Figure 6.3c), using a scaling factor of about 0.003. Figure 6.4 shows different shifts in energies for the amorphous spectrum and different scaling factors were used to minimize the difference between the simulated spectrum and the transient spectrum at 4983 eV. The simulation of the rutile is overall satisfactory (Figure 6.3c and Figure 6.4) confirming that a similar physics of localization for the photoexcited electrons is present in rutile  $\text{TiO}_2$  as in anatase.

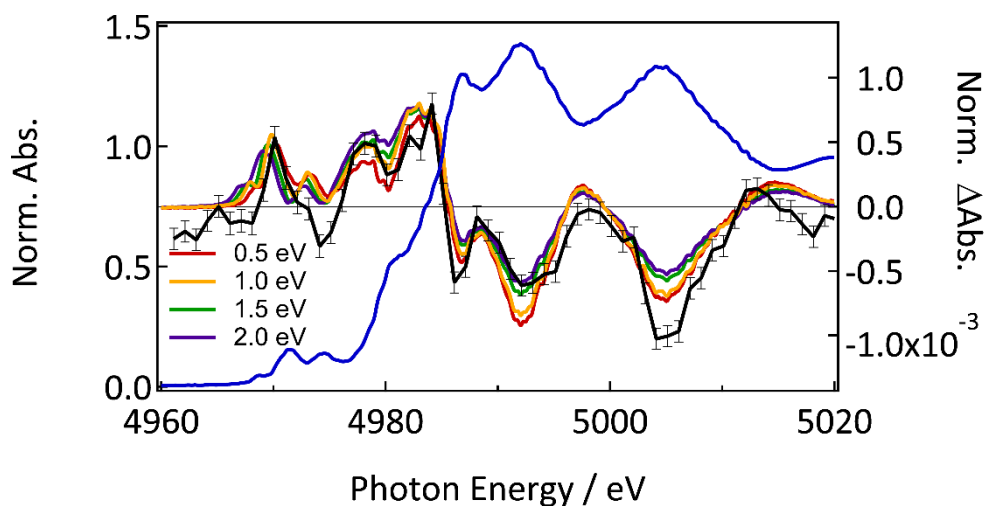


Figure 6.4 - Simulated spectra (amorphous shifted in energy minus rutile spectrum) using different energy shifts. The difference simulated spectra have been rescaled with different factor in order to match the positive feature at 4983 eV. The rescaling factors are 0.33, 0.30, 0.24, 0.21% for shifts of 0.5, 1.0, 1.5 and 2.0 eV respectively.

For what concern the kinetic traces (Figure 6.5), in the previous work<sup>164</sup> for bare and sensitized anatase NPs, they were fitted using a bi-exponential functions convoluted with the instrument response function (about 70 ps). The decay kinetic at 4.982 keV is shown in

Figure 6.5 for both anatase and rutile. The anatase has decay constants of 0.31 and 6 ns, while for rutile, both a monoexponential and a biexponential fit can be used. The monoexponential yields to a decay constant of 1.39 ns and the biexponential to decay constants of 0.51 and 36 ns (Table 6.1), but these have an uncertainty higher than their absolute value due to the limited time window probed.

Table 6.1: Parameters resulting from mono and biexponential fitting using functions convoluted with the instrument response of the system (70 ps).  $A_{1,2}$  are the amplitudes and  $\tau_{1,2}$  the time decay constants of the fitting functions. The high uncertainty of the biexponential fitting is due to the limited time window probed.

	<b>Monoexponential</b>	<b>Biexponential</b>
$\tau_1$ (ns)	$1.39 \pm 0.13$	$0.51 \pm 1.37$
$\tau_2$ (ns)	-	$36 \pm 3530$
$A_1$	$0.85 \pm 0.02$	$0.48 \pm 1.64$
$A_2$	-	$0.41 \pm 1.67$

The decay time constants for the case of dye sensitized anatase NPs were about twice longer, due to the  $e^-$  and  $h^+$  separation imposed by the dye injection mechanism. Moreover, the decay kinetics in different spectral regions of the anatase sample, *i.e.* pre-edges (4979 eV), edge (4982 eV) and post-edge (5150 eV), were the same within the error bars, indicating that electronic and structural changes were given by the same species. As discussed in chapter 5, the biexponential decays are intrinsically linked to the nature of the electrons trapping sites. Indeed, the trapping sites of the electrons are pentacoordinated which arises from an oxygen vacancy defect in the material. They have two different possible configurations depending on which of the two types of oxygen, *i.e.* axial or equatorial, is absent on the Ti site. This is supported by the ratio of the amplitude for the two decay constants which is about  $\frac{1}{2}$  as the probability for an axial/equatorial oxygen vacancy. In the case of rutile, the observed kinetic is slower than bare anatase in the time window explored (Figure 6.5). This data set though, was acquired in a narrow time window and therefore the uncertainty on the fit variables for a biexponential fitting (Table 6.1) does not allow a quantitative comparison.

Overall, as said above, the agreement between the simulated data and the experimental transient for the rutile NPs is similarly satisfactory to anatase. Moreover, also if the ground state spectrum of rutile does not present the feature  $A_2$ , as a consequence of the low concentration of pentacoordinated Ti sites in this crystal phase of TiO<sub>2</sub>,<sup>174</sup> this feature is clearly seen in the rutile transient spectrum. This shows the power of time resolved XAS in semiconductors which relies on the selective enhancement of the signal from defects that are

the trapping sites for charge carriers in the material, also when the concentration is too low to be detected using conventional XAS.

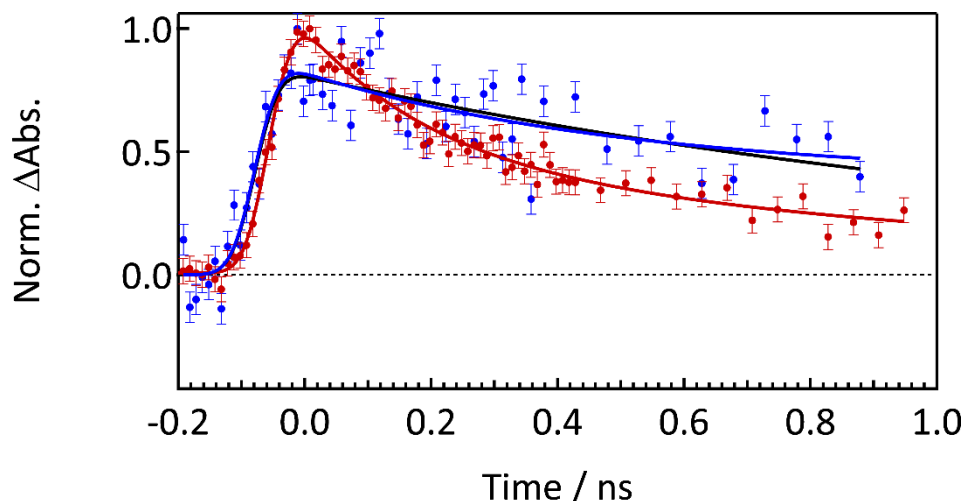


Figure 6.5 - Comparison between the time traces at 4982 eV of anatase (red dots, taken from ref.<sup>17</sup>) and rutile (blue dots, this work) TiO<sub>2</sub> NPs upon excitation at 3.5 eV and 260 kHz with 48 mJ/cm<sup>2</sup>. The solid blue and red lines are obtained by the fitting the data using biexponential functions convoluted with the instrument response function of the system (70 ps), the black line is obtained by fitting the rutile decay kinetic by a monoexponential.

Furthermore, recently excess electron localization has been studied via scanning tunnelling microscopy (STM) in anatase and rutile.<sup>160</sup> It was shown that in rutile, excess electrons can still retain a certain mobility through hopping in the lattice while for anatase the trapped electron remains next to oxygen vacancies. The polaronic state in rutile was found to be  $0.7 \pm 0.1$  eV below the Fermi energy while for anatase, it was  $1.0 \pm 0.1$  eV. XAS cannot deliver such type of information but similar conclusions are drawn for the general fate of photoexcited electrons in rutile, indeed they appear to be trapped next to oxygen vacancies, as for the anatase case. Moreover, it should be noticed that for the transient spectra of these polymorphs there is a clear difference in the scaling factor used for simulating these time resolved results, which is related to the excitation and quantum yields. The scaling factor is about 5 times lower for rutile if compared to bare anatase NPs (*i.e.* 0.3 % instead of 1.6 % respectively). The excitation yield is about 30% higher for rutile, considering that the excitation fluence is the same and the NPs concentration in the colloids was set to an optical density of 1.2 at 3.5 eV for both cases. Indeed, Figure 6.6 shows that rutile has a 30% higher absorption at 3.5 eV compared to anatase and this results in a higher excitation yield because of the lower concentration of sample used for the same fluence.

Therefore, the lower scaling factor must be attributed to a lower quantum efficiency, which shows a smaller tendency of electron localization in pentacoordinated sites. This effect can be related to the lower probability of localizing electrons next to oxygen vacancies<sup>160</sup> but also to the lower concentration of superficial pentacoordinated sites,<sup>174</sup> showed by the ground state spectrum. In any case, rutile is less inclined to surface trapping than anatase.

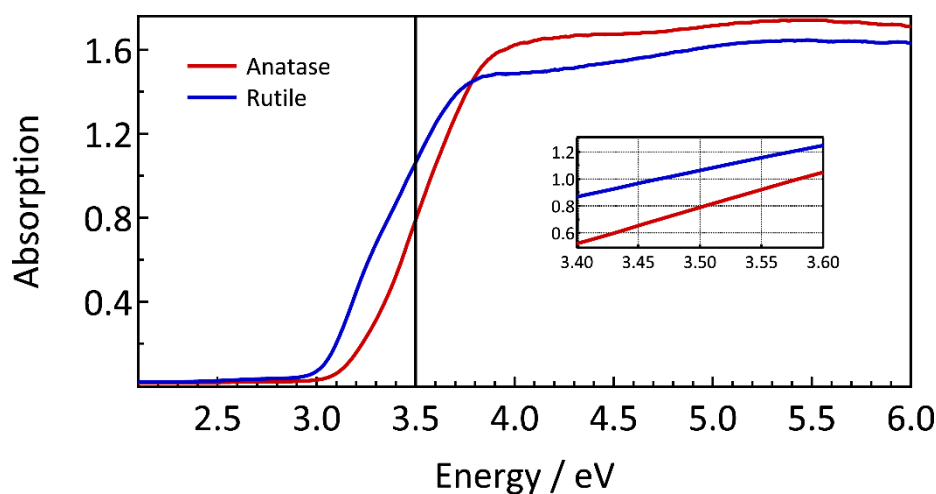


Figure 6.6 - UV-Vis diffuse reflectance spectra of anatase (red curve) and rutile (blue curve) powders collected using an integrating sphere. The excitation energy used during the ps-XAS experiment (3.5 eV) is highlighted in the figure. In the inset there is a zoom around this energy region.

### 6.3 Conclusions

To conclude, electron localization occurs in rutile next to oxygen vacancies, which are mainly at the surface region, similarly to the anatase.<sup>197</sup> The main difference observed is in the relative quantum efficiency for this process, which is more than 5 times lower for rutile and this is attributed to the lower concentration of oxygen vacancies and/or a lower tendency to localization in their proximity. The less pronounced tendency for surface trapping could be the reason for the lower efficiency of rutile in photocatalytic reactions,<sup>198</sup> whose origin is still debated.<sup>199</sup> Indeed, for an efficient photocatalytic reaction, kinetics as well as thermodynamics play a fundamental role in the efficiency. Charge carriers should not only have a redox potential able to thermodynamically drive the reaction towards the products but they should also live long enough, *i.e.* hundreds of ps<sup>200</sup>, in order to have the time to react with the molecules adsorbed onto the surface before recombining. This means that trapping is detrimental from the thermodynamic point of view because it lowers the reductive potential of electrons but on the other hand it helps the kinetic perspective, because it increases the lifetime of the photogenerated carriers. Indeed, charge carriers which are trapped can live up to ms, therefore are favourable spots, if placed at the surface, to undergo chemical reactions. Finally, similarly to the outlook presented for the anatase in the previous chapter, also the understanding of rutile NPs would benefit from free electron laser measurements. This not only provide information on the electron trapping process in the femtosecond time scale but also open the possibility to measure the hole dynamics in the valence band. Indeed, as mentioned in chapter 5.3, the high flux allows to measure simultaneously x-ray emission

together with the x-ray absorption signal and therefore gain insights on the fate of the occupy states in the valence band of the semiconductor.





## 7 Lead Halide Perovskites

### 7.1 The rise of hybrid organic/inorganic perovskites

In the search of novel photovoltaic technologies, dye-sensitized solar cells (DSSCs) dominated the scene for about 20 years from the first appearance.<sup>5</sup> In 2009, the hybrid halide perovskite  $\text{CH}_3\text{NH}_3\text{PbI}_3$ , a new material in the field of light to energy conversion, has been used as photosensitizer in a sensitized solar cell.<sup>7</sup> From this point on, the scientific community started an intense work to optimize the conversion efficiency and another milestone in the photovoltaic applications of the hybrid organic/inorganic perovskite (HOIP) was its implementation as an absorber in an all-solid state device.<sup>9,105,201</sup> In this configuration, the HOIP is grown in a mesoporous  $\text{TiO}_2$  layer which acts as electron acceptor and it is in contact with a solid hole transport material (*e.g.* Spiro-MeOTAD, as showed in Figure 7.1).

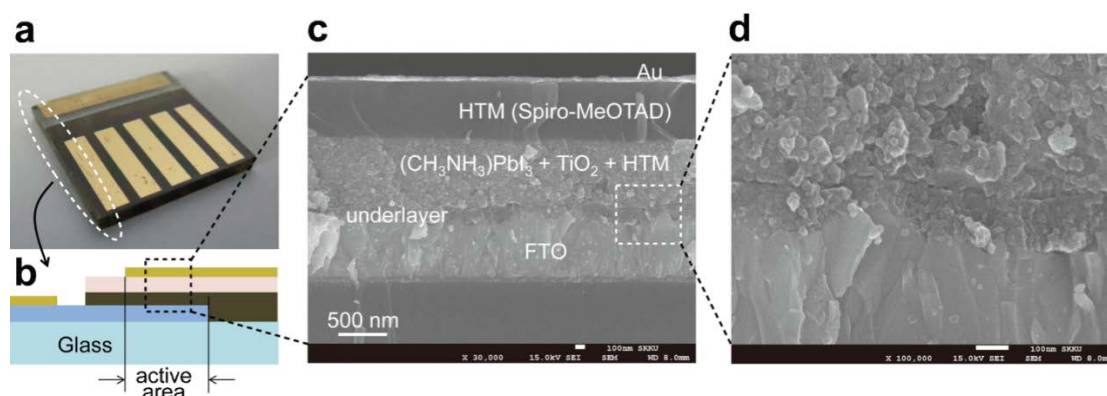


Figure 7.1 - (a) Real solid-state device. (b) Cross-sectional structure of the device. (c) Cross-sectional SEM image of the device, showing (from top to bottom): the gold electrode, the hole transport material (HTM, spiro-MeOTAD), the mesoporous  $\text{TiO}_2$  with  $\text{CH}_3\text{NH}_3\text{PbI}_3$  as an absorber and the fluorine doped tin oxide (FTO) layer. (d) Active layer/FTO underlayer-interfacial junction structure. Taken from ref.<sup>105</sup>.

Since then, solar cells with HOIP achieved over 20% certified efficiency in only 5 years of research, which is a remarkable performance in such a short time.<sup>8</sup> Lead halide perovskites have a longer history than that emerging from the recent application in the energy conversion. In 1958, Möller reported photoconductivity in  $\text{CsPbX}_3$  systems<sup>97</sup> (where X is a halide atom) which were later recognized as ionic semiconductors.<sup>202</sup> In 1978, Weber reported the crystal structure of  $\text{CH}_3\text{NH}_3\text{PbX}_3$ .<sup>203</sup> The discovery of HOIP gave rise to the work of Mitzi *et al.* in the 1990s, who demonstrated efficient field effect transistor (FET) devices,<sup>204</sup> a first proof of the application potential for this class of materials.

Nowadays the word “perovskite” is becoming synonymous of HOIP and the number of publications on this topic exceeds 500 for 2015 only.<sup>205</sup> The major advantages of HOIP

devices over conventional solar technologies are their low processing temperature (150 °C) and composition of Earth-abundant elements, which make them ideal candidates for low-cost solar cells. Although the development of this technology benefited vastly from the earlier research in photovoltaics, particularly the architecture of DSSCs, HOIP appeared to have efficient ambipolar charge carrier transport, meaning that it can efficiently transport electrons and holes. Snaith *et al.* showed this property by replacing a TiO<sub>2</sub> layer with the insulating Al<sub>2</sub>O<sub>3</sub> obtaining still a high-efficiency device.<sup>9</sup>

Halide perovskites showed to be materials with a broader range of optoelectronic applications than simply photovoltaics. They have been employed successfully for light-emitting diodes (LEDs) which have high efficiency and tunable emission energies.<sup>206,207</sup> Moreover, they exhibited stimulated emission for lasing in the form of thin films<sup>69</sup> but also nanowires single crystals.<sup>70</sup> In a photocatalytic water splitting device powered by CH<sub>3</sub>NH<sub>3</sub>PbI<sub>3</sub> thin film they have been able to split water with 12.3% efficiency.<sup>208</sup> Finally, they can be used for high energy radiation detection, indeed large single crystals of CsPbBr<sub>3</sub><sup>209</sup> and films of CH<sub>3</sub>NH<sub>3</sub>PbI<sub>3</sub><sup>210</sup> demonstrated to detect x-ray.

## 7.2 Geometric and electronic structure

Historically, perovskites are named after Lev Perovskiy, a Russian mineralogist. This class of compounds has the same type of crystal structure as CaTiO<sub>3</sub>. In general, their formula is AMX<sub>3</sub> where A and M are cations and X an anion. The ideal perovskite has a simple cubic crystal structure in which corner sharing octahedral networks MX<sub>6</sub> have a M-X-M 180° bond angle and A ions in the interstices (Figure 7.2,  $\alpha$ -CsPbI<sub>3</sub>).<sup>211</sup> The archetype cubic structure lowers its symmetry when temperature or pressure changes are applied, in ways which depend on each compound. In particular, halide perovskites change the angle between M-X-M from the ideal 180° (as in the undistorted perovskite denoted as the  $\alpha$ -phase), yielding the  $\beta$ -phase after the first phase transition, the  $\gamma$ -phase after the second and finally the non-perovskite structure  $\delta$ -phase (Figure 7.2).<sup>212</sup> For what concerns the electronic structure, halide perovskites are generally direct-gap semiconductors, meaning the valence band (VB) maximum and conduction band (CB) minimum occur at the same point of the Brillouin zone<sup>211</sup> (see chapter 2.1 for a general introduction). This explains the high extinction coefficient of this material, which can absorb photons without the need of a phonon assisted transition. State of the art approach is to calculate the band structure using many body perturbation theory with GW approximation including spin-orbit coupling, which influences the band energies.<sup>213</sup> The density of states in perovskites shows that the VB is dominated by the halide p-orbitals while the CB has mainly Pb 6p character (Figure 7.3).<sup>25,214</sup> The bandgap energy, which is about 1.6 eV for CH<sub>3</sub>NH<sub>3</sub>PbI<sub>3</sub>, can be easily tuned by changing the methylammonium cation or simply the halide anion. The latter, because it is directly involved in the band formation, can easily be explained by the different electronegativity of the halides.

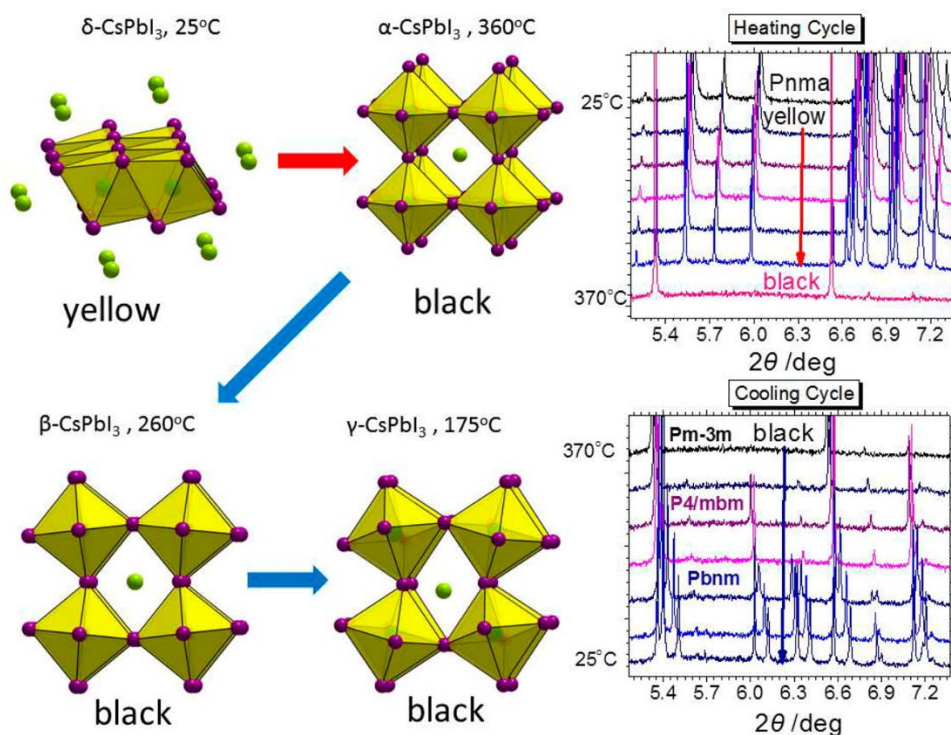


Figure 7.2 - A case study of the phase transition scheme as observed with synchrotron powder diffraction ( $\lambda = 0.413906 \text{ \AA}$ ) for the  $\text{CsPbI}_3$  compound. Initially, the room temperature stable  $\delta$ -phase (yellow) converts to the black perovskite  $\alpha$ -phase upon heating above  $360^\circ\text{C}$ . On cooling, the perovskite structure remains kinetically stabilized converting to the black perovskite  $\beta$ - and  $\gamma$ -phases at  $260$  and  $175^\circ\text{C}$ , respectively. Full conversion of the  $\gamma$ - to the initial yellow  $\delta$ -phase occurs after  $\sim 48\text{h}$ . Taken from ref.<sup>212</sup>.

The bandgap energy increases proportionally with the halide electronegativity, therefore in the order  $\text{Cl}^- > \text{Br}^- > \text{I}^-$ .<sup>215</sup> The reason for the bandgap tuning by the organic part, of which the partial density of states appears several eV below the valence band maximum<sup>25,211</sup> (Figure 7.3), is purely structural. Indeed, through structural and Coulombic interactions, it can deform the perovskite lattice and lead to a bandgap change.<sup>212</sup> Particularly, it is the octahedral tilting which is influenced by different cations and is responsible for the changes in the electronic structure close to the band edges, as demonstrated by a study<sup>212</sup> comparing optical absorption and structural data.

Interestingly, the  $\text{CH}_3\text{NH}_3^+$  ions are free to rotate between the octahedral cages at room temperature and this seems to have profound consequences on the electronic structure.<sup>216</sup> Indeed, orientations in which cations lower the symmetry of the structure change the bandgap from direct to indirect (Figure 7.4).

Regarding the exciton binding energy ( $E_b$ ), a general rule in semiconductor physics indicates that it is directly proportional to the bandgap energy of the material,<sup>217</sup> meaning that  $\text{CH}_3\text{NH}_3\text{PbBr}_3$  (bandgap energy of  $\sim 2.3$ ) has a higher  $E_b$  than  $\text{CH}_3\text{NH}_3\text{PbI}_3$  (bandgap energy of  $\sim 1.6$ ). The experimental values of  $E_b$  measured for  $\text{CH}_3\text{NH}_3\text{PbI}_3$  at room temperature though, span at least from  $55 \text{ meV}$  to below  $10 \text{ meV}$ .<sup>218</sup>

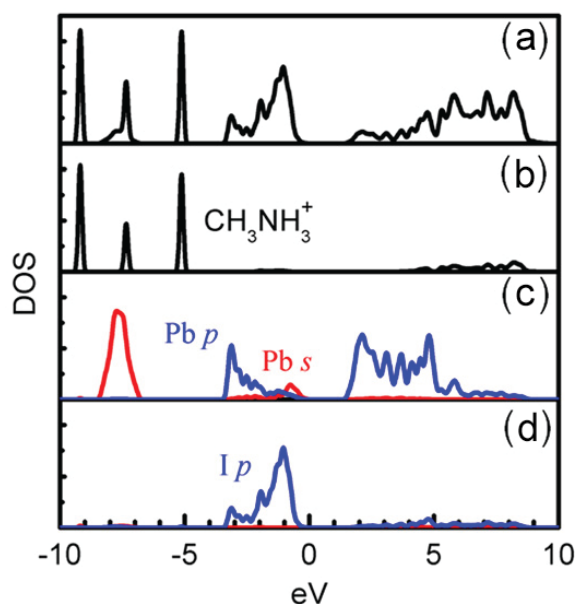


Figure 7.3 - Total density of states (DOS) of  $\text{CH}_3\text{NH}_3\text{PbI}_3$  in the cubic structure (a) and partial DOS for  $\text{CH}_3\text{NH}_3^+$  (b), Pb (c) and I (e) obtained by first-principles calculations using generalized gradient approximation (GGA) for the exchange correlation. The zero in DOS is referred to the valence band maximum. The Pb partial DOS is enlarged by five times for a clear indication of the s orbital contribution. Taken from ref.<sup>25</sup>.

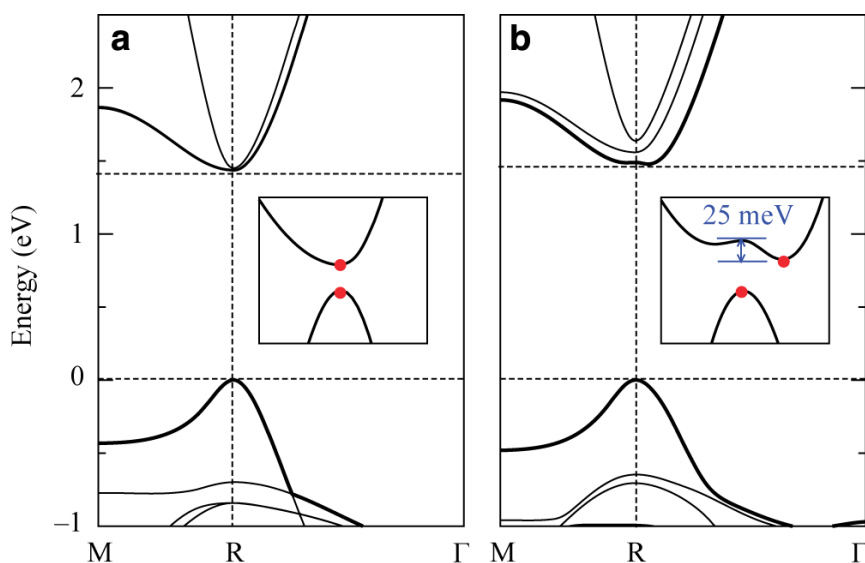


Figure 7.4 - Band structure of the fully relaxed  $\text{CH}_3\text{NH}_3\text{PbI}_3$  crystal obtained using first-principles calculations with generalized gradient approximation (GGA). The bands are shown for molecule orientations along (a) (111) and (b) (011) direction. The insets show a magnification of the bands (which have been shifted in energy for convenience) around the bandgap and highlight the changes in the VB maximum and CB minimum caused by rotation of  $\text{CH}_3\text{NH}_3^+$ . Note that for the (011) orientation the bandgap becomes indirect. Taken from ref.<sup>216</sup>.

It is important to understand the nature of the charge carriers upon photoexcitation for photovoltaic devices but the thermal energy at room temperature (*i.e.* 25 meV) is within the range of experimental values found for  $E_b$  and it is therefore not easy to predict the behavior

in this material. Recently, Grancini *et al.*<sup>57</sup> rationalized this problem of finding a univocal value for the exciton binding energies in HOIPs. Indeed, they found that the electron-hole interaction in  $\text{CH}_3\text{NH}_3\text{PbI}_3$  and  $\text{CH}_3\text{NH}_3\text{PbBr}_3$  is sensitive to the microstructure of the material and therefore fabrication procedures influence the  $E_b$ , which explains the different experimental values found in the literature.

From a point of view of defects in the material, taking into account the low processing temperature used for the synthesis of halide perovskites, a high concentration of intrinsic structural defects is intuitively expected, such as vacancies and/or interstitial atoms. In reality, the small Urbach tail energy ( $\sim 15$  meV),<sup>219,220</sup> which can easily compete in sharpness with high temperature processed semiconductors commonly used in photovoltaics (Figure 7.5), points to a low density of traps<sup>221</sup> (estimated  $\sim 10^{10} \text{ cm}^{-3}$  in single crystals).<sup>222</sup> Moreover, a computational study using density functional theory<sup>223</sup> showed that even upon formation of intrinsic defects, gap states which could act as deep traps are absent in the DOS. These results explain at least partially the fact that the perovskites can be efficient semiconductors even when grown using simple solution processes.

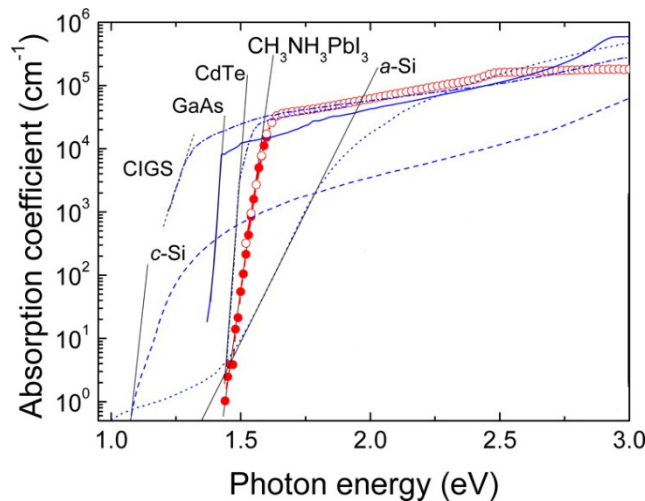


Figure 7.5 - Absorption coefficient for a thin film of  $\text{CH}_3\text{NH}_3\text{PbI}_3$  compared with other semiconductors used in photovoltaics applications. The sharpness of the absorption edge (highlighted by a black line) is inversely proportional to the Urbach tail energy of which a low value, indicates high crystalline quality of the material and therefore low presence of defects. Surprisingly, the low temperature processed  $\text{CH}_3\text{NH}_3\text{PbI}_3$  film shows an Urbach tail similar to the one of GaAs, a monocrystalline direct semiconductor of very high electrical quality. Taken from ref.<sup>220</sup>.

Interestingly,  $\text{CH}_3\text{NH}_3\text{PbI}_3$  can be either *n*- or *p*- self-doped by changing the ratio of methylammonium halide ( $\text{CH}_3\text{NH}_3\text{I}$ ) to lead iodide ( $\text{PbI}_2$ ), which are the synthetic precursors of this perovskite.<sup>224</sup> This means that tuning film composition by changing film formation method and process conditions, changes the electronic properties of  $\text{CH}_3\text{NH}_3\text{PbI}_3$ . The main defects playing a role in the ambipolar self-doping behavior are  $\text{Pb}^{2+}$  vacancies for the *p*-type; and  $\text{I}^-$  vacancies and  $\text{CH}_3\text{NH}_3^+$  interstitials for the *n*-type.<sup>25,224</sup> The sister perovskite  $\text{CH}_3\text{NH}_3\text{PbBr}_3$  shows unipolar self-doping behavior instead, where only *p*-type conductivity



is observed under thermal equilibrium growth conditions.<sup>225</sup> This is because the formation energy of a  $\text{CH}_3\text{NH}_3^+$  interstitial is too high due to the smaller lattice constant when compared to  $\text{CH}_3\text{NH}_3\text{PbI}_3$ . Therefore, the only intrinsic defects in  $\text{CH}_3\text{NH}_3\text{PbBr}_3$  are Pb vacancies.

### 7.3 Polaronic localization in perovskites

The nature of charge carriers in perovskites as quasiparticles, such as polarons, and therefore their intrinsic self-trapping mechanism due to electron-phonon coupling in the lattice, have been investigated in the last year. At first, the hypothesis of having charge carriers as large polarons was introduced to explain the long carrier diffusion length and long lifetimes in polycrystalline thin films.<sup>226</sup> Indeed, in the form of large polarons, charge carriers would be protected from scattering with defects and trapping.<sup>226</sup> The hypothesis that carriers in ionic perovskites would polarize the lattice was later confirmed by Green *et al.*<sup>227</sup> who showed the major impact of polarons in determining the excitonic properties of  $\text{CH}_3\text{NH}_3\text{PbI}_3$  and  $\text{CH}_3\text{NH}_3\text{PbBr}_3$ . In fact, including polaronic effects results in theoretical binding energies, calculated using effective longitudinal optical phonon energies deduced from permittivity measurements, consistent with the experimental values. In a detailed theoretical study, Tretiak *et al.*<sup>50</sup> used hybrid exchange-correlation functional to investigate  $\text{CsPbI}_3$  and  $\text{CH}_3\text{NH}_3\text{PbI}_3$  polaron binding energies. The binding energies obtained suggest formation of small polarons, particularly in the case of the organometallic perovskites. Indeed, for Cs perovskite the binding energies are around 300 and 900 meV for holes and electrons respectively and for HOIP about 600 meV for holes and 1300 meV for electrons (Figure 7.6). This difference is attributed to the molecular rotation degree of freedom of  $\text{CH}_3\text{NH}_3^+$  which can cooperate with the volumetric lattice strain to stabilize the polarons.<sup>50</sup>

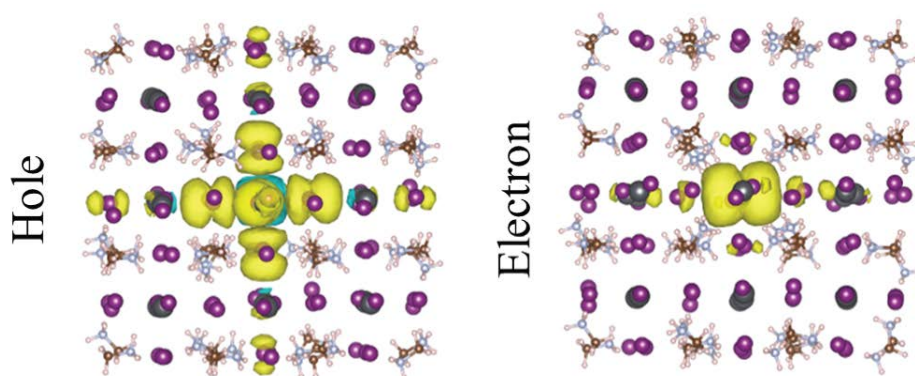


Figure 7.6 - Spin density (total electron density of electrons of one spin minus the total electron density of the electrons of the other spin) calculated for  $\text{CH}_3\text{NH}_3\text{PbI}_3$  clusters using an *ab initio* simulation. Taken from ref.<sup>50</sup>.

These theoretical findings could explain the modest mobilities of charge carriers in HOIP,<sup>228</sup> despite the low charge carrier effective masses and suggest that Cesium based perovskite are potentially better materials for optoelectronic applications.

## 7.4 Stability issues

Although HOIP materials have been able to reach outstanding solar conversion efficiencies after a few years of research, this is of course not the only criterion to assess the performance of a photovoltaic device. Indeed, a critical requirement for a solar cell is the long term stability which ensures a duration of several years for the photovoltaic module. The problem with HOIP became prominent within the last two years, when independent research groups began to find multiple degradation factors.<sup>13,229-234</sup> First of all, HOIP having an ionic structure, it suffers from moisture degradation. In presence of moisture, the first step of decomposition proposed<sup>235</sup> is the deprotonation of  $\text{CH}_3\text{NH}_3^+$  by water, forming methylamine, hydrated HI and  $\text{PbI}_2$ . Elsewhere in the literature<sup>236</sup> is proposed that the exposure of  $\text{CH}_3\text{NH}_3\text{PbI}_3$  to moisture produces hydrate products rather than simply  $\text{PbI}_2$ . Even if the exact mechanism is still under discussion,<sup>230</sup> it is clear that a controlled environment during the synthetic procedure and a well-sealed module during operation is necessary to avoid degradation. Similar precautions of a controlled environment and encapsulation should be applied to avoid oxygen induced degradation.<sup>231</sup> Molecular oxygen reacts with the photoexcited electrons in the perovskite materials forming superoxide ( $\text{O}_2^-$ ) which initiates the degradation process. The reaction of superoxide with the methylammonium moiety of the perovskite rapidly decompose it to methylamine,  $\text{PbI}_2$  and  $\text{I}_2$ . Also UV light can diminish performances of HOIP devices during long-term operation.<sup>13,237</sup> In this case, the hypothesis is that there is an analogy with the photodecomposition process of binary halides (*i.e.*  $\text{PbX}_2$ ,  $\text{X}=\text{Cl}, \text{Br}, \text{I}$ ).<sup>232</sup> Moreover, a severe problem which is harder to be overcome, is related to the limited thermal stability of  $\text{CH}_3\text{NH}_3\text{PbI}_3$ . Initially, it was supposed to be stable up to 300 °C,<sup>238,239</sup> but recent results<sup>240,241</sup> showed that the decomposition temperature is at 140 °C. Considering that standard operating conditions of a solar device are at 80 °C, this is considered a critical issue. It has been observed that substituting the halide from  $\text{I}^-$  to  $\text{Br}^-$  can increase the thermal stability of the HOIP<sup>234</sup> but still this does not fully solve this problem.

Finally, probably the major source of instability is the migration of defects in presence of an electric field.<sup>13,233</sup> Iodine vacancies and interstitials can easily diffuse across the perovskite crystal and migrate to the electrodes. Also  $\text{CH}_3\text{NH}_3^+$  and  $\text{Pb}^{2+}$  vacancies can migrate but with higher activation barriers and therefore on longer time scales. These defects accumulate at the electrodes and modify the electronic landscape hampering charge extraction at the selective contacts.

## 7.5 $\text{CsPbX}_3$ perovskites

Most of the problems leading to limited stability of HOIP are reduced by employing a fully inorganic perovskite. Recently, Kovalenko *et al.*<sup>22,242,243</sup> synthesized monodisperse colloidal quantum dots of fully inorganic cesium lead halide perovskites. Interestingly, the bandgap energy is easily tunable through compositional modulations and quantum size effects over

the entire visible spectral region of 410-700 nm (Figure 7.7). At first, the high photoemission quantum yield of up to 90% suggested applications such as light emitting diode and lasing.<sup>69</sup>

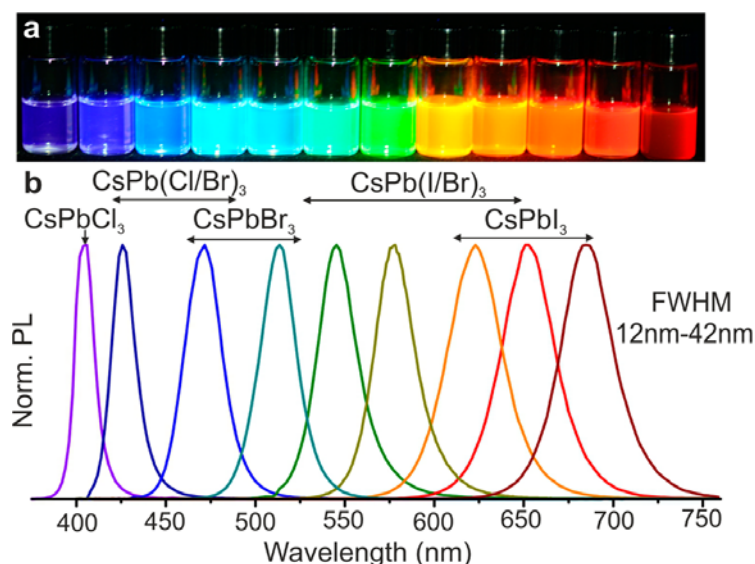


Figure 7.7 - Colloidal perovskite CsPbX<sub>3</sub> nanocrystals (X = Cl, Br, I) exhibit size- and composition-tunable bandgap energies covering the entire visible spectral region with narrow and bright emission: (a) colloidal solutions in toluene under UV lamp and (b) representative PL spectra. Taken from ref.<sup>22</sup>.

For what concerns solar cell application, there was a general belief that the organic cation, either for its organic nature or anisotropic geometry, played an essential role in the high performances of the solar device. Kulbak *et al.*<sup>244</sup> challenged this assumption by demonstrating that the substitution of CH<sub>3</sub>NH<sub>3</sub><sup>+</sup> with Cs<sup>+</sup> does not modify the open circuit voltage of the cell. From that point onwards perovskite solar devices based on Cs started to flourish,<sup>245,246</sup> confirming the intuitive hypothesis of improved stability over the organic counterpart.<sup>247</sup> In particular, the easy bandgap tunability of this material makes it a perfect candidate for tandem solar cell applications.<sup>246</sup> This year, a Caesium-containing perovskite solar cell obtained 21.1% output power, while also demonstrating a record-level reproducibility.<sup>248</sup> Indeed, the addition of inorganic Cesium to formamidinium and methylammonium, results in a triple cation perovskite which is less sensitive to processing conditions.

In this thesis, the physics of CsPbX<sub>3</sub> nanocrystals is investigated by means of ultrafast spectroscopy. The reasons of this choice are in particular the time-resolved x-ray absorption spectroscopy measurements, which require high sample stability because they employ rather high laser fluences. CsPbX<sub>3</sub> is therefore an ideal model system to study the charge carrier dynamics of lead perovskites in general and not only because more stable, but also because presents a similar physics to the organic-inorganic perovskites. In fact, there are many observations which indicate that the hybrid and purely inorganic perovskite bear several similarities: a) photoemission and inverse photoemission studies show that they have similar



electronic structures;<sup>249</sup> b) this is supported by calculations of the electronic band structure of CsPbBr<sub>3</sub> and CsPbCl<sub>3</sub>,<sup>22,249-251</sup> which show similar trends as in the case of organic ones,<sup>25,214,216,252-254</sup> with the VB being dominated by the halide p-orbitals (I 5p, Br 4p or Cl 3p), with a weak contribution of Pb 6s orbitals, while the CB is mainly dominated by the Pb 6p-orbitals. Finally, the orbitals of the cation (methylammonium or Cs) are either far below the maximum of the VB or far above the minimum of the CB; c) both types show high PL quantum yield, which reaches 90% in the inorganic case<sup>22</sup> and 70% in the organic-inorganic case;<sup>70,255</sup> d) transient absorption (TA) studies from the femtosecond to the nanosecond regime also point to an overall similar behaviour of the charge carrier dynamics in organic<sup>256-258</sup> and inorganic ones.<sup>259,260</sup> Therefore, inorganic perovskites represent good model systems for investigating the fate of photoinduced charge carriers of perovskites, while offering great promise of applications in solar energy conversion.



## 8 Femtosecond transient absorption of CsPb(ClBr)<sub>3</sub>

### 8.1 Introduction

The investigation of charge carrier dynamics upon photoexcitation in lead halide perovskites is the key to develop a rational approach for improving devices' performances. Over the last two years, several fs-transient absorption spectroscopy (fs-TAS) studies have been performed, from the IR to the UV spectral region,<sup>10,11</sup> with the aim of understanding the excited state physics of hybrid organic-inorganic perovskites. Despite this interest though, many features in their transient spectra remain still poorly understood.

In general, the most intense feature in the transient absorption spectrum of CH<sub>3</sub>NH<sub>3</sub>PbI<sub>3</sub> corresponds to a decrease in absorption around the bandgap energy (*i.e.*  $\sim 1.6$  eV, 750 nm in Figure 8.1). There is a general consensus that this signal is due to a bleaching which derives from a charge carriers band filling effect that is a direct result of the Pauli exclusion principle.<sup>261</sup> On the other hand, a contribution from stimulated emission which would have the same signal sign, cannot be excluded in that energy region. Wang *et al.*<sup>262</sup> could distinguish an additional shoulder on the low energy side of the main bleaching signal ( $\sim 1.59$  eV), which perfectly overlaps with the static photoluminescence. They have attributed it to stimulated emission but they observed it only when the Stokes shift induced by specific material morphologies was substantial (*i.e.* few tens of meV). In other cases, the stimulated emission and photoinduced bleaching are possibly overlapped in the same transient feature.

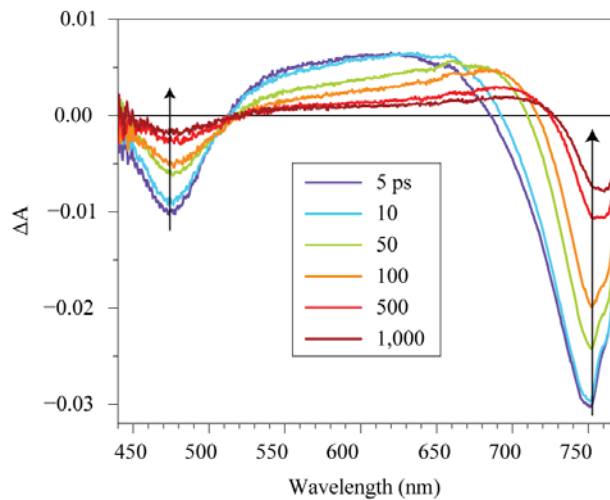
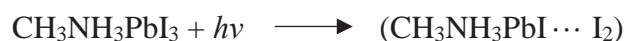


Figure 8.1 - Femtosecond TA spectra of a CH<sub>3</sub>NH<sub>3</sub>PbI<sub>3</sub> film excited at 3.20 eV (387 nm). The arrows indicate the recovery of the bleach signals discussed in the text. Taken from ref.<sup>261</sup>.

At energies above  $\sim 1.70$  eV (about 700 nm and below in Figure 8.1), a broad photoinduced absorption band represented a feature difficult to be interpreted for a few years.<sup>105,261</sup> In 2015, Price *et al.*<sup>62</sup> attributed this signal to a photoinduced reflection due to refractive index changes upon photoexcitation. Indeed, materials with significant values of the refractive index such as perovskites, can undergo an important change in reflectivity upon photoexcitation, which can affect the shape of the fs-transient signal. Recently, this interpretation has been partially challenged by Grancini *et al.*<sup>57</sup>, at least for the photoinduced absorption localized right next to the blue region of the main photobleach ( $\sim 1.67$  eV for  $\text{CH}_3\text{NH}_3\text{PbI}_3$  and  $\sim 2.45$  eV for  $\text{CH}_3\text{NH}_3\text{PbBr}_3$ ). In their interpretation this photoinduced absorption, when present as a well-structured peak, is a fingerprint of the exciton population and derives directly from the self-normalization of the exciton energy due to exciton-exciton interaction.

Another strongly debated energy region, placed at about 2.58 eV for  $\text{CH}_3\text{NH}_3\text{PbI}_3$  ( $\sim 470$  nm in Figure 8.1), shows a transient feature which corresponds to a decrease in absorption upon photoexcitation, where the static absorption spectrum already presents an absorption edge. Xing *et al.*<sup>263</sup>, by comparing the dynamics of this feature and the main photobleach at the bandgap edge, attributed this signal to a second valence band in the material. Wang *et al.*<sup>262</sup> instead, interpreted it as signal deriving from impurities of  $\text{PbI}_2$  which are left in the sample from the synthetic procedure. Indeed, they found a correlation between the presence of  $\text{PbI}_2$  and the intensity of this transient signal. Finally, Stampelcoskie *et al.*<sup>264</sup> provided an interpretation known as the *dual excited state* model. The hypothesis, based on the spectral data analysis of the precursors, is that this spectral feature derives from a charge transfer excited-state which produces reversibly an  $\text{I}_2$ -like species, as in the following reaction:



In the last year, a first principles band structure calculation<sup>265</sup> supported the model of a dual valence band in  $\text{CH}_3\text{NH}_3\text{PbI}_3$ , which is the most accepted one at the moment.<sup>11</sup> Moreover, recently Anand *et al.*<sup>266</sup> revealed a more complex multiband character of the electronic structure, thanks to the extension of the fs-TA studies to the UV range (up to 3.54 eV). Their findings in the UV region require a description beyond the picture with one conduction and two valence band. They could either be explained by adding another valence band or a conduction band state to the previous model of Xing *et al.*<sup>263</sup>.

On the low energy side of the absorption onset, about 50 meV below the main bleaching feature in  $\text{CH}_3\text{NH}_3\text{PbI}_3$ , a photoinduced absorption signal has been recently attributed to bandgap renormalization (BGR)<sup>62</sup> in contradiction to the transient electroabsorption (EA) interpretation given elsewhere in literature.<sup>56</sup> Figure 8.2 shows this transient increase in absorption for  $\text{CH}_3\text{NH}_3\text{PbI}_3$  which clearly persists for only 1 ps. The fact that both explanations are plausible was already suggested in 2014 by Deschler *et al.*<sup>255</sup>. The latter interpretation is based on the fact that an electric field generated within a solid or a molecule can perturb the optical absorption through mechanism such as the Stark effect, which results in a shift of the absorption spectrum. This is supported by the fact that the same feature was recently observed in electroabsorption spectroscopy measurements of  $\text{CH}_3\text{NH}_3\text{PbI}_3$ <sup>267</sup> and

$\text{CH}_3\text{NH}_3\text{PbBr}_3$ <sup>268</sup> (at about 2.30 eV, same energy offset/difference to the bandgap). On the other hand, the BGR interpretation, is supported mainly by the dynamics of the signal which is indeed short living, *i.e.* a few ps.<sup>62</sup> Upon bandgap photoexcitation the high concentration of charge carriers can shift the optical absorption due to many-body exchange-correlation effects. This exchange-correlation correction to the bandgap energy deriving from the presence of free charge carriers is called BGR and it is a many body effect, thus possible only in solids and not in molecular systems.<sup>60</sup> The charge carriers have to interact to produce this effect, therefore their concentration has to be significantly high and the BGR vanishes in a few ps after photoexcitation because of charge carrier recombination.

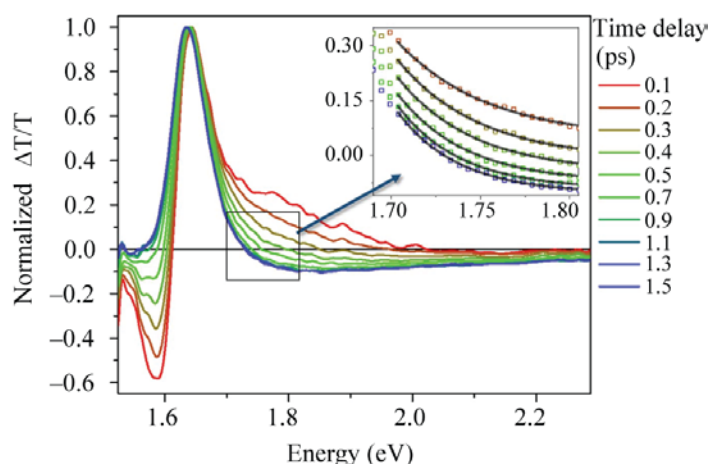


Figure 8.2 - Normalized fs-TA spectra of a  $\text{CH}_3\text{NH}_3\text{PbI}_3$  film excited at 2.25 eV. In the inset, a zoom of the spectral broadening at early times which indicates a hot-carrier distribution. Readapted from ref.<sup>62</sup>.

At lower energies, between  $\sim 1.2$  up to  $0.7$  eV for  $\text{CH}_3\text{NH}_3\text{PbI}_3$ , Sheng *et al.*<sup>269</sup> observed a broad photoinduced absorption signal, labelled here in Figure 8.3 as  $\text{PA}_1$ . This was interpreted as an interband exciton transition, similarly to the interpretation of Deng *et al.*<sup>270</sup> for  $\text{CH}_3\text{NH}_3\text{PbBr}_3$ , where an analogous photoinduced absorption signal was detected in the corresponding energy region with respect to the bandgap position (from  $\sim 1.9$  to  $1.5$  eV). Interestingly, Wu *et al.*<sup>271</sup> investigated  $\text{CH}_3\text{NH}_3\text{PbI}_3$  thin films prepared using different synthetic methods, namely with and without  $\text{PbCl}_2$ , a precursor which is known to improve performances in the photoconversion yield but does not change the stoichiometry or the bulk structure of the material.<sup>272</sup> In both cases, they observed a broad bleaching signal upon photoexcitation in the energy region between  $\sim 1.5$  to  $1.0$  eV, which overlaps with the spectral region where Sheng *et al.* detected the photoinduced absorption. This contradictory observation has been attributed to the formation of a self-trapped band-edge exciton at the material surface, the formation of which could be fostered by the presence of a preexisting band tail for the valence band states. Indeed, the presence of a band tail in these materials was confirmed by the ultraviolet photoemission spectra presented in this study, which clearly showed a tail of states above the valence band, extending to within the gap of the

semiconductor. This tail arises from surface states and therefore its presence could be strongly influenced by the synthetic method adapted.

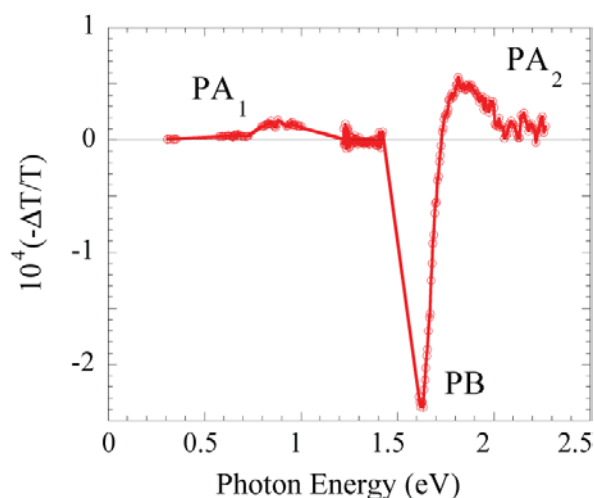


Figure 8.3 - Femtosecond-TA spectrum around  $t = 0$  excited at 3.1 eV (400 nm). In the transient spectrum are highlighted the photoinduced absorptions ( $PA_1$  and  $PA_2$ ) and the main photobleach (PB). Readapted from ref.<sup>269</sup>.

In the mid infrared region, between  $1600$  and  $800\text{ cm}^{-1}$  (*i.e.* from  $\sim 0.20$  to  $0.10\text{ eV}$ ), Narra *et al.*<sup>32</sup> detected a broad photoinduced absorption using a ns-TAS setup. The absorption increases monotonically toward smaller wavenumber and is therefore attributed to intraband transition of free electrons in the conduction band.

In general, the reader might have noticed an apparent contradiction, consisting in the attribution of some feature to excitonic physics and others to free charge carriers. It should be kept in mind, though, that exciton and free charge carriers can co-exist in the same material under certain specific conditions. In fact, the fraction of free charges and excitons is not only determined by the exciton binding energy, but also by the excitation density which influences how often electrons and holes meet to form excitons.<sup>273</sup> Although in  $\text{CH}_3\text{NH}_3\text{PbI}_3$  at room temperature, numerical modelling shows a dominant population of free charge carriers,<sup>273</sup> the coexistence of free charges and excitons has been observed in time-resolved fluorescence measurements,<sup>274</sup> which show an excitation density *vs.* photoluminescence dependence that can only be explained taking into account this effect.

Either way, the most important problem in understanding the room temperature equilibrium between free charge carriers and excitons in hybrid organic/inorganic perovskites, derives from the difficulty in estimating a univocal exciton binding energy. As a matter of fact, the exciton binding energies reported for organic-inorganic perovskites range from  $10$  to  $70\text{ meV}$ .<sup>275-278</sup> These results span around the value of the thermal energy at room temperature (about  $25\text{ meV}$ ). The reason for the difficulty in finding a general accepted value can be found in a recent work from G. Grancini *et al.*<sup>57</sup>. There, they showed the role of the material microstructure in the electron hole interaction and how long range order can control exciton

formation in  $\text{CH}_3\text{NH}_3\text{PbI}_3$  and  $\text{CH}_3\text{NH}_3\text{PbBr}_3$ . This is due to the permanent dipole associated with the methylammonium cation, which - depending on the long-range order in the lattice -, can be more or less free to rotate in the inorganic cage contributing to lattice polarization that screens the electron hole Coulomb interaction. This means that different fabrication procedures and morphologies strongly influence the physics of organic/inorganic perovskites.<sup>57</sup>

Wu *et al.*<sup>12</sup> investigated  $\text{CsPbBr}_3$  quantum dots in solution using fs-TAS upon 3.1 eV excitation and the reported spectra show similar near bandgap transient features than those discussed before in the context of organic/inorganic perovskites. At  $\sim 2.58$  eV ( $\sim 480$  nm in Figure 8.4) there is the main photobleach of the absorption onset, discussed previously for  $\text{CH}_3\text{NH}_3\text{PbI}_3$ .<sup>261</sup> On the low energy side of this transient feature,  $\sim 2.75$  eV ( $\sim 450$  nm in Figure 8.4), is present a broad increase in absorption, attributed to the photoinduced reflection due to refractive index change upon photoexcitation in  $\text{CH}_3\text{NH}_3\text{PbI}_3$ .<sup>62</sup> Only at short time scales ( $< 1$  ps), can be observed the photoinduced absorption feature at  $\sim 2.50$  eV ( $\sim 495$  nm in Figure 8.4) which is contradictorily associated to BGR and transient EA in  $\text{CH}_3\text{NH}_3\text{PbI}_3$ .<sup>255</sup> Finally, a weak and broad photoinduced absorption is present between  $\sim 2.30$  and  $2.07$  eV ( $\sim 540$  and  $600$  nm in Figure 8.4) which is compatible with the interband transitions observed in the transient spectra of organic/inorganic perovskites.<sup>269,270</sup> This correspondence is not surprising though, because - as discussed in chapter 7.5 -, several points indicate strong similarities in the physics of hybrid and Cs based perovskites.

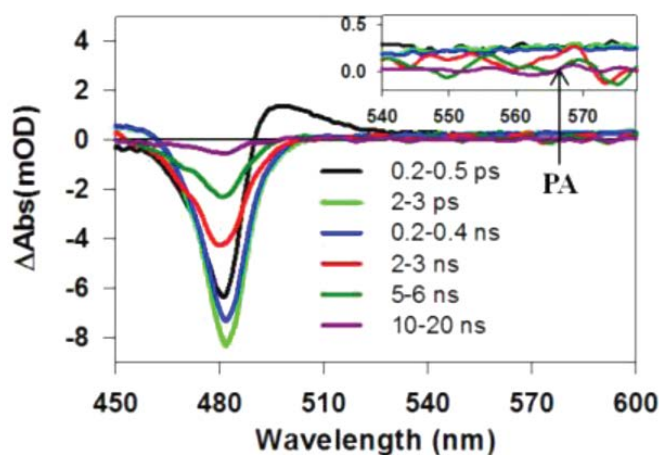


Figure 8.4 - Femtosecond-TA spectra of  $\text{CsPbBr}_3$  quantum dots excited at 3.1 eV (400 nm). In the inset, a zoom of the broad photoinduced absorption (PA) below bandgap energy. Taken from ref.<sup>12</sup>.

As opposed to HOIP, the exciton binding energy of  $\text{CsPb}(\text{ClBr})_3$  (about 50 meV)<sup>22</sup> should unambiguously result in exciton formation, with a minor influence of the structure and the long range order considering the absence of a permanent cationic dipole which could screen the electron hole interaction. Indeed, as showed by several photoluminescence studies,<sup>38,279-281</sup> fully inorganic lead halide perovskites exhibit a long-lived band-edge emission (*i.e.* up to several ns) which is due to the recombination of excitons. This means that there is an

unambiguous exciton presence in this material which has a lifetime over the time window explored in the present chapter. Studying fully inorganic perovskite has some advantages. In fact, the high sensitivity of hybrid perovskite to external environmental factors (*e.g.* humidity),<sup>13</sup> sample handling and experimental conditions during data acquisition<sup>11</sup> makes the interpretation of the spectroscopic results challenging. Indeed, Sum *et al.*<sup>11</sup> urged the community "to exercise caution" because the uncontrolled sources of damaging could easily influence the results in the fs-TAS measurements. Cs-perovskites in general do not suffer from stability problems, as mentioned in chapter 7.5.

## 8.2 Results and discussion

### 8.2.1 Investigation of the transient spectral features

Here, it is described the physics of a fully inorganic perovskite, CsPb(ClBr)<sub>3</sub>, upon photoexcitation at 3.1 eV, using fs-TAS with a white light continuum probe spanning from 3.1 to 1.8 eV (details in chapter 3.1.1). Therefore, this chapter mainly deals with spectral features in the low energy region of the bandgap position, because the material studied has a bandgap of  $\sim 2.6$  eV. This energy region has rarely been explored in the literature, because most of the studies have been performed on CH<sub>3</sub>NH<sub>3</sub>PbI<sub>3</sub> (bandgap energy of  $\sim 1.6$  eV) and thus would require the use of a near infrared probe, instead of the most common whitelight probe, to investigate the physics in this part of the spectrum.

To mitigate possible laser-induced damaging, the suspension is recirculated using a flow cell and a peristaltic pump which refreshes the sample at each laser shot. In Figure 8.5 absorption and emission spectra demonstrate the stability of this material upon bandgap irradiation.

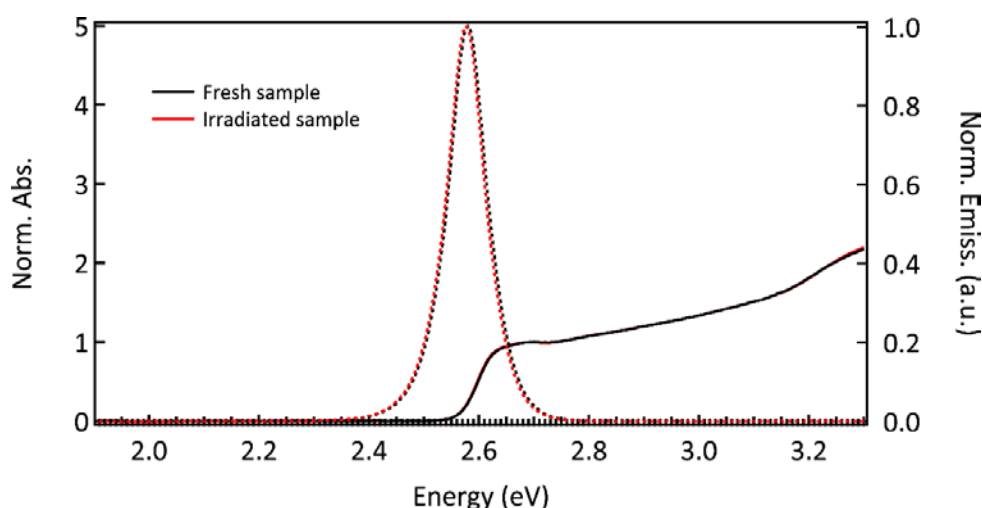


Figure 8.5 - Photoluminescence (dotted curves) and absorption (solid curves) spectra before (black curves) and after (red curves) about 30 hours of laser irradiation at 3.1 eV, 1 kHz and different fluences between 2.5 and 100  $\mu\text{J}/\text{cm}^2$ . The absorption spectrum is normalized around 2.6 eV to compensate for the change in concentration due to the evaporation of the solvent.



These conditions allow a systematic study of the excitation fluence dependence that helps revealing the nature of the different spectral features. Therefore, measurements at 7 different excitation fluences were performed (Figure 11.1 appendix, chapter 11).

The transient absorption spectra of  $\text{CsPb}(\text{ClBr})_3$  at 18 and 100  $\mu\text{J}/\text{cm}^2$  are shown respectively in Figure 8.6a and b and for the different fluences at 300 fs and 1 ns delay in Figure 8.7a and b. In order to have a structured discussion of the different transient features, the spectra are divided in four different energy regions. This division has just the functional reason of simplifying the discussion but, as it will be shown in the following lines, the different spectral features are not independent from each other but strongly correlated. In region 1 (red in Figure 8.6 and Figure 8.7, from 1.75 to 2.4 eV) there is a weak photoinduced absorption ( $\text{PA}_1$ ) which shows minor spectral changes in the 1 ns probe window.

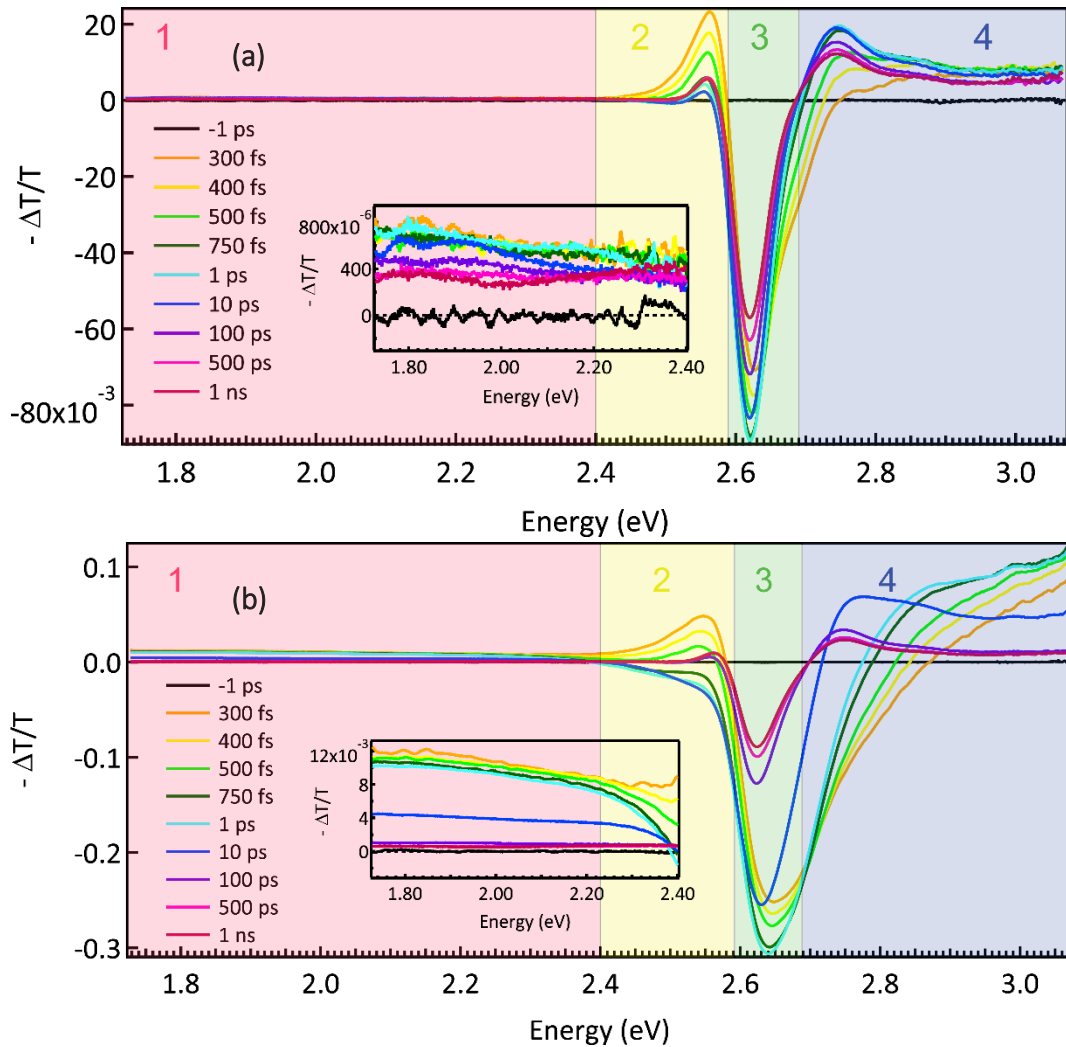


Figure 8.6 - Femtosecond transient spectra at different time delays upon photoexcitation at 3.1 eV with a fluence of 18 (a) and 100  $\mu\text{J}/\text{cm}^2$  (b). The spectra are divided in four energies regions, numbered from 1 to 4 in order of increasing energy, to aid the discussion of the different transient features. The inset shows a zoom into signal  $\text{PA}_1$  in region 1.

Region 2 (yellow, from 2.4 to 2.59 eV) instead, is characterized by extremely complex dynamics which see first a photoinduced absorption (PA<sub>2</sub>) followed by a photobleaching signal (PB<sub>2</sub>) and finally a long lived photoinduced absorption (PA<sub>i2</sub>). Feature PB<sub>2</sub> is not observed for fluences < 37  $\mu\text{J}/\text{cm}^2$ . In region 3 (green, from 2.59 to 2.69 eV) there is the strongest transient feature which is a photobleaching (PB<sub>3</sub>) where the main dynamics consist in a decay and a broadening which are influenced by the excitation fluences. Finally, region 4 (blue, from 2.69 to 3.07 eV) contains a photoinduced absorption signal that persist up to 1 ns. In particular, PA<sub>4</sub> refers to the positive peak with a maximum at  $\sim 2.75$  eV.

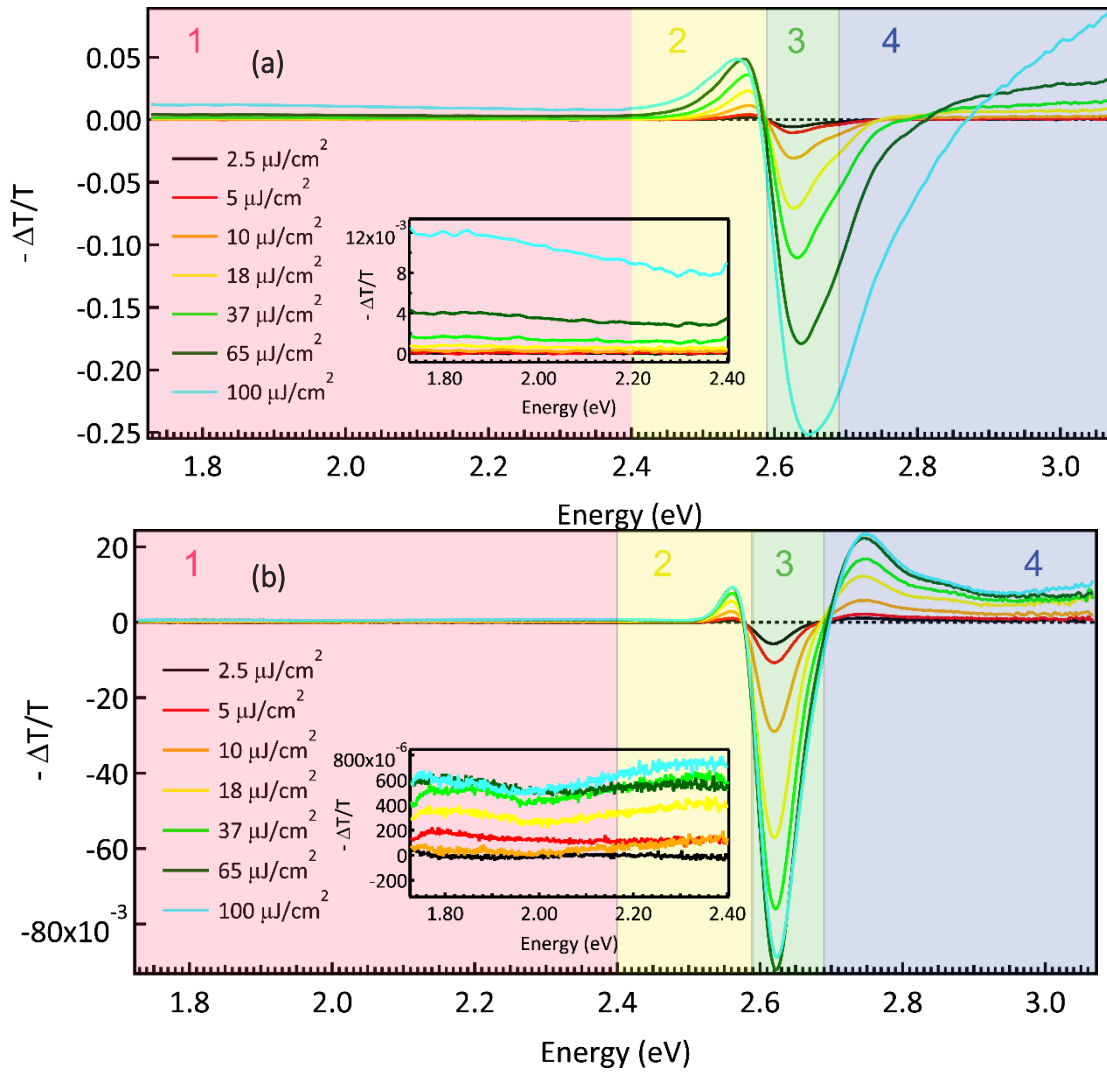


Figure 8.7 - Fluence dependence of the transient spectra at 300 fs (a) and 1 ns (b) after photoexcitation at 3.1 eV . The inset shows a zoom into signal PA<sub>1</sub> in region 1.

At early time delays and pump fluences  $\geq 10$   $\mu\text{J}/\text{cm}^2$ , the low energy side of region 4 overlaps with the initially broad PB<sub>3</sub> signal which leads to the photobleaching signal PB<sub>4</sub>.

The first feature that is analyzed is the broad photoinduced absorption  $PA_1$ , in the spectral region 1, which has been clearly observed also in the case of  $CsPbBr_3$  NCs.<sup>282</sup> This transient feature is very weak in intensity (maximum  $\sim 4\%$  of the main bleach peak around 2.62 eV) and therefore at the limit of the signal to noise ratio for fluences  $\leq 10 \mu J/cm^2$  (Figure 11.2 appendix, chapter 11). In general, this low energy side of the bandgap has been poorly investigated in the case of  $CH_3NH_3PbI_3$  as mentioned above. Here, in contrast to the findings of Wu *et al.*<sup>271</sup> on  $CH_3NH_3PbI_3$ , an increase in absorption is observed upon photoexcitation, which was assigned to a transition of the photo-generated excitons to higher energy states in hybrid organic inorganic perovskites.<sup>269,270</sup> Indeed, the probe light in this energy region does not have enough energy to explore transitions across the optical gap and therefore can only promote intraband transitions. A similar broad photoinduced absorption tail has been observed in other semiconductors, namely CdSe QDs<sup>283</sup> and  $PbI_2$  films<sup>260</sup> where it was also associated with intraband transitions. This broad spectral feature is structureless in  $CsPb(ClBr)_3$  for the energy region explored apart from the fact that  $-\Delta T/T$  decreases with the energy probed, as apparent at high fluences (Figure 8.7a inset). This tendency might evoke a Drude like absorption typical of free charge carriers, but the expected quadratic relation between energy probed and  $-\Delta T/T$  is definitely not observed.

A more intense photoinduced absorption signal ( $PA_2$ ) is found on the low energy side of the bandgap at about 2.56 eV. This sub-bandgap transient absorption feature has been recently observed in  $CH_3NH_3PbI_3$ , at the corresponding energy of 1.6 eV, and attributed to BGR.<sup>62</sup> Indeed, the photoinduced charge carriers can cause a shrink of the bandgap resulting in a shifted joint density of states (JDOS).<sup>77</sup> In the present results, this transient feature appears immediately after photoexcitation and decays within a few picoseconds. Since a hot-carrier distribution occupies fewer states at the now lowered band edge than a cooler carrier distribution, a signal decrease is expected as the carrier temperature reduces over time.<sup>62</sup> The gradual occupation of the normalized energy states can potentially lead to a bleach of this transient signal,<sup>62</sup> and this is clearly visible in our data for fluences  $\geq 37 \mu J/cm^2$  ( $PB_2$ ). Increasing the fluence, not only results in clear bleach of this feature at about 1 ps delay, but also an increasing width of  $PA_2$  toward the low energy side (Figure 8.7a). This indicates that increasing the charge carrier density increases the magnitude of the shift in the JDOS. The nature of the  $PB_2$  was not extensively discussed in the work of Price *et al.*<sup>62</sup> but the energy position and the fact that is observed only above certain carrier densities is reminiscent of a biexciton stimulated emission. Biexciton emission has been observed through photoluminescence (PL) measurements<sup>38</sup> in  $CsPbBr_3$  NCs at 10 K and high fluences (*viz.* 14 mJ/cm<sup>2</sup>) but has never been detected in transient absorption spectra. The energy separation between bandgap and biexciton emission under those experimental conditions was about 50 meV, which is compatible with the feature position observed here (about 70 meV). In the PL measurements performed on  $CsPb(ClBr)_3$  NCs (chapter 9), there is evidence for a similar biexciton contribution to the emission dynamics as in  $CsPbBr_3$ .<sup>38</sup> Unfortunately, in the measurements on  $CsPb(ClBr)_3$  the lack of femtosecond time resolution and/or low temperature prevents an unambiguous determination of the spectral position of the bi-exciton

emission, and a comparison with the ultrafast time dynamics presented in this chapter. As mentioned in the introduction, the BGR is just one of the possible interpretations found in the literature for PA<sub>2</sub>. Indeed, Trinh *et al.*<sup>56</sup> attributed the shift of the JDOS in CH<sub>3</sub>NH<sub>3</sub>PbI<sub>3</sub> to a transient EA effect. This derives from the electric field of hot charge carriers which is proportional to the excess energy and therefore, while hot carriers cool down, the intensity of this signal decreases as well. For the data collected here, BGR and transient EA would both explain the results of the short lived PA<sub>2</sub> feature.

Interestingly, for all fluences investigated, a photoinduced absorption feature (PA<sub>2</sub><sup>i</sup>) appears after 1 ps or hundreds of ps (delay proportional to the pump fluence) and persists unchanged until 1 ns. Although BGR can potentially explain the short lived feature as well as the transient EA effect, BGR cannot explain a nanosecond signal because it is a short lived process, being related to high charge carrier densities.<sup>62</sup> Moreover, the shape and peak position (maximum at 2.560 eV) of this feature is the same at all fluences (spectral region 2 in Figure 8.7b) in contrast to the PA<sub>2</sub> signal. Therefore, even if both features fall in a similar energy region, PA<sub>2</sub><sup>i</sup> has to have a different physical nature than PA<sub>2</sub>. In these spectra, the long lived PA<sub>2</sub><sup>i</sup> can be attributed to a photoinduced transient EA effect, which - as discussed below -, is generated by the electric field of the excitons. Indeed, as it will be shown, the appearance of this feature corresponds to formation of excitons in the material.

The most prominent feature in absolute intensity is the photoinduced-bleach at about 2.62 eV (PB<sub>3</sub>), basically the bandgap energy of the material. This feature has been extensively discussed in earlier studies and assigned to band filling effects.<sup>255,261</sup> Similarly to CH<sub>3</sub>NH<sub>3</sub>PbI<sub>3</sub>,<sup>261</sup> we observe a fluence dependent blue-shift and broadening of this negative peak, which indicates charge carrier accumulation. Indeed, by increasing the fluence the charge carrier density in the bands increases and as direct result of the Pauli exclusion principle optical transitions slightly above the band gap energy are more and more depleted.<sup>261</sup> In the spectra there are no signs of a Stokes-shifted stimulated emission from the band edge exciton, which up to date could be seen only by Wang *et al.* in CH<sub>3</sub>NH<sub>3</sub>PbI<sub>3</sub> films.<sup>262</sup> Figure 8.8 presents the fluence dependence of PB<sub>3</sub>, PA<sub>1</sub> and PA<sub>2</sub> at 300 fs delay. In the excitation density region explored, PB<sub>3</sub> (measured at 2.620 eV) shows a roughly linear dependence, while PA<sub>1</sub> (measured at 1.800 eV) increases exponentially due to the change in shape as discussed above (namely that  $-\Delta T/T$  becomes inversely proportional to the energy probed); PA<sub>2</sub> (measured at 2.516 eV) instead saturates because of the broadening at high fluence which shifts spectral weight in the low energy region.

Feature PB<sub>3</sub> extends into region 4 where its tail decays quickly to give place to PA<sub>4</sub>. Reproducing the tail of PB<sub>3</sub> (from 2.770 eV to 3.040 eV) using a Maxwell-Boltzmann distribution allows to estimate the temperature of the charge carriers.<sup>62,77</sup> The equation used has the form:

$$\frac{\Delta T}{T} = A \cdot \exp\left(-\frac{\hbar \cdot \omega}{k_b \cdot T_e}\right) - B$$

in which  $T_e$  represents the extracted temperature of the charge carriers at a given time delay,  $\hbar \cdot \omega$  is equal to the probe energy and  $k_b$  is the Boltzmann constant.

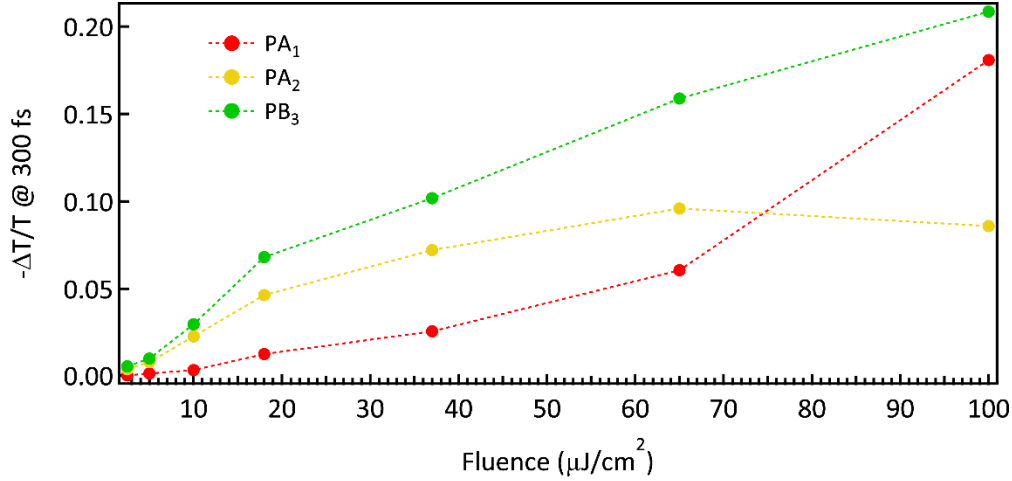


Figure 8.8 - Intensity of the transient signal at 1.800 (PA<sub>1</sub>), 2.561 eV (PA<sub>2</sub>) and 2.620 eV (PB<sub>3</sub>) upon photoexcitation at 3.1 eV and 300 fs of time delay. In order to have all the signals graphically comparable, PA<sub>1</sub> is multiply by 15, PA<sub>2</sub> is multiply by 2 and PB<sub>3</sub> is multiply by -1.

Figure 8.9 shows the results of these fittings at 100  $\mu\text{J}/\text{cm}^2$  fluence. Repeating such an analysis for all fluences between 18 and 100  $\mu\text{J}/\text{cm}^2$  yields the temperature decays depicted in Figure 8.10.

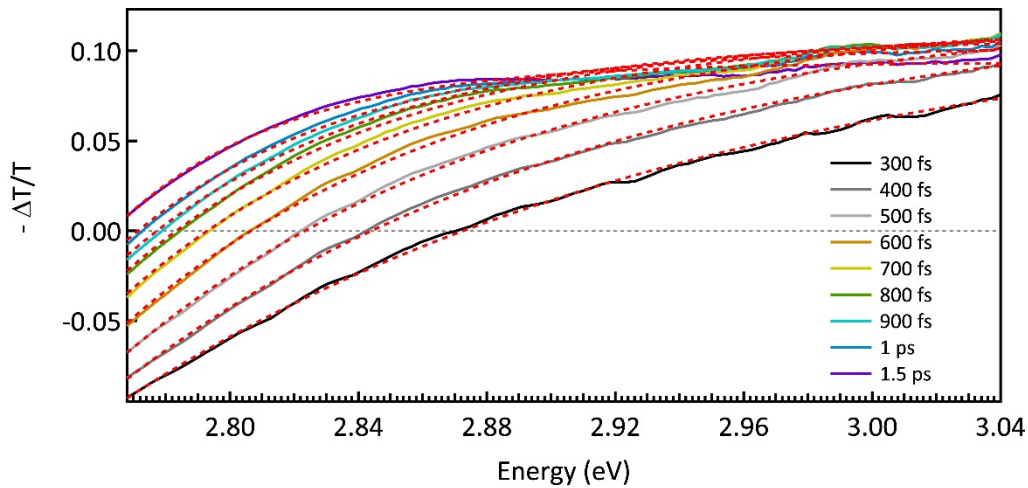


Figure 8.9 - Results of the fit (red dotted curves) at different time delays for the fluence of 100  $\mu\text{J}/\text{cm}^2$ , using a Maxwell-Boltzmann distribution to extract the temperature of the charge carriers in the high energy region of PB<sub>3</sub> (*i.e.* from 2.770 eV to 3.040 eV). The quality of the fit reduces at higher time scales because PA<sub>4</sub> contributes increasingly to the signal.

Although the appearance of PA<sub>4</sub> hinders the use of Maxwell-Boltzmann distribution above 1 ps for fluences < 100  $\mu\text{J}/\text{cm}^2$ , these results show a trend of slower cooling rate with higher carrier densities, as already seen for hybrid organic-inorganic perovskites.<sup>62,77</sup> The reduction of the cooling rate with fluence increase is due to a hot phonon bottleneck effect, which occurs when a high phonon emission rate in presence of high carrier density results in a non-equilibrium phonon population.<sup>77</sup> In this case, the excess of hot phonon population increases the phonon reabsorption, reducing the net thermalization rate.<sup>77</sup> Yang *et al.*<sup>77</sup> associated this effect with the poor coupling between optical and acoustic phonons, which does not allow the dissipation of excess energy.

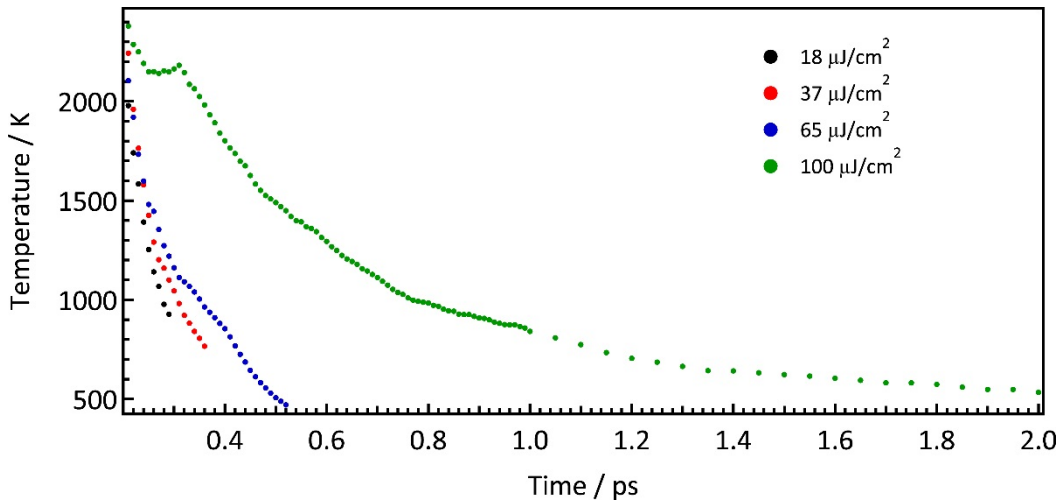


Figure 8.10 - Temperature decays of charge carriers upon photoexcitation at 3.1 eV with different fluences. The temperature is extracted by reproducing the high energy side of PB<sub>3</sub> (from 2.770 to 3.040 eV) with a Maxwell-Boltzmann distribution but the fittings are hindered above certain time delay, which depends on the fluence, due to the appearance of PA<sub>4</sub>.

In CH<sub>3</sub>NH<sub>3</sub>PbI<sub>3</sub> films a feature corresponding to the positive peak PA<sub>4</sub> has recently been assigned to self-normalization of the exciton energy, which causes a blueshift of the exciton absorption band due to exciton-exciton interactions.<sup>57</sup> For this reason, its rise can be considered as the fingerprint of exciton formation in the material.<sup>57</sup> A similar many body effect on the optical spectrum was already been observed in two-dimensional lead iodine quantum wells<sup>56</sup> as a result of the mutual exciton-exciton interaction which renormalizes the exciton self-energy. PA<sub>4</sub> and therefore the exciton formation is present at all fluences explored (not surprisingly, considering the exciton binding energy of about 50 meV)<sup>22</sup> but is delayed as the fluence increases. This is due to the phonon bottleneck, because the probability of a direct transition from very hot pairs of charge carriers to exciton is very small.<sup>284</sup> Indeed, the electron-hole pairs are excited with about 0.5 eV of excess energy and the interaction between electron-hole pairs to form an exciton from free charge carriers created upon photoexcitation is likely to take place after the charge carriers have relaxed to the edges of their bands. This observation is the key to explain the present results.



To paraphrase, a transition between free charge carriers to excitons at a time scale which is controlled by the fluence via the phonon bottleneck is observed. 3.1 eV excitation produces only free charge carriers at short time scales which form excitons on longer time scales, namely after relaxation in the bands. The transient spectrum in Figure 8.6b shows that PA<sub>2</sub> (which stems from BGR or a transient EA effect) and a long blue tail of the photobleach due to band filling are present at 300 fs. As soon as PA<sub>4</sub> forms, the EA feature on the low energy side (PA<sub>1</sub>) is also present since both arise from the excitons generated in the material.

At 18  $\mu\text{J}/\text{cm}^2$  this transition takes place in about 1 ps and the dynamics of PA<sub>1</sub>, PB<sub>3</sub> and PA<sub>4</sub> are identical (Figure 8.11a). This indicates that these features are probing the transition between the same state, namely the exciton. By contrast, these features have different rates in the first tens of ps at 100  $\mu\text{J}/\text{cm}^2$  as Figure 8.11b shows.

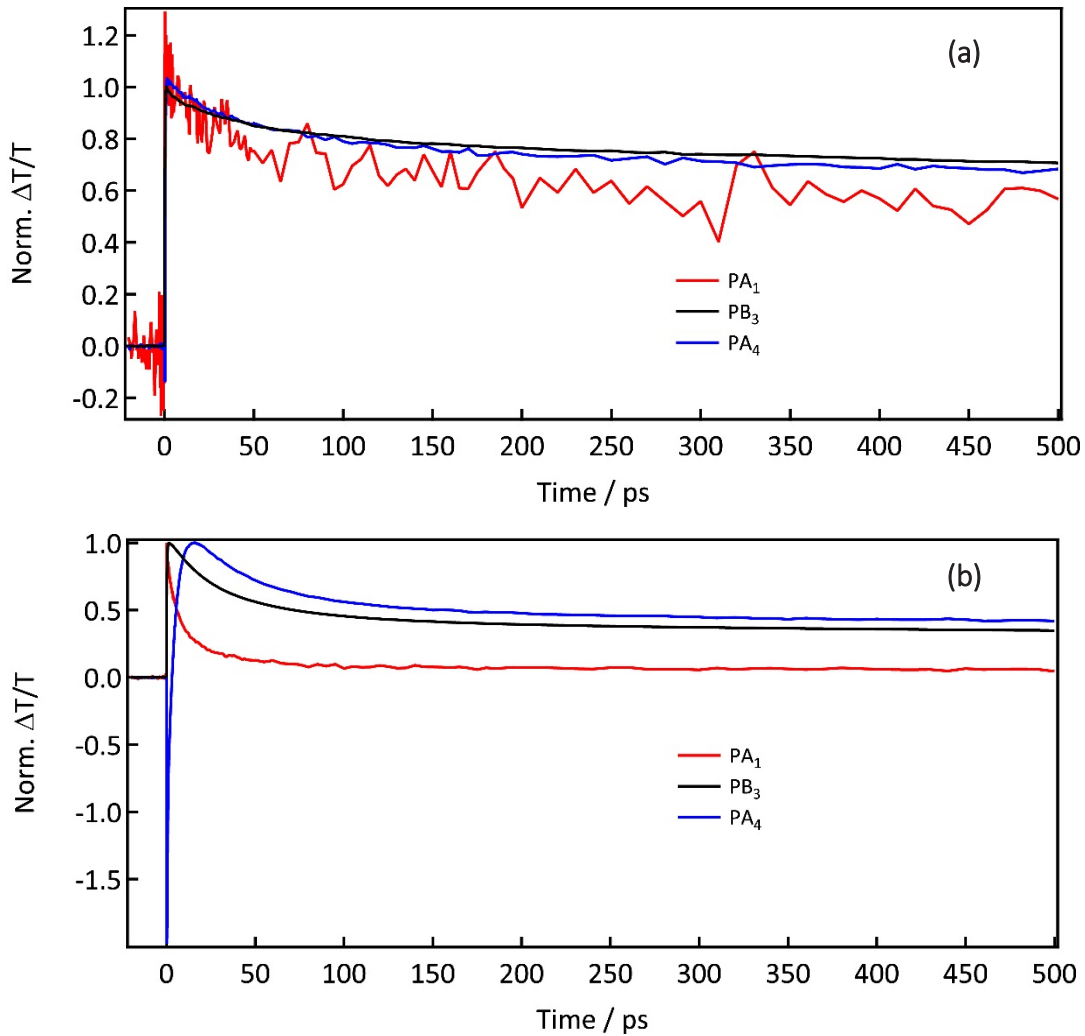


Figure 8.11 - Kinetic traces upon photoexcitation at 3.1 eV with 18 (a) and 100  $\mu\text{J}/\text{cm}^2$  (b) measured at 1.800 eV (PA<sub>1</sub>, red curve), 2.620 eV (PB<sub>3</sub>, black curve) and 2.746 eV (PA<sub>4</sub>, blue curve).

This difference in dynamics between 18 and 100  $\mu\text{J}/\text{cm}^2$  is due to the delayed appearance of the excitonic feature PA<sub>4</sub> at high fluence. Indeed, while there is a delayed PA<sub>4</sub> at 100  $\mu\text{J}/\text{cm}^2$ , this is not the case for the photobleach PB<sub>3</sub>, which reflects free charge carriers in addition to excitons.

In Cs perovskites, as well as in the hybrid organic/inorganic ones, the exciton is assumed to be of a Wannier-Mott type, considering the rather moderate exciton binding energy.<sup>22,57</sup> This exciton, as the Frenkel one, does not possess a static dipole moment in bulk materials, which is necessary to create the electric field that gives rise to the transient EA signal PA<sub>i2</sub> observed in these measurements. Dipole moments of excitons in semiconductor nanostructures have been found since the '80s,<sup>285</sup> and derive from the quantum confinement of electrons and holes. Indeed, the different confining potentials in various spatial directions for electrons and holes, lead to a spatial separation of the electron and hole wave function which provides a permanent dipole to the material.<sup>286</sup> In the case of the NCs investigated here, a quantum confinement is not expected because the exciton Bohr radius is estimated to be between 7 and 5 nm,<sup>22</sup> but the particle size of the sample is 12 nm. Therefore, in principle, the mechanism discussed above should not take place here. In molecular and ionic crystals, the formation of a charge-transfer (CT) exciton is a source of an electric field because it possess a static dipole moment.<sup>287,288</sup> Indeed, this exciton has electron and hole separated in two different spatial position after transfer of an electron from a donor site to an acceptor site. The radius of a CT exciton is in-between a Frenkel and Wannier-Mott one.<sup>289</sup> The formation of this species is also common at interfaces, thus its understanding is essential in the development of excitonic solar cells where the charge separation is needed at the donor/acceptor interface.<sup>36</sup> In the sample used here, the suspension is stabilized through a mixture of oleyamine and oleic acid. The surface interactions between these molecules and the CsPbBr<sub>3</sub> interface was recently investigated by De Roo *et al.*<sup>290</sup>. From their work, emerges a rather complex surface chemistry where an oleyammonium cation binds to surface bromide through electrostatic interaction and the oleate anion binds to the surface Cesium or Lead ions (Figure 8.12). Considering the high surface-to-volume ratio of these samples, a significant density of interfacial CT exciton, which could arise from a transient charge transfer of an electron and/or hole to these organic molecules, cannot be excluded. These transient species could have an analogy to those investigated by Wu *et al.*<sup>12</sup> in CsPbBr<sub>3</sub> quantum dots with electron and hole acceptors. In order to rule out any effect related to quantum confinement or the interfacial formation of a CT exciton, bulk crystal of Cs perovskites should be investigated using fs-TAS.

Finally, there is a case in which an exciton could carry a permanent dipole moment that is independent on the size of the sample and therefore more intrinsic to the material. Self-trapped excitons can give rise to an asymmetric distribution of charge carrier density due to the localization of electron and hole in different spatial position through the interaction with the surrounding lattice. Particularly for CsPb(ClBr)<sub>3</sub> NCs, the formation of a weakly localized exciton has been revealed using ps x-ray absorption spectroscopy (chapter 9), where a small polaron hole and delocalized electron are coupled through Coulomb interaction.



Unfortunately, the significantly different experimental conditions (*viz.* the highest fluence used here is about 2 orders of magnitude lower than the fluence of the x-ray experiment and different excitation energies were used) do not allow for a direct comparison of the decay dynamics to corroborate this hypothesis.

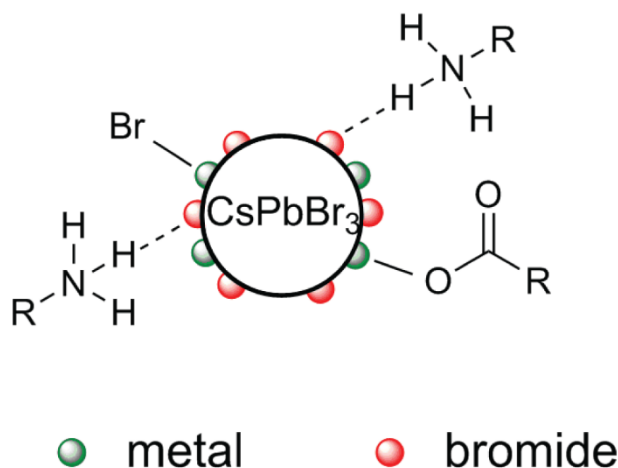


Figure 8.12 - Schematic of the interfacial interaction between CsPbBr<sub>3</sub> NCs and the organic molecules in solution. The oleylammonium cation binds to surface bromide, probably through a hydrogen bridge, and it donates one electron to the nanocrystal-ligand bond. The bromide or oleate anion binds to the surface Caesium and Lead ions.

Anyhow, whichever excitonic mechanism is acting to generate the electric field in this NCs, EA must be invoked to explain the photoinduced absorption feature PA<sub>i2</sub> which lasts for over 1 ns in the transient spectra.

### 8.2.2 Investigation of the temporal dynamics

For investigating the time scales involved in the different processes, a global fitting for fluences  $\geq 18 \text{ uJ/cm}^2$  (lowest fluence with sufficient S/N in all the spectral regions to make reliable fits) has been performed, using 23 time traces for each map (Figure 8.13). To reproduce the kinetic traces, at least 6 exponential decay functions are needed, which are convoluted with the instrument response function (IRF) of this setup (100 fs FWHM). Moreover, to give similar weight to the different spectral regions and reproduce correctly also the time scales of the low energy region (*i.e.* region 1), the intensity of these 3 time traces (*i.e.* energy of 1.80, 2.00 and 2.20 eV) is multiplied by 15, a multiplication factor which brings their intensity on the same order of magnitude of all the other kinetic traces.

Table 8.1 reports the resulting time constants which in the light of the previous discussion can be easily interpreted. Additionally, to further support the interpretation, Figure 8.14 shows the decay associated spectra (DAS) obtained from the global fitting amplitudes for 18 and 100  $\mu\text{J/cm}^2$ . It should be considered that the interpretation and analysis of DAS with time

dependent spectral shifts caused by energetic relaxation processes is challenging,<sup>291</sup> therefore in this work DAS have only used to support the previous findings.

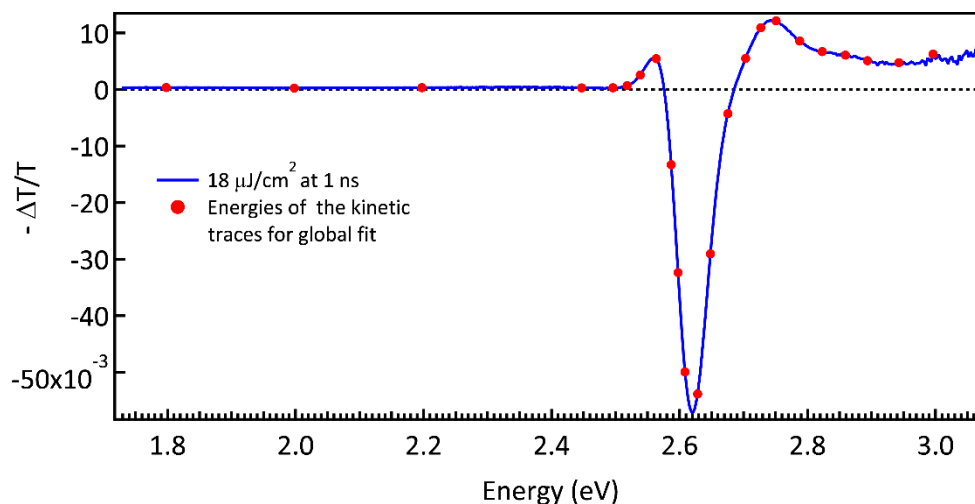


Figure 8.13 - Transient spectrum at 18  $\mu\text{J}/\text{cm}^2$  and 1 ns reporting the 23 energies (red dots) chosen for the global fit of the dynamics.

Table 8.1 – Time constants in ps resulting from the global fitting over the entire spectral map for the different fluences. In order to reproduce correctly the data is used a 6 exponential function convoluted with the IRF of 100 fs.

Fluence ( $\mu\text{J}/\text{cm}^2$ )	$\tau_1$	$\tau_2$	$\tau_3$	$\tau_4$	$\tau_5$	$\tau_6$
18	<0.1	0.22	1.60	46.2	865	> 1000
37	<0.1	0.24	4.42	41.7	149	> 1000
65	<0.1	0.21	4.64	19.3	65.7	> 1000
100	<0.1	0.34	5.63	18.7	80.3	> 1000

The first time constant ( $\tau_1$ ) is well below the IRF and mostly reproduces nonlinear artefacts. For this reason, it is not reported in the DAS. The second time constant ( $\tau_2$ ) is about 200 fs for all fluences and is assigned to carrier cooling due to carrier-carrier scattering, in analogy with the results on  $\text{CH}_3\text{NH}_3\text{PbI}_3$ .<sup>260</sup> This cooling process corresponds spectrally to the redshift of PB<sub>3</sub>, which was discussed previously, as it is clearly shown by the black traces in Figure 8.14. The third time constant ( $\tau_3$ ) instead, varies from 1.6 to 5.6 ps and increases with the fluence. It can be attributed to carrier-phonon scattering. Indeed, the cooling process is

directly affected by the phonon bottleneck which slows down the cooling of charge carriers with increasing carrier density *i.e.* with the fluence which is exactly what is observed here.<sup>260</sup> The cooling basically corresponds to the exciton formation in the material. Figure 8.14 shows indeed, the formation of the PA<sub>4</sub> at  $\sim 2.75$  eV which is an excitonic finger print. The other two time constants ( $\tau_4$  and  $\tau_5$ ) systematically decrease with the increase of the fluence, which is the typical behavior of Auger recombination. The reversal of  $\tau_5$  between  $100 \mu\text{J}/\text{cm}^2$  and  $65 \mu\text{J}/\text{cm}^2$  is within the uncertainty of the fit. This would imply that the fluences investigated here using a global fitting are in an Auger regime. Also Figure 8.14 does not show particularly complex dynamics for these DAS, which basically resemble the transient at those time delays indicating a simple decay of intensity for the different spectral features.

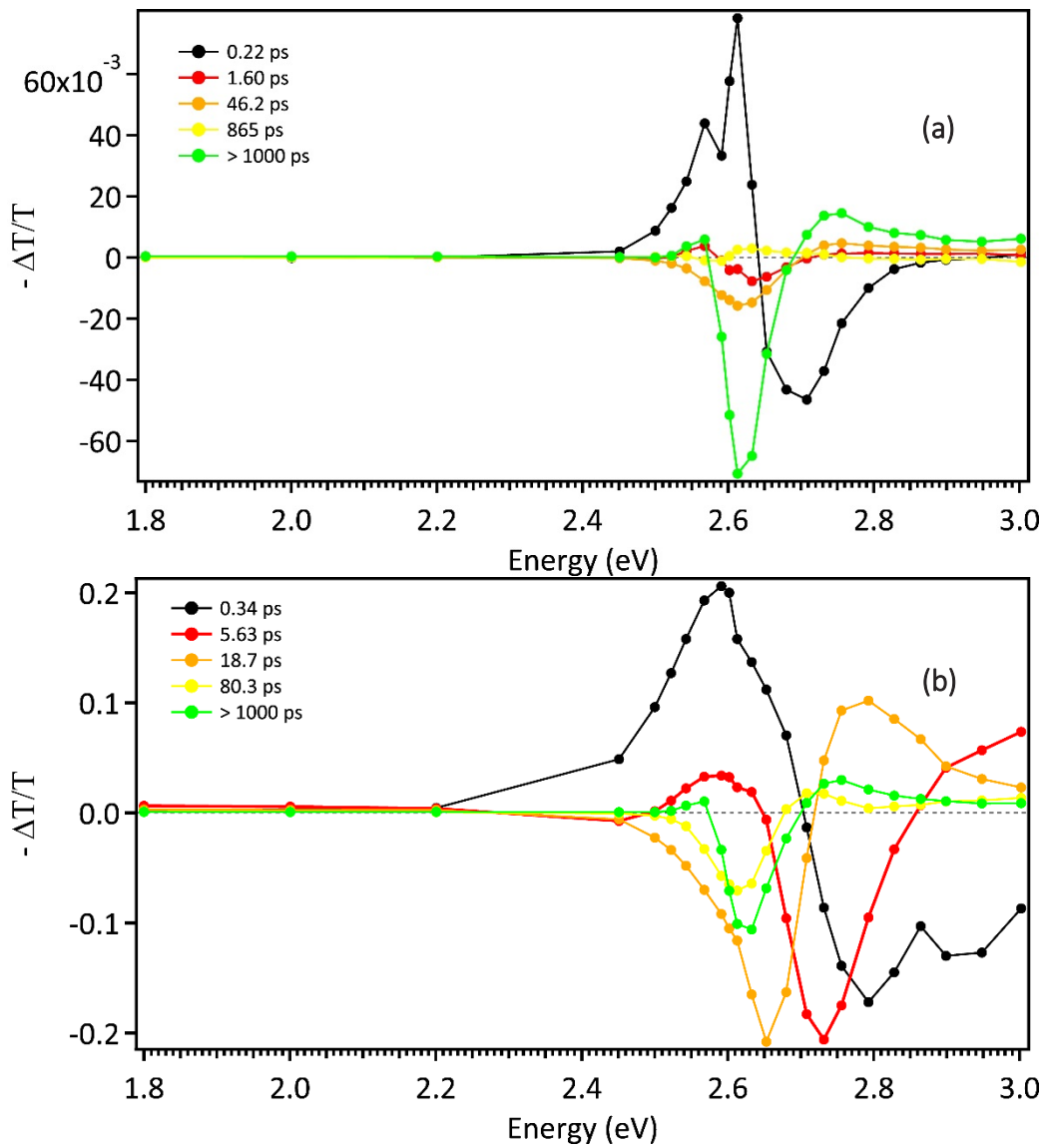


Figure 8.14 - Decay associated spectra for the data at 18 (a) and  $100 \mu\text{J}/\text{cm}^2$  (b).

To investigate the recombination mechanism at the band edge of the semiconductor a similar strategy as that of Manser *et al.*<sup>261</sup> is used. Plotting the normalized kinetic traces of PB<sub>3</sub> (at 2.620 eV) as  $(\Delta T/T)^{-1}$  can help to distinguish between purely excitonic recombination (which has linear behavior) and three-body-Auger recombination. The recovery kinetics for the bandgap recombination, thus the recovery of PB<sub>3</sub>, can be modelled using a rate equation of the type:

$$-\frac{dn}{dt} = An + Bn^2 + Cn^3$$

Where  $n$  is the photogenerated carrier density at time  $t$ . In this equation, the first term represents trap state mediated recombination, the second-order term is exciton or free charge carrier recombination and the third is the three body Auger recombination.<sup>261</sup>

Excluding the data at 2.5 and 5  $\mu\text{J}/\text{cm}^2$  which are linear (Figure 8.15), an increase that behaves as a function of  $\sqrt{t}$  is observed which can be explained as Auger recombination.<sup>261</sup> The observation of Auger recombination in CsPb(ClBr)<sub>3</sub> NCs is in contrast to the dominant bimolecular deactivation observed in CH<sub>3</sub>NH<sub>3</sub>PbI<sub>3</sub> at relatively high fluences by different authors.<sup>261,292</sup> Piatkowski *et al.*<sup>292</sup> investigated the recombination mechanisms at different fluences in hybrid organic/inorganic perovskite finding that CH<sub>3</sub>NH<sub>3</sub>PbI<sub>3</sub> does not show Auger recombination at the same fluence in which FAPbI<sub>3</sub>, where FA stands for the formamidinium cation, shows to be strongly influenced by this mechanism. From this observation is clear that the recombination processes in lead halide perovskites are strongly influenced by the nature of the cation.

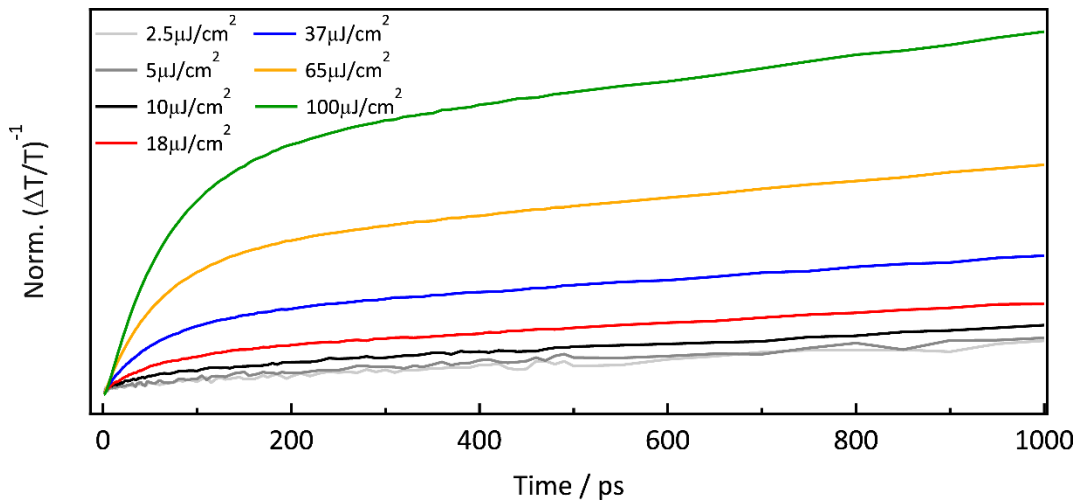


Figure 8.15 - Normalized kinetic traces for different fluences at the energy of 2.620 eV (around the maximum of PB<sub>3</sub>) in  $(\Delta T/T)^{-1}$ . The linear behavior over time is shown only at 2.5 and 5  $\mu\text{J}/\text{cm}^2$  and for the other fluences the growth is proportional to  $\sqrt{t}$  indicating that Auger recombination is the primary process.

Finally,  $\tau_6$  is longer than the probed time window in our measurements (*i.e.* 1 ns) and is likely due to geminate recombination, considering that the fluorescence in this material last for several nanoseconds.<sup>22</sup> The green DAS of Figure 8.14 in this case simply resemble the transient spectra at 1 ns, indicating this last decay.

### 8.3 Conclusions

To conclude, in this work the exciton formation in  $\text{CsPb}(\text{ClBr})_3$  NCs upon photoexcitation at 3.1 eV is mapped in real time. This has been possible thanks to a systematic study about the effects of the fluence on the photoinduced dynamics. Indeed, significant charge carrier density together with an excess energy are able to sensibly delay the Coulombic interaction between electrons and holes due to the phonon bottleneck and therefore slow down the process of exciton formation in the material. Thanks to this observation, the apparent contradiction in the interpretation of a photoinduced absorption feature on the red side of absorption onset, which was previously attributed to BGR and transient EA, has been solved. In fact, although the short lived signal (*i.e.* few ps) could arise from both these effects, the long lived one (*i.e.* up to 1 ns) is due to transient EA generated by the exciton electric field. Three hypothesis on the nature of this exciton are made in order to explain the presence of a permanent dipole leading to EA: a quantum confinement effect; a CT exciton at the interface due to the presence of the organic ligands; a self-trapped exciton which presents a non-symmetric charge distribution. The first two could be simply ruled out by the fs-TAS investigation of a bulk material, such as single crystal. The last hypothesis though, is at the moment the most likely, because a weakly localized exciton has been observed in  $\text{CsPb}(\text{ClBr})_3$  NCs using ps-XAS (chapter 9). These findings are an important step in the general understanding of the ultrafast physics of perovskites. Moreover, this work highlights the presence of a dominant Auger recombination process at relatively high fluence, in contrast to the results on  $\text{CH}_3\text{NH}_3\text{PbI}_3$ . This different behavior, which is strongly influenced by the cation nature, becomes significant in the use of lasing devices in which this material is the active medium. It is not of importance for solar cell applications, where the charge carrier density is well below the one where Auger recombination is present in the data.



## 9 Picosecond x-ray absorption and photoluminescence of $\text{CsPbBr}_{3-x}\text{Cl}_x$ nanocrystals

### 9.1 Introduction

In this chapter the charge carrier dynamics of  $\text{CsPbBr}_3$  and  $\text{CsPb}(\text{ClBr})_3$  nanocrystals (NCs) is investigated using ps-XAS and time-correlated single photon counting (TCSPC). Both techniques have a comparable time resolution, in the order of hundreds of ps (see chapter 3 for details), and aim at probing complementary aspects of the charge carriers' fate. As highlighted for the case of  $\text{TiO}_2$  (chapter 5 and 6), time resolved XAS is an extremely sensitive tool to map the localization of electrons and holes. Time resolved photoluminescence instead, is a suitable method to observe radiative processes due to free charge carriers, excitons, biexcitons and self-trapped excitons or trap states in general.  $\text{CsPbX}_3$  NCs are chosen for their high stability, which is a required condition for time-resolved synchrotron studies, but besides this, they share a similar physics with the hybrid organic-inorganic perovskites (details in chapter 7.5).

Despite the intense interest in organic-inorganic perovskites over the last years, a clear understanding of the fate of the photoinduced charge carriers still remains limited. Lead halide perovskites, as discussed in chapter 7, exhibit a sharp absorption onset at the optical band edge, with a small extension of the Urbach tail ( $\sim 15$  meV)<sup>293,294</sup>, a long carrier lifetime and low non-radiative losses<sup>255,295</sup> (photoluminescence quantum yield  $>70\%$ )<sup>70,255</sup>, all elements pointing to a low density of traps<sup>221</sup> ( $\sim 10^{10} \text{ cm}^{-3}$  in single crystals).<sup>296-298</sup> However, the charge carrier mobilities in organic-inorganic perovskites are rather modest,<sup>228</sup> at least 1 order of magnitude lower for the electrons than in materials such as Silicon or Gallium Arsenide, and this could be related to the suggested formation of polarons (details in chapter 7.3). Furthermore, as far as applications are concerned, understanding the recombination dynamics of photogenerated charges is important, and in particular, to which extent exciton or free carriers recombination dominates. In general, photovoltaic materials require efficient separation of photocarriers and the exciton binding energies ( $\sim 10$ -70 meV), reported for organic-inorganic perovskites,<sup>275,276,299</sup> are on the same order of magnitude as the room temperature (RT) thermal energy, raising the question whether the excited states dissociate into free carriers or recombine as excitons. This fundamental question also relates to the issue whether transport of energy occurs by free carriers or by a bound exciton that later dissociates into free carriers at heterojunctions.<sup>300-302</sup>

Photoluminescence studies have been performed to address these questions, but with contrasting results. In refs<sup>303-306</sup>, the RT PL was attributed to exciton recombination but this was based on indirect evidence, while in ref.<sup>276</sup>, it was attributed to free carrier recombination, arguing that excitons generated by low-density excitation are almost fully ionized at RT since

the binding energy is comparable to the RT thermal energy.<sup>11,299,16</sup> Recently, He *et al.* suggested that the RT PL is due to weakly localized excitons, while they observed the free carriers emission at higher energies under high fluences.<sup>307</sup> They suggested that the weakly localized excitons are due to band tail states, presumably arising from the disorder introduced by the organic cation. These excitons can be either partly localized (one charge carrier is localized with the other carrier bound to it by Coulomb attraction) or fully localized (both charge carriers are localized).

To clarify the issue of charge localization or lack thereof, a tool is needed that is site-sensitive and/or element specific and can probe the system at RT. Electron paramagnetic resonance (EPR) has been used to determine charge localization in solar materials<sup>154</sup> but it requires low temperatures (LT). Shkrob *et al.*<sup>308</sup> studied CH<sub>3</sub>NH<sub>3</sub>PbI<sub>3</sub> and CH<sub>3</sub>NH<sub>3</sub>PbBr<sub>3</sub> samples irradiated at 355 nm by EPR LT (< 200 K) and reported localization of holes at the organic cations and of the electrons at Pb<sup>2+</sup> centres. Formation of clusters along with a change of color of the crystal surface during the measurements suggests that the samples were undergoing radiation damage. Aside from these considerations, EPR lacks the time resolution that would help identify the formation and evolution of charge carriers (*e.g.* trapping at defects or via coupling to phonons, etc.).

In this chapter, the fate of photoexcited charge carriers in inorganic Cs-based perovskites is probed by ps-XAS. The aim is to identify the charge localization or its absence in the photoexcited sample by monitoring each of the actors involved: the Br, the Pb and the Cs atoms. In the latter case, one of the important questions is to assess the role that the cation plays (if it does) in the charge carrier dynamics. In order to address these issues, ps-XAS (*viz.* 80 ps resolution) at the Br K-edge (near 13.474 keV), the Pb L<sub>3</sub>-edge (near 13.035 keV) and the Cs L<sub>2</sub>-edge (near 5.359 keV) of CsPbBr<sub>3</sub> and CsPb(ClBr)<sub>3</sub> perovskite NCs<sup>22</sup> excited at 3.5 eV (experimental details in chapter 3.2.2 and 3.4.2) is implemented. Moreover, TCSPC measurements are performed under similar experimental conditions (details in chapter 3.3.1), to investigate the fluorescence dynamics and compare them with the results of the ps-XAS studies, in order to get a complementary point of view. Here, the main open question which can aid to interpret the data of ps-XAS is: does the decay dynamics in the x-ray measurements correspond to the one observe in the photoluminescence experiment? Finally, the use of these two perovskites aims at exploring the effect of halide substitution. As seen in chapter 8, CsPb(ClBr)<sub>3</sub> is a material with a band-gap energy and an exciton binding energy between those of the pure bromide and pure chloride Cs-based perovskites (the stoichiometric composition is about two Br<sup>-</sup> ions to one Cl<sup>-</sup>).

In the next sections, the results of the XAS and photoluminescence measurements will be presented independently. A final interpretation, which aims at reconciling the findings of these two techniques, will be discussed in a separate section.



## 9.2 Results and discussion

As a preliminary step to all the measurements in this chapter, a systematic study of the stability upon 355 nm irradiation at 260 kHz was performed for  $\text{CsPb}(\text{ClBr})_3$  in toluene, using a free flowing liquid jet. These are the same experimental conditions used for the x-ray absorption measurements and are similar to the photoluminescence experiment, where the only difference is the repetition rate of the laser (*i.e.* 82 kHz, details in chapter 3). When comparing UV-Vis absorption and photoluminescence spectra recorded before and after 30 minutes of laser irradiation, an irreversible blue shift of the absorption and the emission is observed at fluences above 30  $\text{mJ}/\text{cm}^2$ , which can therefore be considered as the damage threshold (Figure 9.1).

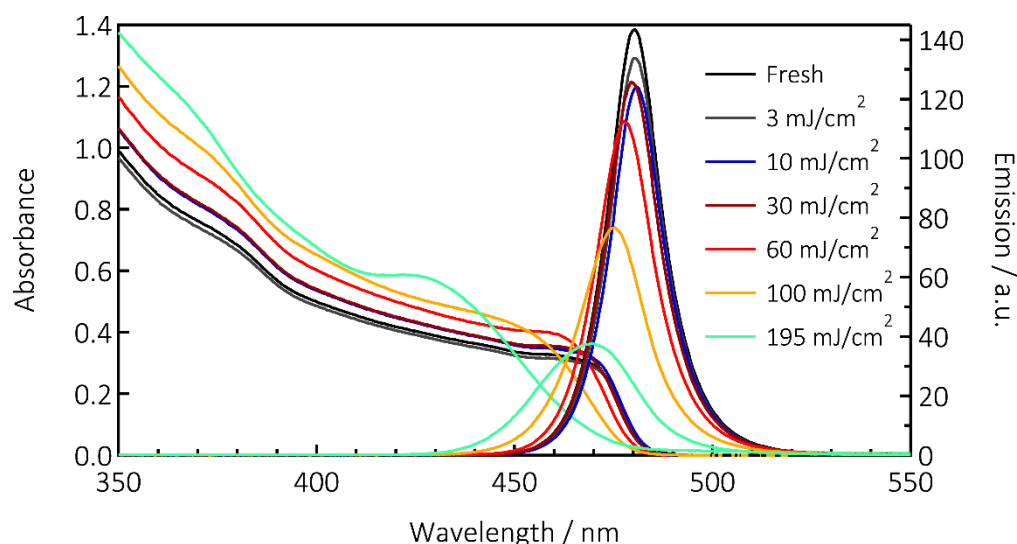


Figure 9.1 - Photoluminescence and absorption spectra after 30 minutes of laser irradiation at 355 nm and 260 kHz using different fluences for  $\text{CsPb}(\text{ClBr})_3$  NCs. The changes observed in the optical properties of the samples are irreversible.

Therefore, all the measurements in this work have been performed at a maximal fluence of 15  $\text{mJ}/\text{cm}^2$ . After 12 hours of ps-XAS measurements of  $\text{CsPb}(\text{ClBr})_3$  at 15  $\text{mJ}/\text{cm}^2$  no change in the absorption and emission spectra was observed (Figure 9.2), which confirms that negligible damage has incurred to the samples. A small difference in the absorption spectrum is observable for  $\text{CsPbBr}_3$  (Figure 9.2), which appears as a change in the scattering properties of the sample but, this change does not affect the XAS spectra (Figure 11.3 appendix, chapter 11) and is therefore of no importance to this study.

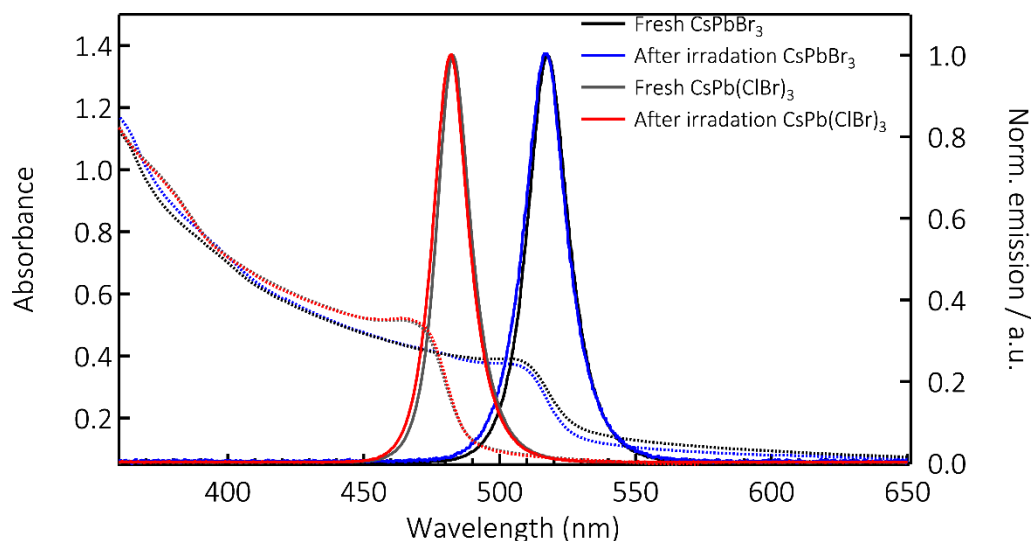


Figure 9.2 - Absorption spectra (dotted) and photoluminescence spectra (full lines) of CsPb(ClBr)<sub>3</sub> (grey and red traces) and CsPbBr<sub>3</sub> (black and blue traces) NCs. The same spectra are shown after >12 hours of laser irradiation at 355 nm, 260 kHz rep. rate and a fluence of 15 mJ/cm<sup>2</sup>.

### 9.2.1 X-ray absorption spectroscopy at Br K-edge, Pb L<sub>3</sub>-edge and Cs L<sub>2</sub>-edge

In this section the nature of the photoinduced changes observed at each atomic edge using ps-XAS will be discussed. As a general reminder, in XAS spectra a change of oxidation state is commonly manifested by a shift of the edge energy position (*i.e.* the ionization potential for the atomic core orbital in question), which increases or decreases in energy depending, respectively, on whether the atom has been oxidized or reduced.<sup>309</sup> However, the origin of the edge shift contains other causes, *e.g.* the type of ligand and the bond distance between the atom of interest and its neighbors.<sup>310-312</sup> Photoinduced structural changes will therefore have a direct impact on the edge, even in the absence of an oxidation state change.<sup>313,314</sup> Since the above-edge transitions probe the unoccupied density of states above the Fermi level, a reduction of intensity right above the edge reflects the filling of unoccupied states, similar to the band filling found in optical studies of semiconductors.<sup>315</sup>

Figure 9.3 shows the steady state Br K-edge absorption spectrum of CsPb(ClBr)<sub>3</sub> and CsPbBr<sub>3</sub> NCs detected in partial fluorescence yield (PFY) mode. They are basically identical but somewhat different to those reported for organic CH<sub>3</sub>NH<sub>3</sub>PbBr<sub>3</sub> perovskites<sup>316</sup> in the sense that in the latter, the above-edge feature at about 13.49 keV is more intense than the edge feature at about 13.47 keV (Figure 9.3). Interestingly, the Br K-edge absorption spectrum of the Br<sup>-</sup> ions in the present samples is quite similar to that of the aqueous Br<sup>-</sup>.<sup>317</sup> Since Br<sup>-</sup> has a fully filled 4p<sup>6</sup> valence orbital, the signal is entirely due to above edge transitions into the ionization continuum with the x-ray absorption near-edge structure (XANES) modulations rapidly damping out. Figure 9.4 shows the transient Br K-edge spectra (difference spectrum of the x-ray absorbance of the excited minus the unexcited sample) of CsPb(ClBr)<sub>3</sub> and CsPbBr<sub>3</sub>, recorded 100 ps after laser excitation.

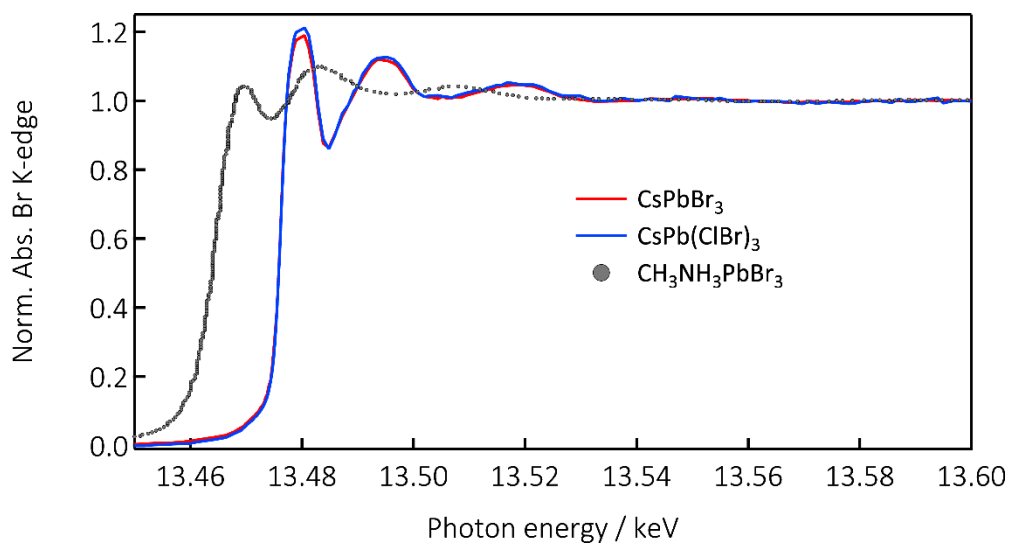


Figure 9.3 - PFY x-ray absorption spectra at the Br K-alpha emission near the edge region of CsPbBr<sub>3</sub> (red trace) and CsPb(ClBr)<sub>3</sub> (blue trace) NCs. In grey dots the TFY x-ray absorption spectrum of CH<sub>3</sub>NH<sub>3</sub>PbBr<sub>3</sub> NPs at the Br K-edge taken from ref.<sup>316</sup>.

Transient XAS were recorded in total fluorescence yield (TFY) detection mode.

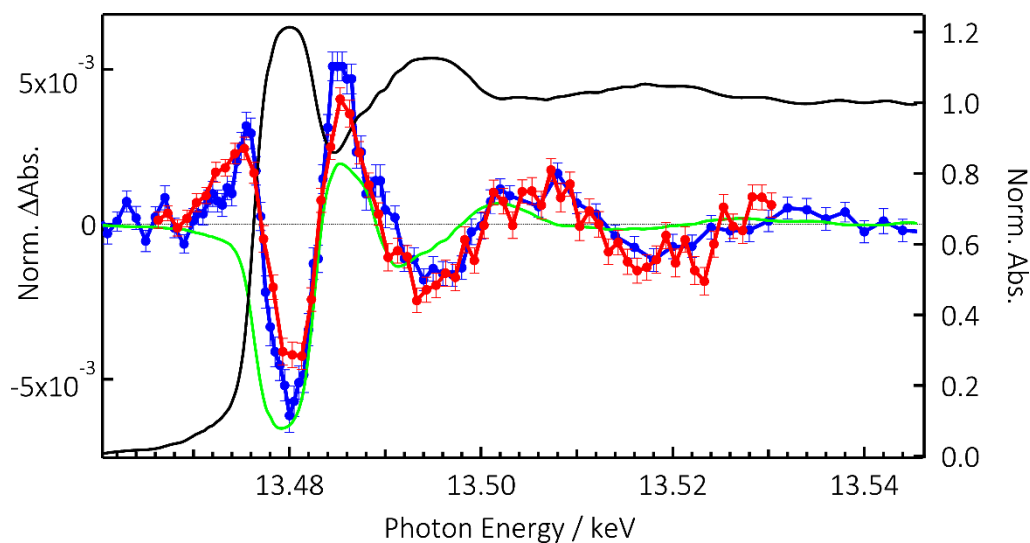


Figure 9.4 - PFY x-ray absorption spectrum of CsPb(ClBr)<sub>3</sub> at the Br K-edge (black trace) with transients at 100 ps of CsPb(ClBr)<sub>3</sub> (blue trace) and CsPbBr<sub>3</sub> (red trace) excited at 355 nm with 15 mJ/cm<sup>2</sup>. The transients were recorded in total fluorescence yield (TFY) detection mode. The green trace represents the difference of the steady state spectrum (black trace) shifted by +5 eV minus the unshifted steady-state spectrum.

The two transients exhibit the same profile, though with somewhat different amplitudes, showing an increased absorption below and above (around 13.485 keV) the edge and a decreased one at the edge (13.480 keV). At higher energies, clear modulations are also

appearing. As can be seen from Figure 9.5 the transients are identical at 100 ps and 1 ns time delay, to within error bars.

In the present systems, as mentioned in chapter 7, the VB is dominated by the halogen np orbitals (in the present case Br 4p or Br4p/Cl3p) and to a lesser extent, by the Pb 6s orbitals.<sup>22,216,249,251,252</sup> The holes created in the VB upon photoexcitation can either be delocalized or become localized at defects or a regular lattice site via a self-trapping process. In the case of delocalization, only a tiny fraction of the charge would be “felt” by each atom and no edge shift would be detected. In the case of localization, the removal of a full or partial electron charge, *i.e.* the localization of a full or partial hole charge, would turn the bromide to Br<sup>0</sup>(4p<sup>5</sup>) (case of a full charge) leading to an edge shift to higher energies. In addition, this would open a channel for the 1s-4p transition that lies just below the edge. This behavior of the XAS transients has been reported after electron abstraction of photoexcited aqueous Br<sup>-</sup> at the K-edge<sup>317</sup> and aqueous I<sup>-</sup> at the L<sub>1</sub>-edge.<sup>318</sup> It is reproduced here with the resonance at 13.477 keV attributed to the 1s-4p transition, while the minimum at 13.48 keV and the maximum at 13.486 keV are typical of a first derivative-like shape due to a blue shift of the edge.

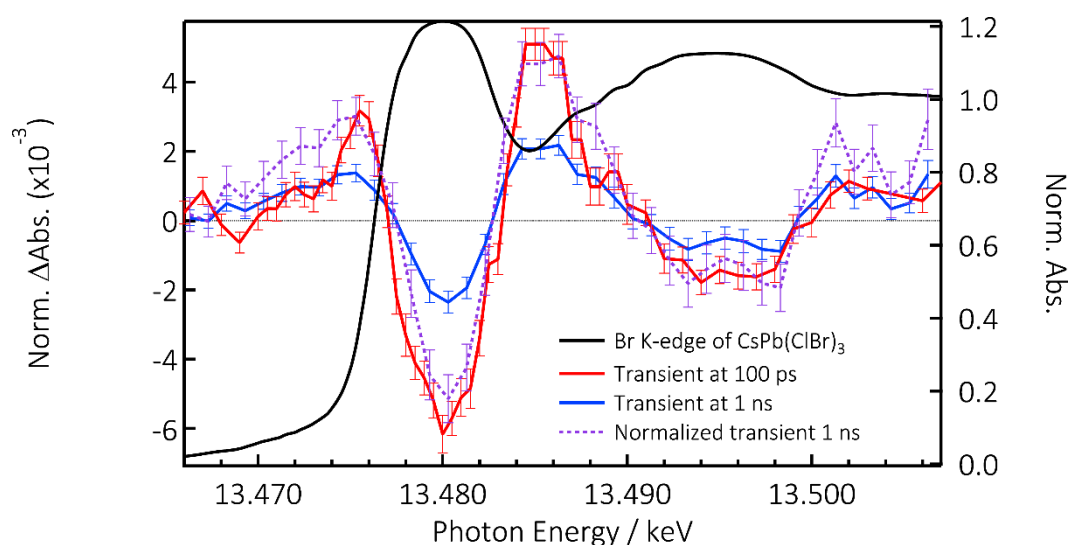


Figure 9.5 - PFY x-ray absorption spectrum of CsPb(ClBr)<sub>3</sub> NCs at the Br K-edge (black trace) with the transient spectra at 100 ps (red trace), 1 ns (blue trace) and 1 ns normalized to the 100 ps intensity (violet dotted trace).

An estimate of the magnitude of the photoinduced blue shift of the Br K-edge (Figure 9.4) can be made by taking the difference of the blue-shifted ground state spectrum minus itself. This approach works quite well, as demonstrated in the case of photoionized halides in aqueous solutions,<sup>317,318</sup> charge transfer in metal complexes,<sup>319,320</sup> and charge trapping in colloidal TiO<sub>2</sub> nanoparticles (chapter 6). However, it neglects the other sources of edge shifts mentioned above, such as structural changes, nor does it account for the changes in the occupancy of orbitals below the edge, which correspond to the pre-edge (bound-bound)

transitions. Bearing in mind these limitations, the difference spectra are simulated for shifts of +1 to +8 eV, which are compared to the experimental transient in Figure 9.6. The PFY spectrum (Figure 9.3) was used to simulate these differences because the wide energy range explored allows a fine pre- and post-edge normalization.

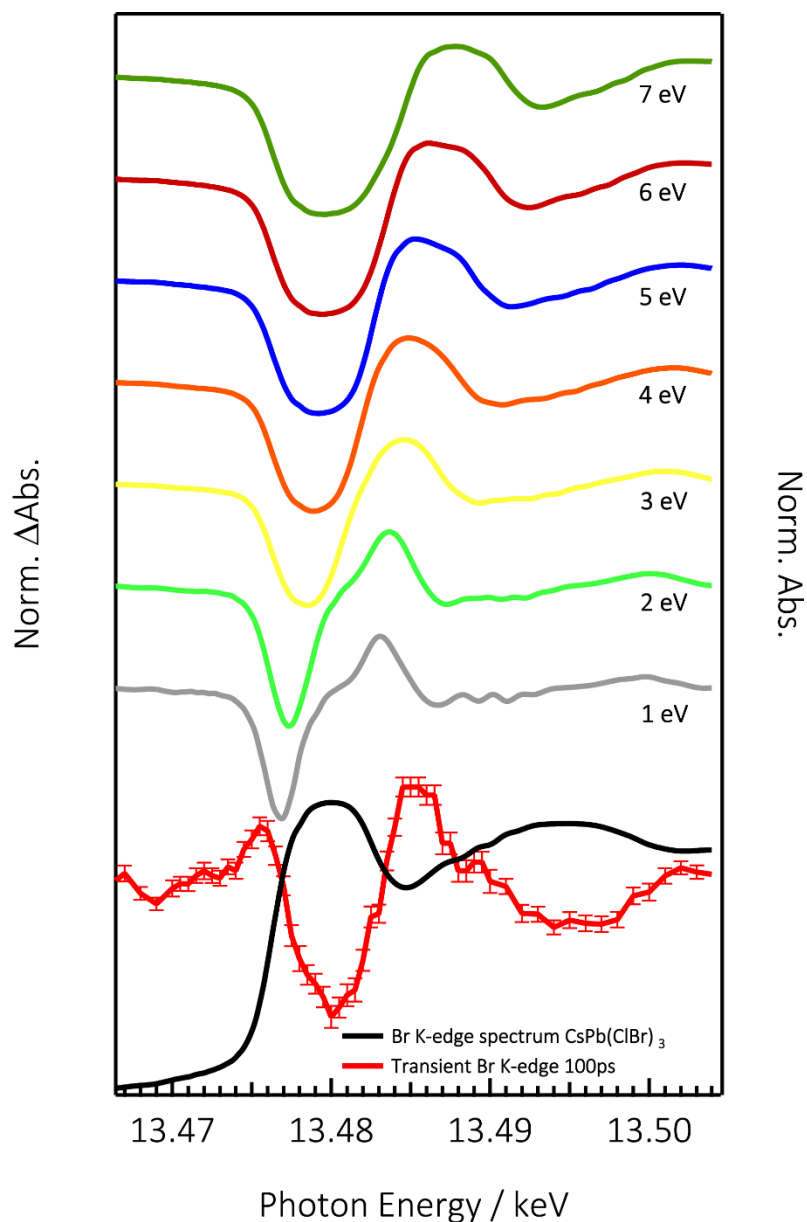


Figure 9.6 - PFY x-ray absorption spectrum of  $\text{CsPb}(\text{ClBr})_3$  NCs at the Br K-edge (black trace) with the transient at 100 ps upon photoexcitation at 355 nm (red trace) and calculated difference spectra of the ground state spectrum minus the unshifted one for different values of the shift (1 to 8 eV, different offsets on the graph). The difference spectra have been rescaled with factors between 0.05 and 0.006 in order to best match the intensity of the experimental negative transient feature at 13.480 keV.

However, since the transients were recorded in TFY mode (chapter 3.2.2), this may cause an additional source of deviation between the experimental transients and calculated difference spectra. Although none of the difference spectra really satisfactorily matches the first derivative-like shape between 13.48 and 13.49 keV, the 5-6 eV shift is the best at capturing the 13.48 keV to 13.485 keV region. In the case of aqueous bromide turning to neutral bromine upon electron abstraction, Elles *et al.*<sup>317</sup> reported an edge shift of ~5 eV, which is close to the present value. It should be stressed again that the deviations below 13.48 keV (appearance of the 1s-4p resonance around 13.475 keV) cannot be accounted for in the difference spectra. Also, the deviations above 13.485 keV are due to structural changes in the environment of Br<sup>-</sup> ions after they have been oxidized. The Br K-edge has been reported to be particularly sensitive to the chemical environment and undergo significant edge shifts depending on its environment, even without a change of the oxidation state.<sup>310-312</sup>

The appearance of the 1s-4p resonance at 13.475 keV and the estimated oxidation shift of ~5 eV both point to a full positive charge localizing at the Br centres. Charge localization may be caused by small hole polaron formation either at a defect or at a regular site of the lattice. In either case, the consequence of the charge localization is a bond elongation between the Br atoms that have turned neutral and their nearest neighbors. The fact that the transient exhibits rather clear modulations above the edge points to a well-defined change of local structure around Br atoms. This would not be the case if trapping at defects occurs, as these have a distribution of different structures, which cannot lead to clear modulations in the above-edge region, as it is the case for, *e.g.*, anatase TiO<sub>2</sub>.<sup>164</sup> On the other hand, a well-defined structure can be generated upon polaron formation at regular Br-sites of the lattice. This should be a small polaron, since a full positive charge localizes on the Br atoms. Another point in favor of an intrinsic self-trapping mechanism is given by the fluence dependence of this transient signal at 13.480 keV and 100 ps for CsPb(ClBr)<sub>3</sub> NCs (Figure 9.7). Indeed, the intensity of the transient remains perfectly linear over a wide range of fluence (from 0 to 15 mJ/cm<sup>2</sup>) which cannot be explained by defect localization. This is because, as mentioned above, there is a low density of defects in perovskite materials and therefore the population of these trap states would show saturation at lower charge carrier densities than the one explored here, as suggested by a previous photoluminescence study.<sup>321</sup> Finally, the high quantum yield of 90% for the band gap PL also points to the overwhelming majority of charge carriers being in the regular lattice, rather than at defects.

The time evolution of the Br K-edge transient x-ray signal was recorded at 13.480 keV and is shown in Figure 9.8 for both samples. To within error bars the time traces are identical, with a drop of the intensity within the first 5 ns, followed by a long component stretching over 100 ns. However, the inset to Figure 9.8 shows differences between the 2 samples at sub-ns times with a slower decay for the fully brominated sample. The kinetic traces were phenomenologically fitted using a biexponential function convoluted to the instrument response function of 80 ps, and the time constants and pre-exponential factors are given in Table 9.1.

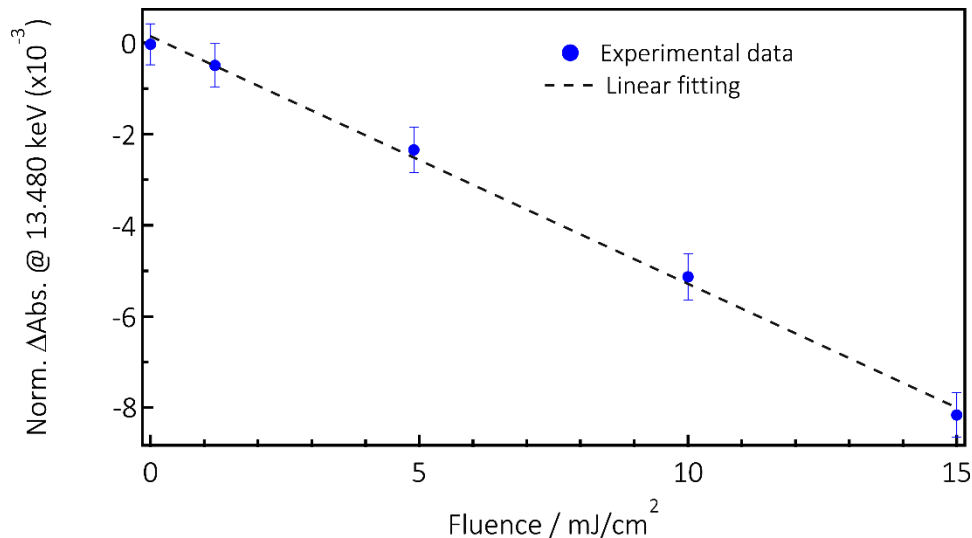


Figure 9.7 - Fluence dependence of the intensity of the Br K-edge transient signal at 13.480 keV for CsPb(ClBr)<sub>3</sub> NCs photoexcited at 355 nm. The black dashed line shows a linear fitting of the experimental data (blue dots).

Table 9.1 - Parameters of the biexponential fit for the kinetic traces in Figure 9.8.

Sample	$\tau_1(A_1)$	$\tau_2(A_2)$
<b>CsPb(ClBr)<sub>3</sub></b>	195±25 ps (72%)	132±30 ns (28%)
<b>CsPbBr<sub>3</sub></b>	542±44 ps (64%)	104±14 ns (36%)

While the long component is almost identical in both cases (100-130 ns), the short one increases by a factor of 2.5-2.7 from CsPb(ClBr)<sub>3</sub> to CsPbBr<sub>3</sub> and its amplitude is over 60% for both samples. In general, biexponential decay has typically been reported for the room temperature photoluminescence of organic perovskites at mild fluences.<sup>255,305,307,322,323</sup> Moreover, the photoluminescence of Cs perovskites showed to have longer time decays when the material has a larger bandgap,<sup>22</sup> similarly to the trend observed in the x-ray transient signal decays. The short component is usually on the order of a few ns, while the long one spans from tens to hundreds of ns. Here though, the laser fluence is quite intense (15 mJ/cm<sup>2</sup>) and for a reliable comparison between x-ray and photoluminescence decays, a fluorescence study of CsPb(ClBr)<sub>3</sub> NCs under similar experimental conditions is presented in the next section.



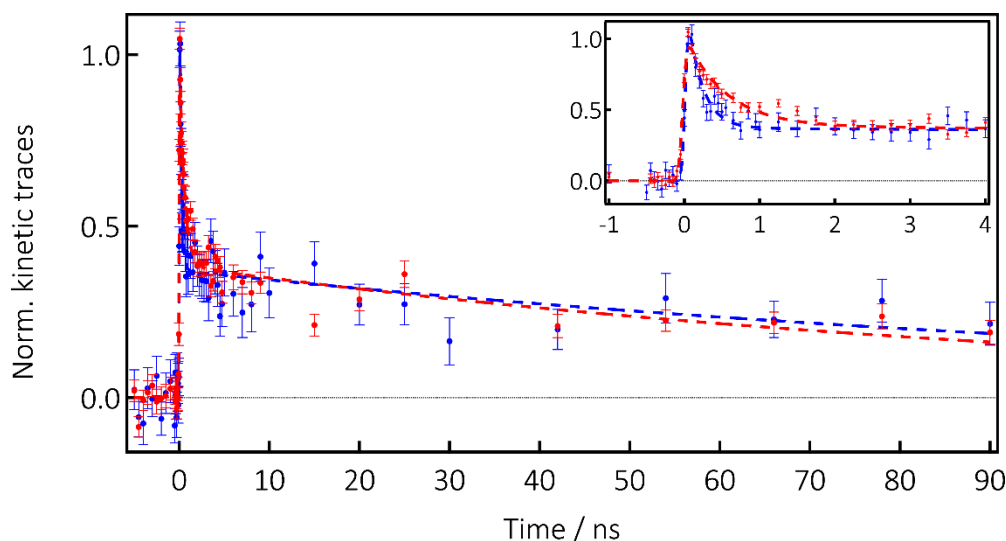


Figure 9.8 - Kinetic traces of the x-ray signal at 13.048 keV upon photoexcitation at 355 nm of CsPb(ClBr)<sub>3</sub> (blue dots) and CsPbBr<sub>3</sub> (red dots) NCs using a fluence of 15 mJ/cm<sup>2</sup>. The dashed lines represent a biexponential fit yielding the fit parameters listed in Table 9.1. The inset is a zoom of the first 4 ns after excitation.

To ensure that the signals at the edge and above the edge belong to the same transient species, time traces at 13.480 keV and 13.4863 keV are recorded for both samples (Figure 9.9), showing that they are identical.

Figure 9.10 shows the steady state Pb L<sub>3</sub>-edge spectra of CsPb(ClBr)<sub>3</sub> and CsPbBr<sub>3</sub> NCs. The two spectra are identical, and they are also quite similar to the Pb L<sub>3</sub> spectrum reported<sup>316</sup> for CH<sub>3</sub>NH<sub>3</sub>PbBr<sub>3</sub> nanoparticles. They are overall rather featureless, which is typical of Pb L-edge spectra.<sup>324</sup> This is due to the very short core-hole lifetimes, which broaden all transitions, making their assignment difficult.

Using high energy resolution fluorescence detection (HERFD) x-ray absorption near-edge spectroscopy (XANES), which exploits the apparent reduction in the core-hole lifetime broadening, Glatzel and co-workers<sup>325</sup> could unravel more details of the Pb XANES in various Pb<sup>2+</sup>-containing compounds, in particular PbO, whose Pb L<sub>3</sub>-edge XANES and HERFD spectra are reproduced in Figure 11.4 (appendix, chapter 11) and compared with the XANES spectrum of the present sample. The HERFD spectrum of PbO reveals three features at 13.032 keV, 13.042 keV and 13.054 keV, which are also visible in the TFY XANES spectrum of PbO. However, the PFY spectrum showed here does not show such clear-cut features. Of course, these are expected to lie at different energies since it is a different compound. The analysis of the spectra in ref.<sup>312</sup> was carried out by simulating the density of states in order to reproduce the spectra. It was concluded that the pre-edge feature at 13.032 keV is dominated by the Pb p-orbitals, but it arises in the L<sub>3</sub>-edge spectrum due to their strong mixing with Pb d-orbitals. At higher energies, the spectrum is dominated by the Pb d-orbitals, with a weak contribution of Pb p-orbitals. Interestingly, O-ligand orbitals also contribute to the 13.032 keV and 13.054 keV features in the PbO spectrum.



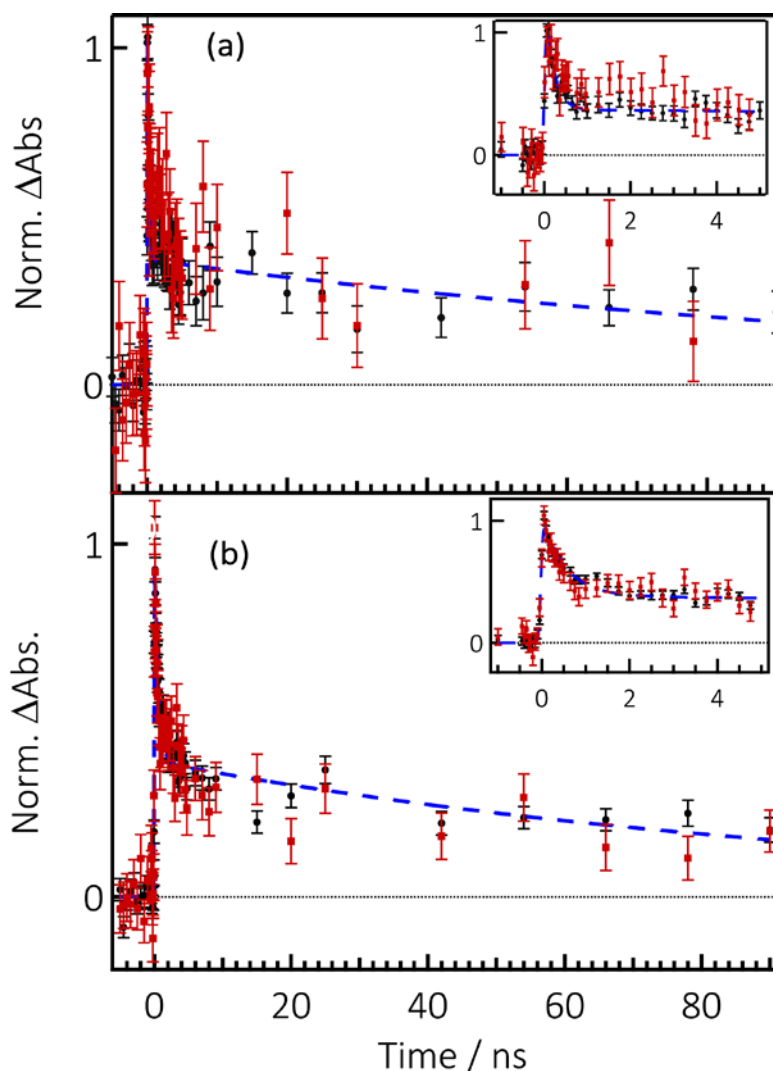


Figure 9.9 - Normalized kinetic traces at 13.480 (black dots) and 13.4863 keV (red squares) and fit using a biexponential (blue dotted curve) of CsPb(ClBr)<sub>3</sub> (a) and CsPbBr<sub>3</sub> (b) NCs upon photoexcitation at 355 nm.

Figure 9.11 also shows the Pb L<sub>3</sub>-edge transients obtained for the two samples. The data are much noisier than in the case of the Br K-edge but here again, the transients for the two samples have a similar profile (bearing in mind the large error bars), which differs significantly from that of the Br K-edge transients. Indeed, the Pb L<sub>3</sub>-edge transients show a decreased absorption right at the top of the edge (near 13.05 keV), which is attributed to Pb 6d orbitals, possibly also 6p orbitals, while the signal seems to turn positive in the region above 13.065 keV. The transients cannot be interpreted in terms of a chemical edge shift, which would be caused by a change of oxidation state of the Pb<sup>2+</sup> ions. In the present case, this would turn them to Pb<sup>+</sup> centres, and the electron localization would have led to an edge shift as discussed above.

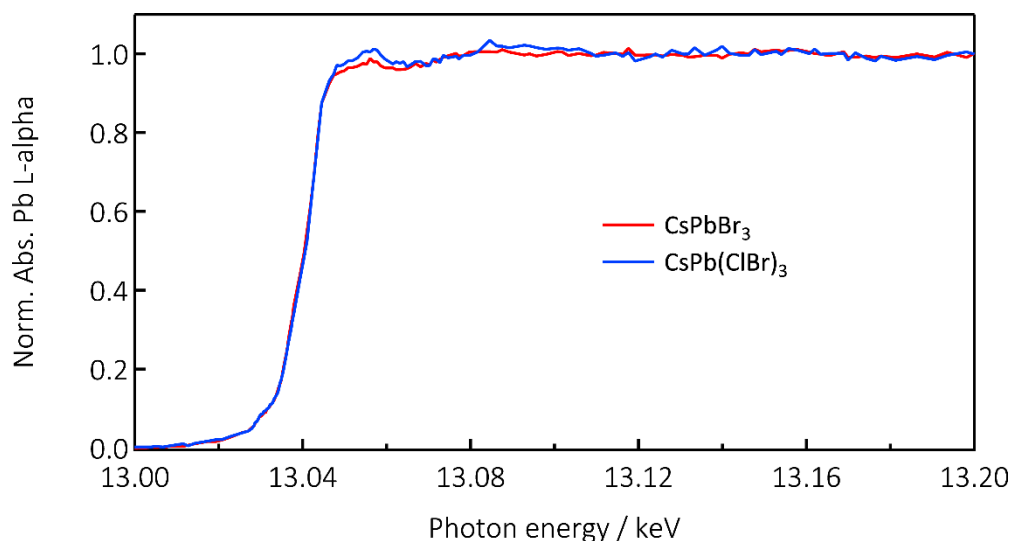


Figure 9.10 - PFY x-ray absorption spectra near the edge region of  $\text{CsPbBr}_3$  (red trace) and  $\text{CsPb(ClBr)}_3$  (blue trace) NCs at the Pb  $L_3$ -edge. The difference in intensity at about 13.05 keV between the two compounds is related to a higher density of unoccupied states due to the presence of Cl.

There is no hint of a red (or even blue) shift of the edge in the transients as verified in Figure 11.5 (appendix, chapter 11). Rather, the decreased intensity right at the edge (*i.e.* above the Fermi level), is due to the fact that upon laser excitation, electrons are transferred to the CB (*i.e.* above the Fermi level), filling the Pb 6p and 6d orbitals, where they remain delocalized at 100 ps time delay, thus reducing the transition probability as a result of the lower density of unoccupied states.

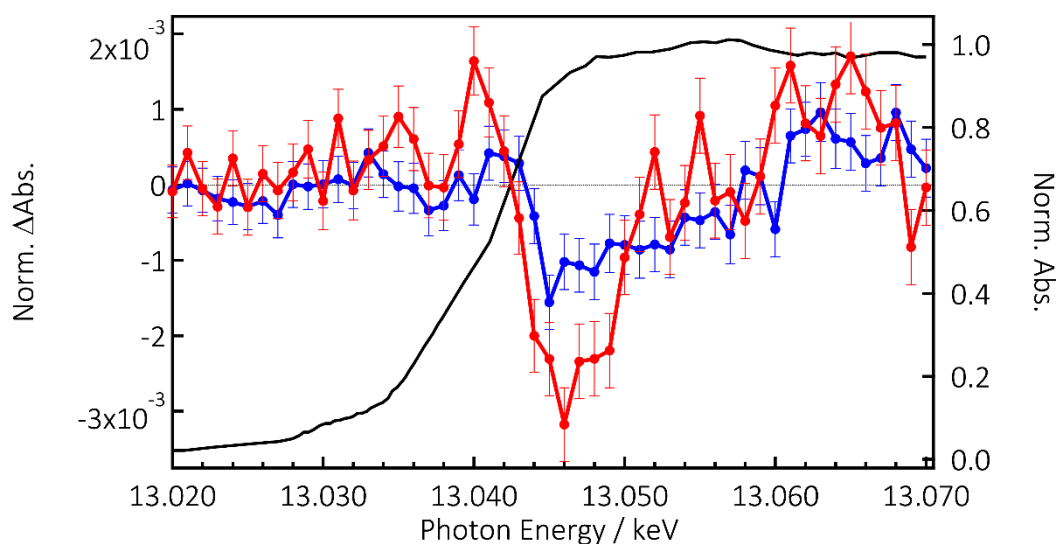


Figure 9.11 - PFY steady-state x-ray absorption spectrum of  $\text{CsPb(ClBr)}_3$  NCs at the Pb  $L_3$ -edge (black trace) and transient spectra at 100 ps time delay after photoexcitation at 355 nm with  $15 \text{ mJ/cm}^2$  of  $\text{CsPb(ClBr)}_3$  (blue trace) and  $\text{CsPbBr}_3$  (red trace).

Fully delocalized charges in the CB imply that the oxidation shift of the edge is negligible, while the observable effect is just a decrease of the transition probability from the core orbital to the CB, due to a diminution of the unoccupied density of states. Concerning the positive features around 13.040 and 13.065 keV, structural changes may well cause the latter, which is expected if polaron formation occurs around the  $\text{Br}^0$  atoms. On the other hand, the appearance of the 13.040 keV resonance in the chlorinated sample points to an electronic effect. Since the density of unoccupied states of Pb has decreased after excitation, a positive feature originating from them is excluded and the most likely candidates would be Br-ligand orbitals. In PbO the edge regions have a significant contribution from ligand O orbitals.<sup>325</sup> The same applies here, since it is known that the CB contains a small contribution of halogen orbitals.<sup>22,251</sup> The pre-edge signals could reflect the increased density of unoccupied states of the Br-ligands after photoexcitation. Due to the poor signal-to-noise ratio, time traces at this edge could not be recorded.

Finally, Figure 9.12 shows the Cs  $L_2$ -edge which is characterized by a prominent “white line” at 5.363 keV, followed by a rather featureless above edge region. Since Cs is in the +1 oxidation state, the white line edge is due to the  $2p_{1/2}$ -6s transition. Under 355 nm excitation, no photoinduced changes could be observed at the Cs  $L_2$ -edge, as seen in Figure 9.12, notwithstanding the fact that the experiments were carried out during the same measurement campaign as those at the Br and Pb edges.

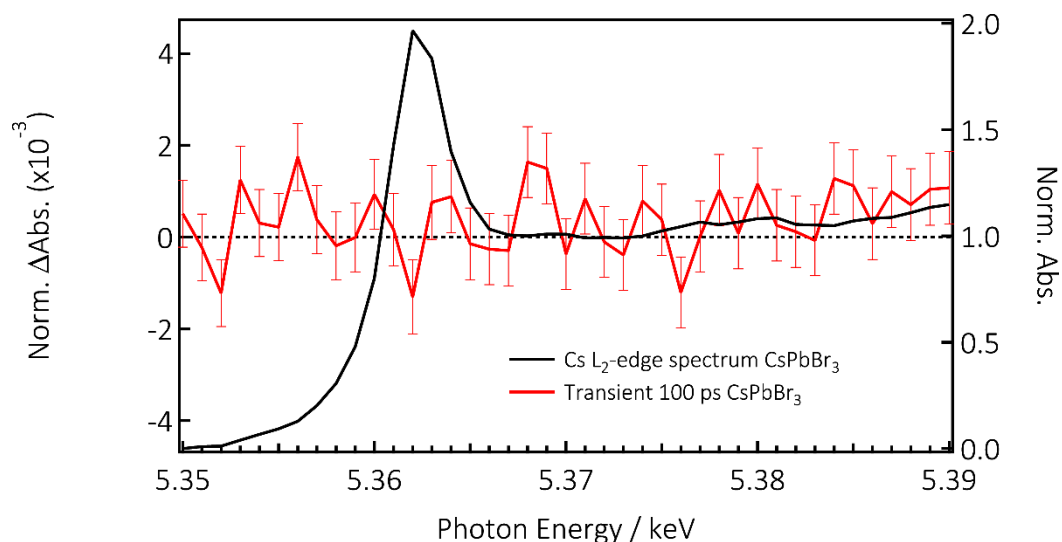


Figure 9.12 - X-ray absorption spectrum of CsPbBr<sub>3</sub> NCs at the Cs  $L_2$ -edge (black trace) with the transient spectra at 100 ps (red trace) showing no signal within the S/N of the measurement.

Therefore, it can be concluded that the Cs atoms are not affected by the photoexcitation, because there is no signature of an electronic (at the edge) or structural (above the edge) change. As far as the former is concerned, this is understandable since the density of states (DOS) calculations of organic and inorganic perovskites show that the states of the cation are

either far from below the top of the VB or far above the bottom of the CB<sup>22,25,214,216,252-254</sup> and therefore, they do not contribute to the charge carrier dynamics. As for the lack of signature on the above edge region, it is remarked that already the steady state ground state spectrum is featureless and therefore this region is rather insensitive to structure. It can be concluded that the cation is not a direct player in the fate of the charge carriers, at least for time scales > 80 ps.

To recapitulate the picosecond x-ray absorption results: the main observation is that at 100 ps and longer holes are fully localized at Br atoms, most likely forming small polarons, while electrons remain delocalized in the CB over hundreds of ps (and probably longer). The Cs cation does not show any effect upon photoexcitation leading to the conclusion that it plays a role in the architecture of the material but not its electronic properties. The conclusion of localized holes and delocalized electrons is reminiscent of the weakly localized exciton in organic-inorganic perovskites discussed by He *et al.*<sup>307</sup>, who argued that they form due to band tail states. In their picture, these band tail states mainly stem from the CB. The results of this XAS study shows that on the contrary, it is the hole that causes the localization rather than the electron.

### 9.2.2 Photoluminescence

The TCSPC measurements have been performed only for the CsPb(ClBr)<sub>3</sub> sample, but considering the similarities observed in the previous section between the two samples, the analysis of the PL dynamics of one halide composition should be enough to compare the results with the ps-XAS data and derive general conclusions.

Figure 9.13 shows the photoluminescence dynamics of CsPb(ClBr)<sub>3</sub> at several fluences. A faster decay is observed with increasing fluence for most of the kinetic traces. Indeed, excluding the 2 lowest fluences (*i.e.* 80 nJ/cm<sup>2</sup> and 0.8 μJ/cm<sup>2</sup>) and the 2 highest ones (*i.e.* 3 mJ/cm<sup>2</sup> and 8 mJ/cm<sup>2</sup>), which are similar within the signal to noise ratio of the measurement, this trend is clearly observable for all the other kinetic traces. Decreased PL lifetime with increasing fluence has been associated in the literature to processes such as Auger<sup>326</sup> and biexciton<sup>38</sup> recombination whose weight is proportional to the number of excited charge carriers (see chapter 2.3 for an introduction to these topics). These processes act on faster time scales than common geminate recombination and therefore become effective recombination channels when the fluence increases.<sup>279</sup> A global fit is used to reproduce the decay times at different fluences (Figure 9.13), justified by the fact that similar physical processes are present at all fluences but with different weights. All luminescence decay curves can be reproduced with the following time constants: <300 ps, 875 ps, 5.34 and 19.08 ns.

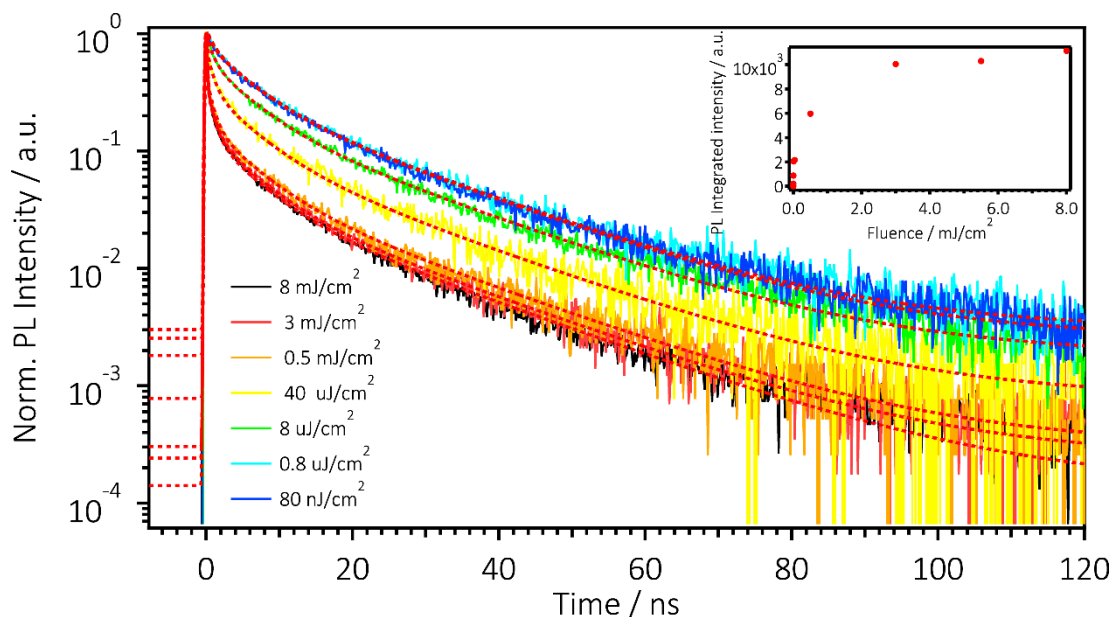


Figure 9.13 - Normalized photoluminescence kinetic traces for CsPb(ClBr)<sub>3</sub> NCs upon photoexcitation at 355 nm with different fluences and global fitting curves (red dotted curves) using a quadri-exponential function. The inset shows the total photoluminescence intensity at different fluences, which is obtained by integrating the kinetic traces until 120 ns delay.

Individual fits of each trace unambiguously show the need of a four exponential function for the 8 mJ/cm<sup>2</sup> data (Figure 9.14), while with lower fluences, a bi-exponential suffices to reproduce the decay as indicated by the negligible pre-exponential factors of the global fitting for the first two time components (Table 9.2).

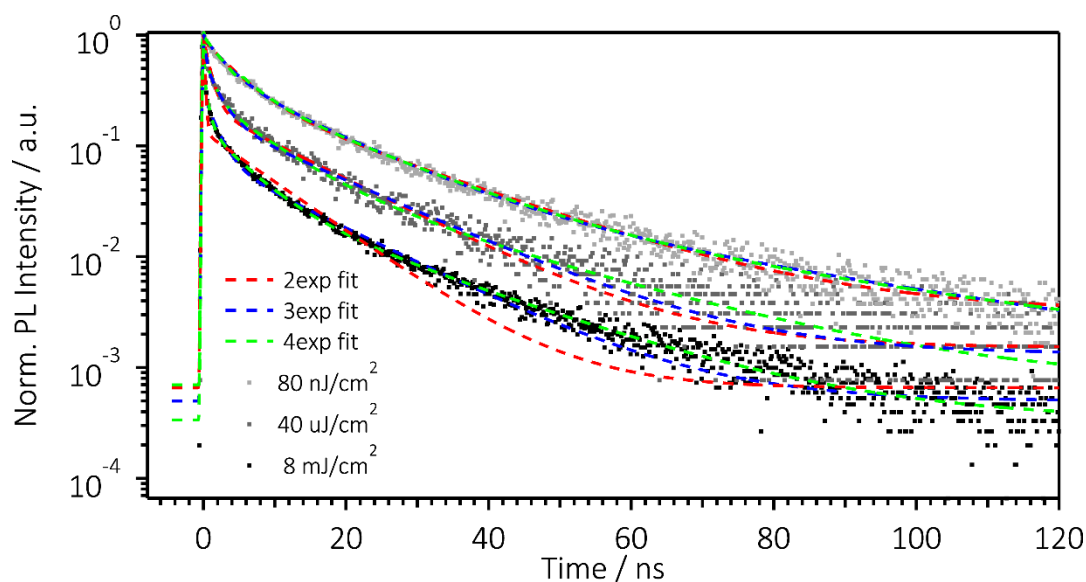


Figure 9.14 - Normalized photoluminescence kinetic traces for CsPb(ClBr)<sub>3</sub> NCs upon photoexcitation at 355 nm with 80 nJ/cm<sup>2</sup> (light grey dots), 40 μJ/cm<sup>2</sup> (dark grey dots) and 8 mJ/cm<sup>2</sup> (black dots) and independent fitting functions with bi-exponential (red dotted curves), tri-exponential (blue dotted curves) and quadri-exponential (green dotted curves) decays.

This behavior corroborates the hypothesis that the fast time components (<300 and 875 ps) are related to recombination paths that depend on the charge carrier density in the bands (*viz.* Auger and biexciton recombination).

Table 9.2 - Weights of the different time components (W1 for <300 ps, W2 for 875 ps, W3 for 5.34 ns and W4 for 19.08 ns) in the global fit function at the different fluences.

	$\tau$ (ns)	80nJ/cm <sup>2</sup>	800nJ/cm <sup>2</sup>	8μJ/cm <sup>2</sup>	40μJ/cm <sup>2</sup>	0.5mJ/cm <sup>2</sup>	3mJ/cm <sup>2</sup>	8mJ/cm <sup>2</sup>
<b>W<sub>1</sub></b>	<0.3	0.003	0.003	0.013	0.047	0.128	0.136	0.162
<b>W<sub>2</sub></b>	0.87	0.028	0.033	0.059	0.095	0.117	0.122	0.131
<b>W<sub>3</sub></b>	5.34	0.322	0.320	0.330	0.334	0.294	0.305	0.291
<b>W<sub>4</sub></b>	19.08	0.647	0.643	0.598	0.525	0.460	0.437	0.416

Also the fluorescence spectrum of CsPb(ClBr)<sub>3</sub> shows red-shift at high fluences (Figure 9.15), which has been already associated in the literature to a significant contribution of biexciton emission for CsPbBr<sub>3</sub>.<sup>38</sup> In fact, there is a clear reversible redshift of the emission peak together with a change in spectral shape, which can be more clearly seen in Figure 9.16. The emission spectrum at 3 μJ/cm<sup>2</sup> can be fitted with a simple Voigt function, as done in a previous work on CsPbBr<sub>3</sub>.<sup>38</sup> This is not the case for the emission recorded at 6.5 mJ/cm<sup>2</sup>. As pointed out by Wang *et al.*<sup>38</sup>, the biexciton emission energy is lower than the exciton one and occurs at high irradiance. In their work they could spectrally separate the two emission peaks working at low temperature (*viz.* 10 K). Here, room temperature and 1 second integration time do not allow to separate the two spectral components and the final result is a red-shifted asymmetric luminescence spectrum due to the overlap of the excitonic and biexcitonic emission.

When investigating the effect of the fluence on the photoluminescence absolute intensity (*i.e.* integrated over the entire time range probed), a saturation is observed (see inset in Figure 9.13), similarly to a recent work on CsPbBr<sub>3</sub> and CsPbI<sub>3</sub> nanoparticles.<sup>279</sup> This behavior agrees with the hypothesis of a competition between radiative (here excitonic) and non-radiative (here Auger) recombination, where the non-radiative processes become more prominent at higher fluence.<sup>279</sup>

To conclude, the optical fluorescence investigates the manifestation of effects mediated by Coulomb interactions that emerge with increasing the fluences and lead to higher order

excitonic states but does not show clear features of trapping, having the emission centered near the band gap region.

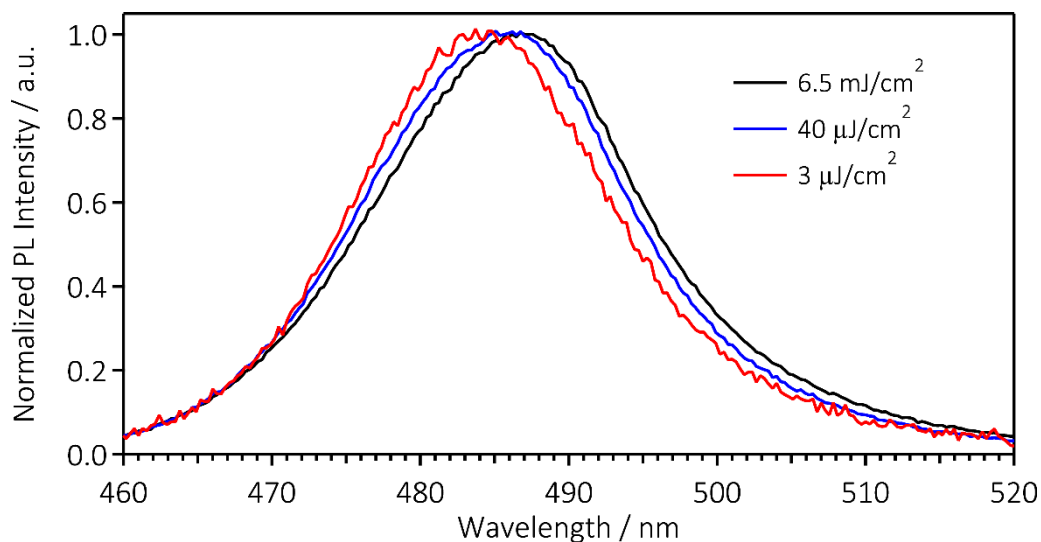


Figure 9.15 - Normalized photoluminescence spectra of CsPb(ClBr)<sub>3</sub> NCs upon photoexcitation with 355 nm at 6.5 mJ/cm<sup>2</sup> (black curve), 40 µJ/cm<sup>2</sup> (blue curve) and 3 µJ/cm<sup>2</sup> (red curve). The spectral shift shown in this figure is reversible and therefore does not imply laser damaging.

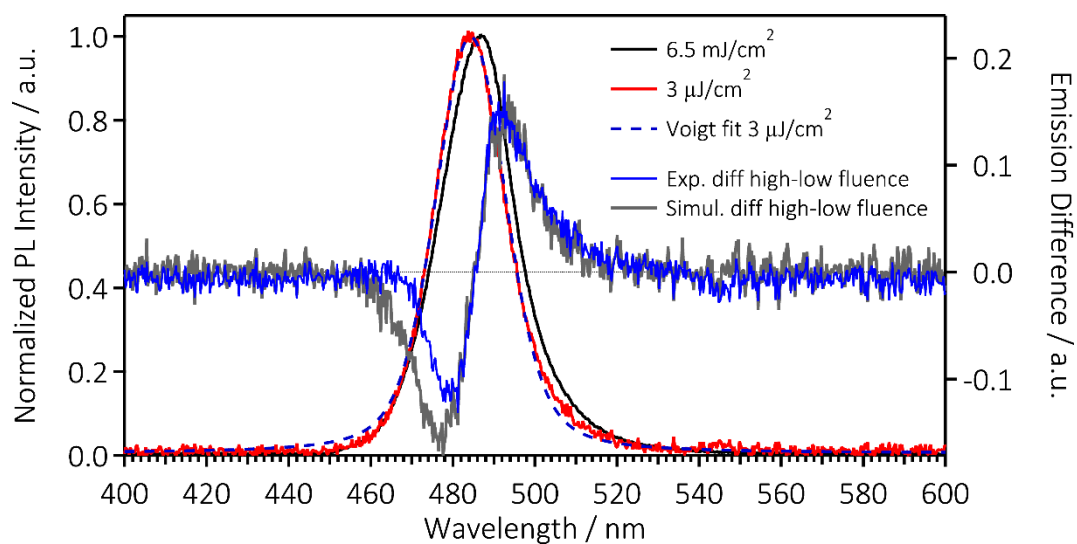


Figure 9.16 - Normalized photoluminescence spectra of CsPb(ClBr)<sub>3</sub> NCs upon photoexcitation with 355 nm at 6.5 mJ/cm<sup>2</sup> (black curve) and 3 µJ/cm<sup>2</sup> (red curve) which is fitted by a Voigt function (blue dotted curve). The difference between the 6.5 mJ/cm<sup>2</sup> and 3 µJ/cm<sup>2</sup> spectra (blue curve) is compared with the simulated difference from the rigidly red-shifted 3 µJ/cm<sup>2</sup> spectrum (grey curve).

### 9.2.3 The emerging picture of the photophysics of CsPbBr<sub>3-x</sub>Cl<sub>x</sub> perovskites

This section attempts to find an interpretation which reconciles the results of XAS and PL presented previously. As mentioned in the introduction, these two techniques have a different sensitivity for the observed excited states which often makes them complementary, therefore their comparison should result in a more profound interpretation.

Figure 9.17 shows the kinetic traces of the ps-XAS at the Br K-edge (13.480 keV and 15 mJ/cm<sup>2</sup>) and PL at 8 mJ/cm<sup>2</sup>, both for CsPb(ClBr)<sub>3</sub> NCs. As observed in Figure 9.13, because the PL dynamics at 8 and 3 mJ/cm<sup>2</sup> are indistinguishable, the dynamics at 8 mJ/cm<sup>2</sup> should be comparable with those at 15 mJ/cm<sup>2</sup>, the fluence used for the synchrotron experiments. Interestingly, the short time components (*i.e.* the first nanosecond, see inset Figure 9.17) match between the x-ray and PL decays, bearing in mind the limited instrument response function of the TCSPC setup (*i.e.* 300 ps) and S/N of the ps-XAS measurements. On the other side, the two techniques clearly present different results on the long time scales, as already indicated by the fitting time constants (Table 9.1 and Table 9.2). In particular, the ps transient x-ray signal is longer lived (*i.e.* hundreds of ns) than the PL (*i.e.* tens of ns and more than one time component). Another striking difference between the two measurements is the signal intensity fluence dependence, which is perfectly linear in the case of the x-ray transient signal (Figure 9.7) and saturates in the case of the PL (inset Figure 9.13). It should be mentioned, though, that for the x-ray fluence dependence the signal intensity is measured at the maximum of the transient signal of the Br K-edge (*i.e.* 13.480 keV) and at 100 ps, while for the PL fluence dependence, it is the total emission of the sample integrated over the entire time range probed.

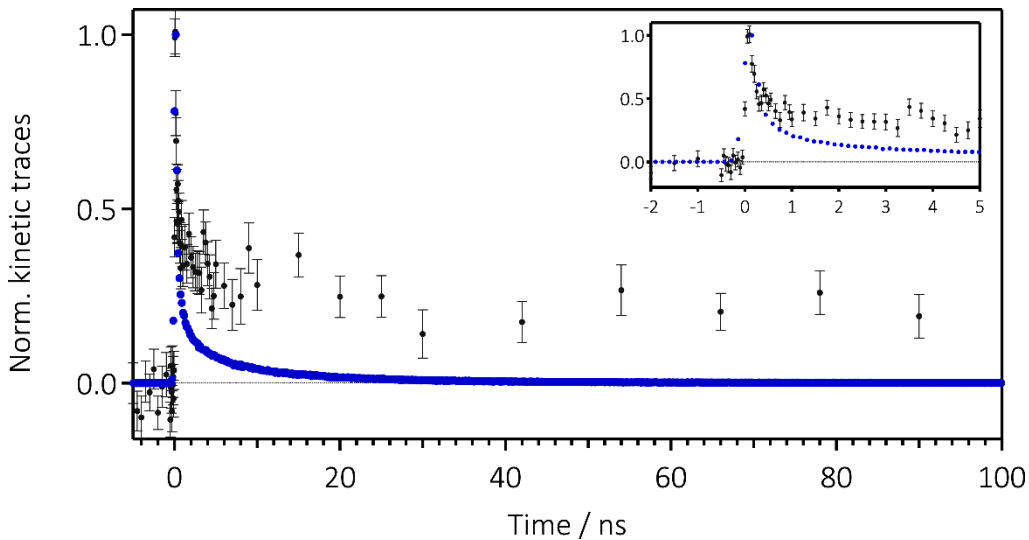


Figure 9.17 - Normalized kinetic traces of photoluminescence (blue dots) and x-ray absorption spectroscopy at 13.480 keV (black dots) for CsPb(ClBr)<sub>3</sub> NCs. In the inset a zoom of decay in first 5 ns after photoexcitation.



This explains why a mechanism competing with the radiative recombination, such as the Auger process, has an impact on the shape of the fluence dependence of the PL but not of the ps-XAS.

From these observations can be concluded that x-ray and fluorescence dynamics could observe the same excited state at short time scales (*i.e.* in the first ns) but a different one in the tens of ns. The PL results clearly point to the observation of excitonic physics (*i.e.* exciton and biexciton emission) and the x-ray ones to a localized hole (*i.e.* small polaron). Therefore, the common excited state observed at short time scales could be compatible with the weakly localized exciton, recently reported in organic perovskites upon PL measurements by He *et al.*<sup>307</sup>. This exciton would consist of a localized hole and delocalized electron bound to it by Coulomb attraction. On the other side, it is singular that the static PL spectrum collected at high fluence (Figure 9.15) does not exhibit any clear emission from this localized exciton. This could be due to the low emission quantum yield of this state, but in this case the PL dynamics would not be influenced by the presence of this localized exciton and the interpretation which points to the same state probed at short time delays for the two techniques would be inconsistent. It cannot be excluded though, that the emission from this localized excitonic state is only redshifted  $\sim 10$  nm from the main bandgap emission ( $\sim 100$  meV at these energies) and therefore is not distinguished from the biexciton contribution in the present measurements, although the previous PL study on CsPbBr<sub>3</sub><sup>38</sup> did not point in this direction.

If assuming that PL and XAS probe different states at short time delays after excitation, the TR-XAS could still be probing the weakly localized exciton discussed above (which, in this case, would be characterized by a low emission quantum yield) while the PL would monitor simple exciton and biexciton recombination. This would imply that the similarity between the fast kinetic decays is just on happenstance. On the other hand, in the case that the two measurements probe the same state at short time delays (namely the weakly localized exciton with a significant emission quantum yield), then the long time component of the x-ray signal could be due to hole trapping in defects. Indeed, trapping from defects leads to non-geminate and mostly non-radiative recombination. This would not only explain the difference in kinetic decays between XAS and PL measurements but also the fact that the ps-XAS presents a longer lived signal since non-geminate recombination is slower than geminate one. As mentioned earlier, defects have a small concentration in the substances studied here, but are still unavoidable, particularly at the surface of the NCs. The long time component is a minority of the total x-ray signal (*i.e.*  $\sim 30\%$ ) and therefore compatible with the small concentration of defect sites in the material. To conclude then, on longer time scales the PL still monitors geminate recombination of excitons while the TR-XAS looks at a different state which could have two origins, namely the weakly localized exciton and the holes trapped in defects of the material.

To be able to discriminate between these two hypothesis, it is necessary to measure a transient of the Br K-edge, tens of ns after the laser excitation. This would provide detailed information

on the long lived species and a clear difference in the transient XANES spectrum would be observed if the signal derives from defect trapping. Indeed, because defects have a distribution of different structures, this cannot lead to clear modulations in the above-edge region as the one observed in the transient spectra collected at short time delays for self-trapped holes, *i.e.* this would be a sign of defect trapping. Moreover, the study of single crystals instead of NCs would decrease any signal due to defects in the material, where the surface of the sample as a primary role, and this could help in ruling out the last hypothesis.

### 9.3 Conclusions

In summary, ps-XAS and ps-PL are used to investigate the fate of the charge carriers in photoexcited inorganic pure (Br) and mixed halide (Br/Cl) perovskites nanoparticles in solution. The main observation is that the excited species probed at short time for XAS is attributed to a weakly localized exciton and consists of a localized hole and delocalized electron bound to it by Coulomb attraction. The PL measurements could in principle probe the same state at short time delay, considering the similar XAS kinetics in this region, but the absence of a clear emission from this state points toward to an accidental similarity. Therefore, the long lived species of the XAS measurements could originate from the same weakly localized exciton, if the similarity at short time scales with the PL is coincidental, or from holes trapped in material's defects. Br K-edge transient measurements at tens of ns after photoexcitation and on single crystals would solve this pending question.

On a broader perspective, the present work highlights the advantages of a time-resolved element-selective tool for the study of charge carrier dynamics in multi-element materials. Time-resolved XAS was previously used to study photoexcited solids such as Silicon and Graphite,<sup>327,328</sup> VO<sub>2</sub><sup>329</sup> or amorphous systems such as Ge-Te-Se alloys.<sup>330,331</sup> Most of these studies were carried out in the soft x-ray domain. Time-resolved Electron-Energy-Loss-Spectroscopy (EELS) is another element-selective approach that can potentially probe the charge carrier dynamics and it was implemented in the case of photoexcited graphite.<sup>332-335</sup> These time-resolved XAS and EELS studies were mainly focusing on photoinduced phase transitions of the type insulator-metal or disorder-order, mostly in non-semiconducting materials. The present work shows for the first time, the probing of all the atomic actors involved in the fate of the charge carriers in a typical semiconductor. The ability to link the charge carrier dynamics probed by optical-domain methods such as photoluminescence or transient absorption from the IR to the UV, with their atomic specificity is a new development in the field.

Further progress in this study would be the use of fs time resolution techniques. In this regards, fs-XAS can be carried out in modern XFEL and fs-PL in a fluorescence up-conversion setup.<sup>336</sup> Particularly, for the Pb L<sub>3</sub>-edge measurements, the use of a dispersive x-ray emission spectrometer (*e.g.* von Hamos geometry)<sup>187</sup> would allow to perform high resolution x-ray absorption spectroscopy, which, thanks to a higher x-ray flux typical of modern FEL, can easily be carried out in a time resolved manner. This allows to overcome

the difficulty in interpreting the Pb  $L_3$ -edge, where the core-hole lifetime broadening does not allow to observe clear features in the XANES region.<sup>325</sup>



## 10 Conclusion and outlook

This thesis demonstrates the potential of time-resolved x-ray absorption spectroscopy (XAS) in investigating the charge carrier dynamics of photoexcited semiconductors. Indeed, chapter 6 and 9 show that ps-XAS is the ideal tool to map electron and hole localization due to its intrinsic sensitivity to oxidation state changes, which results in an edge shift for the probed element. Moreover, the structural sensitivity allows to unravel the origin of charge carrier localization which can arise mainly from extrinsic factors, as in the case of TiO<sub>2</sub> nanoparticles (*viz.* defects of oxygen in the lattice), or intrinsic ones, as for CsPbX<sub>3</sub> nanocrystals (*viz.* the polaronic nature of the hole).

In chapter 8, femtosecond transient absorption (fs-TA) measurements performed on CsPb(ClBr)<sub>3</sub> nanocrystals investigate complementary aspects of the perovskites physics. The fs-TA data reveal many body physics in the material, shedding light on the transition between free charge carriers and excitons that can be tuned in time by using different fluences of photoexcitation. fs-TA spectroscopy observes different facets of the lead halide perovskites physics than ps-XAS, not only for its higher time resolution (*i.e.* about 3 orders of magnitude), but particularly for the lower energies of the probe light, which span around the bandgap energy of the semiconductor. The results of the two techniques highlight the complexity of the charge carrier dynamics in this material, where self-trapped carriers (*here* small polaronic holes) can co-exist with itinerant ones, a scenario already predicted by theory in semiconductors,<sup>47</sup> furthermore, they support the strategy of using different types of spectroscopic tools in order to obtain a complete picture of the ultrafast processes in the investigated sample.

In chapter 5, fs-XAS performed on TiO<sub>2</sub> anatase is used to map electron localization. This study overcomes the gap in time resolution between optical transient absorption and x-ray absorption spectroscopy. The results reveal that femtosecond resolution is essential to investigate the early steps in the charge carrier localization. Indeed, even the 200 fs resolution obtained is not sufficient to track the rise of the signal which is a finger print of the trapping process. On the other hand, given the low signal to noise ratio (S/N) intrinsic to the slicing technique, neither a study using mild pump fluences nor an investigation of the fluence dependence of the transient spectra can be performed. As remarked through the fs-TAS study of lead halide perovskites, fluences can influence the physics observed substantially. This is not true only in the presence of a phonon bottleneck, but it is general for semiconductors where processes such as a Mott transition can take place when the charge carrier density rises above a critical limit. This specific limit in a Mott transition is represented by the situation in which the average distance between excitons is smaller than the exciton Bohr radius; in this case, the overlap between the wavefunctions of the excitons triggers the screening of electron-hole interaction leading to an electron-hole plasma (details in chapter 2.2.1).<sup>58</sup>

Therefore, to achieve a better S/N in transient x-ray absorption studies and ensure being below the critical charge carrier densities, the solution would be to decrease the noise by having a higher probe flux, which would enable pump fluence dependence studies under a mild excitation regime. This is a possibility in x-ray free electron lasers (XFELs), which allow not only higher x-ray flux compared to the slicing technique (*viz.* several orders of magnitude per pulse),<sup>81</sup> but nowadays also a higher time resolution using a timing tool.<sup>337</sup> Indeed, the intrinsic jitter of these machines can be corrected by a post-processing of the data in the presence of a device which records the arrival time of the x-ray and laser pump pulses per each shot. This allows in principle to obtain time resolutions up to 10 fs,<sup>337</sup> but in order to be able to make use of it, the flat liquid jet of 100  $\mu\text{m}$  thickness should be replaced by a thinner device. At 100  $\mu\text{m}$  thickness, the mismatch in group velocity between optical and x-ray pulse would be of several tens of femtosecond, becoming the limiting factor for the instrument response function of the system.

Moreover, the higher x-ray flux allows to use a dispersive x-ray emission spectrometer (*e.g.* von Hamos geometry) which would yield detailed information on the occupied electronic states and high-resolution x-ray absorption spectra (as currently possible in the ps-XAS studies) at femtosecond time-resolution.<sup>187</sup> These results would enrich the information on the investigated systems helping the interpretation of the data. In particular, the investigation of  $\text{TiO}_2$  nanoparticles with the possibility of recording x-ray emission together with the x-ray absorption spectra gives access to the dynamics of the holes in the valence band, in analogy with a recent study on  $\text{ZnO}$  nanoparticles.<sup>338</sup> This is at the moment the best way to simultaneously probe electrons and holes in a metal oxide, because in these materials the valence band is mainly composed of O 2p orbitals and XAS should be performed at the O K-edge ( $\sim 543$  eV). At these energies, high vacuum is required and therefore the experimental conditions are more complex, particularly when working with a liquid suspension. In case of  $\text{CsPbX}_3$  nanocrystals, the use of a dispersive emission spectrometer is interesting mainly for the possibility to perform high energy resolution fluorescence detection (HERFD). In contrast to the total fluorescence yield used in the time resolved x-ray experiments presented in this thesis, HERFD allows to record spectra with a lower experimental broadening than that arising from the lifetime of the deep core hole. Simply by scanning the incident x-ray energy at a fixed x-ray emission energy, it is possible to collect high resolution spectra which are particularly useful to study the fine structural details in the XANES region of heavy elements such as Pb.<sup>325</sup> This would provide a better understanding of the electron dynamics in the conduction band of this semiconductor.

Finally, for what concerns an outlook on the fs-TA measurements, a logical next step would be to perform 2D spectroscopy, using a broadband four wave mixing setup in the visible region of the spectrum.<sup>339</sup> Two-dimensional temperature-dependent spectroscopy was recently implemented on  $\text{CH}_3\text{NH}_3\text{PbI}_3$  in the energy region around the bandgap to address the polaronic nature of the photogenerated charge carriers.<sup>340</sup> Performing a study in the region above the bandgap energy at different time delays upon photoexcitation would provide a systematic view on the effects of the excess energy on the nature of the photoexcited charge

carriers and the resulting relaxation processes. Moreover, the higher time-resolution with respect to fs-TA spectroscopy (*i.e.* about 10 fs),<sup>339</sup> increases the chance to trigger and therefore observe coherent processes such as phonons in the material, which can modulate the optical transient spectrum. The study of these quasi-particles would provide a deeper understanding of the charge carriers intraband relaxation processes which are due to the electron-phonon interaction and in perovskites showed non-trivial effects such as the phonon bottleneck behaviour.<sup>77</sup>





# 11 Appendix

## 11.1 Femtosecond transient absorption of CsPb(ClBr)<sub>3</sub>

Figure 11.1 shows the transient maps, *i.e.* time delay vs energy, upon photoexcitation at 3.1 eV for the 7 different fluences explored in chapter 8. From these maps are derived the spectral transients at different time delays and the kinetic traces reported in chapter 8 and Figure 11.2.

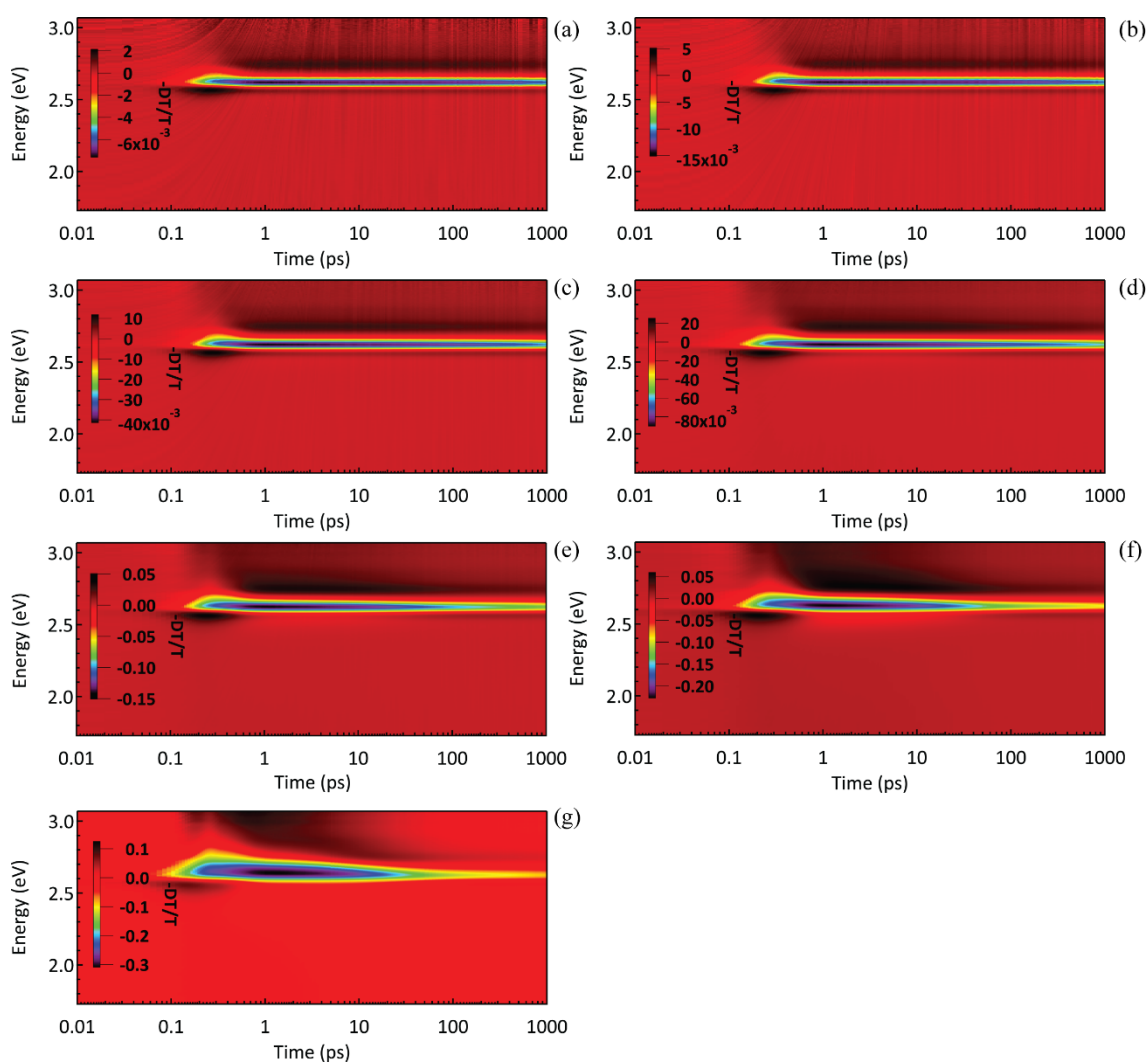
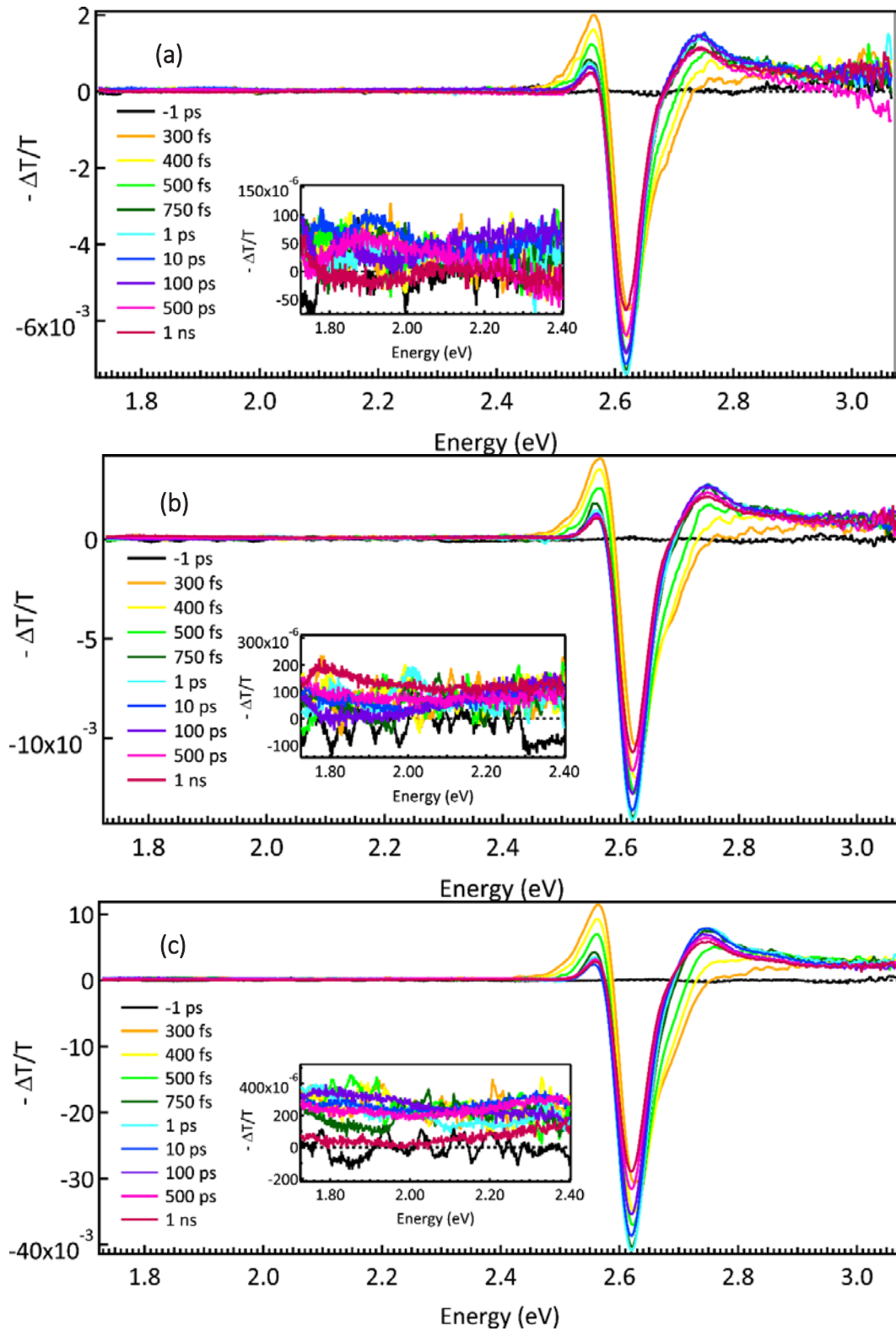


Figure 11.1 - Transient maps upon excitation with 3.1 eV for the fluence of 2.5 (a), 5 (b), 10 (c), 18 (d), 37 (e), 65 (f) and 100  $\mu\text{J}/\text{cm}^2$  (g).



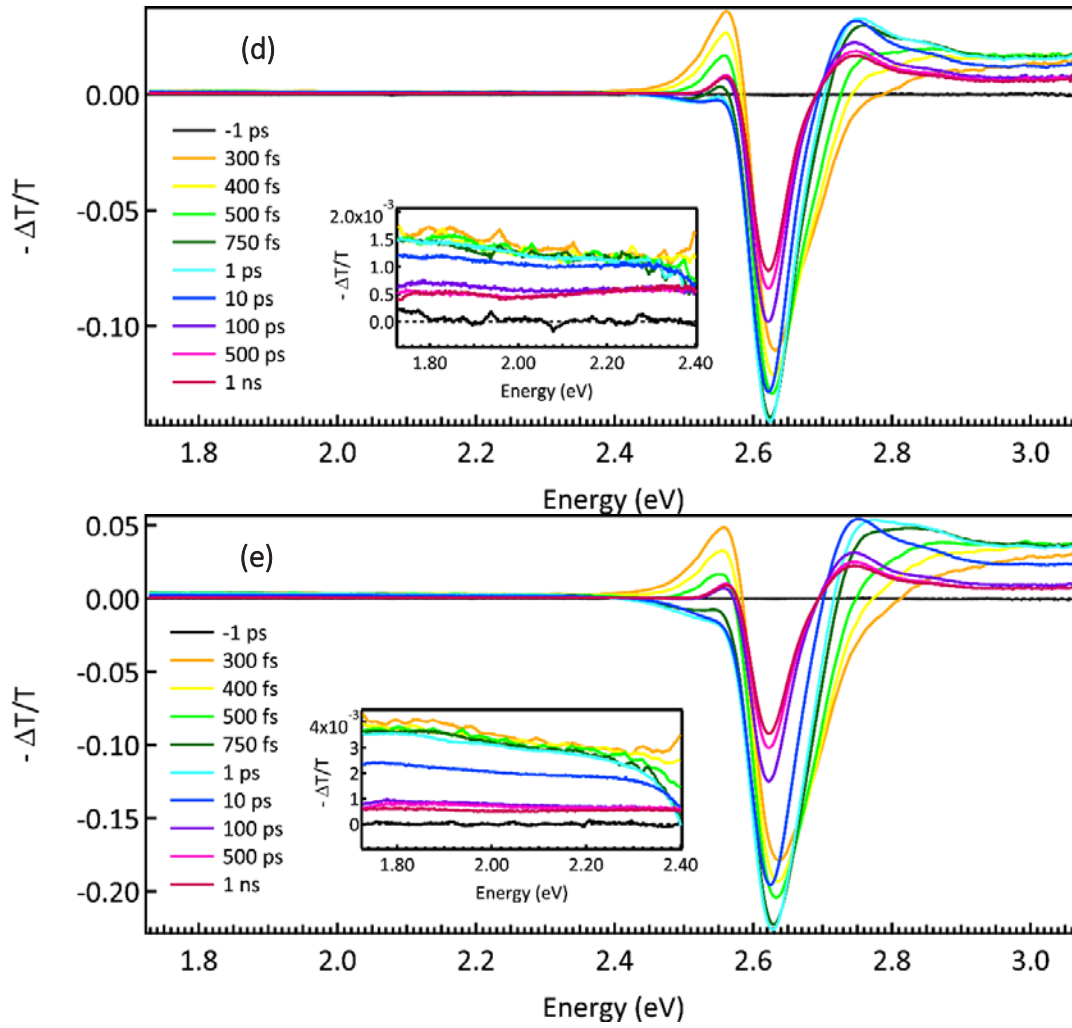


Figure 11.2 - Femtosecond transient spectra at different time delays upon photoexcitation at 3.1 eV with fluence of 2.5 (a), 5 (b), 10 (c), 37 (d) and 65  $\mu\text{J}/\text{cm}^2$  (e). In the inset, there is a zoom of the low energy region (from about 1.8 to 2.4 eV) in which is visible the PA<sub>1</sub> signal.

## 11.2 Picosecond x-ray absorption and photoluminescence of CsPbBr<sub>3-x</sub>Cl<sub>x</sub> nanocrystals

Figure 11.3 shows total fluorescence yield (TFY) ground state spectra of CsPbBr<sub>3</sub> NCs at the Br K-edge collected at 2 hours distance between each other during the ps-XAS measurements. The spectra are identical indicating the absence of sample damaging during the experiment.

Figure 11.4 shows the Pb L<sub>3</sub>-edge XANES and EXAFS spectra of PbO from ref.<sup>325</sup>, recorded in TFY mode and using the High Energy Resolution Fluorescence Detection (HERFD) mode. The TFY spectrum shows only weak features as is often the case with Pb L<sub>3</sub> spectra,<sup>324</sup> while the HERFD spectrum clearly resolves the weak structures at 13.031 keV, 13.040 keV and 13.054 keV. The DOS calculations<sup>325</sup> show that the first of these bands is due to Pb p-orbitals

that are mixed with Pb d-orbitals, with an additional contribution from Oxygen p- and s-orbitals. The latter two are mostly due to Pb d-orbitals.

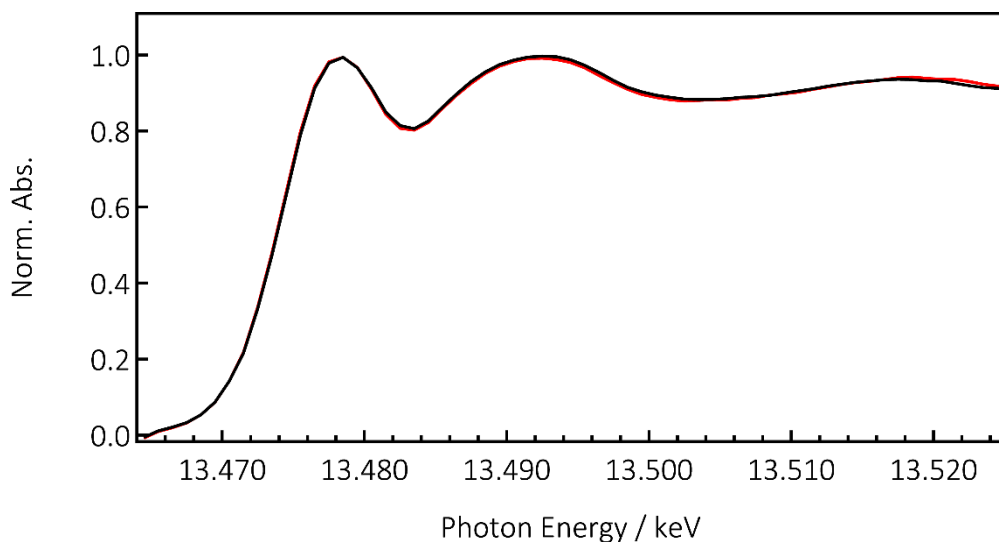


Figure 11.3 - Normalized x-ray absorption spectra of CsPbBr<sub>3</sub> near the Br K-edge region acquired in TFY. The agreement between the spectrum averaged over the first 2 hours of data acquisition of the pump-probe experiment (red curve) and that over the consecutive 2 hours (black curve), supports the absence of damage during the measurements upon irradiation at 15  $\mu\text{J}/\text{cm}^2$  and 3.5 eV.

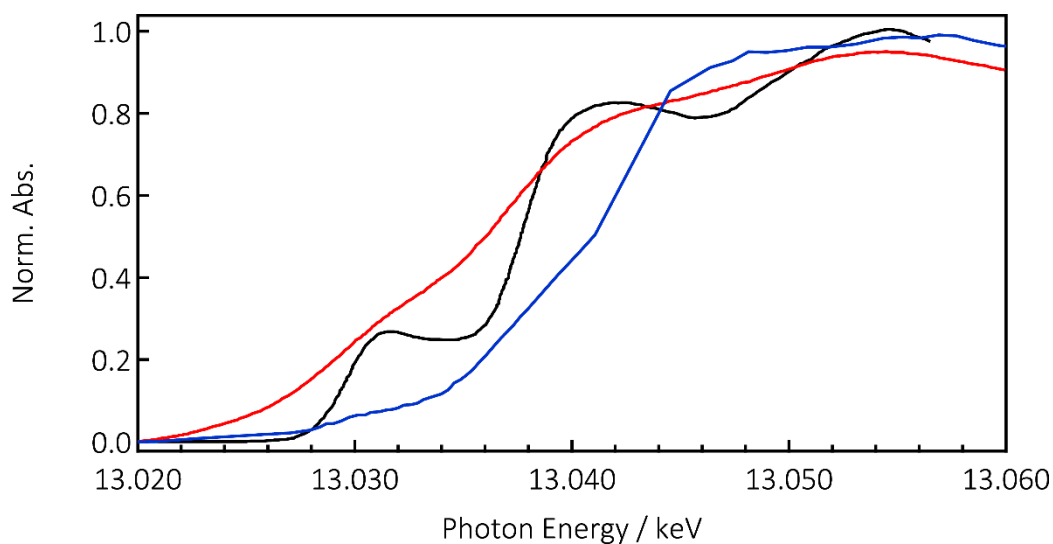


Figure 11.4 - Pb L<sub>3</sub>-edge spectra of CsPb(ClBr)<sub>3</sub> sample (blue). The XANES (red) and the HREFD (black) for PbO are reproduced from ref.<sup>325</sup>.

The partial fluorescence yield (PFY) XANES spectrum of the present CsPb(ClBr)<sub>3</sub> sample is also shown in Figure 11.4. It presents weak shoulders at 13.031 keV, 13.040 keV, 13.046 keV and 13.058 keV. In the absence of calculations, it is difficult to propose an assignment,

but these features may well have some correspondence with the PbO bands, though and not unexpectedly they are shifted in energy due to a different crystal field.

Figure 11.5 is used to investigate if the Pb  $L_3$ -edge transient signal of  $\text{CsPb}(\text{ClBr})_3$  is compatible with an edge shift, either blue or red. In all the computed spectra the rescaling factor used is 0.006, the same as for the Br K-edge simulation of  $\text{CsPb}(\text{ClBr})_3$  with a 6 eV shift. Clearly this approach does not lead to a satisfactory result and therefore the feature observed is rather due to bleaching of a specific transition upon irradiation, as discussed in chapter 9.

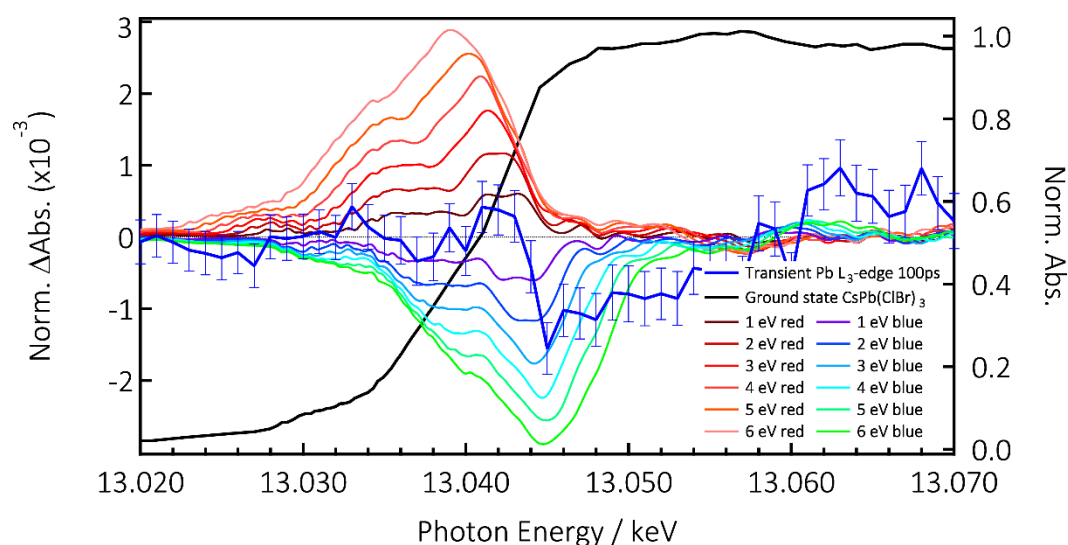


Figure 11.5 - X-ray absorption spectrum of  $\text{CsPb}(\text{ClBr})_3$  NCs at the Pb  $L_3$ -edge (black trace) with the transient at 100 ps upon photoexcitation at 3.5 eV (blue trace) and simulated transient spectra via the rigid shift of different magnitude and signs of the ground state spectrum.



## References

- 1 Parida, B., Iniyar, S. & Goic, R. A review of solar photovoltaic technologies. *Renewable and Sustainable Energy Reviews* **15**, 1625-1636, doi:<http://dx.doi.org/10.1016/j.rser.2010.11.032> (2011).
- 2 Jean, J., Brown, P. R., Jaffe, R. L., Buonassisi, T. & Bulovic, V. Pathways for solar photovoltaics. *Energy & Environmental Science* **8**, 1200-1219, doi:10.1039/C4EE04073B (2015).
- 3 Archer, M. D. & Green, M. A. *Clean Electricity from Photovoltaics*. (World Scientific Publishing Company, 2014).
- 4 Hagfeldt, A., Boschloo, G., Sun, L., Kloo, L. & Pettersson, H. Dye-Sensitized Solar Cells. *Chemical Reviews* **110**, 6595-6663, doi:10.1021/cr900356p (2010).
- 5 Oregan, B. & Gratzel, M. A Low-Cost, High-Efficiency Solar-Cell Based on Dye-Sensitized Colloidal TiO<sub>2</sub> Films. *Nature* **353**, 737-740, doi:10.1038/353737a0 (1991).
- 6 Bach, U. *et al.* Solid-state dye-sensitized mesoporous TiO<sub>2</sub> solar cells with high photon-to-electron conversion efficiencies. *Nature* **395**, 583-585 (1998).
- 7 Kojima, A., Teshima, K., Shirai, Y. & Miyasaka, T. Organometal Halide Perovskites as Visible-Light Sensitizers for Photovoltaic Cells. *Journal of the American Chemical Society* **131**, 6050-6051, doi:10.1021/ja809598r (2009).
- 8 Yang, W. S. *et al.* High-performance photovoltaic perovskite layers fabricated through intramolecular exchange. *Science* **348**, 1234-1237 (2015).
- 9 Lee, M. M., Teuscher, J., Miyasaka, T., Murakami, T. N. & Snaith, H. J. Efficient Hybrid Solar Cells Based on Meso-Superstructured Organometal Halide Perovskites. *Science* **338**, 643-647 (2012).
- 10 Herz, L. M. Charge-Carrier Dynamics in Organic-Inorganic Metal Halide Perovskites. *Annual Review of Physical Chemistry* **67**, 65-89, doi:10.1146/annurev-physchem-040215-112222 (2016).
- 11 Sum, T. C. *et al.* Spectral Features and Charge Dynamics of Lead Halide Perovskites: Origins and Interpretations. *Accounts of Chemical Research* **49**, 294-302, doi:10.1021/acs.accounts.5b00433 (2016).
- 12 Wu, K. *et al.* Ultrafast Interfacial Electron and Hole Transfer from CsPbBr<sub>3</sub> Perovskite Quantum Dots. *Journal of the American Chemical Society* **137**, 12792-12795, doi:10.1021/jacs.5b08520 (2015).
- 13 Berhe, T. A. *et al.* Organometal halide perovskite solar cells: degradation and stability. *Energy & Environmental Science* **9**, 323-356, doi:10.1039/C5EE02733K (2016).

- 14 Ma, Y. *et al.* Titanium Dioxide-Based Nanomaterials for Photocatalytic Fuel Generations. *Chemical Reviews* **114**, 9987-10043, doi:10.1021/cr500008u (2014).
- 15 Santomauro, F. G. *et al.* Femtosecond X-ray absorption study of electron localization in photoexcited anatase TiO<sub>2</sub>. *Scientific Reports* **5**, 14834, doi:10.1038/srep14834 <http://www.nature.com/articles/srep14834#supplementary-information> (2015).
- 16 Liu, L., Zhao, H., Andino, J. M. & Li, Y. Photocatalytic CO<sub>2</sub> Reduction with H<sub>2</sub>O on TiO<sub>2</sub> Nanocrystals: Comparison of Anatase, Rutile, and Brookite Polymorphs and Exploration of Surface Chemistry. *ACS Catalysis* **2**, 1817-1828, doi:10.1021/cs300273q (2012).
- 17 Rittmann-Frank, M. H. *et al.* Mapping of the Photoinduced Electron Traps in TiO<sub>2</sub> by Picosecond X-ray Absorption Spectroscopy. *Angewandte Chemie International Edition* **53**, 5858-5862, doi:10.1002/anie.201310522 (2014).
- 18 Bloch, F. Über die Quantenmechanik der Elektronen in Kristallgittern. *Z. Physik* **52**, 555 (1928).
- 19 Blakemore, J. S. *Solid State Physics*. (Cambridge University Press, 1985).
- 20 Kittel, C. *Introduction to Solid State Physics*. (Wiley, 2004).
- 21 Zhu, T. & Gao, S.-P. The Stability, Electronic Structure, and Optical Property of TiO<sub>2</sub> Polymorphs. *The Journal of Physical Chemistry C* **118**, 11385-11396, doi:10.1021/jp412462m (2014).
- 22 Protesescu, L. *et al.* Nanocrystals of Cesium Lead Halide Perovskites (CsPbX<sub>3</sub>, X = Cl, Br, and I): Novel Optoelectronic Materials Showing Bright Emission with Wide Color Gamut. *Nano Letters* **15**, 3692-3696, doi:10.1021/nl5048779 (2015).
- 23 Murtaza, G. & Ahmad, I. First principle study of the structural and optoelectronic properties of cubic perovskites CsPbM<sub>3</sub> (M=Cl, Br, I). *Physica B: Condensed Matter* **406**, 3222-3229, doi:<http://dx.doi.org/10.1016/j.physb.2011.05.028> (2011).
- 24 Mosconi, E., Amat, A., Nazeeruddin, M. K., Grätzel, M. & De Angelis, F. First-Principles Modeling of Mixed Halide Organometal Perovskites for Photovoltaic Applications. *The Journal of Physical Chemistry C* **117**, 13902-13913, doi:10.1021/jp4048659 (2013).
- 25 Yin, W.-J., Shi, T. & Yan, Y. Unusual defect physics in CH<sub>3</sub>NH<sub>3</sub>PbI<sub>3</sub> perovskite solar cell absorber. *Applied Physics Letters* **104**, 063903, doi:<http://dx.doi.org/10.1063/1.4864778> (2014).
- 26 Bonati, C. *Ultrafast carrier and lattice dynamics in semiconductor and metal nanocrystals*, EPFL, (2007).
- 27 Rodriguez, J. A. & Fernández-García, M. *Synthesis, Properties, and Applications of Oxide Nanomaterials*. (Wiley, 2007).
- 28 Pankove, J. I. *Optical Processes in Semiconductors*. (Dover Publications, 2012).
- 29 Yu, P. Y. & Cardona, M. *Fundamentals of Semiconductors: Physics and Materials Properties*. (Springer, 1996).



- 30 Timoshenko, V. Y., Dittrich, T., Lysenko, V., Lisachenko, M. G. & Koch, F. Free charge carriers in mesoporous silicon. *Physical Review B* **64**, 085314 (2001).
- 31 Matsuzaki, H. *et al.* Photocarrier dynamics in anatase TiO<sub>2</sub> investigated by pump-probe absorption spectroscopy. *Journal of Applied Physics* **115**, 053514, doi:<http://dx.doi.org/10.1063/1.4864219> (2014).
- 32 Narra, S., Chung, C.-C., Diao, E. W.-G. & Shigeto, S. Simultaneous Observation of an Intraband Transition and Distinct Transient Species in the Infrared Region for Perovskite Solar Cells. *The Journal of Physical Chemistry Letters* **7**, 2450-2455, doi:10.1021/acs.jpcclett.6b01111 (2016).
- 33 Liang, W. Y. Excitons. *Physics Education* **5**, 226 (1970).
- 34 Frenkel, J. On the Transformation of light into Heat in Solids. I. *Physical Review* **37**, 17-44 (1931).
- 35 Mott, N. F. The Electrical Conductivity of Transition Metals. *Proceedings of the Royal Society of London. Series A - Mathematical and Physical Sciences* **153**, 699-717, doi:10.1098/rspa.1936.0031 (1936).
- 36 Zhu, X. Y., Yang, Q. & Muntwiler, M. Charge-Transfer Excitons at Organic Semiconductor Surfaces and Interfaces. *Accounts of Chemical Research* **42**, 1779-1787, doi:10.1021/ar800269u (2009).
- 37 Benoit À La Guillaume, C. High intensity excitation effects in semiconductors. *Journal of Luminescence* **12**, 57-66, doi:[http://dx.doi.org/10.1016/0022-2313\(76\)90065-X](http://dx.doi.org/10.1016/0022-2313(76)90065-X) (1976).
- 38 Wang, Y. *et al.* All-Inorganic Colloidal Perovskite Quantum Dots: A New Class of Lasing Materials with Favorable Characteristics. *Advanced Materials* **27**, 7101-7108, doi:10.1002/adma.201503573 (2015).
- 39 Walsh, A., Scanlon, D. O., Chen, S., Gong, X. G. & Wei, S.-H. Self-Regulation Mechanism for Charged Point Defects in Hybrid Halide Perovskites. *Angewandte Chemie International Edition* **54**, 1791-1794, doi:10.1002/anie.201409740 (2015).
- 40 Luca, V. Comparison of Size-Dependent Structural and Electronic Properties of Anatase and Rutile Nanoparticles. *The Journal of Physical Chemistry C* **113**, 6367-6380, doi:10.1021/jp808358v (2009).
- 41 Anderson, P. W. Absence of Diffusion in Certain Random Lattices. *Physical Review* **109**, 1492-1505 (1958).
- 42 Davini, C. A proposal for a continuum theory of defective crystals. *Archive for Rational Mechanics and Analysis* **96**, 295-317, doi:10.1007/bf00251800 (1986).
- 43 Mott, N. F. & Davis, E. A. *Electronic Processes in Non-Crystalline Materials*. (OUP Oxford, 2012).
- 44 Zallen, R. *The Physics of Amorphous Solids*. (Wiley, 1998).
- 45 Emin, D. *Polarons*. (Cambridge University Press, 2013).
- 46 Byrnes, S. J. F. Basic theory and phenomenology of polarons. (2008).

- 47 Suzuki, S. & Toyozawa, Y. Coexistence of Itinerant Electrons and Self-Trapped Electrons. *J Phys Soc Jpn* **59**, 2841-2847, doi:Doi 10.1143/Jpsj.59.2841 (1990).
- 48 Shinozuka, Y. & Toyozawa, Y. Self-Trapping in Mixed Crystal –Clustering, Dimensionality, Percolation–. *Journal of the Physical Society of Japan* **46**, 505-514, doi:10.1143/JPSJ.46.505 (1979).
- 49 Moser, S. *et al.* Electron-Phonon Coupling in the Bulk of Anatase  $\text{TiO}_2$  Measured by Resonant Inelastic X-Ray Spectroscopy. *Physical Review Letters* **115**, 096404 (2015).
- 50 Neukirch, A. J. *et al.* Polaron Stabilization by Cooperative Lattice Distortion and Cation Rotations in Hybrid Perovskite Materials. *Nano Letters* **16**, 3809-3816, doi:10.1021/acs.nanolett.6b01218 (2016).
- 51 Toyozawa, Y., Song, K. S. & Williams, R. T. *Self-Trapped Excitons*. (Springer Berlin Heidelberg, 2013).
- 52 Tsuda, N., Nasu, K., Fujimori, A. & Siratori, K. *Electronic Conduction in Oxides*. (Springer Berlin Heidelberg, 2014).
- 53 Watanabe, M. & Hayashi, T. Time-resolved study of self-trapped exciton luminescence in anatase  $\text{TiO}_2$  under two-photon excitation. *Journal of Luminescence* **112**, 88-91, doi:<http://dx.doi.org/10.1016/j.jlumin.2004.09.001> (2005).
- 54 Chow, W. W., Koch, S. W. & Sargent, M. I. I. *Semiconductor-Laser Physics*. (Springer Berlin Heidelberg, 2012).
- 55 Schweizer, H. *et al.* Ionization of the Direct-Gap Exciton in Photoexcited Germanium. *Physical Review Letters* **51**, 698-701 (1983).
- 56 Trinh, M. T., Wu, X., Niesner, D. & Zhu, X. Y. Many-body interactions in photo-excited lead iodide perovskite. *Journal of Materials Chemistry A* **3**, 9285-9290, doi:10.1039/C5TA01093D (2015).
- 57 Grancini, G. *et al.* Role of microstructure in the electron–hole interaction of hybrid lead halide perovskites. *Nat Photon* **9**, 695-701, doi:10.1038/nphoton.2015.151 <http://www.nature.com/nphoton/journal/v9/n10/abs/nphoton.2015.151.html#supplementary-information> (2015).
- 58 Hendry, E., Koeberg, M. & Bonn, M. Exciton and electron-hole plasma formation dynamics in ZnO. *Physical Review B* **76**, 045214 (2007).
- 59 Pogna, E. A. A. *et al.* Photo-Induced Bandgap Renormalization Governs the Ultrafast Response of Single-Layer  $\text{MoS}_2$ . *ACS Nano* **10**, 1182-1188, doi:10.1021/acsnano.5b06488 (2016).
- 60 Hwang, E. H. & Das Sarma, S. Band-gap renormalization in photoexcited semiconductor quantum-wire structures in the  $\text{GW}$  approximation. *Physical Review B* **58**, R1738-R1741 (1998).
- 61 Reynolds, D. C., Look, D. C. & Jogai, B. Combined effects of screening and band gap renormalization on the energy of optical transitions in ZnO and GaN. *Journal of Applied Physics* **88**, 5760-5763, doi:<http://dx.doi.org/10.1063/1.1320026> (2000).

- 
- 62 Price, M. B. *et al.* Hot-carrier cooling and photoinduced refractive index changes in organic-inorganic lead halide perovskites. *Nat Commun* **6**, doi:10.1038/ncomms9420 (2015).
- 63 Pankove, J. I. *Optical processes in semiconductors*. (Prentice-Hall, 1971).
- 64 Vance, F. W., Williams, R. D. & Hupp, J. T. Electroabsorption spectroscopy of molecular inorganic compounds. *International Reviews in Physical Chemistry* **17**, 307-329, doi:10.1080/014423598230072 (1998).
- 65 Dow, J. D. & Redfield, D. Electroabsorption in Semiconductors: The Excitonic Absorption Edge. *Physical Review B* **1**, 3358-3371 (1970).
- 66 Ziffer, M. E., Mohammed, J. C. & Ginger, D. S. Electroabsorption Spectroscopy Measurements of the Exciton Binding Energy, Electron–Hole Reduced Effective Mass, and Band Gap in the Perovskite CH<sub>3</sub>NH<sub>3</sub>PbI<sub>3</sub>. *ACS Photonics* **3**, 1060-1068, doi:10.1021/acsp Photonics.6b00139 (2016).
- 67 Nozik, A. J. SPECTROSCOPY AND HOT ELECTRON RELAXATION DYNAMICS IN SEMICONDUCTOR QUANTUM WELLS AND QUANTUM DOTS. *Annual Review of Physical Chemistry* **52**, 193-231, doi:doi:10.1146/annurev.physchem.52.1.193 (2001).
- 68 Shah, J. *Ultrafast Spectroscopy of Semiconductors and Semiconductor Nanostructures*. (Springer, 1999).
- 69 Yakunin, S. *et al.* Low-threshold amplified spontaneous emission and lasing from colloidal nanocrystals of caesium lead halide perovskites. *Nat Commun* **6**, doi:10.1038/ncomms9056 (2015).
- 70 Zhu, H. *et al.* Lead halide perovskite nanowire lasers with low lasing thresholds and high quality factors. *Nat Mater* **14**, 636-642, doi:10.1038/nmat4271 <http://www.nature.com/nmat/journal/v14/n6/abs/nmat4271.html#supplementary-information> (2015).
- 71 Goudon, T., Miljanović, V. & Schmeiser, C. On the Shockley–Read–Hall Model: Generation-Recombination in Semiconductors. *SIAM Journal on Applied Mathematics* **67**, 1183-1201, doi:doi:10.1137/060650751 (2007).
- 72 Hall, R. N. Electron-Hole Recombination in Germanium. *Physical Review* **87**, 387-387 (1952).
- 73 Shockley, W. & Read, W. T. Statistics of the Recombinations of Holes and Electrons. *Physical Review* **87**, 835-842 (1952).
- 74 Martí, A., Cuadra, L., López, N. & Luque, A. Intermediate band solar cells: Comparison with shockley-read-hall recombination. *Semiconductors* **38**, 946-949, doi:10.1134/1.1787117 (2004).
- 75 Landsberg, P. T. *Recombination in Semiconductors*. (Cambridge University Press, 1992).

- 76 Chung, S. *et al.* Evidence for a large phononic band gap leading to slow hot carrier thermalisation. *IOP Conference Series: Materials Science and Engineering* **68**, 012002 (2014).
- 77 Yang, Y. *et al.* Observation of a hot-phonon bottleneck in lead-iodide perovskites. *Nat Photon* **10**, 53-59, doi:10.1038/nphoton.2015.213 <http://www.nature.com/nphoton/journal/v10/n1/abs/nphoton.2015.213.html#supplementary-information> (2016).
- 78 Reinhard, M. E. *Ultrafast X-Ray and 2-Dimensional UV Spectroscopic Studies of Hexacyanoferrate Ions in Solution*, EPFL, (2013).
- 79 Consani, C. *Ultrafast One- and Two-Dimensional UV Transient Absorption Spectroscopy of Haem Proteins*, EPFL, (2012).
- 80 Sa, J. *High-Resolution XAS/XES: Analyzing Electronic Structures of Catalysts*. (Taylor & Francis, 2014).
- 81 Pellegrini, C., Marinelli, A. & Reiche, S. The physics of x-ray free-electron lasers. *Reviews of Modern Physics* **88**, 015006 (2016).
- 82 Duncan, W. D. & Williams, G. P. Infrared synchrotron radiation from electron storage rings. *Appl. Opt.* **22**, 2914-2923, doi:10.1364/AO.22.002914 (1983).
- 83 Codling, K. Applications of synchrotron radiation (ultraviolet spectral light source). *Reports on Progress in Physics* **36**, 541 (1973).
- 84 Mobilio, S., Boscherini, F. & Meneghini, C. *Synchrotron Radiation: Basics, Methods and Applications*. (Springer Berlin Heidelberg, 2014).
- 85 Yoshio, S. & Fumihiko, U. X-Ray Focusing with Elliptical Kirkpatrick-Baez Mirror System. *Japanese Journal of Applied Physics* **30**, 1127 (1991).
- 86 Bunker, G. *Introduction to XAFS: A Practical Guide to X-ray Absorption Fine Structure Spectroscopy*. (Cambridge University Press, 2010).
- 87 Lima, F. A. *et al.* A high-repetition rate scheme for synchrotron-based picosecond laser pump/x-ray probe experiments on chemical and biological systems in solution. *Review of Scientific Instruments* **82**, 063111, doi:doi:<http://dx.doi.org/10.1063/1.3600616> (2011).
- 88 Gabard, A. L. *et al.* A 2.9 Tesla Room Temperature Superbend Magnet for the Swiss Light Source at PSI. *Conf.Proc.* **C110904**, 3040-3042 (2011).
- 89 Rittmann-Frank, M. H. *Picosecond X-ray Absorption Studies of Electron Dynamics in Titania Nanoparticles and Ruthenium Dye Sensitizer Complexes*, EPFL, (2014).
- 90 Zholents, A. A. & Zolotarev, M. S. Femtosecond X-Ray Pulses of Synchrotron Radiation. *Physical Review Letters* **76**, 912-915 (1996).
- 91 Beaud, P. *et al.* Spatiotemporal Stability of a Femtosecond Hard\char21{}X-Ray Undulator Source Studied by Control of Coherent Optical Phonons. *Physical Review Letters* **99**, 174801 (2007).

- 92 Danailov, M. B. *et al.* Towards jitter-free pump-probe measurements at seeded free electron laser facilities. *Opt. Express* **22**, 12869-12879, doi:10.1364/OE.22.012869 (2014).
- 93 Gawelda, W., Szlachetko, J. & Milne, C. J. in *X-Ray Absorption and X-Ray Emission Spectroscopy* 637-669 (John Wiley & Sons, Ltd, 2016).
- 94 von Korff Schmising, C. *et al.* Accurate time delay determination for femtosecond X-ray diffraction experiments. *Applied Physics B* **88**, 1-4, doi:10.1007/s00340-007-2678-7 (2007).
- 95 Van Den Zegel, M., Boens, N., Daems, D. & De Schryver, F. C. Possibilities and limitations of the time-correlated single photon counting technique: a comparative study of correction methods for the wavelength dependence of the instrument response function. *Chemical Physics* **101**, 311-335, doi:[http://dx.doi.org/10.1016/0301-0104\(86\)85096-0](http://dx.doi.org/10.1016/0301-0104(86)85096-0) (1986).
- 96 Thamaphat, K., Limsuwan, P. & Ngotawornchai, B. Phase Characterization of TiO<sub>2</sub> Powder by XRD and TEM. *Nat. Sci.* **42**, 357-361 (2008).
- 97 Moller, C. K. Crystal Structure and Photoconductivity of Caesium Plumbahalides. *Nature* **182**, 1436-1436, doi:Doi 10.1038/1821436a0 (1958).
- 98 Chung, I., Lee, B., He, J. Q., Chang, R. P. H. & Kanatzidis, M. G. All-solid-state dye-sensitized solar cells with high efficiency. *Nature* **485**, 486-U494, doi:Doi 10.1038/Nature11067 (2012).
- 99 Linsebigler, A. L., Lu, G. Q. & Yates, J. T. Photocatalysis on TiO<sub>2</sub> Surfaces - Principles, Mechanisms, and Selected Results. *Chemical Reviews* **95**, 735-758, doi:Doi 10.1021/Cr00035a013 (1995).
- 100 Fujishima, A., Zhang, X. T. & Tryk, D. A. TiO<sub>2</sub> photocatalysis and related surface phenomena. *Surf Sci Rep* **63**, 515-582, doi:DOI 10.1016/j.surfrep.2008.10.001 (2008).
- 101 Hoffmann, M. R., Martin, S. T., Choi, W. & Bahnemann, D. W. Environmental Applications of Semiconductor Photocatalysis. *Chemical Reviews* **95**, 69-96, doi:10.1021/cr00033a004 (1995).
- 102 Fujishima, A. & Honda, K. Electrochemical Photolysis of Water at a Semiconductor Electrode. *Nature* **238**, 37-38 (1972).
- 103 Bai, Y., Mora-Seró, I., De Angelis, F., Bisquert, J. & Wang, P. Titanium Dioxide Nanomaterials for Photovoltaic Applications. *Chemical Reviews* **114**, 10095-10130, doi:10.1021/cr400606n (2014).
- 104 Gratzel, M. Solar energy conversion by dye-sensitized photovoltaic cells. *Inorg Chem* **44**, 6841-6851, doi:10.1021/ic0508371 (2005).
- 105 Kim, H.-S. *et al.* Lead Iodide Perovskite Sensitized All-Solid-State Submicron Thin Film Mesoscopic Solar Cell with Efficiency Exceeding 9%. *Scientific Reports* **2**, 591, doi:10.1038/srep00591 <http://www.nature.com/articles/srep00591#supplementary-information> (2012).



- 106 Ning, Z. & Tian, H. Triarylamine: a promising core unit for efficient photovoltaic materials. *Chemical Communications*, 5483-5495, doi:10.1039/B908802D (2009).
- 107 Liu, K., Cao, M., Fujishima, A. & Jiang, L. Bio-Inspired Titanium Dioxide Materials with Special Wettability and Their Applications. *Chemical Reviews* **114**, 10044-10094, doi:10.1021/cr4006796 (2014).
- 108 Xi, B. *et al.* TiO<sub>2</sub> Thin Films Prepared via Adsorptive Self-Assembly for Self-Cleaning Applications. *ACS Applied Materials & Interfaces* **4**, 1093-1102, doi:10.1021/am201721e (2012).
- 109 Thompson, T. L. & Yates, J. T. Surface Science Studies of the Photoactivation of TiO<sub>2</sub>New Photochemical Processes. *Chemical Reviews* **106**, 4428-4453, doi:10.1021/cr050172k (2006).
- 110 Emeline, A. V., Rudakova, A. V., Sakai, M., Murakami, T. & Fujishima, A. Factors Affecting UV-Induced Superhydrophilic Conversion of a TiO<sub>2</sub> Surface. *The Journal of Physical Chemistry C* **117**, 12086-12092, doi:10.1021/jp400421v (2013).
- 111 Hanaor, D. A. H. & Sorrell, C. C. Review of the anatase to rutile phase transformation. *J Mater Sci* **46**, 855-874, doi:10.1007/s10853-010-5113-0 (2011).
- 112 Zhang, H., Chen, B., Banfield, J. F. & Waychunas, G. A. Atomic structure of nanometer-sized amorphous  $\text{TiO}_2$ . *Physical Review B* **78**, 214106 (2008).
- 113 Chen, L. X., Rajh, T., Jager, W., Nedeljkovic, J. & Thurnauer, M. C. X-ray absorption reveals surface structure of titanium dioxide nanoparticles. *Journal of Synchrotron Radiation* **6**, 445-447, doi:doi:10.1107/S090904959801591X (1999).
- 114 Digdaya, I. A. *et al.* Extracting large photovoltages from a-SiC photocathodes with an amorphous TiO<sub>2</sub> front surface field layer for solar hydrogen evolution. *Energy & Environmental Science* **8**, 1585-1593, doi:10.1039/C5EE00769K (2015).
- 115 Diebold, U. The surface science of titanium dioxide. *Surf Sci Rep* **48**, 53-229, doi:[http://dx.doi.org/10.1016/S0167-5729\(02\)00100-0](http://dx.doi.org/10.1016/S0167-5729(02)00100-0) (2003).
- 116 Farges, F., Brown, G. E. & Rehr, J. J. Ti  $K$ -edge XANES studies of Ti coordination and disorder in oxide compounds: Comparison between theory and experiment. *Physical Review B* **56**, 1809-1819 (1997).
- 117 Asahi, R., Taga, Y., Mannstadt, W. & Freeman, A. J. Electronic and optical properties of anatase  $\text{TiO}_2$ . *Physical Review B* **61**, 7459-7465 (2000).
- 118 Scanlon, D. O. *et al.* Band alignment of rutile and anatase TiO<sub>2</sub>. *Nat Mater* **12**, 798-801, doi:10.1038/nmat3697 <http://www.nature.com/nmat/journal/v12/n9/abs/nmat3697.html#supplementary-information> (2013).
- 119 Jiang, N., Su, D. & Spence, J. C. H. Determination of Ti coordination from pre-edge peaks in Ti  $K$ -edge XANES. *Physical Review B* **76**, 214117 (2007).

- 
- 120 Xu, A.-W., Gao, Y. & Liu, H.-Q. The Preparation, Characterization, and their Photocatalytic Activities of Rare-Earth-Doped TiO<sub>2</sub> Nanoparticles. *Journal of Catalysis* **207**, 151-157, doi:<http://dx.doi.org/10.1006/jcat.2002.3539> (2002).
- 121 Choi, W., Termin, A. & Hoffmann, M. R. The Role of Metal Ion Dopants in Quantum-Sized TiO<sub>2</sub>: Correlation between Photoreactivity and Charge Carrier Recombination Dynamics. *The Journal of Physical Chemistry* **98**, 13669-13679, doi:10.1021/j100102a038 (1994).
- 122 Asahi, R., Morikawa, T., Ohwaki, T., Aoki, K. & Taga, Y. Visible-Light Photocatalysis in Nitrogen-Doped Titanium Oxides. *Science* **293**, 269-271, doi:10.1126/science.1061051 (2001).
- 123 Jupille, J. & Thornton, G. *Defects at Oxide Surfaces*. (Springer International Publishing, 2015).
- 124 Wang, S. *et al.* Titanium-Defected Undoped Anatase TiO<sub>2</sub> with p-Type Conductivity, Room-Temperature Ferromagnetism, and Remarkable Photocatalytic Performance. *Journal of the American Chemical Society* **137**, 2975-2983, doi:10.1021/ja512047k (2015).
- 125 Di Valentin, C., Pacchioni, G. & Selloni, A. Reduced and n-Type Doped TiO<sub>2</sub>: Nature of Ti<sup>3+</sup> Species. *The Journal of Physical Chemistry C* **113**, 20543-20552, doi:10.1021/jp9061797 (2009).
- 126 Zhang, J. & Nosaka, Y. Mechanism of the OH Radical Generation in Photocatalysis with TiO<sub>2</sub> of Different Crystalline Types. *The Journal of Physical Chemistry C* **118**, 10824-10832, doi:10.1021/jp501214m (2014).
- 127 Skinner, D. E., Colombo, D. P., Cavaleri, J. J. & Bowman, R. M. Femtosecond Investigation of Electron Trapping in Semiconductor Nanoclusters. *The Journal of Physical Chemistry* **99**, 7853-7856, doi:10.1021/j100020a003 (1995).
- 128 Colombo, D. P. & Bowman, R. M. Femtosecond diffuse reflectance spectroscopy of TiO<sub>2</sub> powders. *The Journal of Physical Chemistry* **99**, 11752-11756, doi:10.1021/j100030a020 (1995).
- 129 Tamaki, Y. *et al.* Dynamics of efficient electron-hole separation in TiO<sub>2</sub> nanoparticles revealed by femtosecond transient absorption spectroscopy under the weak-excitation condition. *Phys Chem Chem Phys* **9**, 1453-1460, doi:10.1039/B617552j (2007).
- 130 Serpone, N., Lawless, D., Khairutdinov, R. & Pelizzetti, E. Subnanosecond Relaxation Dynamics in TiO<sub>2</sub> Colloidal Sols (Particle Sizes  $R_p = 1.0$ -13.4 nm). Relevance to Heterogeneous Photocatalysis. *The Journal of Physical Chemistry* **99**, 16655-16661, doi:10.1021/j100045a027 (1995).
- 131 Mercado, C. C. *et al.* Location of Hole and Electron Traps on Nanocrystalline Anatase TiO<sub>2</sub>. *The Journal of Physical Chemistry C* **116**, 10796-10804, doi:10.1021/jp301680d (2012).

- 132 Furube, A. *et al.* *Physical Chemistry of Interfaces and Nanomaterials VI*, edited by Piotr Piotrowiak, Garry Rumbles, Proc. of SPIE **6643**, 66430J, 0277-786X/07/\$18 · doi: 10.1117/12.733316134 (2007).
- 133 Yoshihara, T. *et al.* Identification of Reactive Species in Photoexcited Nanocrystalline TiO<sub>2</sub> Films by Wide-Wavelength-Range (400–2500 nm) Transient Absorption Spectroscopy. *The Journal of Physical Chemistry B* **108**, 3817-3823, doi:10.1021/jp031305d (2004).
- 134 Thompson, T. L. & Yates, J. T. Monitoring Hole Trapping in Photoexcited TiO<sub>2</sub>(110) Using a Surface Photoreaction. *The Journal of Physical Chemistry B* **109**, 18230-18236, doi:10.1021/jp0530451 (2005).
- 135 Yamada, Y. & Kanemitsu, Y. Determination of electron and hole lifetimes of rutile and anatase TiO<sub>2</sub> single crystals. *Applied Physics Letters* **101**, 133907, doi:doi:<http://dx.doi.org/10.1063/1.4754831> (2012).
- 136 Cavigli, L. *et al.* Carrier recombination dynamics in anatase TiO<sub>2</sub> nanoparticles. *Solid State Sciences* **12**, 1877-1880, doi:<http://dx.doi.org/10.1016/j.solidstatesciences.2010.01.036> (2010).
- 137 Tang, H., Berger, H., Schmid, P. E., Lévy, F. & Burri, G. Photoluminescence in TiO<sub>2</sub> anatase single crystals. *Solid State Communications* **87**, 847-850, doi:[http://dx.doi.org/10.1016/0038-1098\(93\)90427-O](http://dx.doi.org/10.1016/0038-1098(93)90427-O) (1993).
- 138 Rothenberger, G., Moser, J., Graetzel, M., Serpone, N. & Sharma, D. K. Charge carrier trapping and recombination dynamics in small semiconductor particles. *Journal of the American Chemical Society* **107**, 8054-8059, doi:10.1021/ja00312a043 (1985).
- 139 Shkrob, I. A. & Sauer, M. C. Hole Scavenging and Photo-Stimulated Recombination of Electron–Hole Pairs in Aqueous TiO<sub>2</sub> Nanoparticles. *The Journal of Physical Chemistry B* **108**, 12497-12511, doi:10.1021/jp047736t (2004).
- 140 Wang, X. *et al.* Trap states and carrier dynamics of TiO<sub>2</sub> studied by photoluminescence spectroscopy under weak excitation condition. *Physical Chemistry Chemical Physics* **12**, 7083-7090, doi:10.1039/B925277K (2010).
- 141 Fujihara, K., Izumi, S., Ohno, T. & Matsumura, M. Time-resolved photoluminescence of particulate TiO<sub>2</sub> photocatalysts suspended in aqueous solutions. *Journal of Photochemistry and Photobiology A: Chemistry* **132**, 99-104, doi:[http://dx.doi.org/10.1016/S1010-6030\(00\)00204-5](http://dx.doi.org/10.1016/S1010-6030(00)00204-5) (2000).
- 142 Cavigli, L., Bogani, F., Vinattieri, A., Faso, V. & Baldi, G. Volume versus surface-mediated recombination in anatase TiO<sub>2</sub> nanoparticles. *Journal of Applied Physics* **106**, 053516, doi:doi:<http://dx.doi.org/10.1063/1.3211291> (2009).
- 143 Furube, A., Asahi, T., Masuhara, H., Yamashita, H. & Anpo, M. Charge Carrier Dynamics of Standard TiO<sub>2</sub> Catalysts Revealed by Femtosecond Diffuse Reflectance Spectroscopy. *The Journal of Physical Chemistry B* **103**, 3120-3127, doi:10.1021/jp984162h (1999).



- 144 Miyashita, K. *et al.* Photoluminescence study of electron–hole recombination dynamics in the vacuum-deposited SiO<sub>2</sub>/TiO<sub>2</sub> multilayer film with photo-catalytic activity. *Chemical Physics Letters* **369**, 225–231, doi:[http://dx.doi.org/10.1016/S0009-2614\(02\)02009-2](http://dx.doi.org/10.1016/S0009-2614(02)02009-2) (2003).
- 145 Deskins, N. A. & Dupuis, M. Electron transport via polaron hopping in bulk  $\text{TiO}_2$ : A density functional theory characterization. *Physical Review B* **75**, 195212 (2007).
- 146 Di Valentin, C. & Selloni, A. Bulk and Surface Polarons in Photoexcited Anatase TiO<sub>2</sub>. *The Journal of Physical Chemistry Letters* **2**, 2223–2228, doi:10.1021/jz2009874 (2011).
- 147 Moser, S. *et al.* Tunable Polaronic Conduction in Anatase  $\text{TiO}_2$ . *Physical Review Letters* **110**, 196403 (2013).
- 148 Sezen, H. *et al.* Probing electrons in TiO<sub>2</sub> polaronic trap states by IR-absorption: Evidence for the existence of hydrogenic states. *Scientific Reports* **4**, 3808, doi:10.1038/srep03808 <http://www.nature.com/articles/srep03808#supplementary-information> (2014).
- 149 Setvin, M. *et al.* Direct View at Excess Electrons in  $\text{TiO}_2$  Rutile and Anatase. *Physical Review Letters* **113**, 086402 (2014).
- 150 Selcuk, S. & Selloni, A. Facet-dependent trapping and dynamics of excess electrons at anatase TiO<sub>2</sub> surfaces and aqueous interfaces. *Nat Mater* **advance online publication**, doi:10.1038/nmat4672 <http://www.nature.com/nmat/journal/vaop/ncurrent/abs/nmat4672.html#supplementary-information> (2016).
- 151 Di Valentin, C., Pacchioni, G. & Selloni, A. Reduced and n-Type Doped TiO<sub>2</sub>: Nature of Ti<sup>3+</sup> Species. *J Phys Chem C* **113**, 20543–20552, doi:10.1021/Jp9061797 (2009).
- 152 Szczepankiewicz, S. H., Moss, J. A. & Hoffmann, M. R. Slow surface charge trapping kinetics on irradiated TiO<sub>2</sub>. *J Phys Chem B* **106**, 2922–2927, doi:10.1021/Jp004244h (2002).
- 153 Dimitrijevic, N. M., Saponjic, Z. V., Rabatic, B. M., Poluektov, O. G. & Rajh, T. Effect of size and shape of nanocrystalline TiO<sub>2</sub> on photogenerated charges. An EPR study. *J Phys Chem C* **111**, 14597–14601, doi:10.1021/Jp0756395 (2007).
- 154 Berger, T. *et al.* Light-induced charge separation in anatase TiO<sub>2</sub> particles. *J Phys Chem B* **109**, 6061–6068, doi:10.1021/Jp0404293 (2005).
- 155 Mercado, C. C. *et al.* Location of Hole and Electron Traps on Nanocrystalline Anatase TiO<sub>2</sub>. *J Phys Chem C* **116**, 10796–10804, doi:10.1021/Jp301680d (2012).
- 156 Thompson, T. L. & Yates, J. T. Monitoring hole trapping in photoexcited TiO<sub>2</sub>(110) using a surface photoreaction. *J Phys Chem B* **109**, 18230–18236, doi:10.1021/Jp0530451 (2005).

- 157 Egdell, R. G., Eriksen, S. & Flavell, W. R. Oxygen Deficient  $\text{SnO}_2(110)$  and  $\text{TiO}_2(110)$  - a Comparative-Study by Photoemission. *Solid State Communications* **60**, 835-838, doi:Doi 10.1016/0038-1098(86)90607-1 (1986).
- 158 Eriksen, S. & Egdell, R. G. Electronic Excitations at Oxygen Deficient  $\text{TiO}_2(110)$  Surfaces - a Study by EELS. *Surf Sci* **180**, 263-278, doi:Doi 10.1016/0039-6028(87)90048-3 (1987).
- 159 Moser, S. *et al.* Tunable Polaronic Conduction in Anatase  $\text{TiO}_2$ . *Physical Review Letters* **110**, doi:Artn 196403 Doi 10.1103/Physrevlett.110.196403 (2013).
- 160 Setvin, M. *et al.* Direct View at Excess Electrons in  $\text{TiO}_2$  Rutile and Anatase. *Physical Review Letters* **113**, doi:Artn 086402 Doi 10.1103/Physrevlett.113.086402 (2014).
- 161 Thomas, A. G. *et al.* Comparison of the electronic structure of anatase and rutile  $\text{TiO}_2$  single-crystal surfaces using resonant photoemission and x-ray absorption spectroscopy. *Physical Review B* **75**, doi:Artn 035105 Doi 10.1103/Physrevb.75.035105 (2007).
- 162 Berger, T. *et al.* Light-Induced Charge Separation in Anatase  $\text{TiO}_2$  Particles. *The Journal of Physical Chemistry B* **109**, 6061-6068, doi:10.1021/jp0404293 (2005).
- 163 Sekiya, T. *et al.* Defects in anatase  $\text{TiO}_2$  single crystal controlled by heat treatments. *Journal of the Physical Society of Japan* **73**, 703-710, doi:Doi 10.1143/Jpsj.73.703 (2004).
- 164 Rittmann-Frank, M. H. *et al.* Mapping of the Photoinduced Electron Traps in  $\text{TiO}_2$  by Picosecond X-ray Absorption Spectroscopy. *Angew Chem Int Edit* **53**, 5858-5862, doi:10.1002/anie.201310522 (2014).
- 165 Di Valentin, C. & Selloni, A. Bulk and Surface Polarons in Photoexcited Anatase  $\text{TiO}_2$ . *J Phys Chem Lett* **2**, 2223-2228, doi:Doi 10.1021/Jz2009874 (2011).
- 166 Skinner, D. E., Colombo, D. P., Cavaleri, J. J. & Bowman, R. M. Femtosecond Investigation of Electron Trapping in Semiconductor Nanoclusters. *J Phys Chem-Us* **99**, 7853-7856, doi:Doi 10.1021/J100020a003 (1995).
- 167 Colombo, D. P. & Bowman, R. M. Femtosecond Diffuse-Reflectance Spectroscopy of  $\text{TiO}_2$  Powders. *J Phys Chem-Us* **99**, 11752-11756, doi:Doi 10.1021/J100030a020 (1995).
- 168 Serpone, N., Lawless, D. & Khairutdinov, R. Size Effects on the Photophysical Properties of Colloidal Anatase  $\text{TiO}_2$  Particles - Size Quantization or Direct Transitions in This Indirect Semiconductor. *J Phys Chem-Us* **99**, 16646-16654, doi:Doi 10.1021/J100045a026 (1995).
- 169 Yoshihara, T. *et al.* Identification of reactive species in photoexcited nanocrystalline  $\text{TiO}_2$  films by wide-wavelength-range (400-2500 nm) transient absorption spectroscopy. *J Phys Chem B* **108**, 3817-3823, doi:Doi 10.1021/Jp031305d (2004).
- 170 Furube, A. *et al.* Femtosecond visible-to-IR spectroscopy of  $\text{TiO}_2$  nanocrystalline films: Dynamics of UV-generated charge carrier relaxation at different excitation

- wavelengths - art. no. 66430J. *P Soc Photo-Opt Ins* **6643**, J6430-J6430, doi:Doi 10.1117/12.733316 (2007).
- 171 Nemec, H., Kuzel, P. & Sundstrom, V. Charge transport in nanostructured materials for solar energy conversion studied by time-resolved terahertz spectroscopy. *J Photoch Photobio A* **215**, 123-139, doi:DOI 10.1016/j.jphotochem.2010.08.006 (2010).
- 172 Yoo, B.-K., Su, Z., Thomas, J. M. & Zewail, A. H. On the dynamical nature of the active center in a single-site photocatalyst visualized by 4D ultrafast electron microscopy. *Proceedings of the National Academy of Sciences* **113**, 503-508, doi:10.1073/pnas.1522869113 (2016).
- 173 Degroot, F. M. F. *et al.* Differences between L(3) and L(2) X-Ray-Absorption Spectra of Transition-Metal Compounds. *J Chem Phys* **101**, 6570-6576, doi:Doi 10.1063/1.468351 (1994).
- 174 Luca, V. Comparison of Size-Dependent Structural and Electronic Properties of Anatase and Rutile Nanoparticles. *J Phys Chem C* **113**, 6367-6380, doi:Doi 10.1021/Jp808358v (2009).
- 175 Beaud, P. *et al.* Spatiotemporal stability of a femtosecond hard-X-ray undulator source studied by control of coherent optical phonons. *Physical Review Letters* **99**, doi:Artn 174801 Doi 10.1103/Physrevlett.99.174801 (2007).
- 176 Emori, M., Sugita, M., Ozawa, K. & Sakama, H. Electronic structure of epitaxial anatase TiO<sub>2</sub> films: Angle-resolved photoelectron spectroscopy study. *Physical Review B* **85**, doi:Artn 035129 Doi 10.1103/Physrevb.85.035129 (2012).
- 177 Enright, B. & Fitzmaurice, D. Spectroscopic determination of electron and mole effective masses in a nanocrystalline semiconductor film. *J Phys Chem-Us* **100**, 1027-1035, doi:Doi 10.1021/Jp951142w (1996).
- 178 Farges, F., Brown, G. E. & Rehr, J. J. Ti K-edge XANES studies of Ti coordination and disorder in oxide compounds: Comparison between theory and experiment. *Physical Review B* **56**, 1809-1819, doi:DOI 10.1103/PhysRevB.56.1809 (1997).
- 179 Jiang, N., Su, D. & Spence, J. C. H. Determination of ti coordination from pre-edge peaks in TiK-edge XANES. *Physical Review B* **76**, doi:Artn 214117 Doi 10.1103/Physrevb.76.214117 (2007).
- 180 Petkov, V., Holzhuter, G., Troge, U., Gerber, T. & Himmel, B. Atomic-scale structure of amorphous TiO<sub>2</sub> by electron, x-ray diffraction and reverse Monte Carlo simulations. *J Non-Cryst Solids* **231**, 17-30, doi:Doi 10.1016/S0022-3093(98)00418-9 (1998).
- 181 Prasai, B., Cai, B., Underwood, M. K., Lewis, J. P. & Drabold, D. A. Properties of amorphous and crystalline titanium dioxide from first principles. *J Mater Sci* **47**, 7515-7521, doi:DOI 10.1007/s10853-012-6439-6 (2012).
- 182 Zhang, H. Z., Chen, B., Banfield, J. F. & Waychunas, G. A. Atomic structure of nanometer-sized amorphous TiO<sub>2</sub>. *Physical Review B* **78**, 214106, doi:Artn 214106 Doi 10.1103/Physrevb.78.214106 (2008).

- 183 Stoneham, A. M. *et al.* Trapping, self-trapping and the polaron family. *J Phys-Condens Mat* **19**, doi:Artn 255208 Doi 10.1088/0953-8984/19/25/255208 (2007).
- 184 Gonzalez, R. J. & Zallen, R. Optical studies of nanophase titania. *Nato Asi 3 High Tech* **23**, 395-403 (1997).
- 185 Deskins, N. A. & Dupuis, M. Electron transport via polaron hopping in bulk TiO<sub>2</sub>: A density functional theory characterization. *Physical Review B* **75**, doi:Artn 195212 Doi 10.1103/Physrevb.75.195212 (2007).
- 186 Jacimovic, J. *et al.* Pressure dependence of the large-polaron transport in anatase TiO<sub>2</sub> single crystals. *Epl-Europhys Lett* **99**, doi:Artn 57005 Doi 10.1209/0295-5075/99/57005 (2012).
- 187 Szlachetko, J. *et al.* A von Hamos x-ray spectrometer based on a segmented-type diffraction crystal for single-shot x-ray emission spectroscopy and time-resolved resonant inelastic x-ray scattering studies. *Review of Scientific Instruments* **83**, 103105, doi:doi:<http://dx.doi.org/10.1063/1.4756691> (2012).
- 188 Ohno, T., Sarukawa, K., Tokieda, K. & Matsumura, M. Morphology of a TiO<sub>2</sub> Photocatalyst (Degussa, P-25) Consisting of Anatase and Rutile Crystalline Phases. *Journal of Catalysis* **203**, 82-86, doi:<http://dx.doi.org/10.1006/jcat.2001.3316> (2001).
- 189 Hurum, D. C., Agrios, A. G., Gray, K. A., Rajh, T. & Thurnauer, M. C. Explaining the Enhanced Photocatalytic Activity of Degussa P25 Mixed-Phase TiO<sub>2</sub> Using EPR. *The Journal of Physical Chemistry B* **107**, 4545-4549, doi:10.1021/jp0273934 (2003).
- 190 Scanlon, D. O. *et al.* Band alignment of rutile and anatase TiO<sub>2</sub>. *Nat Mater* **12**, 798-801, doi:10.1038/NMAT3697 (2013).
- 191 Luca, V., Djajanti, S. & Howe, R. F. Structural and electronic properties of sol-gel titanium oxides studied by X-ray absorption spectroscopy. *J Phys Chem B* **102**, 10650-10657, doi:Doi 10.1021/Jp981644k (1998).
- 192 Yamamoto, T. Assignment of pre-edge peaks in K-edge x-ray absorption spectra of 3d transition metal compounds: electric dipole or quadrupole? *X-Ray Spectrom* **37**, 572-584, doi:Doi 10.1002/Xrs.1103 (2008).
- 193 Uozumi, T. *et al.* Experimental and Theoretical Investigation of the Pre-Peaks at the Ti K-Edge Absorption-Spectra in Tio<sub>2</sub>. *Europhys Lett* **18**, 85-90, doi:Doi 10.1209/0295-5075/18/1/016 (1992).
- 194 Lee, K. E., Gomez, M. A., Regier, T., Hu, Y. F. & Demopoulos, G. P. Further Understanding of the Electronic Interactions between N719 Sensitizer and Anatase TiO<sub>2</sub> Films: A Combined X-ray Absorption and X-ray Photoelectron Spectroscopic Study. *J Phys Chem C* **115**, 5692-5707, doi:Doi 10.1021/Jp109869z (2011).
- 195 Shirley, E. L. Ti 1s pre-edge features in rutile: a Bethe-Salpeter calculation. *J Electron Spectrosc* **136**, 77-83, doi:10.1016/j.elspec.2004.02.134 (2004).
- 196 Hanley, T. L., Luca, V., Pickering, I. & Howe, R. F. Structure of titania sol-gel films: A study by X-ray absorption spectroscopy. *J Phys Chem B* **106**, 1153-1160, doi:Doi 10.1021/Jp012225h (2002).

- 
- 197 Santomauro, F. *et al.* Femtosecond X-ray absorption study of electron localization in photoexcited anatase TiO<sub>2</sub>. *Sci. Rep.* **5**, doi:doi:10.1038/srep14834 (2015).
- 198 Liu, L. J., Zhao, H. L., Andino, J. M. & Li, Y. Photocatalytic CO<sub>2</sub> Reduction with H<sub>2</sub>O on TiO<sub>2</sub> Nanocrystals: Comparison of Anatase, Rutile, and Brookite Polymorphs and Exploration of Surface Chemistry. *Acs Catalysis* **2**, 1817-1828, doi:10.1021/cs300273q (2012).
- 199 Luttrell, T. *et al.* Why is anatase a better photocatalyst than rutile? - Model studies on epitaxial TiO<sub>2</sub> films. *Scientific Reports* **4**, doi:Artn 4043 10.1038/Srep04043 (2014).
- 200 Tamaki, Y. *et al.* Direct observation of reactive trapped holes in TiO<sub>2</sub> undergoing photocatalytic oxidation of adsorbed alcohols: Evaluation of the reaction rates and yields. *Journal of the American Chemical Society* **128**, 416-417, doi:10.1021/ja055866p (2006).
- 201 Etgar, L. *et al.* Mesoscopic CH<sub>3</sub>NH<sub>3</sub>PbI<sub>3</sub>/TiO<sub>2</sub> Heterojunction Solar Cells. *Journal of the American Chemical Society* **134**, 17396-17399, doi:10.1021/ja307789s (2012).
- 202 Busmundrud, O. & Feder, J. Electrical conduction and phase transitions in CsPbCl<sub>3</sub>. *Solid State Communications* **9**, 1575-1577, doi:[http://dx.doi.org/10.1016/0038-1098\(71\)90610-7](http://dx.doi.org/10.1016/0038-1098(71)90610-7) (1971).
- 203 Weber, D. in *Zeitschrift für Naturforschung B* Vol. 33 1443 (1978).
- 204 Mitzi, D. B., Chondroudis, K. & Kagan, C. R. Organic-inorganic electronics. *IBM J. Res. Dev.* **45**, 29-45, doi:10.1147/rd.451.0029 (2001).
- 205 Stoumpos, C. C. & Kanatzidis, M. G. Halide Perovskites: Poor Man's High-Performance Semiconductors. *Advanced Materials*, n/a-n/a, doi:10.1002/adma.201600265 (2016).
- 206 Li, G. *et al.* Efficient Light-Emitting Diodes Based on Nanocrystalline Perovskite in a Dielectric Polymer Matrix. *Nano Letters* **15**, 2640-2644, doi:10.1021/acs.nanolett.5b00235 (2015).
- 207 Jaramillo-Quintero, O. A., Sanchez, R. S., Rincon, M. & Mora-Sero, I. Bright Visible-Infrared Light Emitting Diodes Based on Hybrid Halide Perovskite with Spiro-OMeTAD as a Hole-Injecting Layer. *The Journal of Physical Chemistry Letters* **6**, 1883-1890, doi:10.1021/acs.jpcllett.5b00732 (2015).
- 208 Luo, J. *et al.* Water photolysis at 12.3% efficiency via perovskite photovoltaics and Earth-abundant catalysts. *Science* **345**, 1593-1596, doi:10.1126/science.1258307 (2014).
- 209 Stoumpos, C. C. *et al.* Crystal Growth of the Perovskite Semiconductor CsPbBr<sub>3</sub>: A New Material for High-Energy Radiation Detection. *Crystal Growth & Design* **13**, 2722-2727, doi:10.1021/cg400645t (2013).
- 210 Yakunin, S. *et al.* Detection of X-ray photons by solution-processed lead halide perovskites. *Nat Photon* **9**, 444-449, doi:10.1038/nphoton.2015.82 <http://www.nature.com/nphoton/journal/v9/n7/abs/nphoton.2015.82.html#supplementary-information> (2015).



- 211 Brenner, T. M., Egger, D. A., Kronik, L., Hodes, G. & Cahen, D. Hybrid organic—inorganic perovskites: low-cost semiconductors with intriguing charge-transport properties. *Nature Reviews Materials* **1**, 15007, doi:10.1038/natrevmats.2015.7 (2016).
- 212 Stoumpos, C. C. & Kanatzidis, M. G. The Renaissance of Halide Perovskites and Their Evolution as Emerging Semiconductors. *Accounts of Chemical Research* **48**, 2791-2802, doi:10.1021/acs.accounts.5b00229 (2015).
- 213 Even, J., Pedesseau, L., Jancu, J.-M. & Katan, C. Importance of Spin–Orbit Coupling in Hybrid Organic/Inorganic Perovskites for Photovoltaic Applications. *The Journal of Physical Chemistry Letters* **4**, 2999-3005, doi:10.1021/jz401532q (2013).
- 214 Umebayashi, T., Asai, K., Kondo, T. & Nakao, A. Electronic structures of lead iodide based low-dimensional crystals. *Physical Review B* **67**, 155405 (2003).
- 215 Butler, K. T., Frost, J. M. & Walsh, A. Band alignment of the hybrid halide perovskites CH<sub>3</sub>NH<sub>3</sub>PbCl<sub>3</sub>, CH<sub>3</sub>NH<sub>3</sub>PbBr<sub>3</sub> and CH<sub>3</sub>NH<sub>3</sub>PbI<sub>3</sub>. *Materials Horizons* **2**, 228-231, doi:10.1039/C4MH00174E (2015).
- 216 Motta, C. *et al.* Revealing the role of organic cations in hybrid halide perovskite CH<sub>3</sub>NH<sub>3</sub>PbI<sub>3</sub>. *Nat Commun* **6**, doi:10.1038/ncomms8026 (2015).
- 217 Choi, J.-H., Cui, P., Lan, H. & Zhang, Z. Linear Scaling of the Exciton Binding Energy versus the Band Gap of Two-Dimensional Materials. *Physical Review Letters* **115**, 066403 (2015).
- 218 Collavini, S., Völker, S. F. & Delgado, J. L. Understanding the Outstanding Power Conversion Efficiency of Perovskite-Based Solar Cells. *Angewandte Chemie International Edition* **54**, 9757-9759, doi:10.1002/anie.201505321 (2015).
- 219 Sadhanala, A. *et al.* Preparation of Single-Phase Films of CH<sub>3</sub>NH<sub>3</sub>Pb(I<sub>1-x</sub>Br<sub>x</sub>)<sub>3</sub> with Sharp Optical Band Edges. *The Journal of Physical Chemistry Letters* **5**, 2501-2505, doi:10.1021/jz501332v (2014).
- 220 De Wolf, S. *et al.* Organometallic Halide Perovskites: Sharp Optical Absorption Edge and Its Relation to Photovoltaic Performance. *The Journal of Physical Chemistry Letters* **5**, 1035-1039, doi:10.1021/jz500279b (2014).
- 221 Shi, D. *et al.* Low trap-state density and long carrier diffusion in organolead trihalide perovskite single crystals. *Science* **347**, 519-522, doi:10.1126/science.aaa2725 (2015).
- 222 Saidaminov, M. I. *et al.* High-quality bulk hybrid perovskite single crystals within minutes by inverse temperature crystallization. *Nat Commun* **6**, doi:10.1038/ncomms8586 (2015).
- 223 Kim, J., Lee, S.-H., Lee, J. H. & Hong, K.-H. The Role of Intrinsic Defects in Methylammonium Lead Iodide Perovskite. *The Journal of Physical Chemistry Letters* **5**, 1312-1317, doi:10.1021/jz500370k (2014).
- 224 Wang, Q. *et al.* Qualifying composition dependent p and n self-doping in CH<sub>3</sub>NH<sub>3</sub>PbI<sub>3</sub>. *Applied Physics Letters* **105**, 163508, doi:doi:<http://dx.doi.org/10.1063/1.4899051> (2014).

- 225 Shi, T., Yin, W.-J., Hong, F., Zhu, K. & Yan, Y. Unipolar self-doping behavior in perovskite  $\text{CH}_3\text{NH}_3\text{PbBr}_3$ . *Applied Physics Letters* **106**, 103902, doi:doi:<http://dx.doi.org/10.1063/1.4914544> (2015).
- 226 Zhu, X. Y. & Podzorov, V. Charge Carriers in Hybrid Organic–Inorganic Lead Halide Perovskites Might Be Protected as Large Polarons. *The Journal of Physical Chemistry Letters* **6**, 4758–4761, doi:10.1021/acs.jpcllett.5b02462 (2015).
- 227 Soufiani, A. M. *et al.* Polaronic exciton binding energy in iodide and bromide organic-inorganic lead halide perovskites. *Applied Physics Letters* **107**, 231902, doi:doi:<http://dx.doi.org/10.1063/1.4936418> (2015).
- 228 Brenner, T. M. *et al.* Are Mobilities in Hybrid Organic–Inorganic Halide Perovskites Actually “High”? *The Journal of Physical Chemistry Letters* **6**, 4754–4757, doi:10.1021/acs.jpcllett.5b02390 (2015).
- 229 Hailegnaw, B., Kirmayer, S., Edri, E., Hodes, G. & Cahen, D. Rain on Methylammonium Lead Iodide Based Perovskites: Possible Environmental Effects of Perovskite Solar Cells. *The Journal of Physical Chemistry Letters* **6**, 1543–1547, doi:10.1021/acs.jpcllett.5b00504 (2015).
- 230 Tong, C.-J. *et al.* Uncovering the Veil of the Degradation in Perovskite  $\text{CH}_3\text{NH}_3\text{PbI}_3$  upon Humidity Exposure: A First-Principles Study. *The Journal of Physical Chemistry Letters* **6**, 3289–3295, doi:10.1021/acs.jpcllett.5b01544 (2015).
- 231 Aristidou, N. *et al.* The Role of Oxygen in the Degradation of Methylammonium Lead Trihalide Perovskite Photoactive Layers. *Angewandte Chemie International Edition* **54**, 8208–8212, doi:10.1002/anie.201503153 (2015).
- 232 Schoonman, J. Organic–inorganic lead halide perovskite solar cell materials: A possible stability problem. *Chemical Physics Letters* **619**, 193–195, doi:<http://dx.doi.org/10.1016/j.cplett.2014.11.063> (2015).
- 233 Azpiroz, J. M., Mosconi, E., Bisquert, J. & De Angelis, F. Defect migration in methylammonium lead iodide and its role in perovskite solar cell operation. *Energy & Environmental Science* **8**, 2118–2127, doi:10.1039/C5EE01265A (2015).
- 234 Misra, R. K. *et al.* Temperature- and Component-Dependent Degradation of Perovskite Photovoltaic Materials under Concentrated Sunlight. *The Journal of Physical Chemistry Letters* **6**, 326–330, doi:10.1021/jz502642b (2015).
- 235 Niu, G. *et al.* Study on the stability of  $\text{CH}_3\text{NH}_3\text{PbI}_3$  films and the effect of post-modification by aluminum oxide in all-solid-state hybrid solar cells. *Journal of Materials Chemistry A* **2**, 705–710, doi:10.1039/C3TA13606J (2014).
- 236 Christians, J. A., Miranda Herrera, P. A. & Kamat, P. V. Transformation of the Excited State and Photovoltaic Efficiency of  $\text{CH}_3\text{NH}_3\text{PbI}_3$  Perovskite upon Controlled Exposure to Humidified Air. *Journal of the American Chemical Society* **137**, 1530–1538, doi:10.1021/ja511132a (2015).
- 237 Leijtens, T. *et al.* Stability of Metal Halide Perovskite Solar Cells. *Advanced Energy Materials* **5**, n/a–n/a, doi:10.1002/aenm.201500963 (2015).



- 238 Stoumpos, C. C., Malliakas, C. D. & Kanatzidis, M. G. Semiconducting Tin and Lead Iodide Perovskites with Organic Cations: Phase Transitions, High Mobilities, and Near-Infrared Photoluminescent Properties. *Inorg Chem* **52**, 9019-9038, doi:10.1021/ic401215x (2013).
- 239 Heo, J. H. *et al.* Efficient inorganic-organic hybrid heterojunction solar cells containing perovskite compound and polymeric hole conductors. *Nat Photon* **7**, 486-491, doi:10.1038/nphoton.2013.80 <http://www.nature.com/nphoton/journal/v7/n6/abs/nphoton.2013.80.html#supplementary-information> (2013).
- 240 Dualeh, A., Gao, P., Seok, S. I., Nazeeruddin, M. K. & Grätzel, M. Thermal Behavior of Methylammonium Lead-Trihalide Perovskite Photovoltaic Light Harvesters. *Chemistry of Materials* **26**, 6160-6164, doi:10.1021/cm502468k (2014).
- 241 Dualeh, A. *et al.* Effect of Annealing Temperature on Film Morphology of Organic–Inorganic Hybrid Perovskite Solid-State Solar Cells. *Advanced Functional Materials* **24**, 3250-3258, doi:10.1002/adfm.201304022 (2014).
- 242 Nedelcu, G. *et al.* Fast Anion-Exchange in Highly Luminescent Nanocrystals of Cesium Lead Halide Perovskites (CsPbX<sub>3</sub>, X = Cl, Br, I). *Nano Letters* **15**, 5635-5640, doi:10.1021/acs.nanolett.5b02404 (2015).
- 243 Lignos, I. *et al.* Synthesis of Cesium Lead Halide Perovskite Nanocrystals in a Droplet-Based Microfluidic Platform: Fast Parametric Space Mapping. *Nano Letters* **16**, 1869-1877, doi:10.1021/acs.nanolett.5b04981 (2016).
- 244 Kulbak, M., Cahen, D. & Hodes, G. How Important Is the Organic Part of Lead Halide Perovskite Photovoltaic Cells? Efficient CsPbBr<sub>3</sub> Cells. *The Journal of Physical Chemistry Letters* **6**, 2452-2456, doi:10.1021/acs.jpcllett.5b00968 (2015).
- 245 Sutton, R. J. *et al.* Bandgap-Tunable Cesium Lead Halide Perovskites with High Thermal Stability for Efficient Solar Cells. *Advanced Energy Materials* **6**, n/a-n/a, doi:10.1002/aenm.201502458 (2016).
- 246 Beal, R. E. *et al.* Cesium Lead Halide Perovskites with Improved Stability for Tandem Solar Cells. *The Journal of Physical Chemistry Letters* **7**, 746-751, doi:10.1021/acs.jpcllett.6b00002 (2016).
- 247 Kulbak, M. *et al.* Cesium Enhances Long-Term Stability of Lead Bromide Perovskite-Based Solar Cells. *The Journal of Physical Chemistry Letters* **7**, 167-172, doi:10.1021/acs.jpcllett.5b02597 (2016).
- 248 Saliba, M. *et al.* Cesium-containing triple cation perovskite solar cells: improved stability, reproducibility and high efficiency. *Energy & Environmental Science* **9**, 1989-1997, doi:10.1039/C5EE03874J (2016).
- 249 Endres, J. *et al.* Valence and Conduction Band Densities of States of Metal Halide Perovskites: A Combined Experimental–Theoretical Study. *The Journal of Physical Chemistry Letters* **7**, 2722-2729, doi:10.1021/acs.jpcllett.6b00946 (2016).

- 250 Heidrich, K., Kunzel, H. & Treusch, J. Optical-Properties and Electronic-Structure of CsPbCl<sub>3</sub> and CsPbBr<sub>3</sub>. *Solid State Communications* **25**, 887-889, doi:10.1016/0038-1098(78)90294-6 (1978).
- 251 Murtaza, G. & Ahmad, I. First principle study of the structural and optoelectronic properties of cubic perovskites CsPbM<sub>3</sub> (M=Cl, Br, I). *Physica B* **406**, 3222-3229, doi:10.1016/j.physb.2011.05.028 (2011).
- 252 Mosconi, E., Amat, A., Nazeeruddin, M. K., Gratzel, M. & De Angelis, F. First-Principles Modeling of Mixed Halide Organometal Perovskites for Photovoltaic Applications. *J Phys Chem C* **117**, 13902-13913, doi:10.1021/jp4048659 (2013).
- 253 Brenner, T. M., Egger, D. A., Kronik, L., Hodes, G. & Cahen, D. Hybrid organic—inorganic perovskites: low-cost semiconductors with intriguing charge-transport properties. *Nature Reviews Materials*, 16011, doi:10.1038/natrevmats.2016.11 (2016).
- 254 Gao, W. *et al.* Quasiparticle band gap of organic-inorganic hybrid perovskites: Crystal structure, spin-orbit coupling, and self-energy effects. *Physical Review B* **93**, 085202 (2016).
- 255 Deschler, F. *et al.* High Photoluminescence Efficiency and Optically Pumped Lasing in Solution-Processed Mixed Halide Perovskite Semiconductors. *The Journal of Physical Chemistry Letters* **5**, 1421-1426, doi:10.1021/jz5005285 (2014).
- 256 Piatkowski, P. *et al.* Direct monitoring of ultrafast electron and hole dynamics in perovskite solar cells. *Physical Chemistry Chemical Physics* **17**, 14674-14684, doi:10.1039/c5cp01119a (2015).
- 257 Piatkowski, P. *et al.* Unraveling Charge Carriers Generation, Diffusion, and Recombination in Formamidinium Lead Triiodide Perovskite Polycrystalline Thin Film. *J Phys Chem Lett* **7**, 204-210, doi:10.1021/acs.jpcclett.5b02648 (2016).
- 258 Ponseca, C. S. *et al.* Mechanism of Charge Transfer and Recombination Dynamics in Organo Metal Halide Perovskites and Organic Electrodes, PCBM, and Spiro-OMeTAD: Role of Dark Carriers. *Journal of the American Chemical Society* **137**, 16043-16048, doi:10.1021/jacs.5b08770 (2015).
- 259 Wu, X. X. *et al.* Trap States in Lead Iodide Perovskites. *Journal of the American Chemical Society* **137**, 2089-2096, doi:10.1021/ja512833n (2015).
- 260 Flender, O., Klein, J. R., Lenzer, T. & Oum, K. Ultrafast photoinduced dynamics of the organolead trihalide perovskite CH<sub>3</sub>NH<sub>3</sub>PbI<sub>3</sub> on mesoporous TiO<sub>2</sub> scaffolds in the 320-920 nm range. *Physical Chemistry Chemical Physics* **17**, 19238-19246, doi:10.1039/c5cp01973g (2015).
- 261 Manser, J. S. & Kamat, P. V. Band filling with free charge carriers in organometal halide perovskites. *Nat Photon* **8**, 737-743, doi:10.1038/nphoton.2014.171 <http://www.nature.com/nphoton/journal/v8/n9/abs/nphoton.2014.171.html#supplementary-information> (2014).
- 262 Wang, L., McCleese, C., Kovalsky, A., Zhao, Y. & Burda, C. Femtosecond Time-Resolved Transient Absorption Spectroscopy of CH<sub>3</sub>NH<sub>3</sub>PbI<sub>3</sub> Perovskite Films:

- Evidence for Passivation Effect of PbI<sub>2</sub>. *Journal of the American Chemical Society* **136**, 12205-12208, doi:10.1021/ja504632z (2014).
- 263 Xing, G. *et al.* Long-Range Balanced Electron- and Hole-Transport Lengths in Organic-Inorganic CH<sub>3</sub>NH<sub>3</sub>PbI<sub>3</sub>. *Science* **342**, 344-347, doi:10.1126/science.1243167 (2013).
- 264 Stampelcoskie, K. G., Manser, J. S. & Kamat, P. V. Dual nature of the excited state in organic-inorganic lead halide perovskites. *Energy & Environmental Science* **8**, 208-215, doi:10.1039/C4EE02988G (2015).
- 265 Leguy, A. M. A. *et al.* Experimental and theoretical optical properties of methylammonium lead halide perovskites. *Nanoscale* **8**, 6317-6327, doi:10.1039/C5NR05435D (2016).
- 266 Anand, B. *et al.* Broadband transient absorption study of photoexcitations in lead halide perovskites: Towards a multiband picture. *Physical Review B* **93**, 161205 (2016).
- 267 Ziffer, M. E., Mohammed, J. C. & Ginger, D. S. Electroabsorption Spectroscopy Measurements of the Exciton Binding Energy, Electron-Hole Reduced Effective Mass, and Band Gap in the Perovskite CH<sub>3</sub>NH<sub>3</sub>PbI<sub>3</sub>. *ACS Photonics*, doi:10.1021/acsphotonics.6b00139 (2016).
- 268 Bouduban, M. E., De Jonghe, J. & Moser, J.-E. Photoinduced Stark effect in colloidal systems: a case study with MAPbBr<sub>3</sub> and AQU/nC60. *Swiss Chemical Society Fall Meeting 2015* (2015).
- 269 Sheng, C. *et al.* Exciton versus Free Carrier Photogeneration in Organometal Trihalide Perovskites Probed by Broadband Ultrafast Polarization Memory Dynamics. *Physical Review Letters* **114**, 116601 (2015).
- 270 Deng, X. *et al.* Ultrafast Carrier Dynamics in Methylammonium Lead Bromide Perovskite. *The Journal of Physical Chemistry C* **120**, 2542-2547, doi:10.1021/acs.jpcc.5b11640 (2016).
- 271 Wu, X. *et al.* Trap States in Lead Iodide Perovskites. *Journal of the American Chemical Society* **137**, 2089-2096, doi:10.1021/ja512833n (2015).
- 272 Gratzel, M. The light and shade of perovskite solar cells. *Nat Mater* **13**, 838-842, doi:10.1038/nmat4065 (2014).
- 273 D'Innocenzo, V. *et al.* Excitons versus free charges in organo-lead tri-halide perovskites. *Nature Communications* **5**, 3586, doi:10.1038/ncomms4586 <http://www.nature.com/articles/ncomms4586#supplementary-information> (2014).
- 274 Wang, W. *et al.* Dynamical co-existence of excitons and free carriers in perovskite probed by density-resolved fluorescent spectroscopic method. *ArXiv* (2016).
- 275 Tanaka, K. *et al.* Comparative study on the excitons in lead-halide-based perovskite-type crystals CH<sub>3</sub>NH<sub>3</sub>PbBr<sub>3</sub> CH<sub>3</sub>NH<sub>3</sub>PbI<sub>3</sub>. *Solid State Communications* **127**, 619-623, doi:[http://dx.doi.org/10.1016/S0038-1098\(03\)00566-0](http://dx.doi.org/10.1016/S0038-1098(03)00566-0) (2003).

- 276 D'Innocenzo, V. *et al.* Excitons versus free charges in organo-lead tri-halide perovskites. *Nature Communications* **5**, doi:Artn 3586 10.1038/Ncomms4586 (2014).
- 277 Yang, Y. *et al.* Comparison of Recombination Dynamics in CH<sub>3</sub>NH<sub>3</sub>PbBr<sub>3</sub> and CH<sub>3</sub>NH<sub>3</sub>PbI<sub>3</sub> Perovskite Films: Influence of Exciton Binding Energy. *The Journal of Physical Chemistry Letters* **6**, 4688-4692, doi:10.1021/acs.jpcllett.5b02290 (2015).
- 278 Zheng, K. B. *et al.* Exciton Binding Energy and the Nature of Emissive States in Organometal Halide Perovskites. *J Phys Chem Lett* **6**, 2969-2975, doi:10.1021/acs.jpcllett.5b01252 (2015).
- 279 Makarov, N. S. *et al.* Spectral and Dynamical Properties of Single Excitons, Biexcitons, and Trions in Cesium–Lead–Halide Perovskite Quantum Dots. *Nano Letters*, doi:10.1021/acs.nanolett.5b05077 (2016).
- 280 Wei, K., Zheng, X., Cheng, X., Shen, C. & Jiang, T. Observation of Ultrafast Exciton–Exciton Annihilation in CsPbBr<sub>3</sub> Quantum Dots. *Advanced Optical Materials* **4**, 1993-1997, doi:10.1002/adom.201600352 (2016).
- 281 Wang, Y. *et al.* Nonlinear Absorption and Low-Threshold Multiphoton Pumped Stimulated Emission from All-Inorganic Perovskite Nanocrystals. *Nano Letters* **16**, 448-453, doi:10.1021/acs.nanolett.5b04110 (2016).
- 282 Wu, K. F. *et al.* Ultrafast Interfacial Electron and Hole Transfer from CsPbBr<sub>3</sub> Perovskite Quantum Dots. *Journal of the American Chemical Society* **137**, 12792-12795, doi:10.1021/jacs.5b08520 (2015).
- 283 McArthur, E. A., Morris-Cohen, A. J., Knowles, K. E. & Weiss, E. A. Charge Carrier Resolved Relaxation of the First Excitonic State in CdSe Quantum Dots Probed with Near-Infrared Transient Absorption Spectroscopy. *The Journal of Physical Chemistry B* **114**, 14514-14520, doi:10.1021/jp102101f (2010).
- 284 Singh, J. *Excitation Energy Transfer Processes in Condensed Matter: Theory and Applications*. (Springer US, 1994).
- 285 Shimizu, A. Optical Nonlinearity Induced by Giant Dipole Moment of Wannier Excitons. *Physical Review Letters* **61**, 613-616 (1988).
- 286 Warburton, R. J. *et al.* Giant permanent dipole moments of excitons in semiconductor nanostructures. *Physical Review B* **65**, 113303 (2002).
- 287 Bechstedt, F. *Many-Body Approach to Electronic Excitations: Concepts and Applications*. (Springer Berlin Heidelberg, 2014).
- 288 Lanzani, G. *The Photophysics Behind Photovoltaics and Photonics*. (Wiley, 2012).
- 289 Pelant, I. & Valenta, J. *Luminescence Spectroscopy of Semiconductors*. (OUP Oxford, 2012).
- 290 De Roo, J. *et al.* Highly Dynamic Ligand Binding and Light Absorption Coefficient of Cesium Lead Bromide Perovskite Nanocrystals. *ACS Nano* **10**, 2071-2081, doi:10.1021/acsnano.5b06295 (2016).

- 291 Marciniak, H. & Lochbrunner, S. On the interpretation of decay associated spectra in the presence of time dependent spectral shifts. *Chemical Physics Letters* **609**, 184-188, doi:<http://dx.doi.org/10.1016/j.cplett.2014.05.006> (2014).
- 292 Piatkowski, P., Cohen, B., Kazim, S., Ahmad, S. & Douhal, A. How photon pump fluence changes the charge carrier relaxation mechanism in an organic-inorganic hybrid lead triiodide perovskite. *Physical Chemistry Chemical Physics*, doi:10.1039/C6CP02682F (2016).
- 293 De Wolf, S. *et al.* Organometallic Halide Perovskites: Sharp Optical Absorption Edge and Its Relation to Photovoltaic Performance. *J Phys Chem Lett* **5**, 1035-1039, doi:10.1021/jz500279b (2014).
- 294 Sadhanala, A. *et al.* Preparation of Single-Phase Films of CH<sub>3</sub>NH<sub>3</sub>Pb(I<sub>1-x</sub>Br<sub>x</sub>)(3) with Sharp Optical Band Edges. *J Phys Chem Lett* **5**, 2501-2505, doi:10.1021/jz501332v (2014).
- 295 Wehrenfennig, C., Eperon, G. E., Johnston, M. B., Snaith, H. J. & Herz, L. M. High Charge Carrier Mobilities and Lifetimes in Organolead Trihalide Perovskites. *Advanced Materials* **26**, 1584-1589, doi:10.1002/adma.201305172 (2014).
- 296 Dong, Q. F. *et al.* Electron-hole diffusion lengths > 175  $\mu$  m in solution-grown CH<sub>3</sub>NH<sub>3</sub>PbI<sub>3</sub> single crystals. *Science* **347**, 967-970, doi:10.1126/science.aaa5760 (2015).
- 297 Shi, D. *et al.* Low trap-state density and long carrier diffusion in organolead trihalide perovskite single crystals. *Science* **347**, 519-522, doi:10.1126/science.aaa2725 (2015).
- 298 Saidaminov, M. I. *et al.* High-quality bulk hybrid perovskite single crystals within minutes by inverse temperature crystallization. *Nature Communications* **6**, 7586, doi:Artn 7586 10.1038/Ncomms8586 (2015).
- 299 Saba, M. *et al.* Correlated electron-hole plasma in organometal perovskites. *Nature Communications* **5**, doi:Artn 5049 10.1038/Ncomms6049 (2014).
- 300 Antonietta Loi, M. & Hummelen, J. C. Hybrid solar cells: Perovskites under the Sun. *Nat Mater* **12**, 1087-1089, doi:10.1038/nmat3815 (2013).
- 301 Malinkiewicz, O. *et al.* Perovskite solar cells employing organic charge-transport layers. *Nat Photon* **8**, 128-132, doi:10.1038/nphoton.2013.341 <http://www.nature.com/nphoton/journal/v8/n2/abs/nphoton.2013.341.html#supplementary-information> (2014).
- 302 Liu, D. & Kelly, T. L. Perovskite solar cells with a planar heterojunction structure prepared using room-temperature solution processing techniques. *Nat Photon* **8**, 133-138, doi:10.1038/nphoton.2013.342 <http://www.nature.com/nphoton/journal/v8/n2/abs/nphoton.2013.342.html#supplementary-information> (2014).
- 303 Zhang, W. *et al.* Enhancement of Perovskite-Based Solar Cells Employing Core-Shell Metal Nanoparticles. *Nano Letters* **13**, 4505-4510, doi:10.1021/nl4024287 (2013).



- 304 Sun, S. *et al.* The origin of high efficiency in low-temperature solution-processable bilayer organometal halide hybrid solar cells. *Energy & Environmental Science* **7**, 399-407, doi:10.1039/C3EE43161D (2014).
- 305 Savenije, T. J. *et al.* Thermally Activated Exciton Dissociation and Recombination Control the Carrier Dynamics in Organometal Halide Perovskite. *The Journal of Physical Chemistry Letters* **5**, 2189-2194, doi:10.1021/jz500858a (2014).
- 306 Wen, X. M. *et al.* Defect trapping states and charge carrier recombination in organic-inorganic halide perovskites. *J Mater Chem C* **4**, 793-800, doi:10.1039/c5tc03109e (2016).
- 307 He, H. *et al.* Exciton localization in solution-processed organolead trihalide perovskites. *Nat Commun* **7**, doi:10.1038/ncomms10896 (2016).
- 308 Shkrob, I. A. & Marin, T. W. Charge Trapping in Photovoltaically Active Perovskites and Related Halogenoplumbate Compounds. *J Phys Chem Lett* **5**, 1066-1071, doi:10.1021/jz5004022 (2014).
- 309 Wong, J., Lytle, F. W., Messmer, R. P. & Maylotte, D. H. K-Edge Absorption-Spectra of Selected Vanadium Compounds. *Physical Review B* **30**, 5596-5610 (1984).
- 310 Dangelo, P., Dinola, A., Filipponi, A., Pavel, N. V. & Roccatano, D. An Extended X-Ray-Absorption Fine-Structure Study of Aqueous-Solutions by Employing Molecular-Dynamics Simulations. *J Chem Phys* **100**, 985-994, doi:10.1063/1.466581 (1994).
- 311 Filipponi, A. & D' Angelo, P. D. Accurate determination of molecular structures by x-ray absorption spectroscopy. *J Chem Phys* **109**, 5356-5362, doi:10.1063/1.477154 (1998).
- 312 Bordage, A. *et al.* On the sensitivity of hard X-ray spectroscopies to the chemical state of Br. *Physical Chemistry Chemical Physics* **15**, 11088-11098, doi:10.1039/c3cp50367d (2013).
- 313 Gawelda, W. *et al.* Structural determination of a short-lived excited iron(II) complex by picosecond x-ray absorption spectroscopy. *Physical Review Letters* **98**, doi:10.1103/PhysRevLett.98.057401 057401 (2007).
- 314 Bressler, C. *et al.* Femtosecond XANES Study of the Light-Induced Spin Crossover Dynamics in an Iron(II) Complex. *Science* **323**, 489-492, doi:10.1126/science.1165733 (2009).
- 315 Yu, P. Y. & Cardona, M. *Fundamentals of semiconductors : physics and materials properties*. 4th edn, (Springer, 2010).
- 316 Zhu, Q. *et al.* Correlating structure and electronic band-edge properties in organolead halide perovskites nanoparticles. *Physical Chemistry Chemical Physics* **18**, 14933-14940, doi:10.1039/C6CP01843B (2016).
- 317 Elles, C. G., Shkrob, I. A., Crowell, R. A., Arms, D. A. & Landahl, E. C. Transient x-ray absorption spectroscopy of hydrated halogen atom. *J Chem Phys* **128**, doi:10.1063/1.2827456 061102 (2008).

- 318 Pham, V. T. *et al.* Probing the Transition from Hydrophilic to Hydrophobic Solvation with Atomic Scale Resolution. *Journal of the American Chemical Society* **133**, 12740-12748, doi:Doi 10.1021/Ja203882y (2011).
- 319 Gawelda, W. *et al.* Electronic and molecular structure of photoexcited [Ru-II(bpy)(3)](2+) probed by picosecond X-ray absorption spectroscopy. *Journal of the American Chemical Society* **128**, 5001-5009, doi:10.1021/ja054932k (2006).
- 320 Reinhard, M. *et al.* Photooxidation and photoaquation of iron hexacyanide in aqueous solution: A picosecond X-ray absorption study. *Struct Dynam-Us* **1**, doi:Artn 024901 10.1063/1.4871751 (2014).
- 321 Wen, X. *et al.* Defect trapping states and charge carrier recombination in organic-inorganic halide perovskites. *J Mater Chem C* **4**, 793-800, doi:10.1039/C5TC03109E (2016).
- 322 Hutter, E. M., Eperon, G. E., Stranks, S. D. & Savenije, T. J. Charge Carriers in Planar and Meso-Structured Organic-Inorganic Perovskites: Mobilities, Lifetimes, and Concentrations of Trap States. *The Journal of Physical Chemistry Letters* **6**, 3082-3090, doi:10.1021/acs.jpcllett.5b01361 (2015).
- 323 Karki, K. J., Abdellah, M., Zhang, W. & Pullerits, T. Different emissive states in the bulk and at the surface of methylammonium lead bromide perovskite revealed by two-photon micro-spectroscopy and lifetime measurements. *APL Photonics* **1**, 046103, doi:doi:<http://dx.doi.org/10.1063/1.4948645> (2016).
- 324 Merrien, N. *et al.* Redox Mechanisms and Density of Holes by Xas in the Compensated Series Bi<sub>2</sub>-Xpbxsr<sub>2</sub>ca<sub>1</sub>-Xyx<sub>2</sub>cu<sub>2</sub>o<sub>8</sub>+Delta (0-Less-Than-or-Equal-to-X-Less-Than-or-Equal-to-1). *J Solid State Chem* **105**, 112-129, doi:DOI 10.1006/jssc.1993.1199 (1993).
- 325 Swarbrick, J. C., Skyllberg, U., Karlsson, T. & Glatzel, P. High Energy Resolution X-ray Absorption Spectroscopy of Environmentally Relevant Lead(II) Compounds. *Inorg Chem* **48**, 10748-10756, doi:10.1021/ic9015299 (2009).
- 326 Xing, G. C. *et al.* Low-temperature solution-processed wavelength-tunable perovskites for lasing. *Nature Materials* **13**, 476-480, doi:10.1038/NMAT3911 (2014).
- 327 Johnson, S. L. *et al.* Properties of liquid silicon observed by time-resolved x-ray absorption spectroscopy. *Physical Review Letters* **91**, 157403 (2003).
- 328 Johnson, S. L. *et al.* Bonding in Liquid Carbon Studied by Time-Resolved X-Ray Absorption Spectroscopy. *Physical Review Letters* **94**, 057407 (2005).
- 329 Cavalleri, A. *et al.* Band-selective measurements of electron dynamics in VO<sub>2</sub> using femtosecond near-edge x-ray absorption. *Physical Review Letters* **95**, doi:Artn 067405 Doi 10.1103/Physrevlett.95.067405 (2005).
- 330 Fons, P., Brewe, D., Stern, E., Kolobov, A. V. & Tominaga, J. Understanding structural changes in phase change memory alloys. *Mater Res Soc Symp P* **918**, 147-156 191 (2006).



- 
- 331 Stern, E. A. & Brews, D. Ultrafast XAFS measurements on laser excited Ge films. *Aip Conf Proc* **882**, 24-28 937 (2007).
- 332 Carbone, F., Kwon, O. H. & Zewail, A. H. Dynamics of Chemical Bonding Mapped by Energy-Resolved 4D Electron Microscopy. *Science* **325**, 181-184, doi:DOI 10.1126/science.1175005 (2009).
- 333 Carbone, F. *et al.* EELS femtosecond resolved in 4D ultrafast electron microscopy. *Chemical Physics Letters* **468**, 107-111, doi:DOI 10.1016/j.cplett.2008.12.027 (2009).
- 334 van der Veen, R. M., Penfold, T. J. & Zewail, A. H. Ultrafast core-loss spectroscopy in four-dimensional electron microscopy. *Struct Dynam-Us* **2**, 024302, doi:doi:<http://dx.doi.org/10.1063/1.4916897> (2015).
- 335 Carbone, F. Dynamics deep from the core. *Struct Dynam-Us* **2**, 020601, doi:doi:<http://dx.doi.org/10.1063/1.4918727> (2015).
- 336 Chen, K., Barker, A. J., Morgan, F. L. C., Halpert, J. E. & Hodgkiss, J. M. Effect of Carrier Thermalization Dynamics on Light Emission and Amplification in Organometal Halide Perovskites. *The Journal of Physical Chemistry Letters* **6**, 153-158, doi:10.1021/jz502528c (2015).
- 337 HarmandM *et al.* Achieving few-femtosecond time-sorting at hard X-ray free-electron lasers. *Nat Photon* **7**, 215-218, doi:<http://www.nature.com/nphoton/journal/v7/n3/abs/nphoton.2013.11.html#supplementary-information> (2013).
- 338 Milne, C. J. *et al.* in *19th International Conference on Ultrafast Phenomena*. 09.Wed.D.01 (Optical Society of America).
- 339 Al Haddad, A. *et al.* Set-up for broadband Fourier-transform multidimensional electronic spectroscopy. *Opt. Lett.* **40**, 312-315, doi:10.1364/OL.40.000312 (2015).
- 340 Grégoire, P. *et al.* in *CMDS 2016* (Groningen, 2016).



## CURRICULUM VITAE

Ch. de Champvent 10, Jouxkens-Mézery 1008 | +41 78 8888 270 | [fgsantomauro@gmail.com](mailto:fgsantomauro@gmail.com)

### PERSONAL DETAILS

Date of birth: 28<sup>th</sup> of February 1988

Nationality: Italian

### EDUCATION

École Polytechnique Fédérale de Lausanne (EPFL)

**Ph.D. in Photonics**

**2012-present**

University of Milan

**Master in Industrial Chemistry and Management**, summa cum laude

**2010-2012**

Exchange for 5 months at the Department of Chemistry and Applied Biosciences, **ETH Zürich**

University of Milan

**Bachelor in Industrial Chemistry**, summa cum laude

**2007-2010**

Military School Teulié, Milan

**Matura**

**2004-2007**

### EMPLOYMENT

Research assistant

**EPFL and Paul Scherrer Institute**

**2012-present**

Intern (MSc)

**University of Milan and ETH Zürich**

**2011-2012**

Intern

**Viba S.p.A.** – R&D department

**09.2010**

Intern (BSc)

**Institute of Molecular Science and Technologies (IST-CNR)**

**4.2010-7.2010**

Cadet instructor

**Military School Teulié**

**2006-2007**

### AWARDS

Merit Scholarship

**2010**

Merit Scholarship

**2009**

## LANGUAGES

**Italian** mother tongue

**English** fluent

**French** intermediate

**German** basic

## PUBLICATIONS

“Localized holes and delocalized electrons in photoexcited inorganic perovskites: Watching each atomic actor by picosecond X-ray absorption spectroscopy”, F. G. Santomauro, J. Grilj, L. Mewes, G. Nedelcu, S. Yakunin, T. Rossi, G. Capano, A. Al Haddad, J. Budarz, D. Kinschel, D. S. Ferreira, G. Rossi, M. Gutierrez Tovar, D. Grolimund, V. Samson, M. Nachtegaal, G. Smolentsev, M. V. Kovalenko, M. Chergui, *arXiv:1610.02231*, 2016

“Enhancement of UV Photo-catalytic Activity in Greenly Modified Nano-TiO<sub>2</sub>”, F. G. Santomauro, S. Ahmadi, H. Rensmo, D. L. A. Fernandes, J. Sá, *Chemical and Materials Engineering* 4(1), 1-7, 2016

“Femtosecond X-ray absorption study of electron localization in photoexcited anatase TiO<sub>2</sub>”, F. G. Santomauro, A. Lübcke, J. Rittmann, E. Baldini, A. Ferrer, M. Silatani, P. Zimmermann, S. Grübel, J. A. Johnson, S. O. Mariager, P. Beaud, D. Grolimund, C. Borca, G. Ingold, S.L. Johnson, M. Chergui, *Scientific Reports* 5: 14834, 2015

“Hunting for the elusive shallow traps in TiO<sub>2</sub> anatase”, L. J. Antila, F. G. Santomauro, L. Hammarström, D. L. A. Fernandes, J. Sá, *Chemical Communications*, 51: 10914-10916, 2015

“Multifunctional Catalysis Promoted by Solvent Effects: Ti-MCM41 for a One-Pot, Four-Step, Epoxidation–Rearrangement–Oxidation–Decarboxylation Reaction Sequence on Stilbenes and Styrenes”, J. M. Fraile, N. García, J. A. Mayoral, F. G. Santomauro, M. Guidotti, *ACS Catalysis*, 5(6): 3552–3561, 2015

“Time-resolved X-ray absorption and emission spectroscopy on ZnO nanoparticles in solution”, C. J. Milne, J. Szlachetko, T. Penfold, F. G. Santomauro, A. Britz, W. Gawelda, G. Doumy, A. M. March, S. H. Southworth, J. Rittmann, M. Chergui, R. Abela, *19th International Conference on Ultrafast Phenomena*, OSA, 2014

“Direct observation of charge separation on Au localized surface plasmons”, J. Sá, G. Tagliabue, P. Friedli, J. Szlachetko, M. H. Rittmann-Frank, F. G. Santomauro, C. J. Milne, H. Sigg, *Energy and Environmental Science*, 6: 3584-3588, 2013

“Transient mid-IR study of electron dynamics in TiO<sub>2</sub> conduction band”, J. Sá, P. Friedli, R. Geiger, P. Lerch, M. H. Rittmann-Frank, C. J. Milne, J. Szlachetko, F. G. Santomauro, J. A. van Bokhoven, M. Chergui, M. J. Rossi, H. Sigg, *Analyst*, 138: 1966-1970, 2013

